Process development and digitalization of laser-directed energy deposition processing high-strength 7XXX series aluminum alloy

Vom Promotionsausschuss der

Technischen Universität Hamburg

zur Erlangung des akademischen Grades

Doktor-Ingenieur (Dr.-Ing.)

genehmigte Dissertation (kumulativ)

von

Mengjie Wang

aus

Anhui, China

2024

1. Gutachter: Herr PD Dr.-Ing. Nikolai Kashaev

2. Gutachter: Herr Prof. Dr.-Ing. Jean Pierre Bergmann

Tag der mündlichen Prüfung: 11.06.2024

Acknowledgements

Times flies. It has been seven years since I came to Germany to study. During these seven years of study, I am glad that I have found the direction in which I want to dedicate myself for a lifetime. Throughout this journey, I am sincerely grateful to those who have kindly offered me guidance, support, and encouragement.

Primarily, I would like to thank my supervisor, Dr.-Ing. Nikolai Kashaev. He offered me the opportunity to pursue my Ph.D. study. He provides me with enough autonomy to choose the research direction that interested and offered maximum support throughout the research process. I am honored to be able to work in his department.

I sincerely express my gratitude to my colleagues in the WDF department for their scientific and technical support: Dr. Volker Ventzke, René Dinse, Falk Dorn, Stefan Riekehr, Dr. Nowfal Al-Hamdany, Christian Knothe-Horstmann, Siva Teja Sala, Ruslan Kuliiev, Anton Odermatt, Hamdi, Tek, Kay Erdmann, Mirco Erdmann, Jürgen Knaack.

I also appreciate my Chinese friends at Hereon. We have had many enjoyable times together, which have helped me release pressure and overcome difficulties. Special thanks to Dr. Cheng Wang, who was the first Chinese friend I met at Hereon. We hang out on weekends and enjoy food in Hamburg. He shares many interesting things with me and provides assistance in scientific research.

Last but certainly not least, I would like to express my gratitude to my parents for their supports. While they may not understand my experiments, they excel at being the best parents, even though it was their first time being parents.

Geesthacht, 13.06.2024 Mengjie Wang

Abstract

Additive manufacturing has gained considerable attention from both industry and academia in recent years, primarily due to its numerous advantages over conventional subtractive manufacturing technologies. The layer-by-layer deposition process in additive manufacturing offers substantial design freedom, which proves advantageous for weight reduction, improving manufacturability for structures with intricate geometries, and cost-saving. In fusion-based additive manufacturing, materials undergo a process of melting and solidification. The energy sources used for melting materials include laser, arc, and electron beam. Laser-based additive manufacturing has gained widespread popularity due to its ability to operate without a vacuum atmosphere, unlike electron-beam melting, and its superior geometrical accuracy compared with arc-based additive manufacturing.

Lightweight materials and designs are in high demand in the automobile and aerospace industries because of their potential to reduce carbon emissions and minimize environmental impacts. Aluminum alloys with a high density-strength ratio are commonly utilized as lightweight materials. However, the range of applicable Al alloys in laser-based additive manufacturing is limited due to various processing challenges. These challenges include issues such as oxidation, high reflectivity, porosity formation, and cracking susceptibility. Therefore, it is crucial to address these challenges and establish an optimal process window for Al alloys in laser-based additive manufacturing. Al-Zn-Mg-Cu alloys, also known as 7XXX series alloys, are precipitation-strengthening alloys that demonstrate superior strength characteristics when subjected to appropriate ageing treatment. The rapid heating and cooling involved in laser-based additive manufacturing can be advantageous for processing 7XXX series alloys. The non-equilibrium solidification resulting from the rapid cooling promotes grain refinement and increases the solubility of solutes in the α-Al matrix, thereby enhancing the precipitation-strengthening effects during ageing treatment. Consequently, it is valuable to explore the processability of 7XXX series alloys in laser-based additive manufacturing.

The primary objective of this thesis is to develop an appropriate process window for laser-directed energy deposition (L-DED) in order to process high-strength 7XXX series alloys. Furthermore, the aim is to investigate the relationship between process-microstructure-property. Additionally, considerable attention has been given to understanding the mechanism behind defect formation, specifically porosity and cracks.

7XXX series alloys are processed using wire- and powder-based L-DED, respectively. When it comes to structural integrity, specifically in terms of porosity levels and cracking, wire-based feedstock demonstrates superior processability compared with powder-based feedstock. The high porosity levels observed in structures produced by powder-based L-DED are attributed to two main factors: the presence of intrinsic pores inside powder materials and the evaporation of volatile alloying elements during processing. The installation of a self-designed shielding gas nozzle in wire-based L-DED has been found to greatly improve surface roughness, reduce porosity levels, and enhance processing stability. A delayed hot cracking is noticed in wire-based L-DED processing high-strength Al alloys. The delayed hot cracking is correlated to the deposition length of structures and the number of deposited layers. After

conducting a comprehensive analysis of the solidification conditions captured by an infrared thermal camera, microstructural characterization, and residual stress analyzed using high-energy synchrotron X-ray diffraction, it has been determined that the initiation mechanism behind delayed hot cracking in wire-based L-DED is attributed to inadequate backfilling to shrinkage during solidification. This insufficient backfilling results in solidification cracking. Additionally, the competitive growth pattern observed between grains with a preferential growth direction and other misaligned grains relative to the heat flow direction contributes to the occurrence of delayed cracking. Regarding the mechanical properties, as-built structures produced using wire-based L-DED exhibit superior strength while maintaining a satisfactory level of ductility. The superior mechanical properties observed in wire-based L-DED structures can be attributed to two main factors. Firstly, the cyclic heating effects that occur during successive deposition to previously solidified layers act as an ageing treatment leading to the precipitation of strengthening phases. Secondly, the presence of large columnar grains with an epitaxial growth pattern dominates the microstructure, further enhancing the overall strength of the material.

Process monitoring and quality control are two prominent areas of research in additive manufacturing, particularly for achieving consistent properties in structures intended for serial production and industrialization. Existing methodologies rely on machine learning algorithms for post-process quality control, which can aid in ensuring quality and optimizing resource utilization. Nevertheless, these methods cannot prevent material waste since they are implemented after the structures have already been produced.

Another objective of this thesis is to leverage machine learning algorithms for in-situ adjustment of process parameters in laser-based additive manufacturing, to ensure processing stability.

The high-speed camera captures processing images that contain various characteristics, including the melt pool, plume, and spatter. These characteristics exhibit distinct patterns under different processing states. To effectively analyze and classify these images, a convolutional neural network is employed. The convolutional neural network is trained to learn and recognize the specific characteristics of the process images, enabling it to accurately identify the corresponding processing states. The successful categorization of processing states through the identification of processing images using a convolutional neural network has been validated. This enables the in-situ adjustment of process parameters based on the current processing states, thereby ensuring the maintenance of processing stability. As a result, a consistent quantity and distribution of porosity level can be achieved across various deposition layers.

It can be concluded through the comprehensive analysis conducted in this thesis regarding the L-DED processing high-strength 7XXX series Al alloys as follows: It has been demonstrated that using wire as the feedstock in L-DED shows better processability than using powder. Crack-free thin-wall structures with low porosity levels can be built in wire-based L-DED while achieving a good combination of strength and ductility in these structures simultaneously. Additionally, a methodology involving process monitoring and machine learning has been proposed and proven to be effective in maintaining processing stability and consistency.

Zusammenfassung

In den letzten Jahren hat die additive Fertigung sowohl in der Industrie als auch in der Wissenschaft erhebliche Aufmerksamkeit erlangt. Dies liegt vor allem an den zahlreichen Vorteilen, die sie im Vergleich zu herkömmlichen subtraktiven Fertigungstechnologien bietet. Durch das schichtweise Auftragen ermöglicht die additive Fertigung eine große Gestaltungsfreiheit, was sich positiv auf Gewichtsreduzierung, Herstellbarkeit von Bauteilen mit komplexer Geometrie und Kosteneinsparung auswirkt. Bei der schmelzbasierten additiven Fertigung werden die Materialien geschmolzen und wieder erstarrt. Als Energiequelle für den Schmelzprozess kommen Laser, Lichtbogen und Elektronenstrahl zum Einsatz. Die laserbasierte additive Fertigung ist heute weit verbreitet, da sie im Gegensatz zum Elektronenstrahl keine Vakuumatmosphäre erfordert und eine bessere geometrische Genauigkeit als die lichtbogenbasierte additive Fertigung bietet.

Leichtbauwerkstoffe und -konstruktionen sind in der Automobil-, Luft- und Raumfahrtindustrie sehr gefragt, da sie den Kohlenstoffausstoß verringern und negative Umweltauswirkungen minimieren können. Aluminiumlegierungen mit einem hohen Dichte-Festigkeits-Verhältnis gehören zu den typischen Leichtbaumaterialien. Obwohl es zahlreiche Aluminiumlegierungen für spezifische Anwendungen gibt, sind die in der laserbasierten additiven Fertigung verwendbaren Aluminiumlegierungen begrenzt. Al-Zn-Mg-Cu-Legierungen (7XXX-Serie) sind ausscheidungshärtende Legierungen, die nach einer geeigneten Auslagerungsbehandlung eine hohe Festigkeit aufweisen. Schnelle Erwärmung und Abkühlung in der laserbasierten additiven Fertigung bieten Vorteile für die Verarbeitung von Aluminiumlegierungen der 7XXX-Serie. Durch die schnelle Abkühlung kommt es zu einer Nichtgleichgewichtserstarrung, was zu einer Kornfeinung führt und die Löslichkeit von gelösten Stoffen in der α-Al-Matrix erhöht. Dadurch werden die ausscheidungsfestigenden Effekte während der Auslagerungsbehandlung verstärkt. Daher ist es sinnvoll, die Verarbeitbarkeit von Aluminiumlegierungen der 7XXX-Serie in der laserbasierten additiven Fertigung genauer zu untersuchen.

Eines der Ziele der vorliegenden Arbeit besteht darin, ein geeignetes Prozessfenster für das Laserauftragschweißen von hochfesten Aluminiumlegierungen der 7XXX-Serie zu entwickeln und die Korrelation zwischen Prozess, Mikrostruktur und Eigenschaft aufzuzeigen. Ein weiterer Schwerpunkt liegt auf dem Verständnis des Mechanismus der Defektbildung, insbesondere von Porosität und Rissen.

Die Legierungen der 7XXX-Serie werden mit draht- und pulverbasiertem Laserauftragschweißen verarbeitet. Im Vergleich zu Pulver als Ausgangsmaterial weist Draht eine bessere Verarbeitbarkeit hinsichtlich struktureller Integrität, insbesondere in Bezug auf Porosität und Rissbildung auf. Die hohe Porosität in pulverbasierten laserauftragschweißten Strukturen ist auf die intrinsischen Poren in den Pulverpartikeln und die Verdampfung flüchtiger Legierungselemente während der Verarbeitung zurückzuführen. Durch Installation einer selbst entworfenen Schutzgasdüse für drahtbasiertes Laserauftragschweißen werden Oberflächenrauheit, Porosität und Verarbeitungsstabilität erheblich verbessert. Beim drahtbasierten Laserauftragschweißen von hochfesten Aluminiumlegierungen wird eine

verzögerte Heißrissbildung beobachtet. Diese verzögerte Heißrissbildung korreliert mit der Spurlänge der Strukturen und der Anzahl der aufgetragenen Schichten. Nach der Analyse wird festgestellt, dass der Mechanismus der verzögerten Heißrissbildung auf eine unzureichende Auffüllung der Volumendefizite bei der Schrumpfung während der Erstarrung zurückzuführen ist, was zur Erstarrungsrissbildung führt. Das konkurrierende Wachstumsmuster zwischen Körnern mit bevorzugter Wachstumsrichtung und anderen ausgerichteten Körnern relativ zur Wärmestromrichtung trägt zur verzögerten Rissbildung bei. In Bezug auf die mechanischen Eigenschaften weisen die mit drahtbasiertem Laserauftragschweißen hergestellten Strukturen eine überlegene Festigkeit auf, ohne dass dies auf Kosten der Duktilität geht. Dies wird auf zwei Gründe zurückgeführt: Zum einen wirken die zyklischen Aufwärmungseffekte während des aufeinanderfolgenden Auftragens auf zuvor erstarrte Lagen wie eine Auslagerungsbehandlung, was zur Ausscheidung von Verfestigungsphasen führt. Zum anderen dominieren große säulenförmige Körner mit epitaxischem Wachstumsmuster die Mikrostruktur.

Die Prozessüberwachung und Qualitätskontrolle bei der additiven Fertigung sind zwei wichtige Forschungsthemen, da die Eigenschaftskonsistenz von Strukturen für die Serienproduktion und Industrialisierung entscheidend ist. Aktuelle Methoden, die auf Algorithmen des maschinellen Lernens basieren, werden als Post-Prozess-Qualitätskontrolle eingesetzt. Sie können die Qualitätskontrolle unterstützen und Ressourcen einsparen. Allerdings konnen sie nicht vermeiden, dass Material nach der Herstellung der Strukturen verschwendet wird.

Ein weiteres Ziel der vorliegenden Arbeit besteht darin, Algorithmen des maschinellen Lernens zur Aufrechterhaltung der Prozessstabilität durch In-situ-Anpassung der Prozessparameter in der laserbasierten additiven Fertigung einzusetzen.

Die von einer Hochgeschwindigkeitskamera aufgenommenen Verarbeitungsbilder enthalten verschiedene Verarbeitungsmerkmale wie Schmelzbad, Fackel und Spritzer. Diese Verarbeitungsmerkmale unterscheiden sich je nach Verarbeitungszustand. Um diese Merkmale zu lernen und die entsprechenden Verarbeitungszustände zu identifizieren, wird ein Convolutional Neural Network zur Klassifizierung eingesetzt. Es hat sich gezeigt, dass die Verarbeitungszustände erfolgreich kategorisiert werden können, indem die Verarbeitungsbilder mithilfe des Neural Network identifiziert werden. Basierend auf den aktuellen Verarbeitungszuständen können die Prozessparameter in Echtzeit angepasst werden, um die Prozessstabilität aufrechtzuerhalten. Dadurch wird eine gleichbleibende Menge und Verteilung der Porosität in den verschiedenen Auftragslagen erreicht.

Die in dieser Arbeit durchgeführte umfassende Analyse der L-DED-Verarbeitung von hochfesten Al-Legierungen der 7XXX-Serie lässt folgende Schlussfolgerungen zu: Die Verwendung von Draht als Ausgangsmaterial in der L-DED weist eine bessere Verarbeitbarkeit auf als die Verwendung von Pulver. Rissfreie dünnwandige Strukturen mit geringer Porosität können im drahtbasierten L-DED hergestellt werden, wobei gleichzeitig eine gute Kombination von Festigkeit und Duktilität in diesen Strukturen erreicht wird. Darüber hinaus wurde eine Methodik zur Prozessüberwachung und zum maschinellen Lernen vorgeschlagen, die sich als wirksam für die Aufrechterhaltung der Verarbeitungsstabilität und -konsistenz erwiesen hat.

Content

Nomenclature

Variables and material parameters

P_m	(Pa/MPa)	Liquid static pressure
P_c	(Pa/MPa)	Capillary pressure
ΔP_ε	(Pa/MPa)	Pressure drops due to thermal contraction
ΔP_{sh}	(Pa/MPa)	Pressure drops due to solidification shrinkage
UTS	(MPa)	Ultimate tensile strength
YS	(MPa)	Yield strength
A_f	(%)	Fracture strain
k_y	(–)	Hall-Petch coefficient
$\Delta\sigma_{gb}$	(MPa)	Strength resulting from grain refinement
R_{max}	(mm)	Maximum roughness
σ_{xx}	(MPa)	Residual stress along the longitudinal direction
σ_{yy}	(MPa)	Residual stress along the building direction
FPS	(–)	Frames per second
k value	(–)	Ratio of wire feed speed and laser scan speed
E_M	(kJ/g)	Specific energy
v_w	(mm/min)	Wire feed speed
v_s	(mm/min)	Laser scan speed
$\dot{m}$	(g/min)	Mass flow of the wire
P	(W)	Laser power
TEI	(kJ)	Total energy input
VED	(J/mm^3)	Volumetric energy density
LED	(J/mm)	Line energy density
v_{cool}	(K/s)	Cooling rate
TG	(K/mm)	Temperature gradient
f_s	(–)	Fraction of solid during solidification

Abbreviations

AM	Additive Manufacturing
L-DED	Laser-directed energy deposition
SLM	Selective laser melting
SLS	Selective laser sintering
DED	Directed energy deposition
HAZ	Heat-affected zone
ML	Machine learning
CNN	Convolutional neural network
EIGA	Electrode induction melting gas atomization
LSP	Laser shock peening
EHLA	Extreme high-speed laser material deposition
WAAM	Wire arc additive manufacturing
GRF	Growth restriction factor
GP zone	Guinier-Preston zone
SCC	Stress corrosion cracking
PFZ	Particle-free zone
APB	Anti-phase boundary
FCC	Face-centered cubic
HIP	Hot isostatic pressing
SEM	Scanning electron microscopy
EDX	Energy-dispersive X-ray
EBSD	Electron backscatter diffraction
PID controller	Proportional-Integral-Derivative controller

1. Introduction

1.1. Research gaps

Metal additive manufacturing (AM) is a process that produces structures by building layers according to a 3D model [1]. This technology has gained significant attention from academic researchers and industries due to its ability to produce structures with complex geometries, reduce weight, and save costs [2]. The feedstock for metal AM can be in the form of wire or powder [1]. In powder-based AM, where a laser is used as an energy source, the powders either be fed through a nozzle (laser-directed energy deposition, L-DED) or spread like a powder bed (selective laser melting, SLM, and selective laser sintering, SLS) [1]. Lightweight materials and designs are in high demand in industries such as automobile and aerospace, as they can reduce carbon emissions and minimize environmental impacts. Aluminum alloys are particularly attractive due to their lightweight nature and high density-strength ratio [3]. However, despite the availability of various Al alloys designed for specific applications, such as casting and wrought Al alloys, the range of materials suitable for AM is still limited [4]. Most previous studies in the field of AM have primarily focused on the Si-rich Al alloys, see the publication number for different Al alloys in AM (Figure 1a) [5]. Nevertheless, high-strength alloys, such as those from the 7XXX series alloys, are extensively utilized in the automobile [6] and aerospace industries (Figure 1b) [7]. The 7XXX series alloys, known as precipitation-strengthening alloys, exhibit superior strength [8]. Despite their widespread use, these alloys have not been recognized as suitable materials for AM due to several challenges associated with processing 7XXX series alloys, including oxidation, porosity formation, and cracking susceptibility. In comparison to powder-bed AM technologies, L-DED has multiple application areas, such as coating [9], repairing [10], and building 3D structures without space restrictions [11]. To expand the range of applicable materials in L-DED and leverage the lightweight and high-strength properties of 7XXX series alloys, it is important to evaluate their processability and develop an appropriate process window.

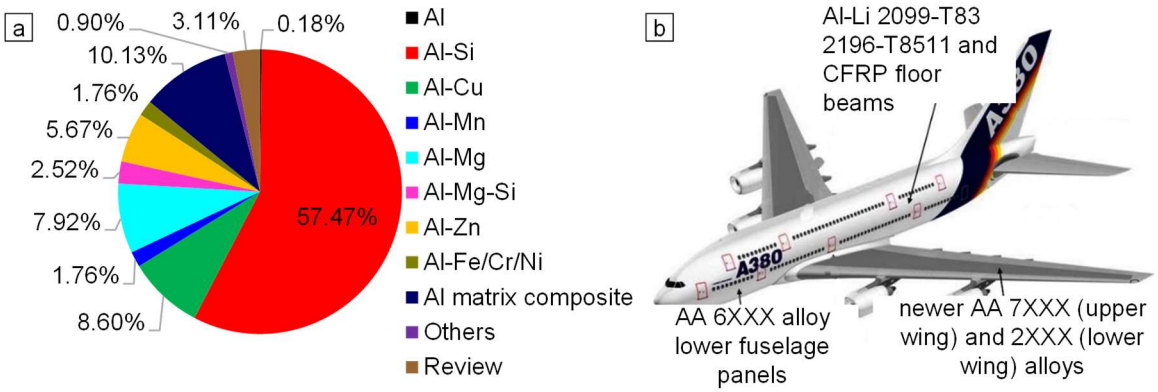

Figure 1. (a) Percentage of publication papers regarding the processing of different Al alloys in AM from year 2006 – 2022 [5]. (b) Component made of high-strength Al alloys in Airbus A380 (depicted and adopted from [7]).

Previous research has focused on studying the impact of process parameters on the buildability of structures. For instance, when the laser power is kept constant during the building of a thin-wall structure using L-DED, the arc-like morphology of deposited tracks could result in structural collapse [12] or uneven thickness along the building direction [13]. In addition, maintaining a constant laser power could result in heat accumulation and the formation of bumps at the start and the end of deposition tracks [14]. Various process parameters, including laser power, scan speed, powder feed rate, etc., play a crucial role in determining the properties of as-built structures. The performance of the L-DED processing is also influenced by the process systems (such as laser and nozzle) and powder quality. In L-DED, powders are delivered through a nozzle to the substrate using the carrier gas from the powder feeder. The movement of the nozzle and substrate is controlled by a CNC machine, a robot, or a combination of both during layer-by-layer deposition. The acceleration and deceleration phases in each parallel scanning path can also contribute to bump formation [15]. These challenges can be addressed through process parameter optimization, such as reducing laser power or increasing scan speed. Nevertheless, this optimization process typically requires numerous experimental iterations or the implementation of a sensor-based loop control system. The robot programs that control the motion of the nozzle and substrate, as well as the switch status of the laser and powder feeder, have not been systematically explored in previous studies. Therefore, it is worth investigating whether these issues can be alleviated or eliminated through improved control of robot programs and switch status. Furthermore, scanning strategies, which involve designing the path for building 3D structures, have been studied to understand their impact on residual stress, distortion, cracking resistance, microstructure, and mechanical properties. One approach involves using alternating scanning directions in different layers. By rotating the scanning direction between two adjacent layers, it is possible to reduce surface roughness [16], distortion [17], and texture heterogeneity [18] in as-built structures. The effects of scanning strategies have primarily been investigated in SLM. However, there are still lots of possibilities for exploring the impact of scanning strategy on the properties of structures produced using L-DED.

In wire-based L-DED processes, the wire can be fed laterally [19] or coaxially [20] in relation to the laser beam. To prevent oxidation, the shielding gas is used to create an inert gas atmosphere and protect deposited layers. In coaxially wire-based L-DED, the shielding gas can be conveyed through the optic head to protect the deposition from the top. The lateral L-DED setup can be adapted from a laser welding apparatus [21], where high flexibility in path direction is not required. In this case, the shielding gas is conveyed through the wire feed nozzle, similar to a welding apparatus [22]. Previous studies have shown that a side-feeding strategy should be employed to avoid wire entanglement during back feeding and prevent oxidized metal vapor from falling onto the track surface during front feeding [23]. In this case, Ar is conveyed through the wire feed nozzle and directed towards one side of the built thin-wall structures, creating an asymmetrical flow relative to the melt pools during processing. The impact of shielding gas on the directed energy deposition (DED) process and the properties of as-built specimens, such as geometry and porosity level, have been extensively studied, with particular attention given to the flow rate of shielding gas [24-26]. In most DED processes, the shielding gas is coaxially conveyed through the optic head and symmetrically blown from the top onto the melt-pool surface [24, 27]. To achieve a symmetrical blowing direction in a modified laser welding apparatus, additional components would need to be purchased to

enable the coaxial conveying of shielding gas through the optic head. Considering the known effects of blowing directions in single-track deposition [23], it is important to conduct a comprehensive study on the impacts of the asymmetrical blowing of shielding gas on the L-DED process and the properties of as-built specimens. If the negative effects are observed, it would be worthwhile to investigate whether there are cost-effective solutions to address these issues instead of purchasing extra components for coaxial conveying through the optic head.

Laser-based AM processes for 7XXX series alloys present numerous challenges, including issues with oxidation, porosity formation, and cracking susceptibility. Porosity in AM-produced structures can be categorized into two types: gas pores and lack-of-fusion pores [26]. Gas pores typically have a spherical morphology, while lack-of-fusion pores exhibit an irregular shape. Lack-of-fusion pores are often found periodically within structures, such as in the overlap area between adjacent deposition tracks. The formation of lack-of-fusion pores can result from inappropriate process parameters, such as high scan speed and excessive powder feed rate [26]. Another type of porosity that can be observed is keyhole pores, which are associated with the evaporation of alloying elements [28]. When excessive energy is applied, the recoil pressure caused by evaporation surpasses the surface tension and hydrostatic pressure in melt pools, leading to the activation of keyhole-mode welding [29]. Keyhole pores typically exhibit a large size and irregular geometry [30, 31]. The presence of porosity has a detrimental effect on the mechanical properties of as-built structures. Therefore, it is crucial to investigate the origin of the porosity formation and understand the relationship between porosity level, materials, and processing parameters. This will provide valuable insights for reducing porosity levels in future work.

High-strength Al alloys are susceptible to hot cracking during laser-based AM processes. Hot cracking in these alloys can be classified into two mechanisms: liquation cracking and solidification cracking. Solidification cracking occurs during the final stage of solidification [32]. In the semi-solid state, the grains have already grown, and any remaining liquid needs to fill the spaces between grain boundaries. In the case of insufficient backfilling, the shrinkage can initiate after solidification, creating nucleation sites for cracks that propagate under tensile stress until fracture. The heat transferred from the welds to the heat-affected zone (HAZ) could cause the partial remelting of secondary phases with low boiling points that are distributed along grain boundaries in the HAZ, resulting in the formation of liquid film [33]. Subsequently, this liquid film is torn apart from the solid under the tensile stress, contributing to the formation of the liquation cracks. Hot cracking can occur either in the early stage of processing or during the successive deposition. Several experimental studies have been conducted to investigate the origins of porosity formation in laser-based AM [34-36]. These studies aim to understand and mitigate the factors leading to porosity formation in order to improve the quality of AM-produced structures. Research on analyzing the cracking mechanism in laser-based AM processes is primarily based on simulation and analytics [37, 38]. However, these simulations often make certain assumptions for simplification purposes, which can lead to significant deviations compared with experimental results. While there can be a good agreement between the thermal simulations and experimentally recorded temperatures [39], the calibration of the mechanical simulations with the experimentally obtained data, such as the residual stress, is either not reported [37, 39] or exhibits high deviation [38]. A comprehensive experimental analysis of the cracking mechanisms in laser-based AM is still lacking. To improve the cracking

resistance of high-strength Al alloys and gain insights for designing new materials in laser-based AM, it is crucial to identify the dominant cracking mechanism. Therefore, it is necessary to investigate the cracking mechanisms in laser-based AM processing of difficult-to-process materials through experimental characterization. This will provide valuable information for developing strategies to enhance the quality and reliability of AM-produced structures.

Quality control is a critical aspect of AM processes. Ensuring consistent quality in AM-produced structures can be challenging due to unexpected processing anomalies, which limits the widespread application of AM, particularly in key industries such as. aerospace. To address this issue, significant efforts have been dedicated to process monitoring and quality evaluation for AM. Machine learning (ML) techniques have emerged as valuable tools for supporting manufacturing processes. ML algorithms can assist in the in-situ process monitoring and control. Among these algorithms, the convolutional neural network (CNN) has gained popularity for conducting in-situ monitoring and defect detection based on image recognition. CNN offers higher accuracy and requires fewer manual feature extractions compared with conventional ML algorithms [40]. Images captured during the AM process serve as input data for the CNN model, including processing characteristics such as melt pools [41-43], plume and spatter [44], and layer surface [45, 46]. The images captured during the AM process contain valuable information about the processing characteristics. These images can be utilized for both quantitative and qualitative evaluations of the properties and processing in AM. Quantitatively, the information in the images can be used to characterize properties such as predicting porosity levels [47] and surface roughness [48]. Qualitatively, the images can be used to evaluate the presence of defects and processing anomalies [42, 44]. However, while these works have been successful in predicting defects and diagnosing the processing anomaly, they do not address the simultaneous correction. In order to avoid further deterioration of existing anomalies and minimize material waste, it is crucial to investigate whether in-situ monitoring and adjustment of process parameters are achievable during L-DED. By adopting a CNN model, it may be possible to maintain processing stability and consistency by realizing in-situ adjustments to process parameters.

1.2. Objectives

The scientific objectives of this thesis are based on the identified research gaps mentioned earlier. These gaps include the limited applicability of Al alloys in AM, the need for developing a process window that considers both processing and parameter optimization, understanding the mechanisms behind defect formation in L-DED of high-strength 7XXX series alloys, and exploring the potential of ML for processing monitoring and quality control. Based on these research gaps, the following objectives have been formulated:

- The processability of 7XXX series alloys in both wire- and powder-based L-DED needs to be thoroughly investigated. The focus should be on minimizing the internal defects and preserving the superior mechanical properties of these alloys. In addition to optimizing the process parameters, such as laser power and scan speed, it is also crucial to optimize the overall processing strategy. This includes optimizing the scanning strategy, the material-feed timing, and the material-feed direction.

- A study is required to comprehensively investigate the mechanisms behind defect formation in L-DED processing 7XXX series alloys. This study aims to provide a deeper understanding and theoretical support for future work on material development and process optimization. The experimental investigation should focus on two specific types of defects: porosity formation and hot cracking.

- CNN models need to be employed to learn the processing characteristics from the processing images captured during the AM process. These processing images contain features such as the melt pool, spatter, and plume. The CNN models will be trained to identify different processing states based on the prediction results obtained from analyzing these images. By accurately recognizing the processing states, it will be possible to detect any anomalies or deviations from the desired conditions. In case of the occurrence of processing anomalies, the prediction results from the CNN models can be used to trigger adjustments in real-time, ensuring that the process remains stable and within acceptable limits.

1.3. Structure of the thesis

Chapter 2 provides a comprehensive overview of the state-of-the-art in L-DED, the characteristics of Al alloys in laser-based AM, and the application of machine learning in AM. Specifically, the processing characteristics of powder-based and wire-based L-DED are elaborated in Chapters 2.1.1 and 2.1.2, respectively. Chapter 2.2 delves into the processing of Al alloys in laser-based AM, with a specific focus on strengthening mechanisms (Chapter 2.2.1), processing challenges and current solutions (Chapter 2.2.2), and the development of new materials for AM (Chapter 2.2.3). The strengthening mechanisms of Al alloys discussed in this thesis include grain refinement, precipitation strengthening, and solid solution strengthening. The processing challenges considered encompass oxidation, porosity, residual stress, cracking, and property anisotropy. Further, Chapter 2.3 provides a comprehensive introduction to the current applications of machine learning in AM across different phases, i.e. prior process, in-situ process, and post-process.

Chapter 3 focuses on the experimental aspects of the thesis. In Chapter 3.1, the subsection covers the material preparation of powders and wires used in the L-DED process. Experimental setups for powder-based and wire-based L-DED are illustrated in Chapters 3.2 and 3.3, respectively. Chapter 3.4 introduces the characterization methods employed in this thesis and explains how these methods are applied to analyze and evaluate the specimens obtained from the L-DED process. The corresponding operations for specimen preparation and testing are also described.

To address the objectives outlined above, the experimental design is divided into three categories: the processability of high-strength Al alloys in powder-based L-DED (Chapter 4.2), the processability of high-strength Al alloys in wire-based L-DED (Chapter 4.3), and application of machine learning in L-DED (Chapter 4.4), as shown in Figure 2. Chapters 4.2 and 4.3 focus on the process development related to the first two objectives. These chapters delve into various aspects of optimization, including scanning strategy, retrofitting equipment, parameter-related optimization (such as laser power), and the correlation between process-microstructure-property. Additionally, these chapters analyze the mechanism behind defect

formation, such as porosity and cracks. Chapter 4.4 explores the application of neural networks in AM for both classification and regression problems. This chapter demonstrates how neural networks can be used to identify processing images captured by a high-speed camera during the L-DED process. By utilizing neural networks, in-situ parameter adjustment can be achieved to maintain processing stability, while the quantitative quality control for porosity level can also be implemented.

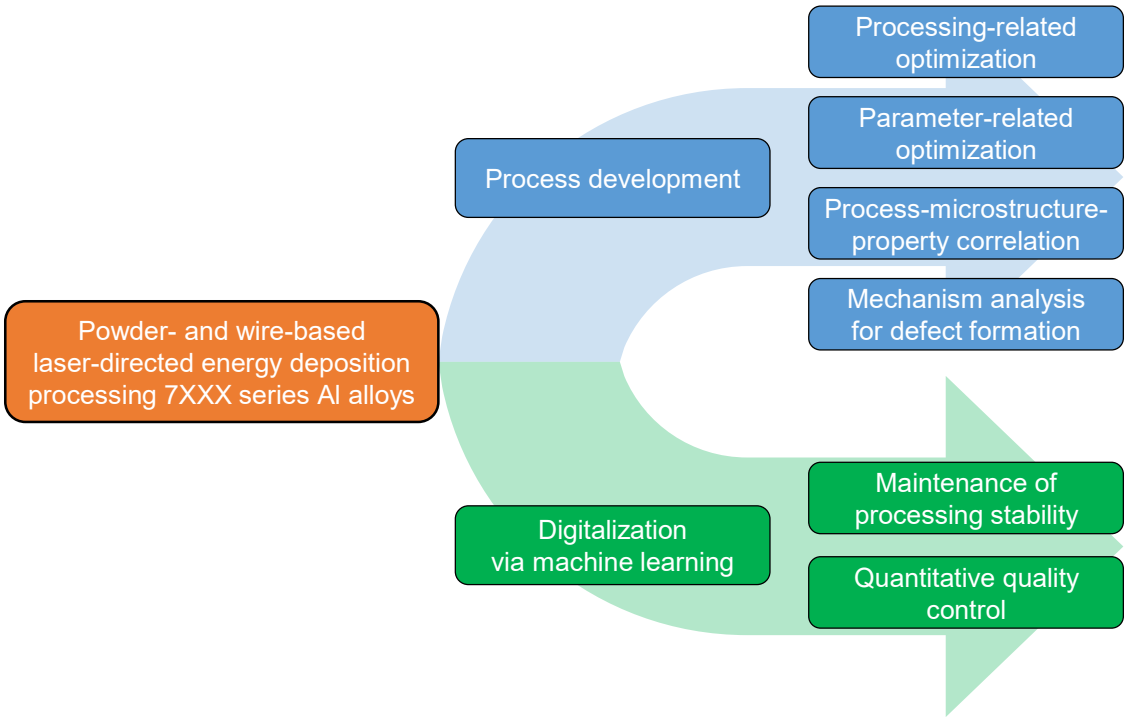

Figure 2. Structure of the experimental design.

The main conclusions drawn from the experimental results and analysis are summarized in Chapter 5. In Chapter 6, the results introduced in this thesis are generally discussed regarding the process development and the digitalization for L-DED processing high-strength 7XXX series Al alloys. The comparison between the processability of high-strength Al alloys in powder-based and wire-based L-DED is discussed in Chapter 6.1. Additionally, this chapter explores future directions for the development of new materials and investigation for processability in AM. In Chapter 6.2, the importance of processing stability in AM is analyzed in terms of its impact on optimizing properties. Furthermore, the potential for utilizing machine learning for the classification and regression problems in AM is explored in this chapter. Future experimental thoughts to realize the in-situ adjustment for multiple process parameters are also proposed here.

2. State of the art

2.1. Laser-directed energy deposition and common materials

2.1.1 Laser-directed energy deposition (powder-based)

Metal additive manufacturing (AM) is a process that builds structures layer by layer based on a 3D model [1]. This technology is appealing to both academic researchers and industries due to its ability to reduce weight, produce structures with complex geometries, and save costs [2]. The feedstock for metal AM can be in the form of wire or powder [1]. In powder-based AM, lasers can be used as an energy source to melt the powders. The powders can either be fed through a nozzle (laser-directed energy deposition, L-DED) or spread like a powder bed (selective laser melting, SLM) [1]. L-DED has various applications, including coating [9], repairing [10], and building 3D structures without space restrictions [11].

In powder-based L-DED, powders are transported by carrier gas from the powder feeder through a nozzle to the substrate, as shown in Figure 3. The laser beam melts the powders, which then solidify to form tracks. The movement of the nozzle and substrate is controlled by a CNC machine, a robot, or a combination of both during the layer-by-layer deposition process. The achievable properties of the final structures are primarily influenced by process parameters, such as laser power, scan speed, and powder feed rate. Additionally, the process systems (such as laser and nozzle, etc.) and powder quality also play a significant role in determining the results [49, 50]. According to the melting process, gas atomization technologies used to produce powders for metal AM can be categorized into four types: induction heating, plasma torch, electrode induction melting gas atomization (EIGA), and plasma atomization [51]. The properties of the powders, such as their morphology, moisture content, and oxidation level, have a significant impact on the L-DED process and the properties of the final structures. For instance, irregularly shaped powders can reduce the flowability of the powders, making it difficult for them to be fed and spread properly [52]. When processing powders with high levels of oxidation, excessive spattering may occur [36]. Moisture in the powders not only deteriorates the processability but also contributes to higher porosity levels within the printed structures [53]. Inappropriate storage conditions for powders can result in the further oxidation of powders and hydrogen absorption, leading to deviations in geometrical accuracy, increased porosity levels, and reduced strength [49]. It is not recommended to use small powders with diameters less than 17 µm since they tend to exhibit increased cohesiveness [54].

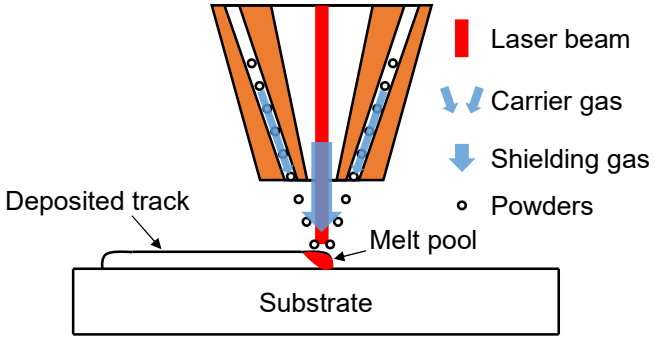

Figure 3. Illustration of powder-based L-DED.

The scanning strategies, which involve designing the path for building 3D structures, have been extensively studied to understand their impact on the residual stress, distortion, cracking resistance, microstructure, and mechanical properties. One approach is to build structures with alternating scanning directions in different layers. By rotating the scanning direction between adjacent layers, the surface roughness [16] and distortion [17] as well as the texture heterogeneity [18] of as-built structures can be reduced. In SLM, the effects of vertical scanning and horizontal scanning on the thermal field have been investigated. It was found that a prism built with a horizontal scanning strategy exhibits more pronounced distortion, while a prism built with a vertical scanning strategy shows more localized distortion [55]. In addition to the rotation of scanning directions, unique path designs such as laser double scanning, alternating scanning sequence (stripes alongside), and subdivision of the scanning area (e.g. chessboard) have also been applied [56]. Optimizing scanning strategies can reduce the residual stress and the cracking susceptibility. These hatch designs in layers can also affect the mechanical properties due to different thermal histories [57]. The tensile strength is significantly influenced by alternating deposition directions between different layers, whereas within one layer, the tensile strength is less dependent on the deposition direction [58]. The scanning strategies offer greater design freedom in SLM compared with L-DED, but there is still potential for further development and exploration of scanning strategies in L-DED.

Materials exhibit differences in processability and properties between powder-based L-DED and SLM. In addition to the differences in powder feeding and spread, the process parameters are also in distinct regimes. Table 1 provides a range of typical parameters used in powder-based L-DED and SLM for processing Al alloys. Except for scan speed, the process parameters in powder-based L-DED are generally higher than those in SLM. The melt pools generated in SLM are substantially smaller than those in L-DED leading to a higher processing precision but a longer processing duration in SLM. The smaller melt pool and HAZ in SLM allow for hybrid manufacturing combining the SLM with laser shock peening (LSP) for Al alloys [59]. This combination can reduce the susceptibility to liquation cracking. However, it is challenging to apply LSP as an interlayer treatment in L-DED due to the relaxation of the introduced compressive stress caused by the lower penetration depth (maximum approx. 1 mm) of LSP [60] and the large HAZ in L-DED.

Table 1. Process regime in powder-based L-DED and SLM.

	Laser power (W)	Spot diameter (mm)	Scan speed (mm/s)	Layer height (mm)	Hatch distance (mm)
Powder L-DED	600-4000	1.28-4.5	2.5-50	0.225-2.2	0.1-1.05
SLM	70-600	0.01-0.2	47.6-8000	0.03-0.06	0.05-0.17

Table 2 presents the hardness of specimens made from AlMgScZr and AlSi10Mg alloys processed using powder-based L-DED and SLM. It is observed that the hardness of specimens processed with SLM is higher compared with those processed with L-DED [61]. Additionally, a higher porosity is observed in L-DED-processed AlMgScZr specimens compared with SLM-processed AlMgScZr specimens [61]. The higher cooling rate in SLM results in a finer microstructure in AlMgScZr alloy [61]. On the other hand, the coarse microstructure and the higher porosity in L-DED-processed specimens are considered to be the reasons for the lower hardness [61]. Researchers at the Fraunhofer Institute for Laser Technology (ILT) have developed a new process based on L-DED, called the Extreme High-Speed Laser Material Deposition (EHLA), which allows for scan speeds hundreds of times faster than traditional L-DED [62]. Despite the high scan speed and the resultant high cooling rate, the AlMgScZr alloy still exhibits poor processability in the high-speed L-DED [63].

Table 2. Hardness of as-built AlMgScZr and AlSi10Mg processed with SLM and L-DED.

Ref.	Materials	AM technologies	Hardness
[61]	AlMgScZr	SLM	Approx. 168 $HV_{0.2}$
[61]	AlMgScZr	L-DED	Approx. 102 $HV_{0.2}$
[61]	AlSi10Mg	SLM	Approx. 115 $HV_{0.2}$
[64]	AlSi10Mg	L-DED	Approx. 60 $HV_{0.1}$

2.1.2 Laser-directed energy deposition (wire-based)

Powder-based L-DED is capable of producing highly precise structures with small sizes, while wire-based L-DED offers nearly 100 % material utilization [65] and a high deposition rate [66]. In wire-based L-DED, the wire can be fed laterally or coaxially relative to the laser beam [67, 68], as illustrated in Figure 4. In lateral wire feeding, the direction of wire feeding plays a crucial role in processability. Based on the relative motion between wire feed and deposition direction, the wire feed direction can be categorized as front feeding, back feeding, and side feeding, as depicted in Figure 5 [69]. The selection of wire feed direction and wire feed nozzle angle must correspond to the chosen process parameters, otherwise, the processing anomalies may occur leading to the termination of deposition [19, 23].

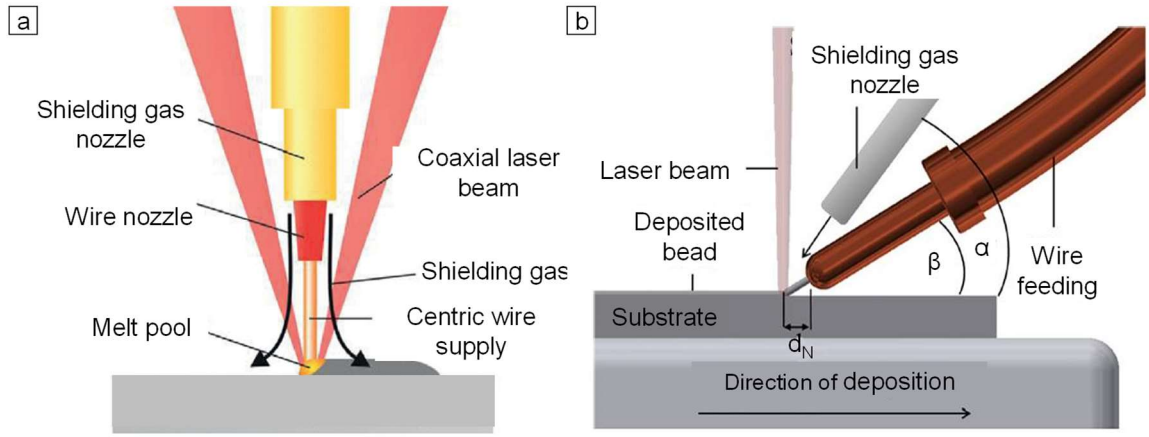

Figure 4. Schematic of (a) coaxial [70] and (b) lateral wire-based L-DED [67].

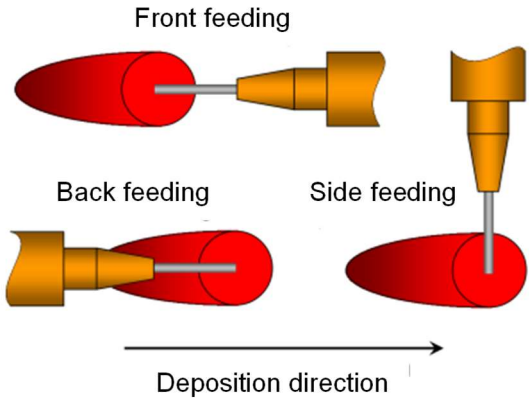

Figure 5. Illustration of front, back, and side wire feed directions [69].

There is another AM technology called wire arc additive manufacturing (WAAM), which utilizes an electric arc as the energy source to melt materials and build 3D structures. Compared with wire-based L-DED, WAAM offers a more cost-effective solution as the electric arc is less expensive than the laser. However, the concentrated heating effects in L-DED can result in rapid cooling and melting, which may be detrimental to processing materials that are prone to cracking, such as high-strength Al alloy [71]. L-DED generates high thermal gradients and resultant thermal residual stresses. When processing pure high-strength Al alloys, WAAM has been successful in producing crack-free structures with low porosity levels [71, 72]. However, there is still a need for solutions to address both high porosity levels and cracking [27, 73]. On the other hand, it is challenging to systematically regulate the energy input in WAAM [74]. Additionally, the higher cooling rate can enhance grain refinement and lead to superior mechanical properties [75], which is the case in L-DED. The controllable energy input in L-DED allows for microstructural adjustment [76] and prevents heat accumulation [14].

2.2. Aluminum alloys in laser-based additive manufacturing

2.2.1 Strengthening mechanisms

Grain refinement

The mechanism of grain refinement for Al alloys has been extensively studied, focusing on two main paradigms: the nucleant paradigm and the solute paradigm [77]. The nucleant paradigm suggests that Al alloys undergo heterogeneous nucleation on specific nucleation sites. On the other hand, the solute paradigm considers the influence of solute atoms during the nucleation and growth process of Al grains. The fundamental goal of the grain-refinement process is to enhance the nucleation ability of the Al melt on nucleation sites and inhibit the growth of these grains [78].

The theory proposed in [79] categorizes the nucleation process into two types: homogeneous and heterogeneous nucleation. Homogeneous nucleation refers to that the nucleation takes place on substrates with the same chemistry as the solid, whereas the nucleation occurs on a family of substrates of chemistry different than that of the solid in heterogeneous nucleation [80]. In homogeneous nucleation, the probability of nucleation is uniform throughout the system, while in heterogeneous nucleation, there are specific sites that exhibit preferential nucleation [81]. The nucleation of Al melt is based on two fundamental conditions: the nuclei must attain a critical size to remain stable within the solidifying metal, and the driving force for nucleation must surpass the free energy barrier. As stated in [79], both homogeneous nucleation and heterogeneous nucleation require the same critical size for nuclei. However, the driving force necessary to overcome the free energy barrier is lower in heterogeneous nucleation compared with homogeneous nucleation. This implies that increasing the number of grains through heterogeneous nucleation is relatively easier.

To achieve grain refinement, the inoculant particles are introduced into the Al melt to serve as heterogeneous nuclei. There are two main theories regarding the origin of these inoculant particles: the nucleant-particle theories and the phase-diagram theories [77]. The nucleant-particle theories propose that Al grains nucleate on the borides or carbides [82]. Studies have shown that the addition of TiB_2 and TiC to Al alloys can effectively refine microstructure [83, 84]. On the other hand, the phase-diagram theories suggest that the peritectic reaction occurring on the primary particles, typically Al_3Ti, contributes to grain refinement [77]. Apart from Al_3Ti, the formation of primary Al_3Sc particles in hypereutectic Al-Sc alloys can also serve as heterogeneous nuclei for the α-Al matrix [85]. It has been observed that aluminides exhibit a more pronounced grain-refining effect compared with borides [77], since there is no clear orientation relationship between α-Al matrix and borides [77], whereas multiple orientation relationships have been identified between the α-Al matrix and Al_3Sc [86], as well as the α-Al matrix and Al_3Ti [87].

In the solute paradigm, the presence of solute atoms can hinder the growth of Al grains [88]. The segregation of solutes disrupts the dendrite growth process and contributes to the formation of a constitutionally undercooled zone in front of the solid-liquid interface [88]. This constitutionally undercooled zone further promotes the nucleation [88]. The Growth Restriction Factor (GRF) is a term used to describe the segregation ability of an alloying element during

solidification. It quantitatively represents the influence of solute elements on restricting the growth of a solid-liquid interface [79]. Different solutes demonstrate different abilities to restrict grain growth. Ti exhibits better growth-restriction effects for Al alloys compared with Si and Mg [89]. In terms of achieving equivalent grain refinement in commercially pure Al alloys, a Si content of 7 wt.% or an Mg content of 0.3 wt.% is required, whereas a Ti content of 0.168 wt.% is sufficient [89]. The growth-restriction effects are not only dependent on the type of solutes but also on their content. In LM24 Al alloy with the addition of Al-5Ti-1B, a study has found an inverse correlation between the grain size and GRF [79]. Similarly, in the hypoeutectic concentrations of Mg in Al-Mg alloys, it has been confirmed that there is an inverse correlation between GRF and grain size [90]. However, as the growth-restriction effects are weakened with higher Mg contents, an increase in GRF does not lead to grain refinement [90]. In Al-Si and Al-Cu alloys, there is a transition point in the GRF-grain size curve [91]. Below this transition point, the grain size decreases with increasing GRF for Cu and Si [91]. However, beyond this transition point, the grain size increases with further increase in GRF [91].

Grain refinement has been proven to be an effective method for enhancing cracking resistance. Fine grains promote the backfilling of molten metal into shrinkage during solidification resulting in smaller and more uniformly distributed shrinkage or gas porosities [92]. The presence of a complex network consisting of numerous grain boundaries reduces the likelihood of hot-cracking initiation and propagation along the grain boundary [92]. The influence of grain size and the fraction of equiaxed grains on the cracking susceptibility can be categorized into three factors: the duration of the mush zone, the capillary pressure, and the permeability of the dendrite network, see Figure 6 [93]. A comprehensive analysis has also been conducted to establish the relationship between grain morphology (shape and size) and the dominant factor determining the cracking susceptibility in laser welding AA6082 Al alloy [93]. The cracking susceptibility decreases as the grain size decreases until it reaches approx. 25 µm. However, when the fraction of equiaxed grains reaches 100 %, further grain refinement worsens the cracking susceptibility. It has been observed that below a grain size of 25 µm, the permeability of the dendrite network becomes the dominant factor determining the cracking susceptibility. On the other hand, in coarse microstructures, the cracking susceptibility is primarily influenced by the duration of the mush zone and the capillary pressure.

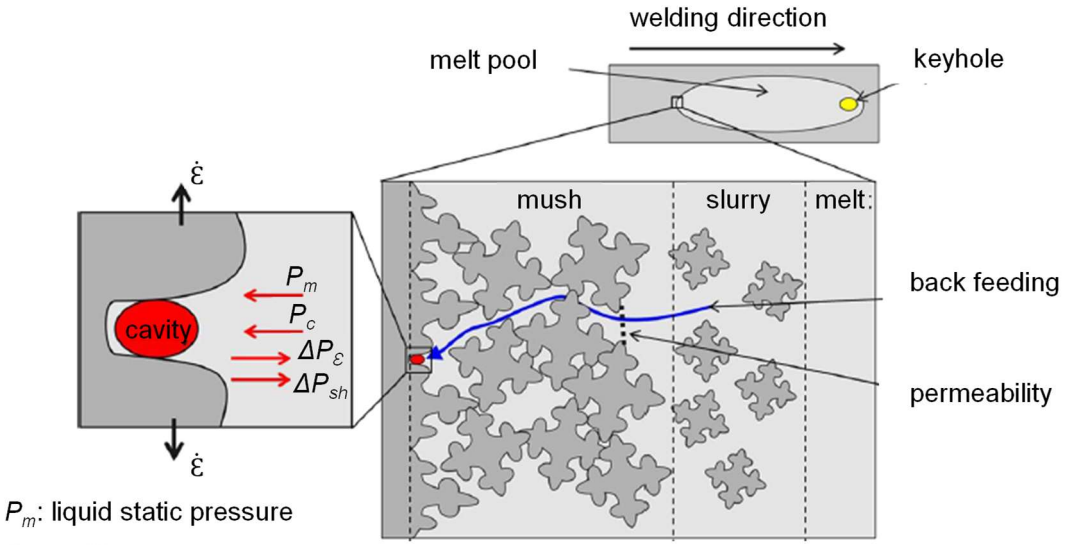

Figure 6. Schematic diagram of semisolid melt pool in front of the solidification front in laser welding [93].

The grain refinement not only reduces the cracking susceptibility [94] but also simultaneously improves the mechanical properties and reduces the degree of anisotropy [95]. According to the Hall-Petch relationship, the strength resulting from grain refinement is inversely proportional to the square of the grain diameter, as shown in Equation 1 [96]. For instance, the friction stir process can increase the ultimate tensile strength (UTS) of cold-rolled AA1050 Al alloy by 46 % through microstructure refinement [97]. The addition of grain refiner (Al-1Ti-3B) to Al-7Si-2.5Cu alloy increases the UTS by 21.5 % and the fracture elongation by 84.6 %, respectively [98].

$$\Delta\sigma_{gb} = \frac{k_y}{\sqrt{d}} \qquad \text{Equation 1}$$

where k_y is the Hall-Petch coefficient; d is the diameter of grains.

Precipitation strengthening

The 7XXX series alloys are known for their high strength due to precipitation strengthening [8]. However, the precipitation dynamics during heat treatment of these alloys are complicated. Typically, a T6 heat treatment process, which involves solid solution treatment, quenching, and artificial ageing, is performed to enhance the properties of the 7XXX series alloys [99, 100]. The primary strengthening precipitate in these alloys is $MgZn_2$, also known as the η phase [101]. The precipitation process during ageing consists of four stages: saturated solid solution, segregation, formation of solute clusters called Guinier-Preston (GP) zone, precipitation as η' phase, and growth and coarsening of η' phase to η phase [8].

At the early stage of ageing, the GP zone and η' phase are formed. As ageing progresses, the GP zone can act as nuclei for the η' phase increasing the number density of the η' phase and enhancing the strength. Prolonged holding at high temperatures leads to the

transformation of the η' phase into the η phase and a decrease in strength. Figure 7 summarizes the precipitation sequence during the heat treatment for AlZnMgCu alloys, while Figure 8 illustrates the nucleation of different phases at various temperatures and holding times [102]. The highest strength is achieved at the peak-aged stage, however, this stage also results in a degradation of the resistance to stress corrosion cracking (SCC) [103].

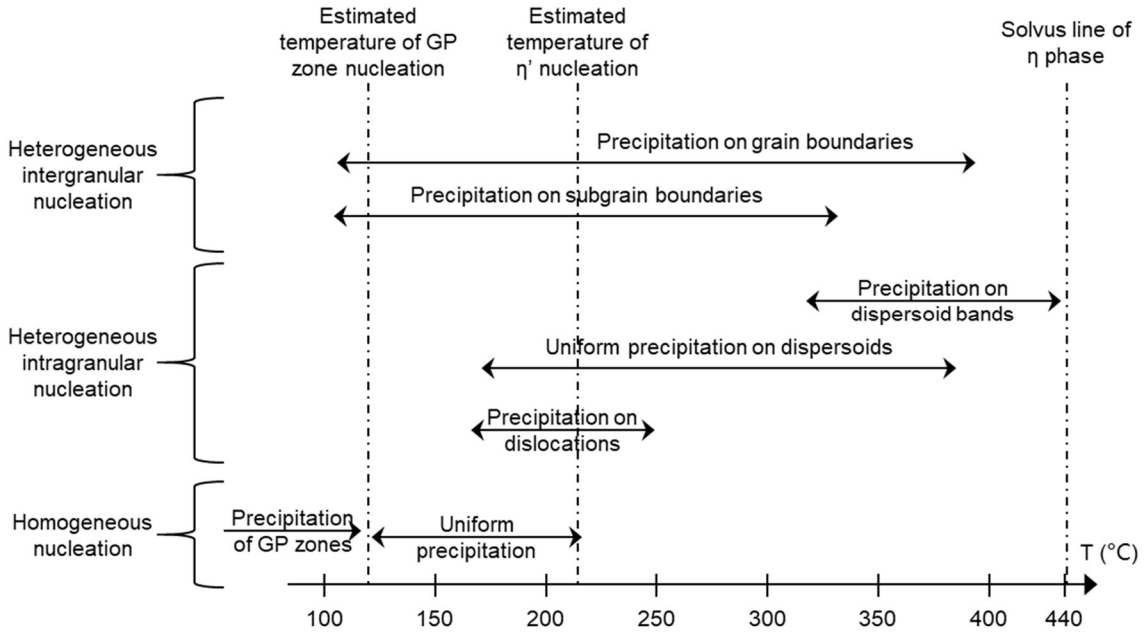

Figure 7. Domain of activation of the different phases during the heat treatment for AA7010 [102].

Two-stage ageing is a heat treatment process that results in the formation of precipitates with a finer size and discrete distribution compared with one-stage ageing, which can further enhance the mechanical properties [104]. The improved mechanical properties in two-stage ageing are primarily attributed to the fine dispersion of GP zones [104]. In the two-stage ageing process, the first ageing treatment is conducted at a lower temperature, which promotes the nucleation of GP zones. These retained GP zones then transform into a fine η' phase during subsequent ageing, leading to higher strength at the peak-aged stage. The ductility after two-stage ageing is influenced by two factors: the particle-free zone (PFZ) and the precipitates around grain boundaries [8]. During the second ageing treatment at a higher temperature, a wider PFZ is generated, along with coarser precipitates. The wider PFZ leads to enhanced stress relaxation and the inhibition of cracking initiation and propagation. Moreover, as the precipitates along grain boundaries coarsen, their number density decreases, resulting in an easier slip for dislocation and the inhibition of crack propagation.

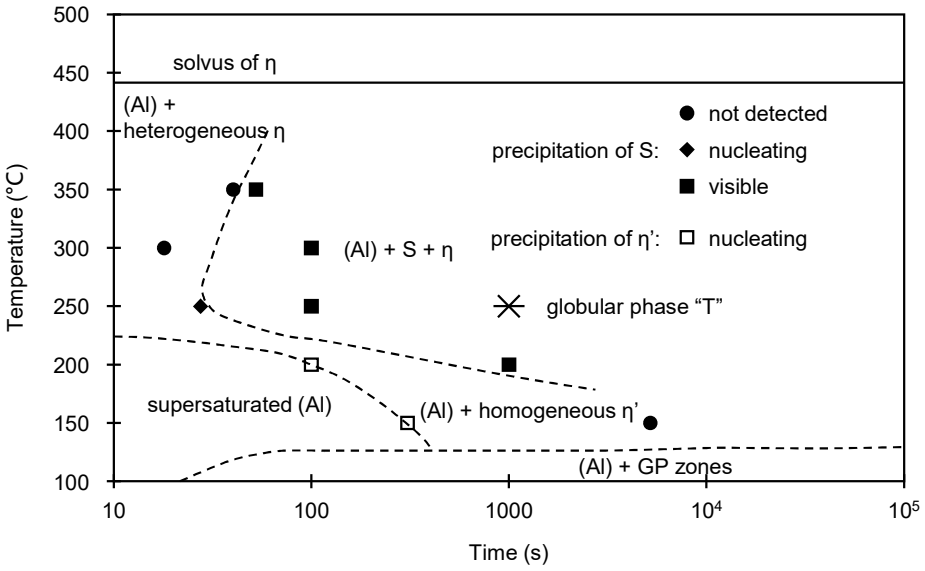

Figure 8. Nucleation diagram for AA7010. The globular phase "T" corresponds to $Al_{32}(Mg,Zn)_{49}$. The S precipitate corresponds to Al2CuMg [102].

The solubility of alloying elements in the α-Al matrix increases with higher cooling rates [25]. By increasing the cooling rate, the supersaturation of solute atoms in the matrix also increases, leading to a greater potential for ageing strengthening [51]. Studies have shown that the degree of solute supersaturation and the number density of precipitates are linearly dependent [52]. In the laser-based AM process, rapid heating and cooling are characteristic features [64, 105]. This means that laser-based AM processing of precipitation-strengthening Al alloys can effectively utilize the potential for increasing the supersaturation of solute atoms and take advantage of the resulting ageing-strengthening effects.

The interaction between precipitates and dislocations plays a crucial role in determining the yield strength (YS) and the work-hardening behavior of precipitation-strengthening alloys [106]. When secondary precipitates are smaller than a critical size, they are energetically more favorable to be cut by dislocations rather than bowed resulting in the formation of an anti-phase boundary (APB) [94]. Under the APB strengthening mechanism, as the particle size increases, it becomes more difficult for dislocations to cut through the particles, leading to stronger strengthening effects [94]. On the other hand, according to the Orowan strengthening mechanism, dislocations tend to bow around the particles instead of cutting through them, when the particle size exceeds a critical value, leading to weaker strengthening effects, as shown in Figure 9 [94]. Particles in the range of 20 – 25 nm exhibit the most effective strengthening effect in Al-6Mg-2Sc-1Zr (wt.%) [94]. The critical particle size for the transition from cutting to bowing by dislocations is estimated to be 3.7 nm in Al-2.8Mg-0.16Sc (wt.%) alloy [106]. Additionally, when the size of Al_3Sc precipitates is 1.8 nm, a banded distribution is observed, while a homogeneous distribution is observed when the size is 6.4 nm [106].

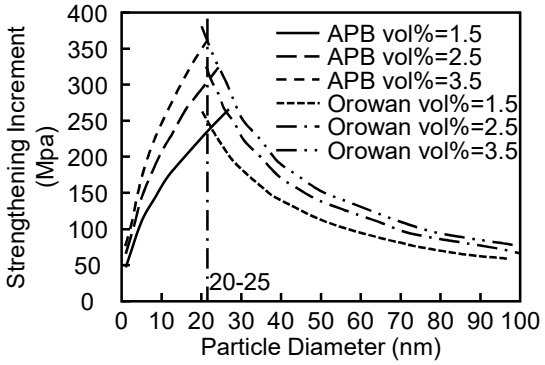

Figure 9. The relationship between strengthening increment and particle diameter. APB vol.%: strength predicted by APB model at a given volume fraction of particles. Orowan vol.%: strength predicted by the Orowan model at a given volume fraction of particles [94].

Solid solution strengthening

The crystal lattice is the main obstacle to dislocation movement in metals [107]. In FCC (face-centered cubic) metals like Al, the Peierls stress, which is the stress required to move dislocations through the lattice, is relatively low, resulting in a low yield strength in pure FCC metal [107]. For non-heat-treatable Al alloys, such as Al-Mg and Al-Mn alloys, solid solution strengthening and grain refinement are the primary mechanisms for increasing their strength [108]. Solid solution strengthening occurs due to the interaction between the moving dislocations and the solute atoms [108]. The maximal solubility of Mg and Mn in the α-Al matrix at the eutectic temperature is 18.9 at.% [109] and 0.62 at.% [110], respectively. In terms of solid solution strengthening in the α-Al matrix, Mn can provide a stronger strengthening effect per atom compared with Mg, especially when synergistically combined with other elements like Si [108]. In the equilibrium processing of binary Al-X alloy systems, first principle calculations have shown that Mg is expected to be the most effective element for solid solution strengthening among Mn, Zn, and Cu [111]. This conclusion is based on using misfit strain as a predictive tool to determine the increase in yield strength (YS) attributed to the solid solution strengthening [111].

The lattice structure of pure Al can be distorted because of the dissolution of solutes. In the case of Al-5Mg (wt.%) alloy, the lattice parameter of the α-Al matrix increases from 0.40493 nm to 0.40715 nm as a result of the Mg dissolution, compared with pure Al [112]. The presence of Mg atoms can act as obstacles that pin moving dislocations in the lattice [107]. Dislocations that are not pinned continue to move by bowing out from these pinned locations [107]. The regions where dislocations are unpinned experience line tension, leading to enhanced strength [107]. In AA5083 H-131 (with main alloying element Mg: 4.77 wt.%, Mn: 0.68 wt.%), the strength increment caused by Mg solid solution strengthening is approx. 82 MPa [107]. In the Al-8Ce alloy system, the introduction of Mg solute atoms can decrease the stacking fault energy, which inhibits the dynamic recovery process during deformation [113]. This inhibition facilitates the formation of dislocation tangles and dislocation networks in the α-Al matrix.

2.2.2 Processing challenges and solutions

Oxidation

Al and alloying elements in 7XXX series alloys are prone to oxidation [114]. In AM, oxidation can lead to an increased possibility of porosity formation because the liquid Al is unable to sufficiently wet the oxide particles [115]. Additionally, the presence of oxide particles in the AM-produced structures can negatively impact fatigue performance, particularly when these particles are distributed on the surface or sub-surface regions [115, 116]. In powder-based AM processes, oxidation can also reduce the flowability of powder particles [114].

In SLM processing Al alloys, oxidation during the fusion process can contribute to increased porosity [117]. While an oxygen level of 0.1 - 0.2 % may be acceptable for processing stainless steel and Ti alloys, it is not low enough for Al alloys [117]. During SLM, Fe or Ti oxides formed can be either broken up and enter the melt pool or be evaporated by the heat generated from the laser, whereas the Al oxides tend to remain on the surface of processed Al alloy specimens [117]. The vaporization of the Al oxide film on top of the melt pool, along with higher surface tension and temperature profile, creates stirring in the melt pool, which disrupts the oxide film on the bottom side [117]. Unmelted powders and pores can become trapped between oxide films on the sides of the melt pool, as depicted in Figure 10. It is crucial to select a reasonable overlap size between two adjacent tracks during processing. Both excessive overlap and insufficient overlap can increase the porosity [117]. Mg, as an alloying element in Al alloys, is particularly susceptible to severe evaporation and oxidation due to its low boiling point (1093 °C) and low evaporation heat (5.272 kJ/kg at ambient pressure) [118]. This evaporation and oxidation of Mg can reduce the level of densification in the final structure.

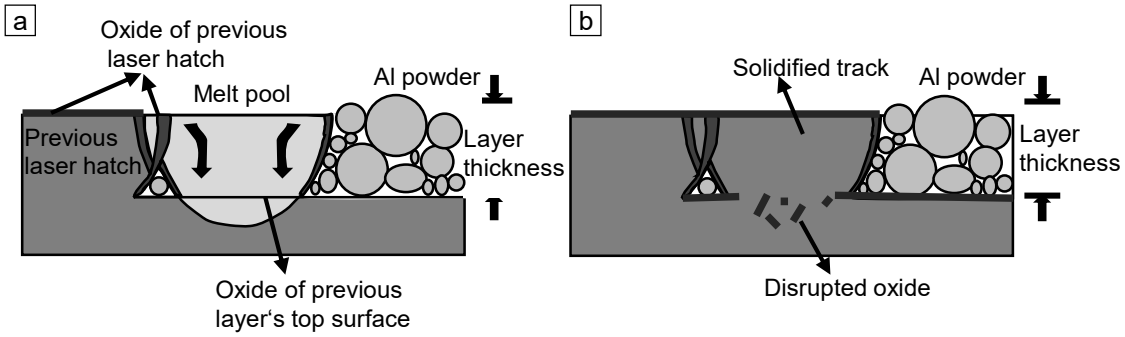

Figure 10. (a) Marangoni convection in the melt pool. (b) Oxidation disruption and solidification of the melt pool [117].

The utilization of oxidized powders can result in wider deposition tracks due to the reduced surface tension, which leads to a greater spatial distribution of melt pools [36]. Additionally, oxidized powders tend to produce more spatter compared with non-oxidized powders [36]. Moreover, the oxygen content in oxidized powders is sufficient to change the negative correlation between surface tension and temperature into a positive correlation, thereby shifting the Marangoni convection flow from outward centrifugal to inward centrifugal [36]. The inward centrifugal flow drives the existing pores to the bottom of melt pools, resulting in an

increased porosity level [36]. In cases where there is insufficient protection from the shielding gas during AM, the geometry of the structure can be severely compromised [24].

Porosity

Porosity in structures produced by AM can be categorized into two types: gas pores and lack-of-fusion pores [26]. Gas pores have a spherical shape, while lack-of-fusion pores have an irregular morphology. Lack-of-fusion pores are found periodically within structures, particularly in the overlap region between adjacent deposition tracks. The occurrence of lack-of-fusion pores can be attributed to inappropriate process parameters, such as excessive scan speed and high powder feed rate [26].

The origins of gas pores in AM-produced structures can be attributed to several factors. Firstly, there are significant differences in solubility between hydrogen in liquid and solid Al alloys [119]. When molten Al reacts with moisture in the surrounding atmosphere, hydrogen is generated [120]. As the solubility decreases during solidification, the supersaturated hydrogen is either stored in the lattice, dislocations, grain boundaries, etc., or precipitates as gas trapped within the solidified materials [119]. Secondly, the evaporation of volatile elements present in 7XXX series alloys can also contribute to the formation of gas pores [121]. If there is insufficient time for vapor to escape, it can become trapped within the melt pools leading to the formation of gas pores. Thirdly, in powder-based AM processes, gas pores may be retained inside powder particles during gas atomization [122], which can also serve as potential sources of porosity in AM-produced structures. Additionally, the contamination of feedstock [123] or substrates [25], as well as the entrapment of shielding gas [26], are other possible reasons for the formation of gas pores. There is another type of porosity known as keyhole pores, which is associated with the evaporation of alloying elements [28]. Under excessive energy input, when the recoil pressure caused by evaporation exceeds the surface tension and hydrostatic pressure within the melt pools, keyhole-mode welding is activated [29]. Keyhole pores are typically characterized by their large size and irregular geometry [30, 31].

The porosity level in AM-produced structures is influenced by the process parameters. Different types of porosity have varying dependences on these process parameters. For instance, the gas porosity tends to be generated under low laser scan speeds, while the keyhole porosity is more likely to form under high scan speeds [28]. The lack-of-fusion porosity can be eliminated through the optimization of process parameters, whereas the gas porosity cannot be completely removed [26]. To reduce the overall porosity level, effective methods include using powders with lower internal porosity that are entrapped during gas atomization, employing a lower shielding gas flow rate, and ensuring that powders are adequately dried before processing [26, 124].

Residual stress

Residual stress is a natural occurrence in AM processes, and it can have an impact on various properties such as fatigue strength and corrosion resistance [125]. In laser-based manufacturing, the rapid heating of the structure’s surface combined with relatively slow heat conduction leads to a significant temperature gradient, which in turn introduces residual stress

[126]. Additionally, a chemical composition gradient in materials can also contribute to the development of residual stress [125].

The distribution and evolution of residual stress in the building direction are influenced by subsequent thermal cycles [127]. When there is a high heat input and long scanning tracks, the level of residual stress along the scanning direction tends to be higher [127]. This is because the scan speed affects the geometry of the melt pool and the direction of cooling, resulting in higher residual stress in the scanning direction compared with the building direction [125]. Some of the residual stress from the previous layer can be relieved by the heat transferred from subsequent melted layers [128]. To reduce residual stress, post-heat treatment or pre-heating of the substrate can be employed [128]. The effectiveness of these methods depends on the solid phase transition temperature of the material being used. For instance, in stainless steel (FV520B), if the solid phase transition temperature is lower than the lowest temperature in the heat cycle in the L-DED process, significant relief of tensile residual stress can be achieved [129]. On the other hand, when the solid phase transition temperature is high, pre-heating can increase the lowest temperature in the heat cycle and improve the stress relaxation [129]. Furthermore, the magnitude of residual stress is also influenced by scanning strategy and process parameters. By adopting appropriate scanning strategies such as the island scanning strategy [130] and optimizing process parameters like high energy input [37], it is possible to decrease the residual stress.

Figure 11 illustrates a potential residual stress state and the resulting distortion in structures produced by L-DED. The highest temperature gradient and subsequent high residual stress are typically found in the initial fewer layers, where the heat is rapidly conducted to the substrate [131]. At the beginning and end of each track, higher tensile stress leads to increased distortion [131]. It is possible to reduce the inhomogeneous distortions by adjusting the process parameters to increase the deposition rate [131].

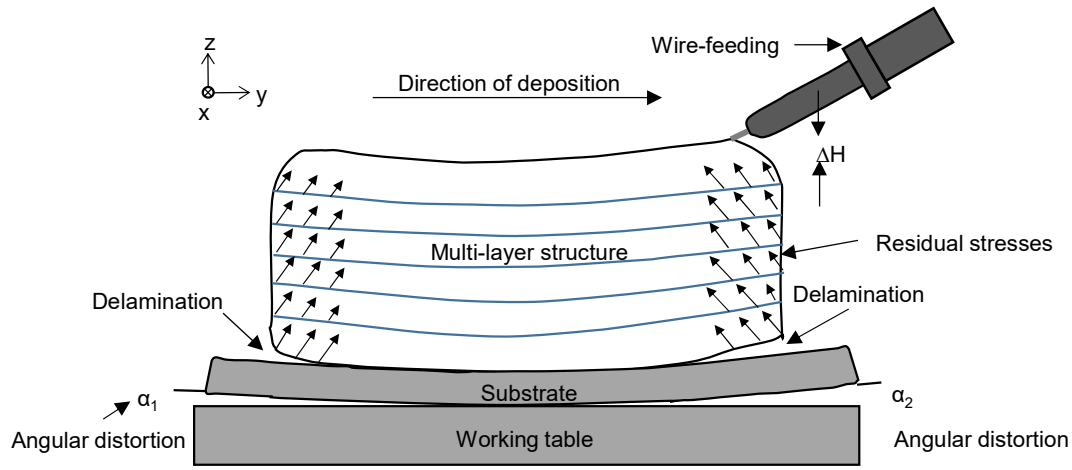

Figure 11. Non-uniform distortion of multi-layer deposition and partial delamination [131].

Cracking

Hot cracking in welding can be classified into three subgroups based on the mechanisms of formation: solidification cracking, liquation cracking, and ductility-dip cracking [132]. These three types of cracking differ from each other primarily in terms of crack nucleation.

Solidification cracking occurs during the final stage of solidification [32]. In the semi-solid state, the grains have grown and any remaining liquid needs to fill the spaces between grain boundaries. Otherwise, the shrinkage can be initiated after solidification, creating potential nucleation sites for cracks that can propagate under tensile stress until fracture. Solidification cracks typically originate in the welds and can propagate along grain boundaries towards the center of the weld surface [133]. The heat transferred from the welds to the HAZ can cause partial remelting of secondary phases with low boiling points that are distributed along grain boundaries in the HAZ, resulting in the formation of a liquid film [33]. The liquid film is then torn apart from the solid under the tensile stress contributing to the formation of the liquation cracks. The liquation cracks are typically generated in the HAZ and can propagate within the HAZ or extend into the fusion zone [134, 135]. Ductility-dip cracking does not have specific nucleation sites. It is attributed to a loss of ductility at a homologous temperature between 0.4 and 0.9 [136]. The cracks can be initiated in either the welds or HAZ if the temperature and tensile stress thresholds are reached [137, 138]. The tensile stress is a crucial factor for crack propagation in all three cracking mechanisms and also plays a significant role in initiating ductility-dip cracks.

Different materials exhibit varying degrees of cracking susceptibility in laser-based AM. Even within a single alloy system, such as Al alloys, there can be significant differences in cracking resistance due to variations in the type or content of alloying elements [4]. Cast Al alloys with a high Si content are often suitable for AM. The addition of Si enhances the flowability of the melt pool and reduces the temperature range of solidification, thereby improving the processability [4, 139]. In contrast, wrought Al alloys, such as those in the 7XXX series alloys, are considered challenging to process. These alloys have lower Si content and a larger solidification temperature range, making them highly susceptible to solidification cracking [139], as depicted in Figure 12. The wide temperature range during the solidification of AA7075 leads to the formation of long interdendritic fluid channels that contribute to cracking, while cast AlSi10Mg with a small solidification temperature range has shorter interdendritic channels that can be easily backfilled [139]. The use of high energy density input in laser processing results in the formation of high-temperature gradients and residual stresses [140], which further promote cracking in AM-produced structures. Additionally, 7XXX series alloys contain significant amounts of volatile elements like Zn and Mg, which can evaporate at elevated temperatures and create porosity in the as-built structures [27, 56]. Despite these processing challenges, 7XXX series alloys are utilized in industries such as automotive [6] and aerospace [141], where both high strength and lightweight properties are required. Consequently, researchers have made efforts to mitigate the cracking susceptibility and improve the processability of these alloys.

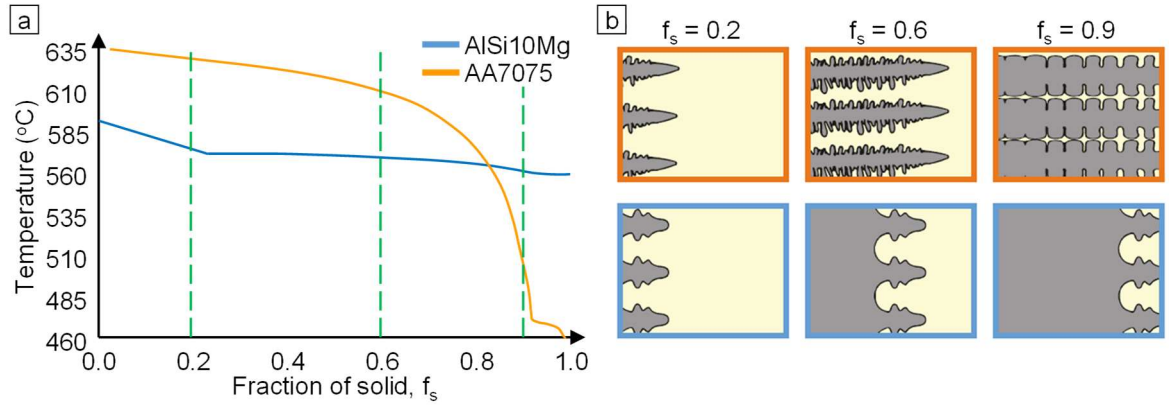

Figure 12. (a) Solidification curves for high-strength wrought AA7075 (orange) and cast AlSi10Mg (blue). (b) Schematical representation of solidification indicates how a large solidification temperature range results in long channels of interdendritic fluid that contribute to cracking. The orange frame shows the dendrite growth of AA7075, while the blue frame represents the dendrite growth of AlSi10Mg. [139]

The processability of difficult-to-process materials can be improved through three phases: pre-processing preparation, in-process actions, and post-processing treatments. Prior to processing, one approach is to modify the cracking-susceptible material by incorporating other materials mechanically [142] or through surface engineering techniques (For example, an alternating adsorption process can be used to generate consistently charged surfaces on Ti alloy and commercially pure Ti powders, promoting the adhesion of nanoparticles) [143]. Another option is to adjust the chemical composition of the raw powder materials before atomization to ensure even dispersion of doping powders [144]. In wire-based L-DED, the chemical composition of the feedstock can be modified by simultaneously feeding the cracking-susceptible wire material with additional wire materials. The feed speed of different wires, adjustment of process parameters, and alignment of the experimental setup are critical factors for achieving smooth deposition [145, 146]. Cracks in laser-based AM can be eliminated by modifying the material composition. Two mechanisms for crack elimination through doping materials are introduced: doping materials such as Si can enhance the flowability of the melt and improve the backfilling for shrinkage during solidification, while doping materials like Zr and TiB_2 can act as nuclei for primary Al grains, leading to grain refinement and the enhanced cracking resistance [67, 95]. During the processing stage, actions can be taken to optimize parameter adjustment and building strategies in order to minimize defects and meet geometrical requirements without compromising material properties [56, 147]. In addition to parameter optimization, other process control techniques can be employed to assist in production. Preheating the substrate before deposition can reduce the cooling rate, temperature gradient, and the resultant residual stress, thereby lowering the cracking susceptibility [148]. The island scanning strategy is another approach that can be used to reduce cracking susceptibility [149]. This strategy involves dividing the deposited layer area into smaller parts. It has been observed that shorter deposition lengths can reduce the residual stress and alleviate the cracking susceptibility [150]. However, it should be noted that the island scanning may result in larger remelted areas between adjacent tracks and a higher porosity level [31]. The cracking cannot be completely prevented either [151]. A novel methodology proposed in a study involves employing interlayer laser shock peening (LSP) during SLM [59]. This technique has been successful in reducing the number density of cracks and improving

the fatigue properties. However, it requires more advanced equipment and is not applicable in L-DED due to the large size of melt pools and HAZ, which can easiliy relieve any introduced compressive residual stress. After the production of structures, hot isostatic pressing (HIP) is commonly conducted to heal small cracks and porosity. HIP is a process subjecting metallic structures to thermal annealing and pressure simultaneouosly [152].

Several experimental studies have been conducted to investigate the origins of porosity formation in laser-based AM [34-36]. On the other hand, research on analyzing the cracking mechanism is often based on simulation and analytics [37, 38]. However, it is important to note that simulations often make certain assumptions for simplification purposes, which can lead to high deviation when compared with experiments. While there can be a good agreement between thermal simulations and experimentally recorded temperatures [39], the calibration of mechanical simulations with experimentally obtained data, such as the residual stress, is either not reported in some cases [37, 39] or exhibits high deviations [38].

Property anisotropy

In structures produced by AM, it is common to observe a bi-modal microstructure within a single deposited layer [153]. This microstructure consists of a fine equiaxed-grain region and a coarse columnar-grain region. The equiaxed grains do not exhibit any preferential growth orientation [153]. In contrast, the columnar grains show a preferential crystallographic orientation, which is typically considered to be parallel to the heat flow direction of the specimens [154]. The growth direction of columnar grains can also deviate from the direction of maximum heat flow. For instance, in the L-DED processing of Inconel 718 alloy, which has the same preferential crystallographic orientation of <100> as Al alloys, if the scanning direction in two adjacent layers is alternated by 180 °, known as bi-directional scanning, the maximum heat flow direction is correspondently alternated, see Figure 13a [155]. In this case, three possible solidification patterns can occur, as depicted in Figure 13b. The angle between the maximum heat flow direction and the horizontal line is 60 °[155]. In solidification pattern 1, the growth direction of primary dendrites in each deposition layer is parallel to the maximum heat flow direction [155]. In solidification pattern 2, the growth direction of primary dendrites in two adjacent layers is perpendicular to each other since the dendrites in the 2nd layer are epitaxially grown from the secondary dendrite arm in the previous layer [155]. However, the first two growth patterns are not observed in the microstructure due to the high driving force required for nucleation and the significant deviation between the growth direction of primary dendrites and the maximum heat flow direction [155]. The third solidification represents a compromise between alignment with the maximum heat flow direction and nucleation difficulty [155]. It is observed in the microstructure of AM-produced structures.

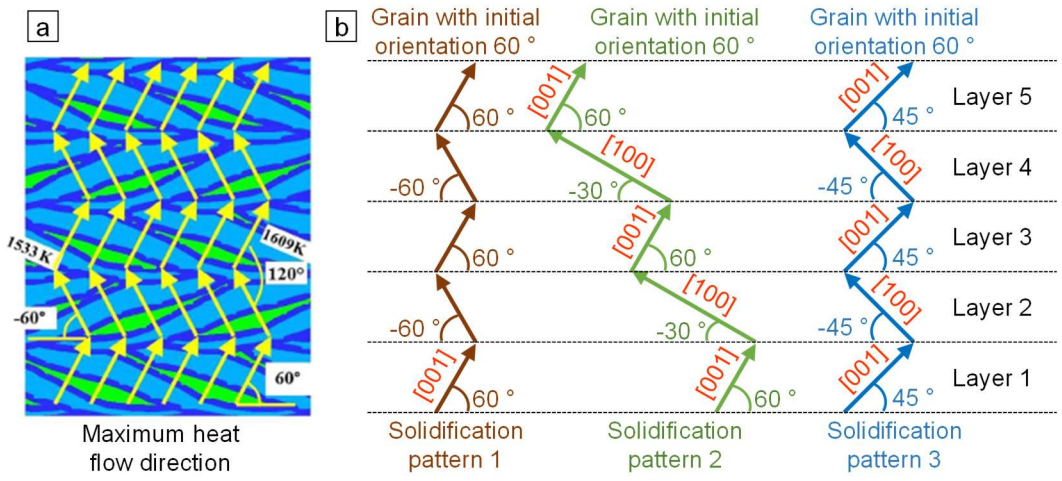

Figure 13. Maximum heat flow directions and solidification patterns of grains with preferential orientation for bi-directional scanning strategy. (a) Calculated temperature field with maximum heat flow directions indicated by yellow arrows. (b) Schematic for primary dendrite growth patterns [155].

The nucleating agent adopts the same crystallographic orientation as the partially melted grains in the previous layer, which is known as epitaxial growth [156], see Figure 14. The equiaxed grains are distributed between every two layers of columnar grains [157]. The epitaxial growth dominates the microstructure in upper deposition layers, resulting in the formation of large columnar grains, whereas the growth of columnar grains is suppressed in the first several layers due to the rapid heat transfer to the substrate, which leads to a high cooling rate [21]. During solidification, grains with a preferential growth orientation succeed in the competitive growth with misoriented grains leading to strong texture in AM-produced microstructure [18]. The competitive growth pattern has been recreated through the phase field simulation. The solutes released from the well-oriented dendrite tips through the dendritic channel impede the continued growth of misoriented dendrites by increasing the level of constitutional undercooling before reaching a state of steady growth [158].

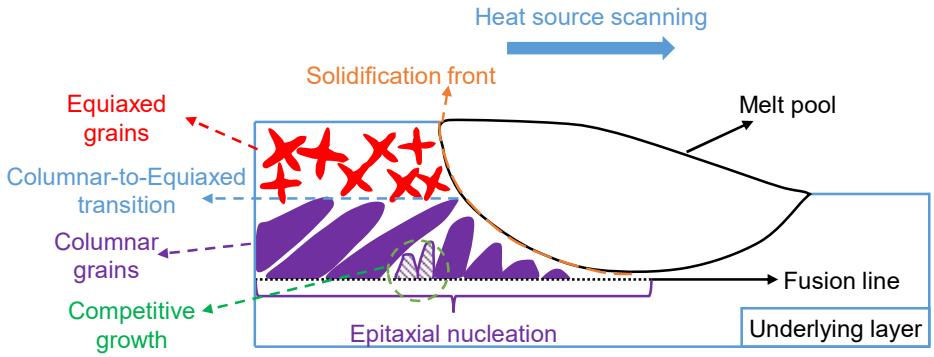

Figure 14. Bi-modal microstructure in AM-produced structure [159].

The presence of columnar grains in AM-processed lightweight materials, such as Al alloys, leads to anisotropy in their mechanical properties, including strength and ductility [153]. For instance, in the WAAM processing of AlZnMgCu alloy [71], it has been observed that the UTS and YS along the building direction are higher than those along the deposition direction, while the ductility remains comparable. This finding is consistent with SLM processing AA7075 alloy

[160]. In contrast, in wire-based L-DED processing of AlMg alloy, a higher strength level is reported in the tensile specimens along the deposition direction [157]. To address this anisotropy issue, various attempts have been implemented from three perspectives, including parameter optimization [157], different scanning strategies [18, 57], and material modification [161]. These approaches aim to improve the anisotropy. It should be noted that despite these efforts, complete elimination of anisotropy in mechanical properties has not yet been achieved. Nonetheless, significant progress has been made in reducing anisotropy through these approaches.

2.2.3 Development of new materials

In addition to studying the processability of existing materials, there is a growing interest in developing new materials specifically for AM. One approach to achieve this is by adjusting the chemical composition of existing alloy systems through the incorporation of dope materials, resulting in the production of composite materials. Another method involves pre-alloying, which increases the content of alloying elements in the material [144].

In terms of incorporating dope materials into the existing alloy systems, it is easier to implement in powder-based AM. This can be conducted during deposition by utilizing multiple powder feeders or prior to deposition by incorporating raw materials with dope materials. However, incorporating multiple wires in lateral wire-based L-DED poses a more complex challenge [145].

Table 3 provides a summary of the incorporation material system and the corresponding improvements for powder-based L-DED and SLM. Various types of dope materials have been successfully incorporated, including Si [95], Y_2O_3 [162], TiB_2 [163], Zr [161], and TiC [164]. These dope materials can be incorporated into the existing alloy systems in the form of micro- or nano-particles through mechanical alloying or chemical engineering. The ball-milling method is commonly adopted to mechanically incorporate raw materials and dope materials.

Several factors, such as the incorporation ratio between the dope materials and raw materials, the ball-to-powder weight ratio, and the ball-milling parameters (e.g., time and rotational speed), play a crucial role in achieving improved processability in AM [25, 164]. By selecting the appropriate parameters and incorporation ratios, it is possible to significantly reduce porosity levels, prevent cracking, and enhance mechanical properties, as shown in Table 3. Conversely, using inappropriate parameters can have a detrimental impact on the processability. For instance, excessive milling energy resulting from a higher ball-to-powder weight ratio can lead to the loss of spheroidicity of raw powders [165]. A high ball-to-powder weight ratio can cause the flattening of powders [165], while low milling energy can increase the roughness of raw powders, even if they maintain a spherical shape leading to the deterioration in powder properties such as flowability, apparent density, and tap density [166]. It is also important to ensure that the dope materials are homogeneously distributed on the surface of raw materials, otherwise, clustering of dope materials may result in heterogeneity in microstructure and mechanical properties [143]. Achieving homogeneous incorporation requires a long milling time [165]. However, it has been observed that when TiB_2 nanoparticles are incorporated into AlSi10Mg powders using ball milling for an extended period, the plastic deformation of the Al matrix occurs [167]. To promote the adhesion of nanoparticles and

achieve a more homogeneous distribution on the surface of raw materials, an alternating adsorption process can be employed instead of ball milling [143].

In terms of the in-situ incorporation by simultaneously feeding multiple materials, achieving the desired chemical composition and homogeneous distribution of alloying elements throughout the microstructure is a challenging task [168]. This challenge can be mitigated by utilizing the laser to remelt the solidified layers [52].

Table 3. Previous achievements regarding the incorporation of dope material into raw material. √: achieved; ×: not achieved; -: not reported.

Ref.	AM technology	Raw material	Dope material	Grain refinement	Improvement			
					Porosity	Cracking	Strength	Ductility
[95]	SLM	AlZnMgCu	Si, TiB_2	√	-	√	√	√
[161]	SLM	AlZnMgCu	Si, Zr	√	-	√	√	√
[169]	SLM	AlZnMgCu	Si	√	√	√	√	√
[139]	SLM	AlZnMgCu	ZrH_2	√	×	√	√	√
[163]	SLM	AlSi10Mg	TiB_2	√	√	√	√	√
[170]	SLM	AlSi10Mg	TiC	√	-	-	√	×
[25]	L-DED	AlMgScZr	TiC	-	√	-	-	-
[164]	L-DED	AlMg	TiC	-	×	-	×	×
[171]	L-DED	AlCuMg	TiB_2	√	√	-	√	√
[172]	L-DED	AlZnMgCu	TiB_2	√	-	-	√	√
[173]	L-DED	AlSi10Mg	SiC	√	×	-	√	√

The processability of the alloying elements can also be improved by pre-alloying the elements that enhance it. In this approach, the alloying elements can be uniformly distributed within the feedstock used for AM [144]. Several new commercial materials have been developed by adjusting the content of alloying elements, and these are summarized in Table 4. The main objective behind these developments is to utilize grain refinement techniques, such as inoculation treatment, to mitigate cracking issues in Al alloys that are prone to cracking during AM processes [5].

Table 4. New commercial Al alloys specific for AM applications developed by modifying the existing alloy systems.

Product name	Alloy system	Raw alloy system	Changed alloying elements	Developer
A20X [174]	AlCuAgMgTiB	AlCuAgMg	Addition of TiB_2	Aeromet
Addalloy® [175]	AlMgZr	AlMg	Addition of Zr	NanoAl
Scalmalloy® [176]	AlMgMnScZr	AlMg	Addition of Sc, Zr	AP works
Scancromal® [176]	AlCrScZr	AlCr	Addition of Sc, Zr	AP works
Scantital® [177]	AlTiScZr	AlTi	Addition of Sc, Zr	AP works
Zicromal® [176]	AlCrZrMn	AlCr	Addition of Zr	AP works

The comparison between the development of new chemical compositions using traditional casting/forging methods and AM technologies is illustrated in Figure 15 [178]. The traditional route typically involves multiple trial runs and consumes a large amount of materials for alloy development, whereas using AM technologies offers the advantage of efficiently obtaining feedstock with the desired chemical composition and enabling batch production.

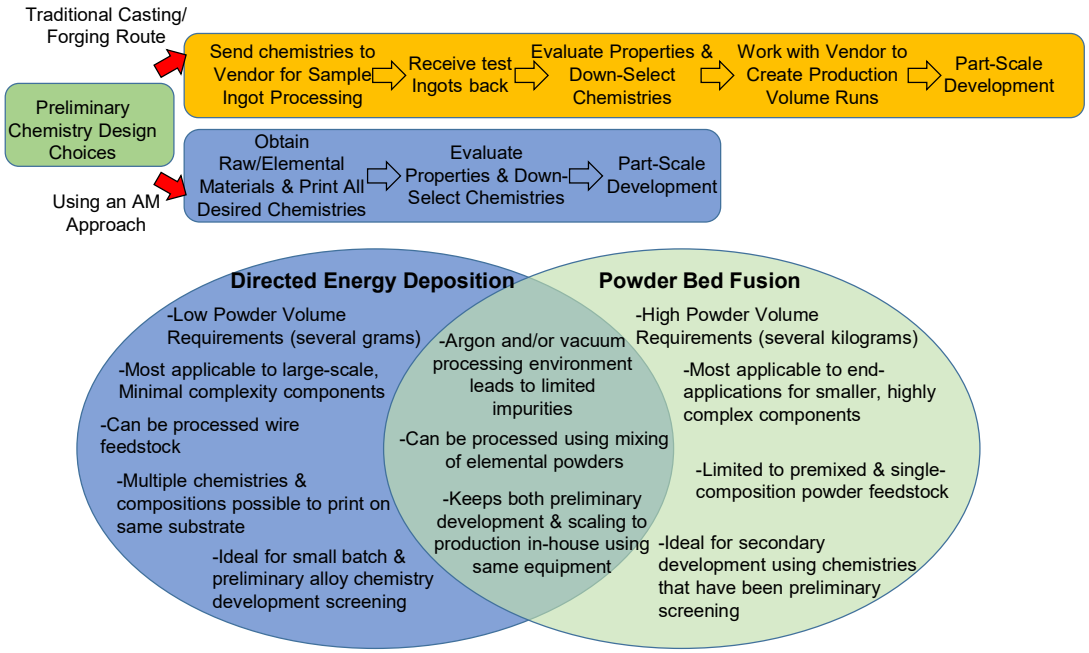

Figure 15. Comparison of material development route using traditional casting/forging and directed energy deposition as well as powder bed fusion [178].

In L-DED, the powder materials can be in-situ modified using multiple powder feeders or prepared before deposition through processes like ball milling and chemical engineering, as mentioned above. L-DED also allows for the production of structures with a graded chemical composition [179]. In contrast, the in-situ modification of chemical composition is not possible in SLM. Additionally, the amount of powders required for a print job in L-DED is significantly less than that in SLM [178], which simplifies the preparation process and reduces material waste associated with mixing powders before printing. Considering that SLM is capable of producing structures with complex geometries, it can be considered as a secondary screening process for new material development. Since the structural integrity of AM-produced structures concerning porosity and cracking may deviate with different geometries [27, 37], it is essential to further test and validate the properties of newly developed materials using SLM-produced structures. The preliminary screening process should be conducted using L-DED. The high-throughput production in L-DED has already been implemented to produce a batch of structures with different chemical compositions [180-183]. This batch production approach efficiently generates a large dataset, which not only accelerates material development through manual means but also facilitates the utilization of ML techniques for material development.

2.3. Application of machine learning in additive manufacturing

In a machine learning (ML) algorithm, the input data is used to produce outcomes and achieve a desired task without being explicitly programmed. Machine learning is a self-learning

process, which automatically optimizes the architecture through iterations. Machine learning algorithms can be categorized into supervised, unsupervised, and semi-supervised algorithms. [184]

In supervised algorithms, all the input data is labeled with their known outcomes (different classes in the case of classification problems or values in the case of regression problems), whereas the input data is not associated with any fixed outcomes in unsupervised algorithms [185]. In semi-supervised algorithms, a fraction of input data is labeled and the others are not labeled. The unlabeled data is used to augment labeled data in a supervised learning context [186]. Compared with supervised algorithms, it saves lots of time in data preparation. The common application of unsupervised learning is clustering analysis, which classifies input data into different groups based on the similarity during the iteration process [185].

Deep learning is a branch of machine learning techniques. Deep learning differs from other machine learning approaches in that it learns representations from input data in a progressive manner, with each layer capturing more meaningful representations [187]. In contrast, other machine learning approaches only learn representations in one or two layers [187]. In deep learning, the process of learning layered representations is achieved through neural networks, which are structured with literal layers stacked on top of one another [187]. The performance of machine learning models is determined by the data preparation and their architecture. The data preparation contains data preprocessing, feature engineering [187], the correlation between input data and output data, the matching accuracy of the input data and the corresponding output data, and the size of the dataset. The architecture of machine learning models consists of the hyperparameters of models, the loss function, the activation function, and the optimizer. To tackle various problems, these factors need to be specifically adjusted.

ML has found widespread application in assisting manufacturing processes. The employment of ML in AM can be divided into three phases, i.e. prior process, in-situ process, and post-process [40]. Table 5 provides a list of previous studies on the application of ML in AM.

In the pre-processing phase, ML can be employed to select and develop suitable material composition [188]. During the design for AM, ML aids in the topology improvement [189]. With numerous controllable process variables in AM, finding the optimal process window becomes challenging. ML algorithms such as neural networks [190-192] are used to expedite parameter studies. ML models are also capable of assisting material development. In [193], the efficient global optimization algorithm is modified based on the Kriging model to design Al-Zn-Mg-Cu-Ti-(Y)-(Ce) alloys with specific compositions and achieve the desired ultimate tensile strength. With the integration of machine learning, density-functional theory, thermodynamic calculations, and experiments, the development of high-entropy alloys can be accelerated [194]. However, compared with topology optimization and parameter prediction, the application of ML in material design is still not exploited, which is attributed to the expense of preparing sufficient datasets and the lack of a comprehensive understanding of physical processes in AM.

ML algorithms are also valuable in supporting the in-situ process monitoring and control. One prevalent algorithm for this purpose is the convolutional neural network (CNN), which

excels in conducting in-situ monitoring and defect detection based on image recognition. CNN offers higher accuracy and requires less feature extraction compared with conventional ML algorithms [40]. During the AM process, images captured for the CNN model contain various elements such as melt pools [41-43], plume and spatter [44], and layer surface [45, 46]. All the information enclosed in the images belongs to the processing characteristics. The images can be utilized for quantitative characterization of the properties, such as the prediction of porosity level [47] and surface roughness [48]. Additionally, they can be used for qualitative evaluation of the processing, including identifying the presence of defects and processing anomalies [42, 44]. By labeling scalograms analyzed from the time-series signal of average emission intensity extracted from thermal images using operando X-ray images, CNN models can achieve a nearly perfect prediction for the presence of keyhole pores during SLM [195]. Nevertheless, while the aforementioned works can predict defects and diagnose the processing anomaly, a simultaneous correction is not possible. In order to prevent the deterioration of existing anomalies and minimize material waste, it is crucial to have an in-situ adjustment of process parameters.

Researchers have also explored the potential of ML in predicting the geometry of as-built single tracks [196] and multiple layers [197]. To reduce the cost associated with the experimental characterization of as-built specimens, some studies have integrated the microstructure and mechanical properties with process-related factors using ML. This allows for the correlation between process parameters and microstructural features, enabling the prediction and tailoring of microstructure [198]. By extracting thermal histories during the AM process, it is possible to predict the quasi-static tensile properties in the local region of thin-wall structures [199]. The process-and-analysis chain has been established using ML for parameter adjustment to achieve high-density structures and predict the strength based on microstructure [200]. The prediction of fatigue life for stainless 316L processed by SLM is feasible by analyzing the process parameters (laser power and powder layer thickness) using either traditional machine learning algorithms or neural networks [201].

Table 5. Application of machine learning for AM in different scenarios.

Ref.	Phases	AM technologies	Materials	Inputs	Algorithms	Outputs	Purpose
[202]	Prior	PolyJet	Acrylic-based photopolymers	Data matrices encode the different unit cell arrangements for microstructure	CNN	Toughness of hierarchical systems + new microstructural pattern	Prediction for high-performance geometrical design of hierarchical systems
[203]		SLM	AlSi10Mg	Encoded AM design features and target components	Hierarchical clustering + SVM classifier	Identification for the final sub-cluster	Computational AM design feature recommendation
[204]		-	-	The density distribution and the last performed update of the densities	CNN	Predicted final structure	Topology optimization
[205]		-	-	Parameters defining the material layout of a unit cell	Sobolev norm neural network	Independent stiffness values	Macroscale topology optimization
[206]		-	-	The optimization result of the coarse grid	Generative adversarial network	Inferred output for the fine grid	Topology optimization
[207]		-	-	A noise of latent dimension	Generative adversarial network + CNN	Volume fraction	Topology optimization
[191]		SLM	Cu	Converted format from microscope images	Convolutional Auto-Encoder	Different clusters	Optimization for process parameters
[192]		SLM	Inconel 625 Steel; AlSi10Mg	Design and process parameters	Voxel-based CNN + CNN	Manufacturability	Prediction for the manufacturability

Table 5. Continuation of application of machine learning for AM in different scenarios.

[41]	In situ	WAAM	Molybdenum	Melt-pool images	CNN	Classification for processing states	Anomaly detection
[42]		SLM	Inconel 625	Pre-processed tensors of melt-pool images	Convolutional Auto-Encoder	Self-clustering	Anomaly detection
[43]		SLM	Inconel 625	Melt-pool images	CNN	Classification for the melt-pool size	Process monitoring for melt-pool size
[44]		SLM	316 L	Melt-pool images	CNN	Classification for three-track morphologies	Anomaly detection
[45]		SLM	Inconel 718	Powder-bed images	CNN	Classification for different powder-bed states	Anomaly detection
[46]		SLM	Ti6Al4V	Powder-bed images	CNN	Classification for flaw or flawless	Anomaly detection
[47]		L-DED	Ti	Melt-pool images	CNN	Prediction for the presence of pores and porosity level	Classification for the present of pores; Regression for the porosity level
[48]		SLM	WE43	Hyperspectral data	CNN	Surface roughness	Quality control
[208]		SLM	316 L	Acoustic signals	Spectral CNN	Classification for different porosity levels	Quality control
[200]	Post	EBM	Ti6Al4V	Process parameter; Surface morphology images	Multi-layer perceptron; CNN	UTS; Porosity level; Surface condition; Microstructural images	Analysis of process-microstructure-properties relationship
[199]		L-DED	Inconel 718	Process-induced temperature sequence	CNN	Mechanical properties	Prediction for mechanical properties
[198]		-	-	Reduced representation for EBSD measurements	CNN	Predicted microstructure	Prediction for microstructural variations
[196]		L-DED	AA2024	Process parameters	ANN	Geometry of tracks	Quality control
[209]		WAAM	Steel	Geometrical parameters of bead	ANN	Offset distance of weld beads	Process parameter optimization
[197]		WAAM	Steel	Process parameters	ANN	Geometrical deviation	Quality control

3. Experimental

3.1. Material preparation

The powder material used for L-DED is gas-atomized AA7050 powder supplied by NANOVAL GmbH & Co. KG. The average size of the powders is reported to be 36 µm by the supplier. It is important to note that during storage and usage, the powders may absorb moisture from the surrounding environment or become further oxidized upon contact with air. This can result in a high content of oxygen and hydrogen in the powders, which can negatively impact both the processing and the properties of as-built specimens. To ensure optimal storage and usage conditions for the powders, it is necessary to analyze the content of oxygen and hydrogen under different conditions. This analysis will help determine the appropriate storage and usage guidelines for the powders. In as-delivered condition, the powders are stored in a sealed container along with a desiccant to minimize moisture absorption. However, if there are any remaining powders that cannot be fully consumed, they are stored in the powder feeder for future use. For this reason, powders that have been stored in the powder feeder for 3 and 7 days respectively are analyzed to assess their oxygen and hydrogen content. This analysis will provide insights into how long the powders can be stored in the powder feeder before their properties are compromised. Heat treatment is commonly utilized to dry powders before processing. However, even with the use of an inert gas or vacuum atmosphere, there is still a risk of further oxidation of the powders. To investigate the effects of drying and oxidation, the powders are subjected to heat treatment at 110 °C and 200 °C for 2 h, respectively.

The gas content contained in the powders is measured by the LECO 836 series elemental analyzer (LECO Corporation). The elemental analyzer can measure the content of oxygen, hydrogen, and nitrogen in a wide spectrum of materials including Al alloys. As shown in Figure 16, the powders stored in a powder feeder for 3 days exhibit a comparable content of oxygen and hydrogen compared with as-delivered powders. Nevertheless, when powders are stored in a powder feeder for 7 days, there is a significant increase in the content of hydrogen and oxygen. This indicates that any remaining powders in the powder feeder should be consumed within 3 days to prevent deterioration of powder quality. The heat treatment at 110 °C for 2 h does not significantly reduce the content of oxygen and hydrogen in the powders. This suggests that the as-delivered powders have a low moisture content. On the other hand, when subjected to heat treatment at 200 °C, the powders experience further oxidation. Considering the low moisture content in the as-delivered powders and the importance of energy conservation and emission reduction, as-delivered powders are directly used for L-DED. Additionally, no powders are stored in a powder feeder for more than 3 days.

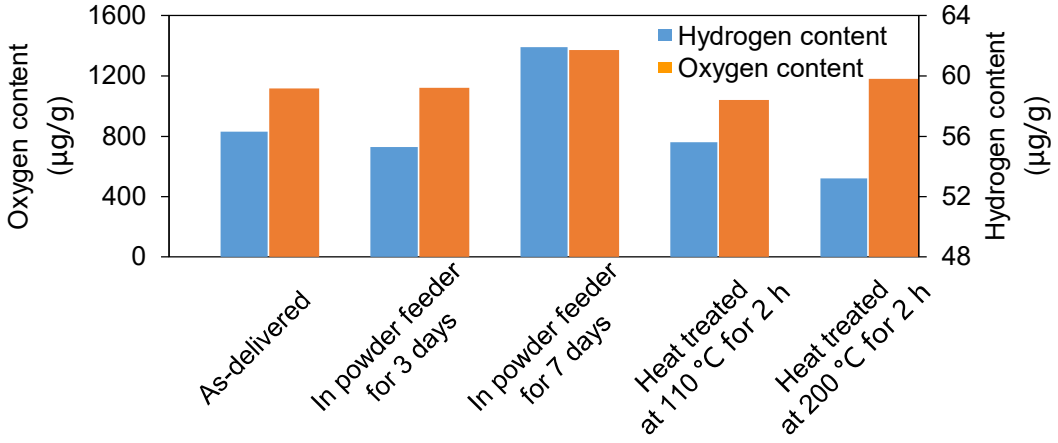

Figure 16. Content of oxygen and hydrogen of powders in different conditions.

The morphology, microstructure, and chemical composition of the powders are analyzed using a Jeol JSM-6490LV scanning electron microscopy (SEM) equipped with energy-dispersive X-ray (EDX) analysis (EDAX Genesis). The SEM operates at an acceleration voltage of 15 kV with a working distance of 10 mm. Figure 17(a, b) shows that the majority of the particles have a spherical morphology, although there are irregularly shaped particles present. The presence of irregular particles may have an impact on the flowability of powders [53]. Gas pores formed during atomization can be observed inside the particles, as shown in Figure 17c. Figure 17d provides a microstructure image of one particle, where the dark area represents the Al matrix and the bright area corresponds to the eutectic phases with a lower boiling point along the grain boundaries. The chemical composition of both the matrix and the eutectic phases is listed in Table 6. The eutectic phases are found to be rich in Zn, Mg, and Cu.

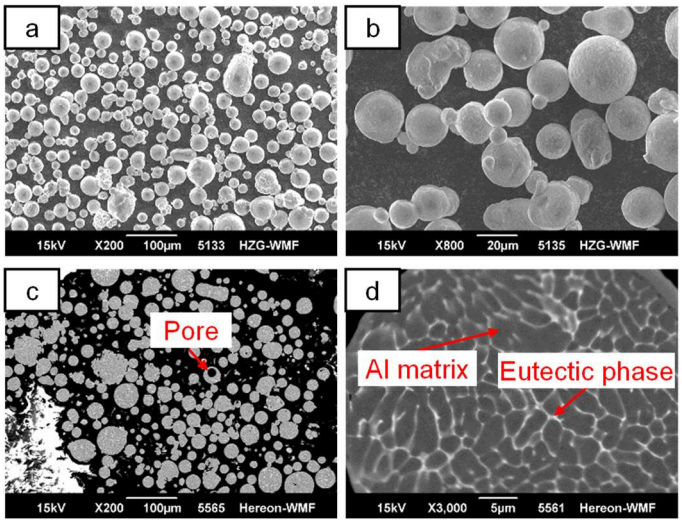

Figure 17. Morphology of AA7050 powder in (a, b); Cross-sectional microstructure in (c, d).

Table 6. Chemical composition of α-Al matrix and eutectic as marked in Figure 17d (in wt. %).

	Al	Mg	Si	Zr	Ti	Cr	Mn	Fe	Cu	Zn
Matrix	91.2	2.4	0.1	0.2	0.1	0.1	0.1	0.1	1.6	4.1
Eutectic	76.1	5.5	0.1	0.1	0	0	0	0.2	8.0	10.0

The wire material utilized for wire-based L-DED is AA7075 wire, which is supplied by Drahtwerk Elisental W. Erdmann GmbH & Co. The wire has a diameter of 1.2 mm. The chemical composition is measured in the as-delivered wires from the supplier using a Jeol JSM-6490LV SEM equipped with EDX analysis. The chemical composition of the AA7075 is provided in Table 7.

Table 7. Chemical composition of AA7075 wire (in wt. %).

Al	Mg	Si	Ti	Cr	Mn	Fe	Cu	Zn
89.5	2.5	0.4	0.1	0.2	0.1	0.2	1.3	5.7

3.2. Powder-based laser-directed energy deposition

The powder-based L-DED process consists of several components, including an Nd: YAG laser (Rofin DY022) with a maximum power of 2.2 kW, provided by Rofin Sinar Laser GmbH. A 6-axis robot (KR 6 R900) from Kuka AG is used to manipulate the deposition process. The system also incorporates a coaxial nozzle (Coax14V3) developed by Fraunhofer IWS. During the process, a substrate (50 mm × 50 mm × 15 mm) made of AA7075-T651 alloy is clamped onto a specimen holder. The holder moves along with the robot arm during deposition, while the position of the nozzle remains fixed. The powder focus is directed onto the surface of the substrate, as shown in Figure 18a. The laser spot diameter used in this process is 1.35 mm. By defocusing the laser beam by +6 mm, the laser focus is positioned 6 mm above the substrate surface. To maintain an inert atmosphere, the entire L-DED process takes place inside a glovebox filled with argon. No shielding gas is coaxially conveyed with the laser beam through the nozzle in these experiments.

The horizontal and vertical scanning strategies used in the L-DED process are depicted in Figure 18b. Each deposition track has a length of 24 mm. In the horizontal scanning strategy, two adjacent deposition tracks have opposite scanning directions and both move horizontally relative to the nozzle. After each layer deposition, the substrate moves down by a predetermined distance known as the z-offset. This pattern is repeated for successive layers. In the vertical scanning strategy, the substrate moves vertically relative to the nozzle during deposition. Figure 18c exhibits four different robot programs categorized by their timing for activating and deactivating the laser and powder feeder. While the position of the nozzle remains fixed, it is illustrated in a relative motion for easier comprehension. The following descriptions outline the different robot programs used in the L-DED process:

1. Robot Program 1: In this program, both the laser and powder feeder are continuously switched on throughout the entire process.

2. Robot Program 2: The powder feeder remains on, while the laser is activated at the beginning and deactivated at the end of each deposition track. Additionally, the laser power is lower during the first 1/4 section and the last 1/4 section of each track compared with the middle section.

3. Robot Program 3: Both the powder feeder and laser are turned on at the start of each track and switched off at the end. Powders are conveyed from the powder feeder to the substrate during this process. However, it takes some time for the powder feeder to the

substrate during this process. Therefore, Robot Program 3 is further divided into two sub-programs:

a) Robot Program 3 (no waiting): The laser and powder feeder are turned on synchronously.
b) Robot Program 3 (waiting): The laser is activated after a delay of 5 seconds following the activation of the powder feeder.

4. Robot Program 4: the powder feeder remains activated throughout the process, while the laser is activated after the substrate has traveled for 5 mm and deactivated 5 mm before reaching the end of each deposition track. The speed at which the robot arm moves is considered the laser scan speed. The motion of the robot arm during the deposition track consists of three phases: acceleration to reach the desired speed at the beginning, uniform motion at a constant speed, and deceleration towards the end. A distance of 5 mm is considered sufficient for both the acceleration and deceleration phases.

In this study, horizontal scanning and vertical scanning were investigated in Robot Programs 1 and 4. However, only vertical scanning was examined in Robot Programs 2 and 3.

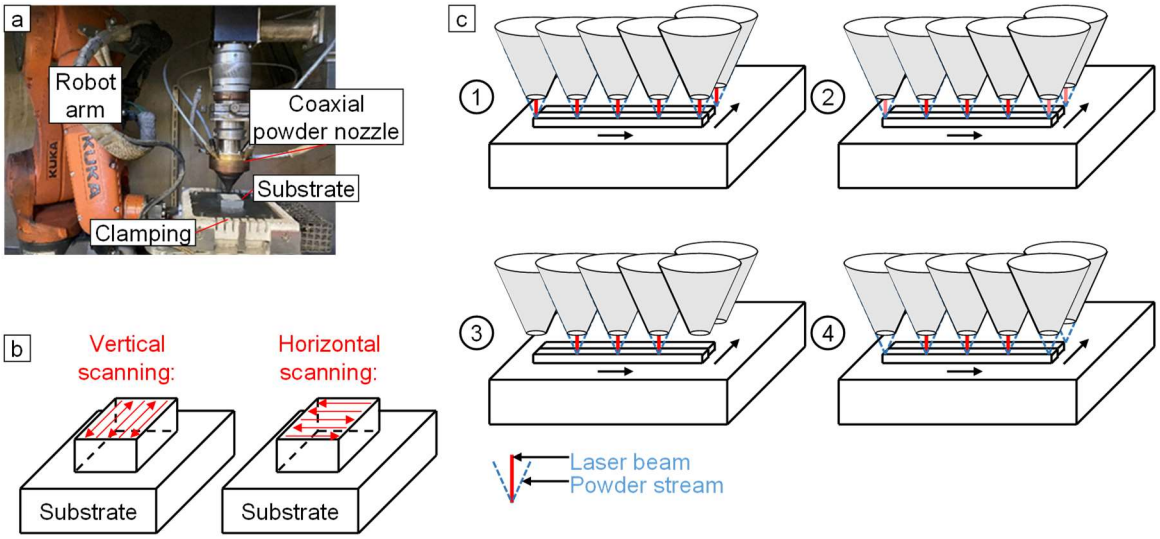

Figure 18. (a) Experimental setup of powder-based L-DED processing. (b) Illustration of vertical and horizontal scanning strategy (scanning direction is indicated by red arrows). (c) Illustration of four robot programs controlling the time for the switching status of laser and powder feed (black arrows represent the deposition sequence).

3.3. Wire-based laser-directed energy deposition

In this study, rolled AA7075 sheets measuring 100 mm × 50 mm × 15 mm were used as substrates for the deposition of AA7075 wire. The L-DED apparatus used in the experiment is depicted in Figure 19a. During the process, the substrate was clamped onto a working table made of AA5087. The feedstock material was melted by a laser with a core-ring profile, specifically, the TruDisk 4001 manufactured by TRUMPF. The laser energy input was distributed separately in the core and ring areas based on the set core-ring ratio. The inner core and outer ring have a diameter of 100 mm and 400 mm, respectively, at the focal position.

Throughout the study, the core-ring ratio remained constant at 15 %. The laser beam spot diameter on the substrate was measured to be 1.5 mm, with a positive defocusing of 36.14 mm (meaning that the laser focus was positioned above the substrate).

To control the deposition path, a CNC machine was employed. To capture clear images of the deposition process, a high-speed camera is attached to the optic head using an extension bracket (as shown in Figure 19a). The camera is focused on the tip of the wire, allowing for sharp images of the processing characteristics during deposition. The camera's focus plane is parallel to the cross-sectional plane of the thin-wall structures. As a result, the images taken during deposition correspond to the cross-sections in the direction of the melt-pool width. To protect the melting area from oxidation, the shielding gas Ar is coaxially conveyed through the wire feed nozzle. Additionally, an extra nozzle conveying Ar is installed and positioned mirror-symmetrically to the wire feed nozzle relative to the thin-wall structure, as depicted in Figure 19(b, c). The side facing the wire feed nozzle is referred to as the front side of the wall, while the side facing the extra nozzle is referred to as the back side of the wall. The relative positions of the wire feed nozzle, extra nozzle, laser beam, and thin-wall structures are illustrated in Figure 19d.

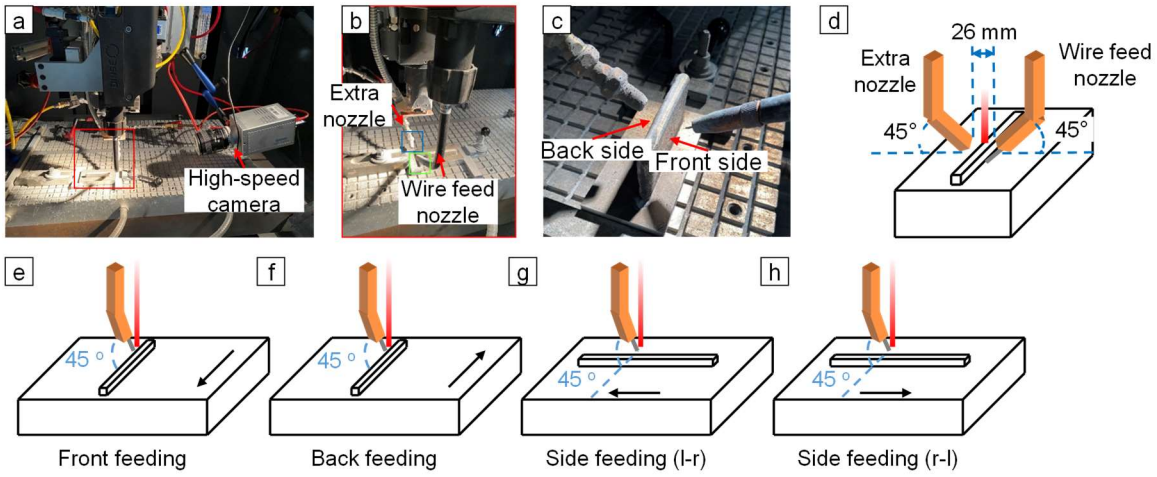

Figure 19. (a) Experimental setup in wire-based L-DED process. (b) Locally magnified area showing the position of extra shielding gas nozzle. (c-d) Illustration shows the relative position of the front side and back side of thin-wall structures and wire feed nozzle and extra nozzle. (e-h) Fours wire feed directions in wire-based L-DED. The black arrow represents the scanning direction.

Figure 19(e-h) illustrates four different wire feed directions. The distance between the wire and the laser spot remained constant for each wire feed direction. The terminology for these wire feed directions is adopted from a previous study [69] but is further clarified in this work. To investigate the effects of different wire feed directions, a single track was deposited on the substrate using each wire feed direction. In Figure 19e, the wire feed direction is nearly opposite to the deposition direction, forming an angle of approx. 135 ° (referred to as front feeding). In Figure 19f, the wire feed direction is almost parallel to the deposition direction, forming an angle of approx. 45 ° (referred to as back feeding). In Figure 19g, the single track was deposited horizontally from left to right relative to the substrate (referred to as side feeding

(l-r)). Conversely, in Figure 19h, the single track was deposited from right to left (referred to as side feeding (r-l)).

The thermal history of different specimens during the L-DED process was monitored using an infrared camera (Optris PI400). The camera has a resolution of 382 × 288 pixels, a frequency of 27 Hz, and s spectral range of 7.5 – 13 µm. To accurately measure the temperature, the emission coefficient of AA7075 during L-DED was calibrated using thermocouples. This calibration process was carried out during a single-track deposition. Both the infrared camera and thermocouples recorded the temperature evolution during deposition. By setting the emission coefficient at 0.32, a good agreement was achieved between the two measurement methods. It is important to note that the emissivity of a material can vary depending on factors such as material composition, surface roughness, and current temperature [210]. However, in this study, a constant emission coefficient was assumed since temperature evolutions of different specimens were compared within the same temperature range, despite the potential fluctuations in emissivity at different temperature ranges.

3.4. Post-process characterization

3.4.1 Geometrical characterization

A 3D profile of as-built structures was generated using a digital microscope (VHX-7000, Keyence). The maximum roughness R_{max}, which is the vertical distance from the highest peak to the lowest valley based on the German standard DIN4768, was adopted to represent the surface roughness of the back side of thin-wall structures. Furthermore, the 3D profile of as-built structures was compared with the intended design geometry prior to processing in order to assess the geometrical accuracy across various robot programs and scanning strategies.

3.4.2 Microstructural characterization

The L-DED-produced specimens were cut along the length direction and ground and polished for cross-sectional observation using an optical microscope (OM, Leica DMI 5000M). Kroll's etchant and Barker's etchant were utilized to reveal the microstructure. To analyze the distribution and chemical composition of secondary phases in the as-built specimens, a scanning electron microscope (SEM, Jeol JSM-6490LV) with connected energy-dispersive X-ray (EDX, EDAXGenesis) capabilities was employed. The number density and distribution of secondary phases were also observed using a scanning electron microscope (SEM, FEI Nova 200).

Electron backscatter diffraction (EBSD) was used to determine the texture, grain orientation, and grain size in order to uncover the relationship between process-microstructure-property. The EBSD analysis was conducted with an effective scan field area of 1875 mm × 1875 mm, a working distance of 13 mm, an acceleration voltage of 25 kV, and a tilt angle of 70 °. The scanned area was located in the middle of the thin-wall structure, which corresponds to the gauge area of the tensile specimens.

3.4.3 Mechanical characterization

The microhardness of the as-built specimens was determined using a Falcon 5000 microhardness tester (INNOVATEST Europe BV) with a load of 0.1 kg and a dwell time of 10 s. The indentation points were positioned in the gauge area of the tensile bars to establish a reliable correlation between hardness and tensile properties. Tensile tests were conducted at a strain rate of 1/s. Three tensile specimens were extracted from the middle of the thin-wall structures along the thickness direction.

The residual stress was calculated using experimental diffraction data obtained at the High Energy Materials Science beamline P07b (EH1) at DESY [211]. The experimental setups are illustrated in Figure 20a, and an example of a measuring pattern is shown in Figure 20b. The thin-wall structure was mounted on the specimen stage in such a way that the building direction of the structure aligned with the z axis (in the direction of σ_{yy}) and the longitudinal direction of the structure aligned with the x axis (in the direction of σ_{xx}), as depicted in Figure 20b.

For measuring residual strain along the building direction, an x-ray beam with an energy of 87.1 keV (wavelength of 0.142353 Å) and a size of 0.5 × 0.5 mm^2 was employed. The distance between the thin-wall structure and the two-dimensional detector type Perkin Elmer XRD 1621 (PE) was set to 1200 mm. Debye-Scherrer rings were recorded for multiple reflections, and the (311) reflection was specifically used to calculate the residual stresses since the grains with the (311) planes are less affected by residual intergranular stress and have a lower influence from the crystallographic texture [212]. To improve statistical accuracy, the specimen was oscillated in the direction of σ_{xx} with a range of ± 2.5 mm for each measurement point, considering the large grain size. The exposure time for each measuring point was set to 10 s. To characterize the variation of residual stress along the building direction, measurements of residual strain were initiated from 0.5 mm below the top surface and moved in steps of 2 mm until reaching the substrate, as depicted in Figure 20b. Additionally, measurements of residual strain along the building direction were conducted at different locations starting from the middle of the structure and moving towards both edges with a step size of ± 5 mm (Figure 20b).

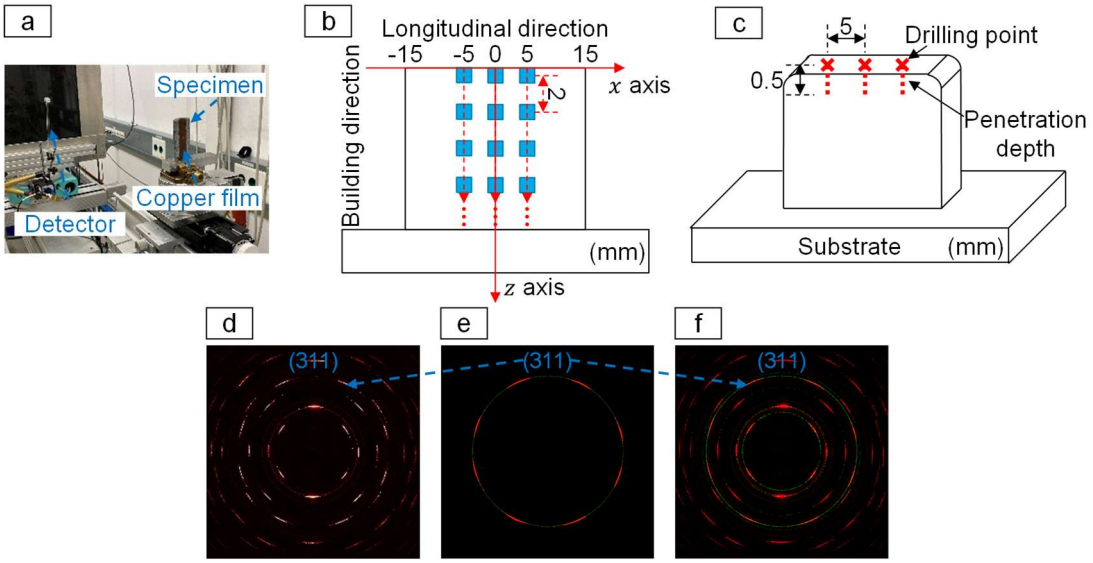

Figure 20. (a) Photos of the experimental setup to measure the diffraction data. (b) Measuring pattern for the thin-wall structure with a deposition length of 30 mm. (c) Sketch showing the position of drilling points in the hole-drilling measurement. (d) Measured partial diffraction rings. (e) Complete (311) diffraction ring after data recovery using ellipse fitting; (f) Full diffraction rings after data recovery. The solid red lines are the diffraction patterns experimentally measured. The dotted green lines are the recovered diffraction patterns.

To mitigate any misalignment effect caused by the specimen geometry during the calculation of residual stress, a thin layer of copper powder was applied to the surface of the specimen. A correction factor was then employed, taking into account the shift of a copper reflection near (311) from Al. The residual stress was determined from the measured strain using the fundamental equation of strain and incorporating the elastic constant E311: 69.39 GPa and the poison's ratio v_{311}: 0.35 for Al obtained. These values were obtained from XEC software [213].

The two-dimensional diffraction pattern obtained for L-DED-processed Al alloys is incomplete due to the absence of certain information, such as the (311) crystal plane, as shown in Figure 20d. This incompleteness is attributed to the intrinsic characteristics of the microstructure, including coarse grains and strong texture. To address this issue, ellipse fitting was employed to recover the partial diffraction patterns, as depicted in Figure 20e and f. This method has been validated as a reliable approach for completing the partial diffraction patterns [214]. Subsequently, the complete diffraction patterns were utilized to calculate the strains for the (311) crystal plane and determine the corresponding residual stress. Additionally, the residual stress was measured on the top surface of the specimens along the longitudinal direction using the hole-drilling method with the PRISM system from Stresstech GmbH. In this method, a hole with a diameter of 1.0 mm was incrementally drilled to a maximum depth of 0.5 mm using a drill made of high-speed steel Co 5 with a TiAlN solid carbide insert. The drilling depth was increased in increments of 0.025 mm increments. The details regarding the hole-drilling measurement technique have been described in [215]. For each specimen, three holes were drilled on the top surface with a distance of 5 mm along the longitudinal direction, as illustrated in Figure 20c.

3.4.4 Image processing

Grayscale images were captured using a high-speed camera with a frame rate of 2000 frames per second (FPS) and an exposure time of 100 μs. These raw images, measuring 1280 × 860 pixels, contain various information such as the melt pool, plume, and spatter. For the purpose of this study, the images were resized to 640 × 430 pixels to reduce computation time and were used for two different analyses: evaluating the processing stability of the deposition process and inputting into a neural network model.

The stability of melt pools during deposition is analyzed based on the melt-pool images in the first layer. The indicator for evaluating the stability of melt pools is the fluctuation of melt-pool area and shape. To extract the melt-pool profile from the raw images, all grayscale images are binarized with a threshold value of 190. The threshold value is determined to accurately capture the melt-pool profile while avoiding any misleading information from the illuminated area surrounding the melt pools. The detailed workflow on how to determine the threshold value can be referred to in **Paper 5** Appendix A.1.

To accurately evaluate the processing stability, it is important to consider the geometrical fluctuation of melt pools. Even if two melt pools have the same area, they can exhibit different geometries. The variation in geometry can be influenced by gas flow, leading to property variations, as reported in [216]. After binarization, all pixel points in the processing image corresponding to the melt pool are assigned a grayscale value of 1, whereas other pixel points corresponding to non-melt-pool areas are assigned a grayscale value of 0. To compare the geometrical deviation of melt pools in different images, it is necessary to compare the grayscale values of each pixel point representing the location of melt pools pixel by pixel between images. To statistically represent this geometrical fluctuation of melt pools during processing, the *dHash* value and *dHash* difference are adopted. These metrics allow us to quantify and analyze the differences in geometry between melt pools in different images.

The *dHash* value is a parameter to compare the grayscale values in two neighboring pixel points in an image row by row. The workflow to calculate the *dHash* value of one image and the *dHash* difference between two images is illustrated in **Paper 5** Figure 8. If the grayscale value of the left pixel is higher than that of the right pixel, the character “1” is recorded. Otherwise, the character “0” is recorded. Subsequent to the comparison of all pixel points, a long string consisting of “1” and “0” is arranged for each image. In this study, since the raw images are firstly binarized to extract the contour of melt pools, the pixel points exhibit either black or white. Characters in the string are considered binary numbers. To save computational time while maintaining the sensitivity to detect subtle differences, every two characters in the string from the first to the last are converted to decimal numbers and stored as a new string. The fully converted string corresponds to the *dHash* value of the image. All the images have the same length of strings because of the same image size. The *dHash* difference is the total number of characters that differ in the identical position in two strings converted from two images.

4. Achievements

4.1. Overview

The results presented in this thesis have been published as peer-reviewed papers in scientific journals. This chapter specifically focuses on the results and discussion of the thesis, which consists of 4 published papers and 1 paper under preparation for submission. The first paper investigates the processability of high-strength Al alloys in powder-based L-DED. The development of the process window considers not only the process parameters but also the robot programs that control the switching status of the laser and powder feeder. This is because the timing for powder feeding and laser radiation can have a significant impact on the processability and the properties of as-built specimens (**Paper 1**). In addition to using powder as feedstock, the thesis also explores the process development for high-strength Al alloys in wire-based L-DED. The aim is to determine whether the form of feedstock can influence the processability. This investigation is presented in **Paper 2 and Paper 3**. In **Paper 2**, the effects of wire feed directions in lateral L-DED were investigated. The study also conducted preliminary research on optimizing process parameters for building one-layer single tracks. Building upon the findings from **Paper 2**, thin-wall structures with multiple layers (up to 100 layers) were built using the determined wire feed directions and the preliminarily optimized parameters in **Paper 3**. Furthermore, in this paper, the process parameters were further optimized to minimize the internal porosity level and prevent cracking in the thin-wall structures. Microstructural characterization and mechanical tests were also conducted to establish a correlation between process-microstructure-property. Due to the lack of comprehensive analysis of cracking mechanisms in L-DED processing of high-strength Al alloys using experimental methods, **Paper 4** is devoted to investigating these mechanisms from both thermal and mechanical perspectives. The experimental methods employed in this study include monitoring the temperature evolution during processing, measuring residual stress in as-built specimens, and analyzing the microstructure of as-built specimens. In order to improve the surface roughness observed in **Paper 4**, **Paper 5** introduces the development of an optimized shielding gas-feeding system. This system not only enhances surface quality but also reduces porosity levels by ensuring processing stability. The significance of processing stability in laser-based AM is emphasized. Hence, the latter part of **Paper 5** is dedicated to maintaining processing stability through machine learning techniques to assist the in-situ adjustment of process parameters.

4.2. Processability of high-strength Al alloys in powder-based laser-directed energy deposition

Paper 1: M. Wang, N. Kashaev, On the optimal process window for powder-based laser-directed energy deposition of AA7050 under different robot programs and scanning strategies, Journal of Manufacturing Processes 90 (2023) 286-299.

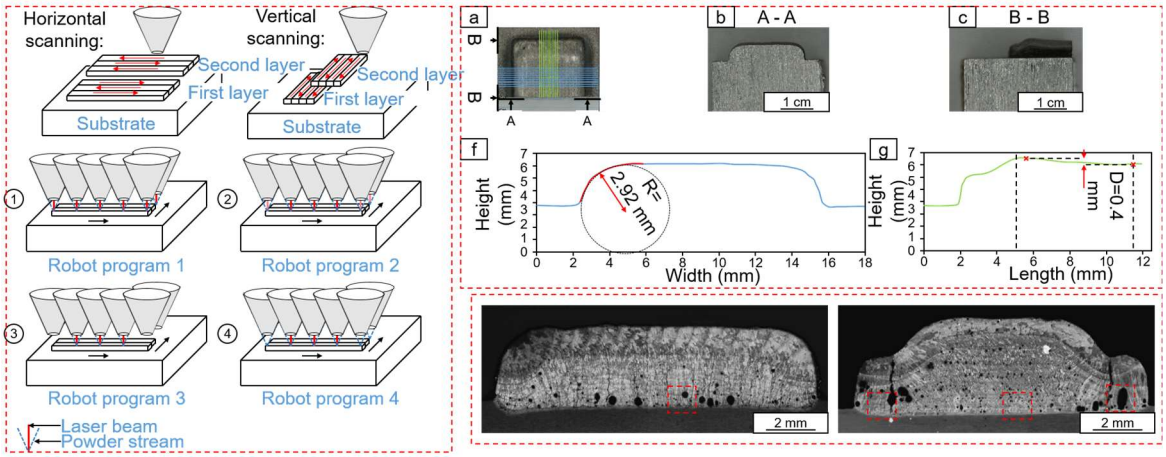

Figure 21. Graphical abstract of **Paper 1**.

The purpose of this study is to explore the feasibility of using AA7050 in powder-based laser-direct energy deposition (L-DED). There is limited information available on the use of 7XXX series alloys in L-DED. Therefore, this study aims to expand the range of applicable Al alloys for this process. Previous research on L-DED has primarily focused on process parameters. The scanning strategy and the robot program controlling the switch status of the powder feeder and the laser were rarely introduced before. Although it is commonly acknowledged that the starts and the stops of the robot during the deposition should be avoided, their impact on the L-DED process and the properties of L-DED-produced specimens were not systematically investigated. Therefore, it is important to conduct a comprehensive and statistical analysis.

This study focuses on examining the effects of robot programs and scanning strategies on the L-DED-processed AA7050 powder. The advantages and disadvantages of each robot program are analyzed in terms of buildability, porosity level, crack initiation, and heat effect on the substrate. Additionally, the research also explores the optimal process parameters through different combinations of robot programs and scanning strategies.

The horizontal and vertical scanning strategies are depicted in Figure 21. Each track has a length of 24 mm. In the horizontal scanning strategy, the scanning directions of two adjacent deposition tracks are opposite, both traveling horizontally relative to the nozzle. After each layer deposition, the substrate moves down a preset distance (z-offset). The successive layers follow the same pattern. In the vertical scanning strategy, the substrate moves vertically relative to the nozzle. Figure 21 also presents four robot programs categorized by different timing for switching on and off the laser and powder feeder. Although the position of the nozzle remains fixed while the substrate placed on the robot arm moves, the relative movement of the nozzle is illustrated for clarity. In robot program 1, the laser and powder feeder remain switched on throughout the entire process. In robot program 2, the powder feeder remains switched on, and the laser is activated at the beginning and deactivated at the end of each track. Additionally, the laser power is lower in the first 1/4 and last 1/4 sections of the track compared to the middle section. In program 3, the powder feeder and laser are activated at the beginning and deactivated at the end of each track. The conveying of powders from the powder feeder to the substrate requires a certain amount of time for the powders to land on the substrate. As a

result, robot program 3 is divided into two subprograms: one where the laser and powder feeder are activated simultaneously, and another where the laser is activated 5 seconds after the powder feeder (hereinafter referred to as robot program 3 (no waiting) and robot program 3 (waiting)). In robot program 4, the powder feeder remains switched on, and the laser is switched on after the substrate has moved for 5 mm and switched off 5 mm before the end of each track. The travel speed of the robot arm is considered the laser scan speed. The movement of each deposition contains three phases: acceleration to reach the set speed at the start; uniform and stable movement; and deceleration at the end. A distance of 5 mm is deemed sufficient for both the acceleration and deceleration phases. In this study, horizontal scanning and vertical scanning were investigated in robot programs 1 and 4, while only vertical scanning was investigated in robot programs 2 and 3.

Based on the findings, the following conclusions can be drawn:

- The acceleration and deceleration phases of the robot arm harm the buildability and geometrical accuracy. Heat accumulation during these phases leads to the formation of bumps at the beginning and the end of deposition tracks. To mitigate this issue, an optimal control strategy involves reducing laser power on both sides of each track or adjusting the timing for switching on the laser and powder feeder.
- Robot programs and scanning strategies have an impact on the initiation of hot cracks. It is observed that higher cracking resistance occurs when the laser remains switched on during deposition. Additionally, when the laser is switched on and off at the beginning and the end of deposition tracks, a horizontal scanning strategy demonstrates higher cracking resistance than a vertical scanning strategy. This difference could be attributed to the varying resistances to the crack propagation in different patterns of grain boundaries.
- The minimal achievable porosity level varies across different combinations of robot programs and scanning strategies. Even when using the same process parameters, such as laser power and laser scan speed, variations in porosity level are evident. This difference is attributed to the changing energy input and thermal history during deposition, influenced by the switching state of the laser and powder feeder.

4.3. Processability of high-strength Al alloys in wire-based laser-directed energy deposition – Part 1

Paper 2: M. Wang, N. Kashaev, Investigation of process window for AA7075 considering effects of different wire feed directions in lateral Laser Metal Deposition, Procedia CIRP 111 (2022) 218-223.

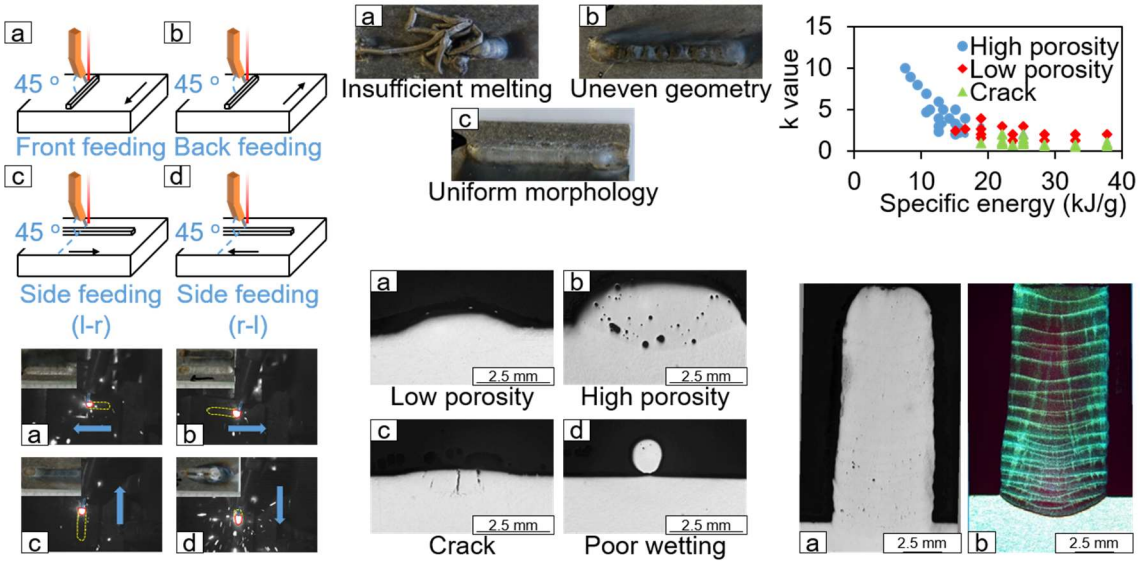

Figure 22. Graphical abstract of **Paper 2**. Side feeding (l-r): using the side feeding strategy to deposit a single track from left to right. Side feeding (r-l): using the side feeding strategy to deposit a single track from right to left.

Based on the type of feedstock, L-DED can be categorized into powder-based and wire-based techniques [123]. Wire-based L-DED offers a higher deposition rate compared to powder-based L-DED [67]. 7XXX series high-strength alloys are extensively utilized in industries due to their high strength-to-density ratio [3]. However, processing these alloys in AM is challenging, particularly their high sensitivity to hot cracking [56] and porosity formation. These difficulties have been reported in studies investigating the processability of 7XXX series alloys in powder-based L-DED [27] and wire and arc additive manufacturing (WAAM) [71, 72]. Given the advantages of 7XXX series alloys and wire-based L-DED, the development of an appropriate process window is necessary.

In wire-based L-DED, the wire can be fed laterally or coaxially relative to the laser beam [67, 68]. This study utilizes a lateral L-DED apparatus, which can be easily reconstructed from a welding apparatus. The results of this study indicate that the interaction among laser beam, wire, and melt pools is dependent on the feed direction of wires. However, there is a scarcity of studies addressing the impacts of wire feed direction. Therefore, this paper aims to explore the consequences of wire feed direction in lateral L-DED and investigate the optimal process window for L-DED processing AA7075 alloy.

Four kinds of wire feed directions are illustrated in Figure 22. The distance of the wire from the laser spot was maintained constant in various wire feed directions. The terminology of the wire feed directions is adopted from [69] and further specified in this study. To examine the effects of different wire feed directions, a single track was deposited on the substrate using each wire feed direction. In front feeding, the wire feed direction is nearly opposite to the deposition direction (at an angle of approximately 135 °). In back feeding, the wire feed direction is nearly parallel to the deposition direction (at an angle of approximately 45 °). In side feeding (l-r), the single track was deposited from left to right in the horizontal direction relative to the substrate. In side feeding (r-l), the single track was deposited from right to left.

The study investigated the impact of wire feed direction on the lateral L-DED process and the properties of deposited single tracks using a high-speed camera. Additionally, the optimal process window for lateral L-DED processing of AA7075 alloy was investigated. The following conclusions can be drawn:

- Under the same process parameters, the wire feed direction can affect the geometry of single tracks, but it does not influence the porosity level. Additional interlayer cleaning is required when using front feeding. The wire might be stuck in the track causing the process to be aborted when using the back feeding.
- The k value, which is the ratio of wire feed speed and scan speed, is a critical parameter that affects the initiation of cracks in the L-DED process. Setting the k value above a certain threshold has been proven to be an effective method for preventing cracking.

4.4. Processability of high-strength Al alloys in wire-based laser-directed energy deposition – Part 2

Paper 3: M. Wang, V. Ventzke, N. Kashaev, Wire-based laser directed energy deposition of AA7075: effect of process parameters on microstructure and mechanical properties, Journal of Materials Research and Technology 21 (2022) 388-403.

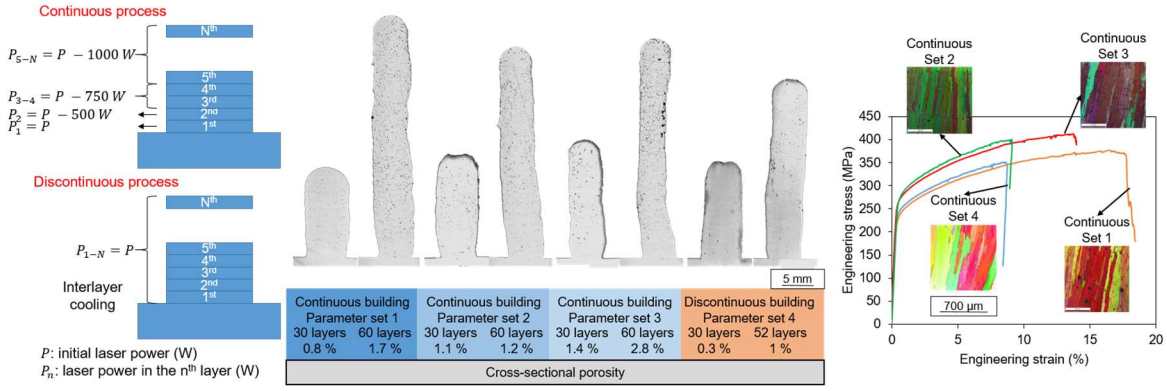

Figure 23. Graphical abstract of **Paper 3**.

Previous research on AM processing of 7XXX series alloys has primarily focused on SLM, WAAM, and powder-based L-DED. There is a lack of knowledge regarding wire-based L-DED for processing 7XXX series alloys. Given the advantages of wire-based L-DED and the potential of 7XXX series alloys, there is a high demand for appropriate process development in this area. In this study, process parameters are optimized and different building strategies are employed to reduce porosity levels and prevent cracking. The microstructure is characterized and the mechanical properties are tested. Thermal analysis is implemented via FEM simulation to better understand the microstructure formation. The correlation of process-microstructure-mechanical properties is revealed within this work.

The process parameters for building thin-wall structures were selected based on the evaluation of the integrity of single tracks in **Paper 2**. Two building strategies were employed

for the thin-wall structures: continuous and discontinuous processes. In the continuous process, the laser power decreased with each subsequent layer, and no interlayer-cooling was implemented between adjacent layers. However, to address processing errors and adjust process parameters between layers, the process was paused after each layer deposition. The program was then restarted after inspecting for the surface defects, which took approximately 40 seconds. In the discontinuous process, an interlayer-cooling time of 1.5 min was set between layers, or the solidified layer was cooled to room temperature before the next deposition. The laser power remained constant in the discontinuous process. The workflow for the process development is illustrated in Figure 23.

In this study, the processability of AA7075 in L-DED was thoroughly investigated. The process parameters and building strategies were optimized to produce crack-free specimens with low porosity levels. The microstructure was characterized using various methods, and the mechanical properties including strength and ductility were investigated. Based on the results, the following conclusions can be drawn:

- The specific energy (the ratio of laser power to the mass flow of the wire) and k value (the ratio of wire feed speed to laser scan speed) are two effective indicators for assessing the overall impact of process parameters on the integrity of single tracks and thin-wall structures. The porosity level exhibits a negative correlation with both the specific energy and the k value. There is a stronger dependence of the porosity level on the specific energy.

- Through process optimization for a 30-layer deposition, the porosity level can be reduced to 0.8 % in the continuous processing, whereby a further reduction to 0.3 % is possible in the discontinuous processing. However, it is important to note that the porosity level deteriorates with further deposition to 60 layers in both building strategies.

- The hardness remains relatively constant in the middle of thin-wall structures indicating stable processing. The average hardness of thin-wall structures produced with four parameter sets is comparable. Fracture surfaces reveal a mixed fracture mode of ductile fracture and shear fracture. The specimen produced with the discontinuous building strategy exhibits the lowest strength, which could be attributed to the presence of large pores and cracks within the specimen. The strength and ductility achieved in this study surpass those reported in previous works on 7XXX series alloys in their as-built states produced by other AM technologies.

- Large columnar grains with epitaxial growth are predominant in the cross-sections of specimens. The growth direction is perpendicular to the interface of melt pools and nearly parallel to the building directions. Despite variations in process parameters and building strategies, all specimens exhibit a fiber texture. Additionally, various precipitates are present in as-built specimens due to the reheating of previously solidified layers when building subsequent layers.

- The superior mechanical properties of these specimens could be attributed to the orientation of long grain boundaries and the distribution of secondary phases. During tensile tests, the tensile stress aligns nearly parallel to the long grain boundaries, where

the secondary phases are distributed. These secondary phases are assumed to serve as preferential sites for cracking initiation. As they are not subjected to high tensile stress in this study, it could potentially lead to a “delayed” fracture.

- Through calibrated transient heat analysis, it was determined that the maximal temperature in the melt pool ranges from 900-1080 °C leading to the evaporation of Zn and no loss of Mg, which is in agreement with the EDX measurement. The epitaxial growth cannot be inhibited by the decreasing cooling rate with the increasing building height resulting in the dominant formation of columnar grains.

4.5. Analysis of cracking mechanisms of 7075 Al alloy in laser-directed energy deposition

Paper 4: Unravelling the cracking mechanism in laser-directed energy deposition processing high-strength aluminum alloy (under preparation for submission)

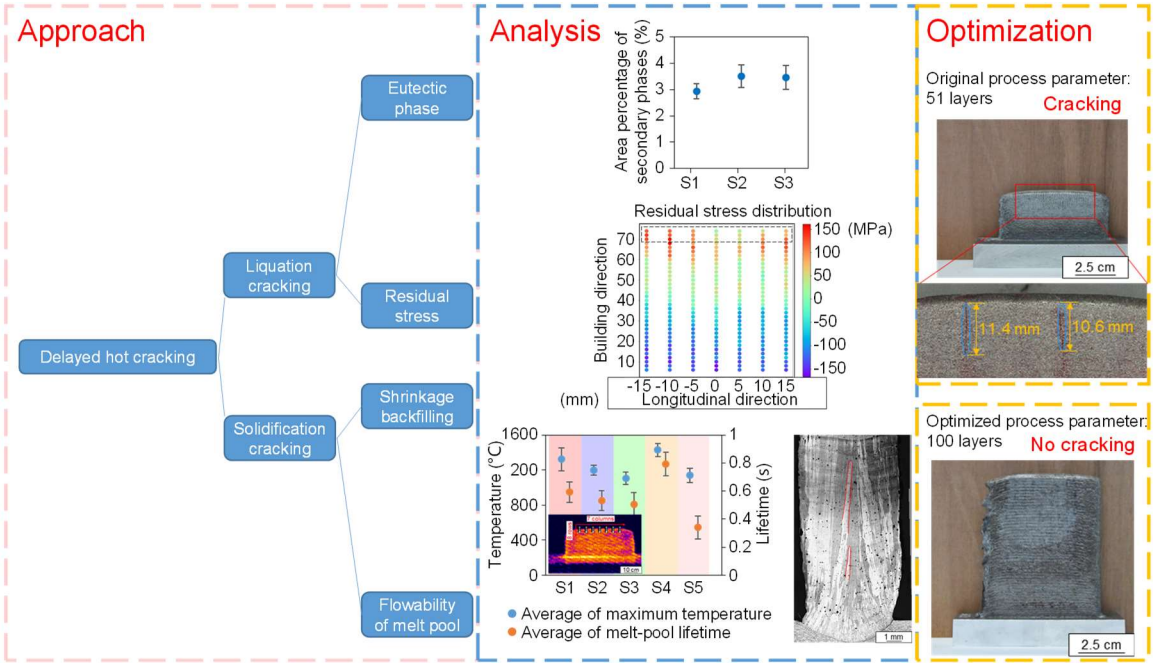

Figure 24. Graphical abstract of **Paper 4**.

High-strength Al alloys are prone to hot cracking in laser-based additive manufacturing (AM). Hot cracking of high-strength Al alloys can be categorized into two mechanisms: liquation cracking and solidification cracking. It remains challenging to fully understand the significance of various factors that contribute to cracking due to the complex physical processes involved in AM. Understanding the mechanisms behind cracking and identifying the primary factors are crucial to preventing cracking, especially when dealing with difficult-to-process materials. Therefore, it is necessary to uncover the cracking mechanisms during successive deposition.

The novelty of this study contains three points:

1. Systematic mechanism analysis regarding the initiation and growth of the macrocracks observed in this study, as shown in Figure 24: The initiation of the macro-cracks observed in this study is induced by insufficient backfilling to shrinkage during solidification. The growth is a consequence of combined solidification cracking and liquation cracking.

2. The adoption of interlayer heat treatment delivers new understandings of the heating effects during successive deposition to previously solidified layers: In AM, the successive deposition could act as intrinsic heat treatment to previously solidified layers and could affect the dynamics of eutectic phases including precipitation, dissolution, and partial remelting. In this study, interlayer heat treatment has been applied to successfully elaborate that the heating effects during successive deposition exhibit no influence on the precipitation and dissolution of secondary phases in previously solidified layers. The formation of secondary phases is the result of nonequilibrium solidification.

3. Propose two processing-related indices that can be used to represent the solidification cracking susceptibility: The melt-pool lifetime and the maximum melt-pool temperature can significantly determine the ability to backfill shrinkage during solidification and can be used to represent the cracking susceptibility. In future works, the evaluation and increase of these two indices could be an efficient method to prevent solidification cracking.

In this study, it was observed that laser-directed energy deposition (L-DED) can produce small-size structures made of AA7075 alloy without cracks. However, as the deposition length increases, the cracking susceptibility is enhanced. Additionally, a “delayed cracking” was observed in large-size structures, where cracks initiated after a certain number of layers were deposited. This study aims to systematically investigate the cracking phenomenon observed during successive deposition and uncover the significance of these influential factors through experimental methods, focusing on solidification conditions, microstructure, and residual stress.

After the initiation of cracks, they grow in two directions parallel to the building direction growing into the macro-cracks. The macro-crack consists of two areas, where the liquation cracks and the solidification cracks dominate, respectively. The reason for the initiation of macro-cracks is analyzed considering the factors that determine the susceptibility for liquation cracking and solidification cracking:

- Analysis of liquation cracking: The direct correlation between the liquation cracking susceptibility and the initiation of the macro-cracks observed in this study cannot be deduced only based on the analysis of three as-built structures with different deposition lengths. Therefore, an interlayer heat treatment (heating at 480 °C for 2 h and followed by water-quenching) was designed to investigate the heating effects during successive deposition to previously solidified layers. The microstructure and residual stress of a crack-free sample produced with optimized parameters are also used to compare and elaborate the role of the liquation cracking mechanism on the initiation of the macro-cracks. It has been confirmed that the successive heating effects exhibit no influence on the precipitation

and dissolution of secondary phases in previously solidified layers. Taking into account the possibility that successive deposition may or may not lead to the partial remelting of eutectic phases, we exclude the initiation of the macro-cracks attributed to the liquation cracking.

- Analysis of solidification cracking: Through analysis of the solidification conditions, it was found that a shorter deposition length enhances the melt-pool flowability and provides more time for Al melt to backfill the solidification shrinkage, whereas a longer deposition length increases the difficulty of backfilling. The melt-pool lifetime and the maximum melt-pool temperature are two important indices that represent the solidification cracking susceptibility. The dependence of solidification cracking susceptibility on solute content is also investigated based on the thermodynamic simulation. During the deposition, grains with a preferential growth direction suppress and eliminate misaligned grains. As the deposition proceeds, misaligned grains that are not eliminated in the early stages deteriorate the backfilling process, leading to delayed solidification cracking.

4.6. Application of machine learning in laser-directed energy deposition

Paper 5: M. Wang, N. Kashaev, On the maintenance of processing stability and consistency in laser-directed energy deposition via machine learning, Journal of Manufacturing Systems 73 (2024) 126-142.

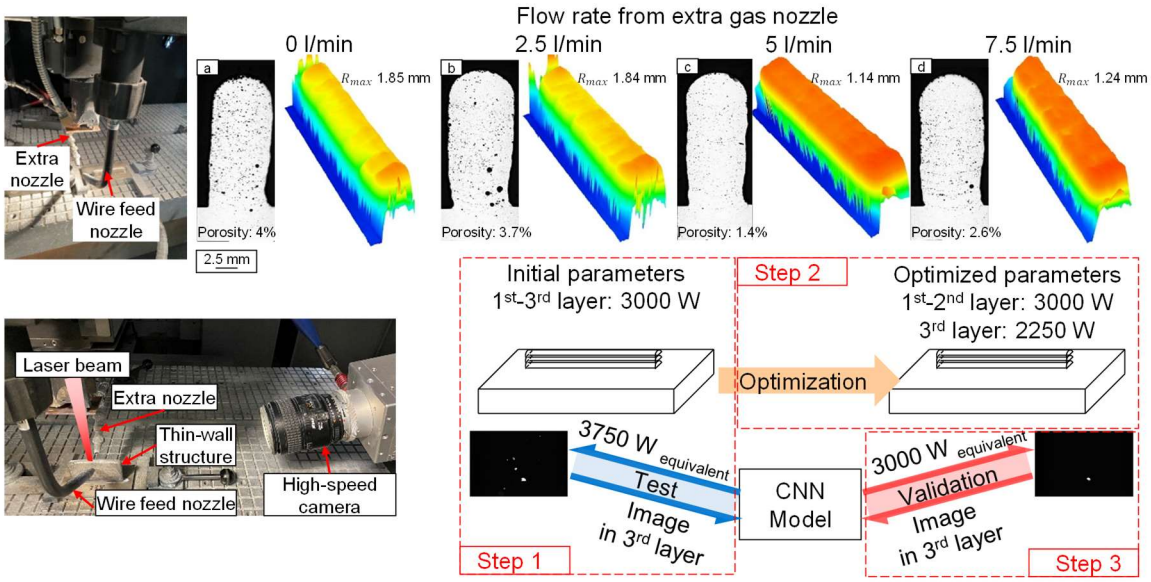

Figure 25. Graphical abstract of **Paper 5**.

In wire-based L-DED, the wire can be either laterally [19] or coaxially [20] fed relative to the laser beam. During processing, the shielding gas is utilized to create an inert gas atmosphere and protect deposited layers from oxidation. In coaxially wire-based L-DED, the shielding gas can be conveyed through the optic head to protect the deposition from the top. The lateral L-DED apparatus can be modified from a laser welding apparatus, as reported in

Papers 2 and 3, where the flexibility of the path direction is not highly in demand. In this case, the shielding gas is conveyed through the wire feed nozzle as in a welding apparatus. According to the previous study in **Paper 2**, it was found that the wire should be fed using the side-feeding strategy to avoid the wire getting stuck in the track during back feeding and prevent oxidized metal vapor from falling on the track surface during front feeding. In this scenario, Ar is conveyed through the wire feed nozzle and directed toward one side of the built thin-wall structures, creating an asymmetrical flow relative to the melt pools during processing. The effects of shielding gas on the directed energy deposition (DED) process and the properties of as-built specimens (e.g. geometry and porosity level) have been studied with a focus on the flow rate of shielding gas [24-26]. In most DED processes, the shielding gas is coaxially conveyed through the optic head and symmetrically blows from the top to the melt-pool surface [24, 27]. To achieve a symmetrical blowing direction in a modified laser welding apparatus, additional components need to be purchased to facilitate the coaxial conveying of shielding gas through the optic head. Considering the existing effects of blowing directions in single-track deposition, as reported in **Paper 2**, it is important to conduct a comprehensive study on the impacts of asymmetrical blowing of shielding gas on the L-DED process and the properties of as-built specimens. If any adverse effects are identified, it would be valuable to investigate whether there is an economical solution to address them rather than purchasing additional components to enable the coaxial conveying through the optic head.

Previous research has demonstrated the potential for machine learning (ML) algorithms to predict defects and diagnose processing anomalies in AM, while simultaneous correction is not currently feasible. An in-situ adjustment of process parameters is essential to prevent the deterioration of existing anomalies and minimize material waste. Therefore, another objective of this study is to propose a novel methodology for monitoring and in-situ adjusting process parameters during L-DED by adopting a CNN model to maintain processing stability and consistency.

A high-speed camera is mounted to the side of the optic head using an extension bracket, as shown in Figure 25. It is focused on the tip of the wire, which allows for the capture of clear images depicting the processing characteristics during deposition. The shielding gas Ar is coaxially conveyed through the wire feed nozzle to the melting area to protect it from oxidation. Additionally, an extra nozzle conveying Ar is installed and positioned mirror-symmetrically to the wire feed nozzle relative to the thin-wall structure. The side facing the wire feed nozzle is designated as the front side of the wall, while the other side facing the extra nozzle is referred to as the back side of the wall. CNN models are developed to recognize the processing images and their corresponding processing states, which facilitate in-situ monitoring and in-situ adjustment of process parameters during L-DED to maintain processing stability and consistency.

In this study, an extra lateral nozzle conveying shielding gas is installed to balance the shielding gas conveyed through the wire feed nozzle. Its impact on the dynamics of melt pools, geometrical accuracy, and the properties of as-built specimens are investigated using thin-wall structures built by L-DED. Furthermore, CNN models are developed to effectively determine the optimal shielding gas flow rate. Finally, a methodology for CNN model-assisted process

monitoring and parameter adjustment is proposed. Based on the experimental results, the following points can be concluded:

- In L-DED, the one-side blowing of shielding gas through the wire feed nozzle leads to processing instability during deposition, which results in the occasional explosion of melt pools and geometrical deviations. The installation of an extra shielding gas nozzle can help counteract the negative effects of one-side blowing. However, it is crucial to determine the appropriate flow rate for conveying the extra Ar to achieve processing stability. Improved processing stability not only enhances geometrical accuracy but also reduces the porosity level of as-built specimens.

- The maximum roughness on the back side can be reflected after several layers have been deposited. The process of determining the optimal gas flow rate is both time- and material-consuming. Deposition processes with different flow rates exhibit distinct characteristics. To aid in the parameter investigation, CNN models are developed using images captured during deposition as input. Even when an inappropriate flow rate is applied, the CNN model can guide adjusting the flow rate based on the current flow rate. With the assistance of the CNN model, the appropriate gas flow rate can be identified based on the images from the first layer. CNN models classify images based on the information related to melt pools, spatter, plume, and distribution of grayscale values in the image.

- A methodology integrating the CNN model and L-DED process has been successfully validated. By analyzing images captured during deposition in single tracks processed with different laser power, the images in higher layers can be categorized to the equivalent process state as in the 1st layer from the training group. Subsequently, the laser power is adjusted to prevent heat accumulation and achieve a process state similar to that of the initial 1st layer, which ensures a consistent processing state throughout manufacturing. The specimen produced with the adjusted parameter demonstrates a thinner wall thickness. Additionally, the porosity level and correspondent pore distribution along the width direction of melt pools in the 3rd layer exhibit high similarity to those in the 1st - 2nd layers. The methodology proposed in this study could be universally applied in other laser-beam-melting-related processes, not only to in-situ monitoring but also for in-situ parameter adjustment

.

5. Conclusions

The thesis focuses on investigating the processability of high-strength Al alloys in both powder-based and wire-based L-DED processes. The research aims to optimize process parameters and implement process-related optimization in these two types of L-DED processes. In the powder-based L-DED process, the effects of different robot programs and scanning strategies are examined considering how these factors impact the buildability, geometrical accuracy, and hot crack initiation. Additionally, the appropriate process window for each combination of the robot program and scanning strategy is studied to achieve porosity reduction and eliminate cracks.

The thesis also examines the effects of wire feed direction on the lateral L-DED process and the properties of deposited single tracks in wire-based L-DED. The process parameters and building strategies are optimized to produce crack-free specimens with low porosity levels. The microstructure is characterized by different methods and the mechanical properties of specimens are tested. Furthermore, the cracking mechanism in L-DED processing of high-strength Al alloy is experimentally investigated. The cracking mechanism deduced in this thesis is further validated by a crack-free thin-wall structure processed with optimized parameters.

To ensure processing stability, an extra lateral nozzle is installed to convey shielding gas and balance the shielding gas flow through the wire feed nozzle. The effects of this setup on the dynamics of melt pools, geometrical accuracy, and properties of as-built specimens are investigated using thin-wall structures built by L-DED. In addition, CNN models are developed to efficiently determine the optimal shielding gas flow rate. Furthermore, a methodology is proposed for CNN model-assisted process monitoring and parameter adjustment. This approach allows for real-time monitoring of the L-DED process and enables adjustments to be made based on the predictions provided by the CNN models. Based on all the comprehensive experimental results obtained, the following conclusions can be drawn:

- In the powder-based L-DED process, the acceleration and deceleration phases of the robot arm can negatively impact the buildability and the geometrical accuracy. This is due to heat accumulation, which leads to the formation of bumps at the start and the end of deposition tracks. To mitigate this issue, an optimal control strategy is proposed, which involves reducing laser power on two sides of each track or adjusting the time for activating the laser and the powder feeder. The robot program and scanning strategy also play a crucial role in determining the buildability and the porosity level. Even with the optimization of process parameters, robot programs, and scanning strategies, a high porosity level and cracks cannot be completely prevented.

- In the wire-based lateral L-DED process, there is a possibility of the wire getting stuck in the track, leading to process abortion when using the back feeding direction for wire feeding. To avoid this issue, it is recommended to utilize side feeding in a bi-directional scanning strategy. This helps prevent process abortion and ensure smooth wire feeding throughout the deposition process. Wire-based L-DED process demonstrates better processability in processing high-strength Al alloys. Through process optimization for a

30-layer deposition, the porosity level can be reduced to 0.8 % in continuous processing. A further reduction to 0.3 % is achievable in discontinuous processing. However, it should be noted that the porosity level slightly deteriorates with an increase in deposition layers. The presence of cracks and large pores in the specimens contributes to the reduction in strength. All specimens exhibit a strong fiber texture, and strengthening precipitates are observed in as-built specimens due to cyclic heating during layer-by-layer deposition. These factors result in the high strength and ductility observed in L-DED processed precipitation-strengthening 7XXX series alloys.

- The cracking susceptibility increases with increased deposition length under the same process parameter. The cracking phenomenon occurs after a certain number of layers have been deposited in structures with longer deposition lengths, so-called “delayed cracking”. The cracks initiate and grow in two directions parallel to the building direction during successive deposition. The initiation of cracks is induced by insufficient backfilling to shrinkage leading to solidification cracking. After the initiation of cracks, the growth of cracks downwards is attributed to the consequence of the liquation cracking. The growth of cracks upwards results from the solidification cracking. The “delayed cracking” is attributed to the competitive growth between grains with different growth directions. As the deposition progresses, grains with preferential growth directions eliminate highly misaligned grains. The timing at which these highly misaligned grains are eliminated affects their size, which in turn prolongs the channel for backfilling shrinkage and deteriorates the permeability. The prolongation of the channel and deterioration of permeability enhance the cracking susceptibility.

- In the wire-based lateral L-DED process, the one-side blowing of shielding gas through the wire feed nozzle can lead to processing instability during deposition. This instability can manifest as occasional explosions of melt pools and geometrical deviation in the deposited structures. The installation of an extra shielding gas nozzle can balance the negative effects of one-side blowing. Determining the appropriate flow rate for conveying the extra shielding gas is crucial for achieving processing stability. Otherwise, the processing stability can still not be reached. Achieving processing stability not only improves the geometrical accuracy but also reduces the porosity level of as-built structures.

- A methodology that integrates a CNN model with the L-DED process has been successfully verified. This methodology utilizes images captured during the deposition process in single tracks processed with different laser powers. By learning from these images, the CNN model can categorize images from higher layers into equivalent process states as observed in the 1st layer from the training group. Using this categorization, the laser power can be adjusted to prevent heat accumulation and achieve a consistent process state throughout the entire manufacturing process. This adjustment ensures that the process state in subsequent layers matches that of the initial 1st layer, leading to improved consistency in the as-built structures. The specimen produced using the adjusted parameter demonstrates a thinner wall thickness. Additionally, the porosity level and corresponding pore distribution along the width direction of melt pools exhibit a high similarity in different layers.

6. Summary and outlook

6.1. Processability of high-strength aluminum alloy in powder- and wire-based laser-directed energy deposition

In terms of the optimal process window investigated in this thesis, wire-based L-DED exhibits better processability for 7XXX series high-strength alloys compared with powder-based L-DED. Wire-based L-DED is capable of producing crack-free structures with lower porosity levels. However, it is important to note that the chemical composition of the materials used in powder-based L-DED and wire-based L-DED are different, despite both being 7XXX series Al alloys. AA7050 and AA7075 are utilized in powder-based and wire-based L-DED processes. The chemical composition of these two alloys can be found in Table 6 and Table 7 in Chapter 3.1. The evaporation of alloying elements during processing is one of the causes of pores in the as-built specimens. Mg and Zn are the main volatile elements in AA7050 and AA7075. The content of Mg and Zn in AA7075 (Mg: 2.5 wt.%, Zn: 5.7 wt.%) is higher than that in AA7050 (Mg: 2.4 wt.%, Zn: 4.1 wt.%). Additionally, AA7050 contains 0.2 wt.% of Zr, which has been proven to refine microstructure and reduce porosity levels and cracking susceptibility. Consequently, when considering pure material, processing challenges for AA7075 should be more difficult compared with processing AA7050.

In terms of the processing aspect, the laser spot diameter utilized in wire-based L-DED and powder-based L-DED is 1.5 mm and 1.35 mm, respectively. The laser power regime in wire-based L-DED (3000 – 4000 W) is significantly higher than that in powder-based L-DED (below 800 W). The laser scan speed is comparable between both AM technologies. When considering laser irradiance (laser power/laser spot diameter) and laser line energy input (laser power/laser scan speed), the laser energy input in wire-based L-DED exceeds that in powder-based L-DED, which can result in higher temperature in the melt pools and increased evaporation of volatile elements. Nevertheless, it should be noted that the material feed rate in wire-based L-DED is in the range of 7.57 – 11.36 g/min, whereas the powder feed rate of 0.11 – 0.55 g/min is applied in powder-based L-DED. Despite the approximately 5-fold difference in laser energy input, the approximately 20-fold difference in material feed rate consumes more energy during processing, leading to lower melt-pool temperatures and less evaporation of volatile elements. This finding is supported by EDX measurements conducted on as-built specimens, which show higher element loss of Mg and Zn in specimens produced by powder-based L-DED. Additionally, gas pores are trapped inside the powder particles due to gas atomization, contributing to pore formation in as-built specimens. Furthermore, compared with individual powder particles, compact bulk wires have a smaller surface area per unit mass. This means that there is less opportunity for wires to absorb moisture from the ambient atmosphere, reducing the potential for hydrogen gas pore formation. Overall, the improved processability of high-strength Al alloys in wire-based L-DED is attributed to the specific process regime of wire-based L-DED and the use of wires as feedstock.

The cracking mechanism observed in wire-based L-DED is identified as solidification cracking, which occurs due to insufficient backfilling to compensate for shrinkage and fractures

under tensile residual stress. Solidification cracking is primarily a material-related issue. One approach to address solidification cracking is by incorporating alloying elements such as Si to enhance the flowability of melt pools and reduce the solidification temperature range. Therefore, the development of process windows for materials in AM should not be limited to existing material systems and optimizing process parameters or scanning strategies. There are two more feasible options to consider: the first option is to modify existing material systems or develop new material systems specifically tailored for AM applications; the second option is to advance current AM technologies in a revolutionary manner. Future research efforts focused on material development for AM will need to address the following points:

- A more comprehensive understanding of the mechanisms underlying the improvement in processability achieved through the addition of dope materials, such as TiB_2 and Si, is necessary. This understanding should encompass material properties, processing, and post-characterizations. Therefore, it is important to evaluate the material properties after modification in terms of laser absorption coefficient, powder flowability, and powder morphology. The processing will be monitored using various techniques, including high-speed cameras and infrared cameras, to observe and analyze any changes that occur during the processing of modified materials. Ultimately, the properties of the as-built specimens will be characterized and correlated with the material properties and processing conditions. This deeper understanding will provide valuable insights for future material design or optimization of AM technologies.

- Powder-based L-DED is well-suited for high-throughput production of specimens with varying chemical compositions, either in a batch or as graded materials within a specimen. This capability makes it an efficient tool for material development, as it can rapidly generate sufficient data and shorten the development cycle. Leveraging the abundance of data, machine learning will be employed to identify correlations between material composition (including the type and content of alloying elements) and processability, as well as the properties of the as-built specimens. By utilizing machine learning algorithms, it becomes possible to tailor the properties of AM-produced structures based on desired specifications and requirements.

6.2. Assistance of machine learning in laser-based additive manufacturing

In this thesis, machine learning is utilized to enable in-situ parameter adjustment, which serves to maintain processing stability and monitor porosity level as a quality control method.

The current status of in-situ parameter adjustment has demonstrated the ability to identify processing states using a single process parameter, such as shielding gas flow rate and laser power. Validation studies have shown that processing images can effectively be used to identify these states and guide in-situ parameter adjustment. The results have also confirmed that this methodology can achieve a consistent porosity level across different layers by utilizing this methodology. However, a potential challenge arises when multiple process parameters need to be adjusted simultaneously. It remains to be seen whether the CNN models can accurately identify the processing states based on the processing images in such cases.

Additionally, computational time poses another challenge for in-situ parameter adjustment. Currently, the trained CNN models require feeding 4751 images as test datasets for prediction. To address this issue, it is necessary to investigate whether a smaller dataset would still be sufficient for accurately identifying the processing states. Therefore, future research on maintaining processing stability through in-situ parameter adjustment will focus on the following points:

- Regarding the in-situ parameter adjustment, the size of the test dataset will be reduced to approx. 400 images. This smaller dataset will be used to identify the processing states and guide the in-situ parameter adjustment. The properties of different layers will be evaluated to validate the effectiveness of this approach. Furthermore, multiple process parameters will be considered variables to test whether the CNN model can accurately identify the corresponding processing states when different process parameters are changed. The goal is to determine whether the CNN model can successfully enable in-situ parameter adjustment for these varied parameters.
- Currently, the parameters for AM are adjusted offline. The CNN models will be integrated into the system of AM apparatus. The signals generated by the CNN models will be processed as machine-readable data, which can then be utilized to control the process parameters through other techniques, such as the Proportional-Integral-Derivative (PID) controller.

Appendix A Declarations

A 1. Contribution of the author

The papers were prepared in collaboration with several co-authors. The scientific results were accomplished within the PhD thesis. The author of this dissertation is the main contributor to the Papers (1-5) in terms of theoretical consideration, planning and implementation of experimental works, analysis of obtained results, and writing of papers. Nikolai Kashaev as the supervisor for the author of this dissertation provided supervision and review for the Papers (1-5). Volker Ventzke accomplished part of the experimental work regarding material characterization and provided the theoretical analysis for Paper 3. Nowfal Al-Hamdany, Yujie Deng, Emad Maawad, and Shengnian Luo accomplished part of the experimental work regarding residual stress analysis using high-energy synchrotron X-ray diffraction and provided the theoretical analysis for Paper 5.

A 2. Permissions

The author has obtained the licenses to reprint the publications that are included in this thesis:

Paper 1: M. Wang, N. Kashaev, On the optimal process window for powder-based laser-directed energy deposition of AA7050 under different robot programs and scanning strategies, Journal of Manufacturing Processes 90 (2023) 286-299.

Paper 2: M. Wang, N. Kashaev, Investigation of process window for AA7075 considering effects of different wire feed directions in lateral Laser Metal Deposition, Procedia CIRP 111 (2022) 218-223.

Paper 3: M. Wang, V. Ventzke, N. Kashaev, Wire-based laser directed energy deposition of AA7075: effect of process parameters on microstructure and mechanical properties, Journal of Materials Research and Technology 21 (2022) 388-403.

Paper 4: Unravelling the cracking mechanism in laser-directed energy deposition processing high-strength aluminum alloy (under preparation for submission)

Paper 5: M. Wang, N. Kashaev, On the maintenance of processing stability and consistency in laser-directed energy deposition via machine learning, Journal of Manufacturing Systems 73 (2024) 126-142.

Appendix B Reprinted publications

Paper 1: M. Wang, N. Kashaev, On the optimal process window for powder-based laser-directed energy deposition of AA7050 under different robot programs and scanning strategies, Journal of Manufacturing Processes 90 (2023) 286-299.

This published paper was incorporated as Chapter 4.2 (with permission from Elsevier).

Journal of Manufacturing Processes 90 (2023) 286–299

Contents lists available at ScienceDirect

Journal of Manufacturing Processes

journal homepage: www.elsevier.com/locate/manpro

On the optimal process window for powder-based laser-directed energy deposition of AA7050 under different robot programs and scanning strategies

Mengjie Wang *, Nikolai Kashaev

Institute of Materials Mechanics, Department of Laser Processing and Structural Assessment, Helmholtz-Zentrum Hereon, Max-Planck-Str. 1, D-21502 Geesthacht, Germany

ARTICLE INFO

Keywords:
Laser-directed energy deposition
Aluminum alloy AA7050
Robot program
Scanning strategy
Porosity level

ABSTRACT

Powder-based laser-directed energy deposition (L-DED) has drawn lots of attention during the last years because of the multiple application areas, such as coating, repairing, and building 3D structures. One challenge in L-DED is the limited variety of applicable materials, especially in the case of aluminum alloys. To broaden the material spectrum, the processability and the optimal process window of high-strength Al-alloy AA7050 are investigated in the present study. Besides the process parameters, special emphasis was paid to the scanning strategy and the robot program controlling. The present results show a strong effect of scanning strategy and robot program on buildability, geometrical accuracy, melt pool visibility, porosity level, and crack initiation. Hot cracks can be reduced or eliminated by choosing an appropriate combination of scanning strategy and robot program. Meanwhile, the geometrical accuracy of specimens with any height was well maintained. Based on the systematic experimental study, appropriate L-DED process parameters were identified for the deposition of structures up to 24 layers with a lower porosity level (about 3.7 ± 0.8 %) and lower amount of hot cracks, which are comparable with that in the 12-layer structure.

1. Introduction

Metal additive manufacturing (AM) builds parts layer by layer following the path generated from a 3D model [1]. Weight reduction, production of parts with complex geometry, and cost-saving are the main reasons why AM is attractive to academic researchers and industries [2]. The feedstock of metal AM can be wire or powder [1]. In powder-based AM using laser as an energy source, powders can be fed by a nozzle (laser-directed energy deposition, L-DED) or spread like a powder bed (selective laser melting, SLM) [1]. L-DED has multiple application areas, such as coating [3], repairing [4], and building 3D structures without space restriction [5].

The quality of AM-produced parts is determined by two important factors: material and process. Aluminum alloys have drawn lots of attention in AM because of their high strength-to-density ratio [6]. However, the physical properties of Al, such as oxidation sensitivity, high heat conductivity, wide solidification range, etc., confine the weldability in AM [7]. Most of the research focused on Al alloys with a higher content of Si [8,9]. Si can improve the properties of melt and enhance the processability of Al alloys [10]. High strength is required under some specific circumstances in the automotive [11] and aircraft industries [12], where Al-Si alloys are not a suitable choice. Age-hardening 7XXX alloys can provide high strength (tensile strength over 600 MPa [13]) and maintain the lightweight synchronously. The sequence of the T6 heat treatment for 7XXX alloys is the solid solution (around 475 °C [14]) – quenching – ageing (around 150 °C [15]). The main hardening phase after ageing is $MgZn_2$ (η phase), which is distributed inside grains and along grain boundaries [16]. The precursor of the η phase is the Guinier-Preston (GP) zone, which is the solute cluster formed due to the segregation of solutes [17]. Two-stage ageing leads to the formation of precipitates with finer size and discrete distribution compared with one-stage ageing, which can further increase the mechanical properties [18].

As a promising material, the higher susceptibility to oxidation [19] and hot cracking [10] as well as the porosity formation [20] are challenges in AM processing of 7XXX alloys. The potential origins for the porosity formation consist of the evaporation of volatile alloying elements (such as Zn and Mg in 7XXX) [20], absorption of moisture in the

* Corresponding author.
E-mail address: mengjie.wang@hereon.de (M. Wang).

https://doi.org/10.1016/j.jmapro.2023.01.011
Received 7 June 2022; Received in revised form 1 December 2022; Accepted 3 January 2023
Available online 14 February 2023

working area [21,22], and internal gas of powders [23], etc. The oxidation of Al alloys increases the possibility for porosity formation [24], reduces the flowability and the processability of powders [19], and deteriorates the fatigue properties of as-built parts [25]. Hot cracking is a general term for two kinds of cracking mechanisms, i.e. solidification cracking and liquidation cracking [26]. Solidification cracking is attributed to insufficient back feeding during solidification [27], while liquidation cracking is induced by the melting of secondary phases along grain boundaries [28]. Under the residual tensile stress, the cracks propagate and lead to the failure of parts. In AM, the characteristics of processing and microstructure promote hot cracking. AM exhibits a high cooling rate, such as 10^2–10^4 K/s in L-DED [29] and 10^6 K/s in SLM [30], which results in a short lifetime of melt pools and a non-equilibrium solidification [31]. The back feeding of melts to the shrinkage or voids becomes more difficult in this scenario. Besides, parts are built layer by layer in AM. The heat input also imposes in previously solidified layers, which equivalently experience cyclic heat treatments. As the temperature in previous layers reaches the melting points of secondary phases along grain boundaries forming a liquid film, cracks could be initiated under residual tensile stress. The residual stress is present in AM-produced parts due to cyclic heating and cooling [32] as well as phase transformation [33]. Furthermore, the layer-by-layer building strategy develops a directional heat flux and a high-temperature gradient, which promotes the formation of large columnar grains [34]. In comparison to fine equiaxed grains, large columnar grains demonstrate worse cracking resistance [35].

7XXX alloys are mainly investigated in the SLM process. The porosity level of specimens can be decreased to <1 % by process parameter optimization, but cracks are observed in all specimens albeit preheating substrates [36]. Hot isostatic pressing (HIP) and different scanning strategies can reduce porosity levels and eliminate small cracks [28]. The most widely used method to eliminate cracks is the incorporation of additives with raw 7XXX powders before SLM processing, such as Si [37], TiB_2 [38], and Zr [39]. Grain refinement and formation of novel eutectic phase caused by additive enhance the crack resistance. Less knowledge has been collected about the L-DED processing of 7XXX alloys [40–42]. The experimental results exhibit a large discrepancy in terms of porosity level and crack inhibition. Nearly full dense specimens (porosity level < 0.5 %) can be produced in [42], while a minimum porosity level of 4.2 % is achieved in [40]. Cracks can be eliminated in both cases. In [41], a specimen processed with optimal parameters exhibits a porosity level of 2.2 % and cracks are present in the cross-section.

In L-DED, powders are fed by carrier gas from the powder feeder through a nozzle to the substrate. During layer-by-layer deposition, the motion of the nozzle and substrate is controlled by a CNC machine, a robot, or a combination of both. Process parameters, such as laser power, scan speed, powder feed rate, etc., could be the primary factor affecting the achievable properties. Process systems (such as laser and nozzle, etc.) and powder quality, also determine results. Some research has been done to investigate the effects of process parameters on the buildability of parts. If the laser power maintains constant during a building job for a thin-wall structure in L-DED, the arc-like morphology of deposited tracks could lead to the collapse of the structure [43] or uneven thickness along the building direction [44]. Besides, the constant laser power could cause heat accumulation and the formation of bumps at the start and the end of deposition tracks [45]. There is an acceleration phase and a deceleration phase in each parallel scanning path. The speed fluctuation could also lead to bump formation [46]. The problems can be tackled by process parameter optimization, such as reducing laser power or increasing scan speed. However, it requires either numerous experimental iterations or a sensor-based loop control system. The robot programs controlling the motion of the nozzle and substrate and the switch status of the laser and powder feeder have not been systematically introduced before. Hence, it is worth investigating whether these problems could be relieved or eliminated by the control for robot programs and switch status.

The scanning strategies, i.e. the path design for building 3D structures, were investigated considering the influences on the residual stress, distortion, cracking resistance, microstructure, and mechanical properties. The parts can be built with alternating scanning directions in different layers. The rotation of scanning direction in two adjacent layers can decrease the surface roughness [47] and distortion [48] as well as the texture heterogeneity [49] of as-built parts. The effects of vertical scanning and horizontal scanning on the thermal field were investigated in SLM. The prism built with a horizontal scanning strategy exhibits pronounced distortion, while the prism built with a vertical scanning strategy demonstrates a more localized distortion [50]. Besides the rotation of scanning directions, unique path designs are also applied, e.g. laser double scanning, alternating scanning sequence (stripes alongside), and subdivision of scanning area (e.g. chessboard) [28]. The residual stress and the cracking susceptibility can be reduced by optimizing scanning strategies. The mechanical properties are also affected by these hatch designs in layers because of the resultant different thermal histories [51]. Alternating deposition directions between different layers exhibit significant effects on the tensile strength, while the tensile strength is less dependent on the deposition direction within one layer [52].

This study addresses the effects of robot programs and scanning strategies on the L-DED-processed AA7050 powder. The advantages and disadvantages of each robot program are analyzed in terms of buildability, porosity level, crack initiation, and heat effect on the substrate. The appropriate process parameters are investigated in various combinations of robot programs and scanning strategies.

2. Material and methods

2.1. Powder characterization

The material used in this experiment is gas-atomized AA7050 powder supplied by NANOVAL GmbH & Co. KG. The average size of powders is 36 μm (as reported by the supplier). The morphology and the microstructure as well as the chemical composition of the powders are characterized by Jeol JSM-6490LV scanning electron microscopy (SEM, acceleration voltage 15 kV, working distance 10 mm) equipped with energy-dispersive X-ray (EDX) analysis (EDAX Genesis). As shown in Fig. 1(a, b), most of the particles have a spherical morphology and irregular particles also exist, which might affect the flowability of powders [53]. The gas pores formed during atomization are observed inside the particles (Fig. 1c). Fig. 1d demonstrates the microstructure of one particle, where the dark area is the Al matrix and the bright area is the eutectic phases with a lower boiling point along the grain boundaries. The chemical composition of the matrix and the eutectic phases is listed in Table 1. The eutectic phases are rich in Zn, Mg, and Cu.

2.2. L-DED process

The L-DED process components contain an Nd:YAG laser (Rofin DY022, max. power: 2.2 kW, Rofin Sinar Laser GmbH), a 6-axis robot (KR 6 R900, Kuka AG), a coaxial nozzle (Coax14V3, Fraunhofer IWS). The substrate (AA7075-T651, in the as-delivered state, 50 mm x 50 mm x 15 mm) is clamped on a specimen holder, which travels with the robot arm during deposition, while the position of the nozzle is fixed and the powder focus is located on the substrate surface, see Fig. 2a. The laser spot diameter is 1.35 mm (defocusing +6 mm: the laser focus is 6 mm above the substrate surface). The whole L-DED process is implemented inside a glovebox filled with argon. As Al alloys are susceptible to oxidation and the oxide film could hinder the process resulting in a higher porosity level of produced specimens [24], processing under an inert atmosphere in the glovebox can lower the possibility of oxidation. Normally in the case of an open atmosphere system, the powders are conveyed by carrier gas from the powder feeder to the

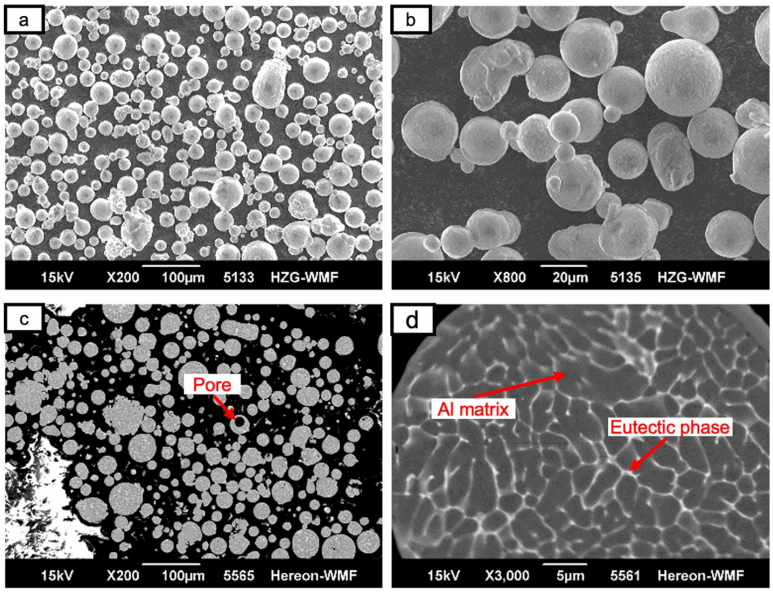

Fig. 1. Morphology of AA7050 powder in (a) 200× and (b) 800× magnification. Microstructure of the cross-section in (c) 200× and (d) 3000× magnification.

Table 1
Chemical composition of the matrix and the eutectic phases along grain boundaries inside one powder particle (in wt%).

	Al	Mg	Si	Zr	Ti	Cr	Mn	Fe	Cu	Zn
Matrix	91.32	2.42	0.08	0.21	0.07	0.06	0.05	0.07	1.62	4.10
Eutectic phases	76.21	5.49	0.11	0.05	0.04	0.03	0	0.16	7.96	9.96

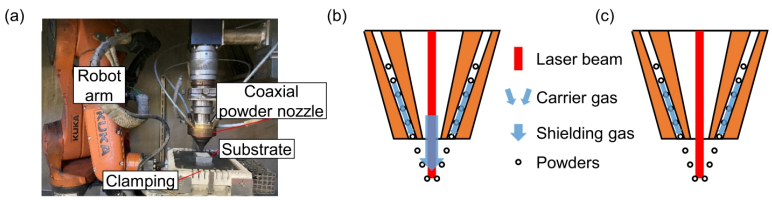

Fig. 2. (a) Experimental setup inside the glovebox. Illustration of powder feeding inside nozzle (b) with shielding gas and (c) without shielding gas.

substrate and the deposited layers are protected against oxidation by shielding gas coaxially conveyed relative to the laser beam, as illustrated in Fig. 2b. However, an inappropriate shielding gas flow rate could shift the powder stream focus position and destabilize the powder flow [54]. In worse cases, the shielding gas could get trapped in melt pools and results in the formation of pores [55]. Hence, given the oxidation protection provided by the glovebox, no shielding gas was coaxially conveyed relative to the laser beam through the nozzle in the present experiments (Fig. 2c). Only the carrier gas is illustrated in Fig. 2c with a flow rate of 3 l/min.

The horizontal and vertical scanning strategies are illustrated in Fig. 3a. Each track has a length of 24 mm. In horizontal scanning, the scanning directions of two adjacent deposition tracks are opposite and both travel in the horizontal direction relative to the nozzle. After each layer deposition, the substrate travels down for a preset distance (z-offset). The successive layers follow the same strategy. In vertical scanning, the substrate travels in a vertical direction relative to the nozzle. Fig. 3b exhibits four robot programs classified by different timing for switching on and off the laser and the powder feeder. Although the position of the nozzle is fixed while the substrate placed on the robot arm travels, the relative motion of the nozzle is sketched for an easier understanding. In robot program 1, the laser and powder feeder are always switched on during the whole process. In robot program 2, the powder feeder stays on and the laser is on at the start and off at the end of each track. The laser power is lower at the first 1/4 section and the last 1/4 section of the track than at the middle. In program 3, the powder feeder and laser are switched on at the start and off at the end of each track. Powders are conveyed from the powder feeder to the substrate. This conveying process requires time until powders land on the substrate. Consequently, robot program 3 is subdivided into two programs: the laser and powder feeder are on synchronously; the laser is on after switching on the powder feeder for 5 s (hereinafter referred to as robot program 3 (no waiting) and robot program 3 (waiting)). In robot program 4, the powder feeder stays on and the laser is on after the substrate travels for 5 mm and off at 5 mm before the end of each track. The travel speed of the robot arm is considered as the laser scan speed.

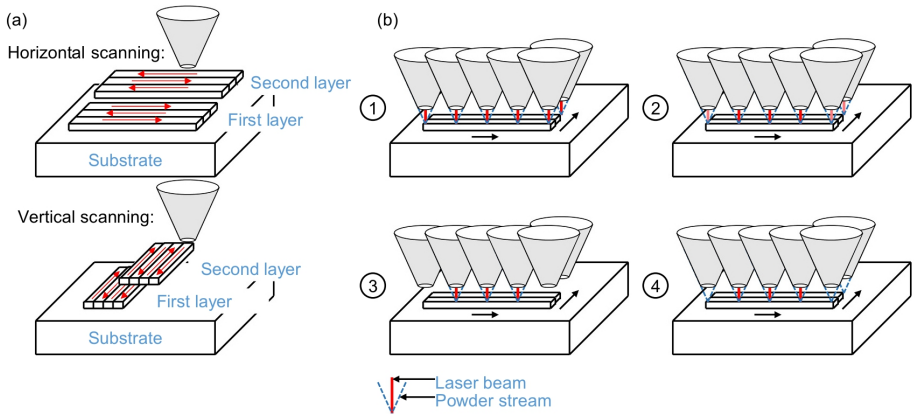

Fig. 3. Illustration of (a) two scanning strategies (horizontal scanning and vertical scanning, red arrows represent scanning directions) and (b) four robot programs in terms of time for switching on and off the laser and powder feeder (black arrows represent the deposition sequence). The control of the laser and powder feeder follows the same principle both in horizontal and vertical scanning, although only horizontal scanning is shown in (b). (For interpretation of the references to colour in this figure legend, the reader is referred to the web version of this article.)

The motion of the robot arm in the deposition track contains three phases: acceleration to reach the set speed at the start; uniform motion; deceleration at the end. 5 mm should be long enough for the acceleration and deceleration phases. In the present study, horizontal scanning and vertical scanning were investigated in robot programs 1 and 4. Only vertical scanning was investigated in robot programs 2 and 3.

2.3. Specimen characterization

A digital microscope (VHX-7000, KEYENCE) was employed to recreate the height profile of the specimens along their width and length directions. The as-built specimens were cut in the same middle position to assure the comparability of porosity level and microstructure. The cutting direction of the specimen for the metallographic preparation is sketched in Fig. 4a. As shown in Fig. 4(b, c), cutting plane 1 is perpendicular and parallel to the deposition direction of tracks in vertical scanning and horizontal scanning, respectively. The relative position between cutting plane 2 and the deposition direction of tracks in vertical and horizontal scanning is opposite compared with cutting plane 1. The specimens were then mounted and ground with abrasive SiC paper followed by diamond polishing and silicon oxide polishing. The prepared specimens were ground and polished three times to gain three cross-sections and the cross-sectional porosity level is averaged. For the microstructure observation, the specimens were immersed in Kroll etchant for 15 s or etched by Barker's reagent. The images for porosity calculation and microstructure observation were captured by optical microscope (OM, Leica DMI 5000 M). The image processing and the porosity calculation were performed in Image J. SEM and EDX analysis were conducted with the same apparatus as for powder characterization.

The microhardness of as-built specimens was measured with Falcon 5000 microhardness tester (INNOVATEST Europe BV) with a load of 0.1 kg and a dwell time of 10 s. The indentation points were set from top to bottom in the middle of specimens. The distance between the neighboring points was 0.27 mm.

3. Results and discussion

3.1. Effects of robot program and scanning strategy on buildability and porosity level

The type of robot program determines the buildability of larger specimens. Fig. 5 exhibits the workflow to evaluate the geometrical accuracy of specimens produced with different robot programs and scanning strategies. The measured geometries and the process parameters are listed in Tables 2 and 3, respectively. The specimen is scanned by the digital microscope from the top and the height measurement is performed in each frame. Every 12 lines are set up along the width direction and the length direction of the specimen to obtain an average height profile (Fig. 5a). The height profiles of the front view (along the width direction, A-A cross-section) and the side view (the length direction, B-B cross-section) of the specimen can be recreated by the 3D microscope, as shown in Fig. 5(b, c, d, e). To quantitatively characterize the geometrical accuracy, a circle is fitted at the edge of the front view (Fig. 5f). The radius of the fitted circle is denoted as *R*. Besides, the maximal height difference along the length direction is measured and denoted as *HD* (Fig. 5g). The lower these two parameters are, the higher

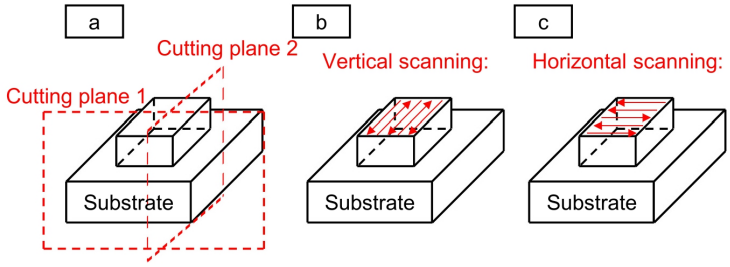

Fig. 4. (a) Cutting planes for metallographic preparation and their direction relative to deposition tracks in vertical scanning (b) and horizontal scanning (c).

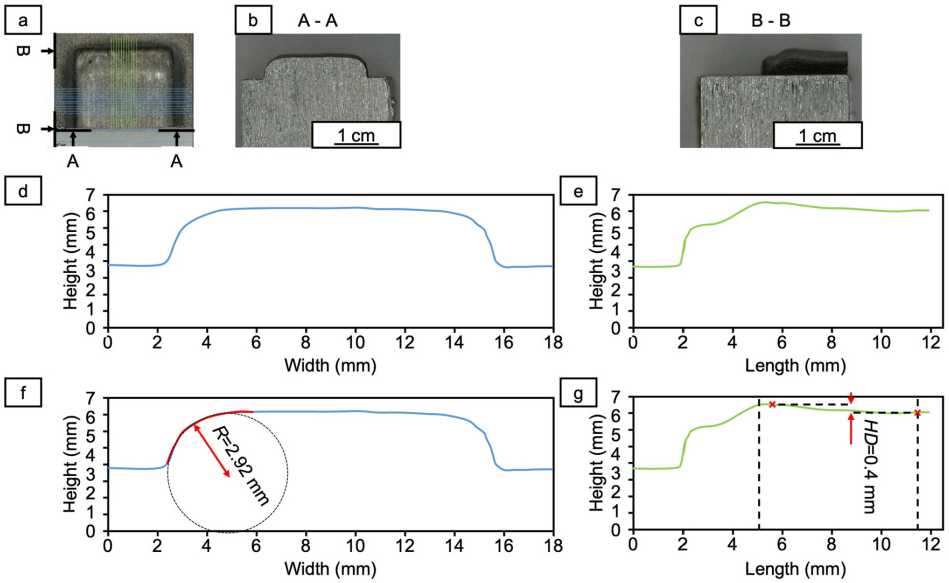

Fig. 5. Evaluation of the geometrical accuracy of a specimen by using the 3D microscope: (a) the top view of the specimen, every 12 lines are set up to measure the average height along the width direction and the length direction of the specimen, respectively; (b) the front view as noted in (a); (c) the side view as noted in (a); (d) the height profile along the width direction; (e) the height profile along the length direction; (f) a circle is fitted to measure the curvature of the edge in the front view and *R* is the radius of the fitted circle; (g) the maximal height difference *HD* along the length direction is measured in the selected area. Specimens were cut by cutting plane 1.

Table 2
Geometrical accuracy of specimens with different layer numbers and produced with different robot programs and scanning strategies concerning the radius of the fitted circle (*R*) and the maximal height difference (*HD*).

Specimen	Robot program and scanning strategy	Deposition layers	*R* (mm)	*HD* (mm)
a	Robot program 1 (horizontal scanning)	6	2.36	0.04
b	Robot program 1 (horizontal scanning)	12	3.87	0.16
c	Robot program 1 (vertical scanning)	6	1.75	0.24
d	Robot program 1 (vertical scanning)	12	5.12	1.61
e	Robot program 2	12	3.55	0.73
f	Robot program 3 (waiting)	12	1.51	0.22
g	Robot program 4 (horizontal scanning)	12	1.38	0.11
h	Robot program 4 (vertical scanning)	12	2.92	0.40

the geometrical accuracy of the specimen. The high *R*-value indicates that the specimen has a collapse tendency at the edge in the A-A cross-section. The high *HD*-value indicates that bumps are generated at the two edges of the specimens along the length direction. In robot program 1 (horizontal scanning), if only 6 layers are deposited, high geometrical accuracy can be achieved. However, with a higher requirement for height, e.g. 12 layers needed to be deposited, *R*-value increases significantly (two edges here are the start and the end of each track in horizontal scanning). The same decreasing geometrical accuracy exists also in robot program 1 (vertical scanning). A relatively uniform geometry can be fulfilled in a 6-layer-deposition. In 12-layer-deposition, the two edges in the A-A cross-sectional view tend to downward collapse (higher *R*-value). The *HD*-value increases from 0.24 mm to 1.61 mm. This indicates that two bumps are generated at the end of deposition tracks. The laser and the powder feeder are always on in robot program 1. The interval time of consecutive laser beam irradiation is shorter at the start and the end of tracks than in the middle causing shorter cooling time and resultant heat accumulation. Moreover, the lower scan speed in the acceleration and deceleration phases leads to higher heat input. Consequently, a larger melt pool is generated and more powders are

Table 3
Process parameters of specimens as numbered in Table 2. Hatch distance is the distance between two adjacent tracks in one layer.

Specimen	Laser power (W)	Scan speed (mm/s)	Hatch distance (mm)	*Z*-offset (mm)	Power feed rate (g/min)	Deposition layers
a	400	8	0.5	0.6	0.22	6
b	400	12	0.5	0.5	0.22	12
c	550	15	0.4	0.6	0.55	6
d	550	20	0.4	0.6	0.55	12
e	500-550-500	20	0.4	0.5	0.55	12
f	600	8	0.5	0.2	0.22	12
g	550	8	0.5	0.4	0.22	12
h	550	8	0.6	0.2	0.22	12

deposited developing bumps causing the inaccurate geometry. The amount of powders absorbed by melt pools is affected by the size of the powder stream focus landed on the specimen surface being processed [55]. The powder stream is focused on the substrate surface prior to the process. The powder stream defocusing distance in the middle area increases faster than that at the edges developing a relatively smaller powder stream focus size. Due to the smaller powder stream focus size in the bump position at the edges, melt pools could absorb more powders leading to higher deposition height. As the process proceeds, the height discrepancy caused by heat accumulation and different powder absorption rates is enlarged and impedes further deposition.

In robot program 2 with 12-layer deposition, the maximal height difference *HD* is lower compared with robot program 1 (vertical scanning), because the lower laser power at the start and the end of tracks reduces the heat accumulation. Thus, multi-layer deposition is feasible. The effects of the magnitude of the difference between laser power in the middle and at two edges have also been studied. The investigated process window is based on specimen e from Table 3: laser power at two edges of tracks ranges from 350 W to 500 W and laser power in the middle is adjusted between 550 W and 625 W. The size of bumps at the edges of the deposition tracks is dependent on the laser power at the two edges of the tracks and independent of the magnitude of the difference between the laser power in the middle and at two sides. However, the bumps cannot be eliminated despite the lower laser power at two edges. No specimen was produced with robot program 3 (no waiting). Conveying powders from the powder feeder to the substrate needs time, if the laser and powder feeder are switched on synchronously, the actual powder feeder rate is less than the set value. The properties of specimens produced with various scan speeds are hard to compare, as the powder feed rate at a certain distance is correlated to the scan speed. Specimen produced using robot program 3 (waiting) can achieve geometrical accuracy without bumps (lower *HD*-value) or collapse (lower *R*-value) since a waiting duration of 5 s is set after switching on the powder feeder providing a longer cooling time on the sides of tracks. Nevertheless, this process is time-consuming and wastes more powders. In robot program 4 (horizontal scanning and vertical scanning), *R* and *HD* are relatively low in 12-layer deposition, therefore, specimens of any height can be produced. However, powders might not be sufficiently melted at the start and the end of the tracks, since the laser is switched on after the nozzle travels for 5 mm and the laser is switched off at 5 mm before reaching the end of the tracks.

Besides the buildability and geometrical accuracy, the cross-sectional porosity level of as-built specimens is also affected by robot programs, as shown in Fig. 6. The definition of cross-sectional porosity level is referred to [56]. Despite the same process parameters, two specimens exhibit different porosity levels. Most of the pores on the cross-section are spherical, which are normally considered gas pores [40] and could be attributed to the evaporation of volatile elements [28] or the internal pores inside the raw powders. In robot program 2 and robot program 4 (vertical scanning), the middle of the specimen is processed with a laser power of 550 W. Laser power at the start and the end of each track could lead to distinct heat history in the whole track. In robot program 2, despite a lower laser power at the start and the end of each track, the laser is still turned on. Nevertheless, the laser is turned off at two sides of the track in program 4. During L-DED, the higher the laser power is, and the longer the laser is on, the more heating energy is imposed on the deposited structure. Hence, higher energy input in robot program 2 increases the temperature during deposition, which could yield more evaporation of alloying elements and therefore results in a higher porosity level. Considering the dependence of buildability and porosity level on robot programs, it is essential to introduce not only the process parameters but also how the robot is programmed in future publications. A comprehensive elaboration of experimental details increases reproducibility.

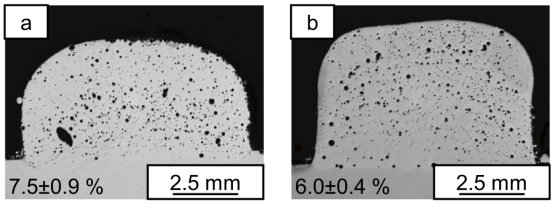

Fig. 6. Cross-section of specimens processed with the same process parameter in the middle area (laser power: 550 W, scan speed: 20 mm/s, hatch distance: 0.4 mm, z-offset: 0.5 mm, powder feed rate: 0.55 g/min, 12-layer-deposition) in (a) robot program 2 and (b) robot program 4 (vertical scanning). A porosity level is noted in the lower-left corner of each image. Specimens were cut by cutting plane 1.

3.2. Melt pool visibility

L-DED builds specimens by depositing material layer by layer. Each layer consists of multiple melt pools with certain overlapping areas. In as-built specimens, melt pool boundaries and layer boundaries can be observed after metallographic preparation with [57] or without etching [40,41]. It is found in the present experiments that the melt pool boundary cannot be noticed in every specimen. To explore the correlation between melt pool visibility and process parameters, three types of melt pool visibility are classified as shown in Fig. 7 (visible, indistinct and invisible). In Fig. 7(a, d), melt pool boundaries can be identified on the entire cross-section. The size of the dilution zone and the heat-affected zone (HAZ) on the substrate is small. In Fig. 7(b, e), melt pool boundaries can be indistinctly recognized on the top of the cross-section. The specimen exhibits a moderate size of HAZ on the substrate. In the case of invisible melt pool boundaries (Fig. 7c), only the melt pool of the last track can be noticed. The size of HAZ on the substrate is significantly larger than that of the deposited structure.

L-DED contains numerous process parameters, such as laser power, scan speed, powder feed rate, etc. The volumetric energy density (*VED*) is typically applied in SLM to manifest the energy input [38]. It is inappropriate to employ the same concept from SLM to L-DED because of different working principles. A linear energy density was introduced to L-DED [58]. However, it is more suitable to adopt linear energy density to represent energy input when building a thin wall structure, since hatch distance is not considered. Besides, laser spot diameter might change during multi-layer deposition, as the working distance between the nozzle and surface of previously solidified layers is not constant without a closed-loop control system. In AM, previously deposited layers experience in-situ heat treatment during subsequent deposition. It was found that the in-situ heat treatment could eliminate the features of melt pools [59]. Hence, the *VED* is modified to indicate the impact of process parameters on HAZ in the last layer. The size of HAZ is positively correlated to laser power and negatively correlated to laser spot diameter and scan speed [60]. As the powder feed rate increases, the size of HAZ decreases [61], so the magnitude of the powder feed rate is also considered a factor affecting the HAZ. The *modified VED* is defined hereby as:

$$modified\ VED = \frac{P}{v^{*}h^{*}d} \tag{1}$$

where P is laser power (W), v is scan speed (mm/s), h is hatch distance (mm), d is laser spot diameter (mm). Laser spot diameter is calculated as reported in [62]. The *defocusing distance* of laser beam as depositing the last layer is considered as:

$$defocusing\ distance = n^{*}z - t + l \tag{2}$$

where n is layer number, z is z-offset, t is height in the middle of as-built specimen, l is initial *defocusing distance* (6 mm).

Fig. 8 shows the correlation between the robot program, the *modified*

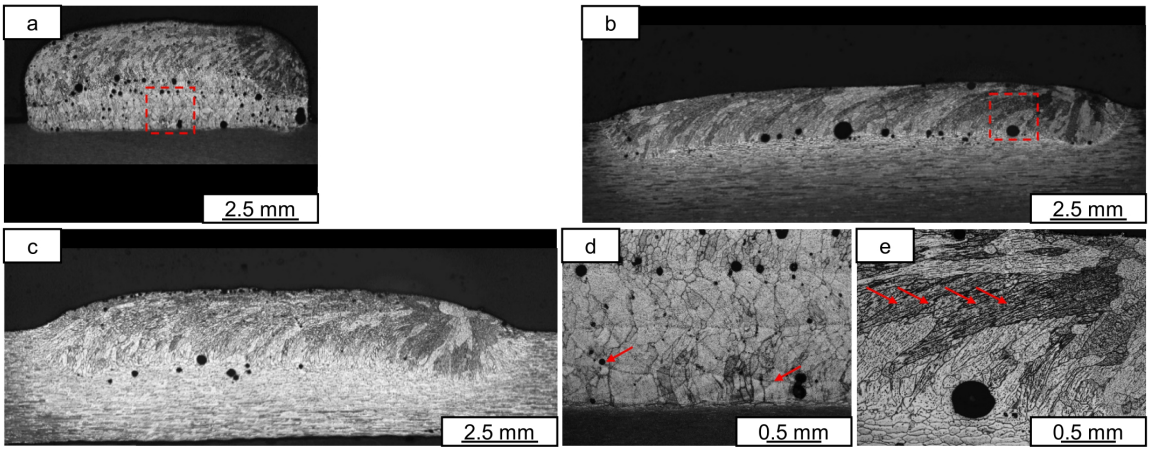

Fig. 7. Criteria evaluating the visibility of melt pool boundaries: (a) visible, count as 1 in Fig. 8; (b) indistinct, count as 0.5; (c) invisible, count as 0; (d) local magnification of the red dotted line marked area in (a); (e) local magnification of the marked area in (b). Melt pool boundaries are pointed by red arrows. Specimens were cut by cutting plane 1. (For interpretation of the references to colour in this figure legend, the reader is referred to the web version of this article.)

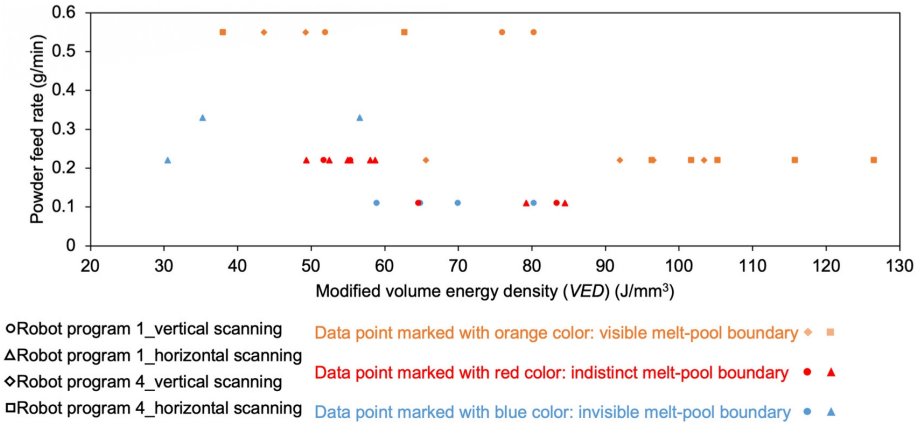

Fig. 8. Correlation among the robot program, the *modified VED*, the powder feed rate, and the visibility of melt pools. Data points with different shapes are employed to represent specimens produced with different robot programs and scanning strategies. Data points are colored to indicate the visibility of the melt pool in these specimens.

VED, the powder feed rate, and the visibility of melt pools. The visibility of melt pools does not exhibit a clear dependence on the robot program. However, the data points corresponding to the specimens that can identify the melt pool boundary can be clearly separated from the data points corresponding to other specimens that have indistinct or invisible melt pool boundaries. In the process regime with a high powder feed rate and high *modified VED*, the melt pool boundary can be easily recognized on the cross-section of specimens.

Given the size of HAZ in substrates in Fig. 7, the hardness of substrates below the remelted boundary could be affected to a different extent compared to the as-delivered state. As-delivered substrate (T651 heat treatment) has an average hardness of 190 $HV_{0.1}$. Fig. 9 demonstrates that the average hardness of the substrate increases with the larger size of HAZ in the substrate. Meanwhile, the hardness profile fluctuates sharply as the size of HAZ increases.

The microstructure near and below the remelted boundary is shown in Fig. 10. Grains of the substrates subjected to the least heat effect exhibit typical rolled direction (Fig. 10(a, d)). The microstructure is homogeneous. Equiaxed grains near the remelted boundary of the substrate with a moderate HAZ indicate the occurrence of recrystallization (Fig. 10b). As the distance to the remelted boundary increases, rolled microstructure dominates again (Fig. 10e). The transformation from rolled microstructure to equiaxed grains is observed even further away from the remelted boundary of the substrate with the largest HAZ (Fig. 10f). Given the comparable grain size of the as-delivered substrate (Fig. 10g) and the substrate after the L-DED process (Fig. 10d), the hardness reduction could be attributed to the precipitation behavior of strengthening secondary phases, which is induced by the heat input during processing.

3.3. Process window identification

Detailed investigations of optimal process parameters were implemented on specimens processed by robot program 1 and robot program

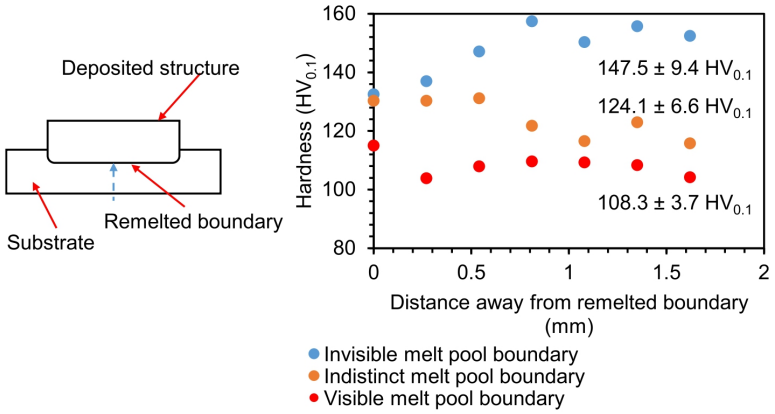

Fig. 9. Hardness profiles of substrates. 7 indentation points were aligned from the remelted boundary along the direction of the blue arrow. 0.27 mm distance between every 2 points. Mean hardness values with standard deviations calculated based on the 7 measurement results for each profile are also shown in the diagram. (For interpretation of the references to colour in this figure legend, the reader is referred to the web version of this article.)

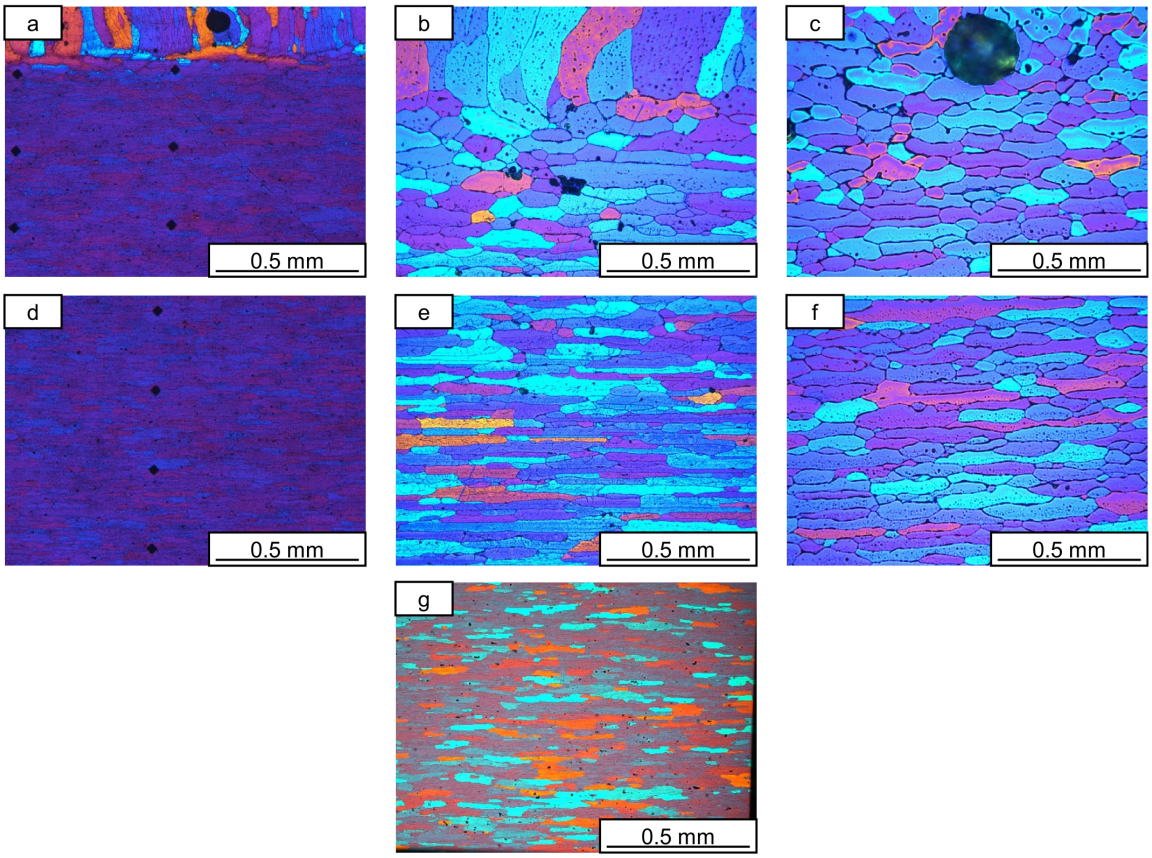

Fig. 10. Microstructure of substrates: (a) near and (d) below remelted boundary of the specimen showed in Fig. 7a (visible melt pool); (b) near and (e) below remelted boundary of the specimen shown in Fig. 7b (indistinct melt pool); (c) near and (f) below remelted boundary of the specimen shown in Fig. 7c (invisible melt pool). (g) Microstructure of the as-delivered substrate. The specimens were etched by Barker's reagent. Specimens were cut by cutting plane 1.

Table 4
Studied process window of specimens produced by different robot programs and scanning strategies.

Program and scanning strategy	Laser power (W)	Scan speed (mm/s)	Hatch distance (mm)	z-offset (mm)	Powder feed rate (g/min)
Robot program 1, vertical scanning	350–600	8–20	0.2–0.5	0.2–0.8	0.11–0.55
Robot program 1, horizontal scanning	400	8–12	0.25–0.5	0.2–0.8	0.11–0.33
Robot program 4, vertical scanning	500–750	8–20	0.4–0.8	0.2–0.5	0.22–0.55
Robot program 4, horizontal scanning	400–800	5–35	0.4–0.6	0.1–0.7	0.22–0.55

4. The number of deposited layers was restricted to 6 in robot program 1 because of the occurrence of uneven geometry after 6 layers. The range of studied process parameters is listed in Table 4. The criteria for judging specimen quality is the cross-sectional porosity level. Compared with other robot programs and scanning strategies, robot program 1 (horizontal scanning) can produce specimens with the lowest porosity level (1.8 ± 0.4 %, Fig. 11b) and no crack is observed. In vertical scanning of robot programs 1 and 4, cracks are distributed on the bottom sides and propagate to the substrate (Fig. 11(a, c), circled by a red dotted line). Cracks occurs also in the middle area of the specimen produced using robot program 4 (Fig. 11e). In robot program 4 (horizontal scanning) (Fig. 11d), two enormous downward cracks were generated between laser-heated and non-laser-heated areas. No crack is noticed in the laser-heated area and the porosity level is relatively low (3.1 ± 0.4 %).

Specimens (Fig. 11c and d) were etched to analyze the mechanism behind the initiation of cracks. In Fig. 12(a, b), columnar grains exhibit an epitaxial growth crossing multiple layers near the substrate. The growth direction of grains in Fig. 12a is perpendicular to the substrate, i. e. parallel to the heat flow direction [63]. Cracks in the middle grow along the columnar grain boundaries. Fig. 12b reveals a zigzag growth pattern of grains, which was also observed in bi-directionally deposited thin-wall structures [9]. Grain boundaries are a preferred location for the segregation of solutes and they can provide a wetting condition for the liquid film, which is formed by partial melting of the eutectic phases at grain boundaries in the heat-affected zone [64]. Hot cracks could be attributed to the rupture of liquid films on grain boundaries. The zigzag

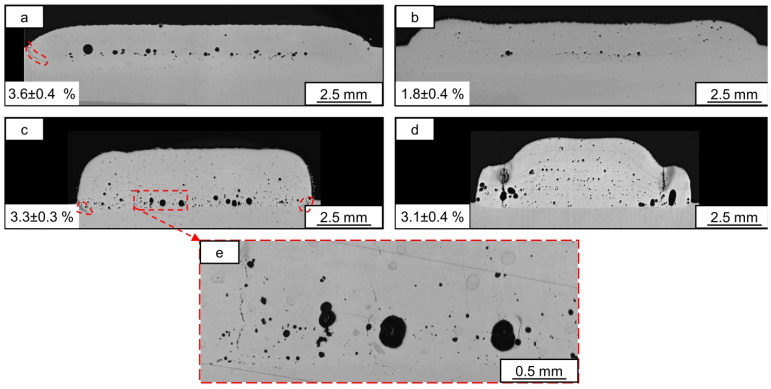

Fig. 11. Cross-section of specimens produced with optimal process parameters based on (a) robot program 1 (vertical scanning), 6-layer-deposition, laser power: 400 W, scan speed: 12 mm/s, hatch distance: 0.45 mm, z-offset: 0.3 mm, powder feed rate: 0.22 g/min; (b) robot program 1 (horizontal scanning), 6-layer-deposition, laser power: 400 W, scan speed: 8 mm/s, hatch distance: 0.5 mm, z-offset: 0.6 mm, powder feed rate: 0.22 g/min; (c) robot program 4 (vertical scanning), 12-layer-deposition, laser power: 550 W, scan speed: 8 mm/s, hatch distance: 0.6 mm, z-offset: 0.2 mm, powder feed rate: 0.22 g/min; (d) robot program 4 (horizontal scanning), 12-layer-deposition, laser power: 550 W, scan speed: 8 mm/s, hatch distance: 0.4 mm, z-offset: 0.5 mm, powder feed rate: 0.22 g/min; (e) magnification of the local area in (c). Porosity levels are noted in the lower-left corner. Specimens were cut by cutting plane 1.

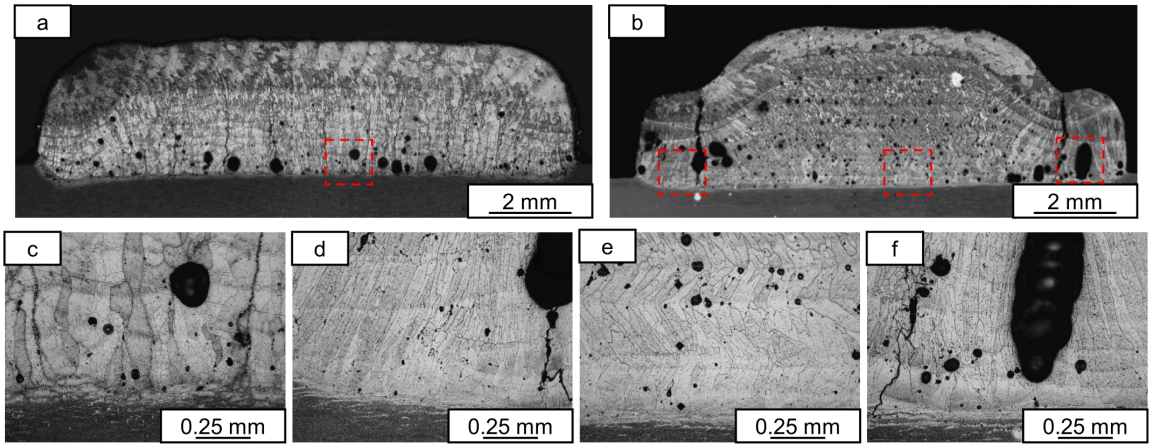

Fig. 12. Etched cross-section of specimens: (a) corresponds to Fig. 11c; (b) corresponds to Fig. 11d; (c) local magnification of the red dotted line marked area in (a); (d) local magnification of the left marked area in (b), (e) middle of the marked area in (b), (f) right part of the marked area in (b). The specimens were cut by cutting plane 1. (For interpretation of the references to colour in this figure legend, the reader is referred to the web version of this article.)

pattern grain boundaries could interrupt crack propagation compared with straight grain boundaries [65]. Consequently, the robot program 4 (horizontal scanning) produced specimen demonstrates a better cracking resistance than the robot program 4 (vertical scanning) produced specimen.

Two sides of the cross-section in Fig. 12b are non-laser-irradiated areas, where powders are melted relying on the heat that remained after laser scanning the middle area. Unlike the zigzag pattern grain boundary in laser-scanned area, columnar grains on two sides have straight grain boundaries and the growth direction is nearly perpendicular to the substrate, which is susceptible to cracking. Moreover, laser-scanned and non-laser-scanned areas experience different heat histories causing the discrepancy between thermal expansion and contraction as well as the resultant thermal stress in the intersection area. The straight columnar grain boundary and the thermal stress promote the formation of large cracks in the intersection area.

The difference between vertical scanning and horizontal scanning in robot program 4 is the travel direction of the substrate/robot arm relative to the nozzle. The cutting plane 1 for the above metallography preparation is perpendicular to deposition tracks in vertical scanning and parallel to deposition tracks in horizontal scanning (Fig. 4a). Various observation viewpoints could cause differences in the observed microstructure and errors in determining whether cracks are present in specimens. Hence, the cutting plane 2 rotated by 90° compared to the cutting plane 1 was also applied. The porosity of vertical scanning produced specimen exhibits a comparable level on cross-sections cut by cutting plane 1 (Fig. 11c) and cutting plane 2 (Fig. 13a). Cracks are noticed in Fig. 13(a, c) suggesting that the observation viewpoints lead to no bias in evaluating microstructure and determining the porosity level of specimens produced by robot program 4 (vertical scanning). In Fig. 13b (horizontal scanning), no crack is noticed. The cross-sectional porosity level is higher than that in Fig. 11d. Hence, to evaluate the presence of cracks in specimens produced by robot program 4 (horizontal scanning), it is reasonable to observe cross-sections either parallel or perpendicular to deposition tracks. The porosity measurement should be conducted on the cross-section perpendicular to the deposition tracks.

Large pores and cracks are distributed near the substrate in Fig. 11c. In this case, the substrate was in an as-delivered state (AA7075-T651) and without pre-treatment before processing. The surface condition might influence the formation of pores and cracks. Sandblasting of substrates prior to processing is usually applied in L-DED to increase the absorptivity of the laser beam by roughening and cleaning the surface [66,67]. In the present experiment, sandblasted substrate increases the porosity level near the substrate and leads to a higher cross-sectional porosity level (Fig. 14a), which is consistent with the findings in [56]. As-delivered substrates have a shiny surface enhancing the laser beam reflection [68]. In terms of porosity reduction, a flat surface with lower laser absorptivity has a more positive effect than a rough surface with higher laser absorptivity.

Prior to powder feeding, the laser was switched on to pre-scan the substrate to increase the substrate temperature (scanning the deposition path of one layer, laser beam spot diameter of 2.4 mm, scan speed of 20 mm/s, laser power of 550 W). The porosity level (3.5 ± 0.8 %, Fig. 14b) is comparable to that of the specimen without preheating (3.3 ± 0.3 %, Fig. 11c). Preheating eliminates the cracks. To confirm this finding and prevent bias due to the observation of only one cross-section, another specimen was reproduced and multiple cross-sections were prepared. All results verified this finding. The higher temperature of substrates decreases the cooling rate and the temperature gradient leading to a reduction of cracking susceptibility [51]. However, single large pores still exist near the substrate. Despite the laser pre-scan, it is assumed that the temperature at the beginning of the process is low causing a short lifetime of melt pools. Due to this fact, gas bubbles do not always have sufficient time to escape from the melt pools and are trapped in melt pools. Therefore, to reduce the porosity level the laser power was set at a higher value of 650 W in the first 4 layers and a lower value of 550 W from the 5th to 12th layer. The porosity level near the substrate and the cross-sectional porosity level were reduced (2.8 ± 0.2 %, Fig. 14c). However, a few cracks were developed. As the temperature gradient increases with increasing laser power [69], a laser power of 650 W in the first 4 layers could lead to a steeper temperature gradient promoting the formation of cracks. Based on the considerations it can be concluded that there should be a reasonable compromise concerning the identified laser pre-scan strategy to reduce the porosity level without a significant increase in the number of hot cracks. The same laser pre-scan strategy was

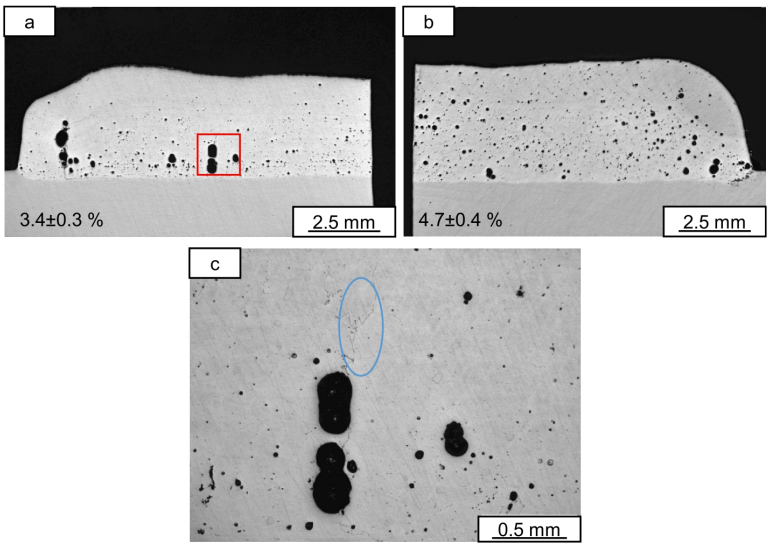

Fig. 13. (a) Cross-section of the specimen from Fig. 11c cut by cutting plane 2; (b) cross-section of the specimen from Fig. 11d cut by cutting plane 2; (c) local magnification of the red bold line marked area in (a) and the crack is circled by the blue line. Porosity levels are noted in the lower-left corner. Specimens were cut by cutting plane 2. (For interpretation of the references to colour in this figure legend, the reader is referred to the web version of this article.)

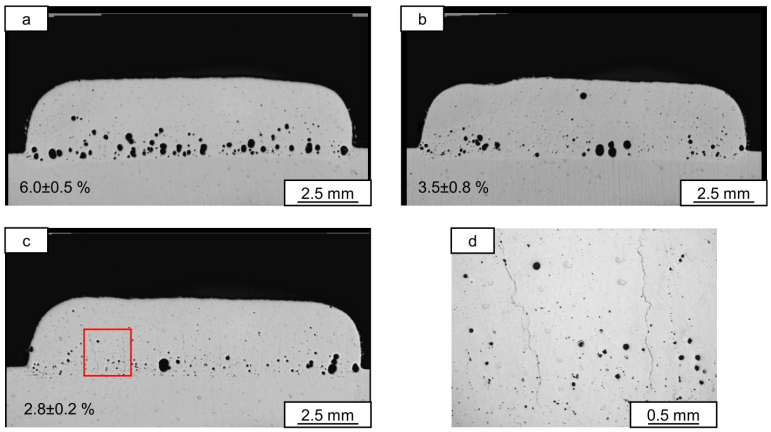

Fig. 14. Specimens produced with the same process parameters as in Fig. 11c, but with (a) a sandblasted substrate; (b) laser pre-scan; (c) laser pre-scan and laser power adjustment during deposition. (d) Local magnification of the area marked with the bold red rectangle in (c). Porosity levels are noted in the lower-left corners. The specimens were cut by cutting plane 1. (For interpretation of the references to colour in this figure legend, the reader is referred to the web version of this article.)

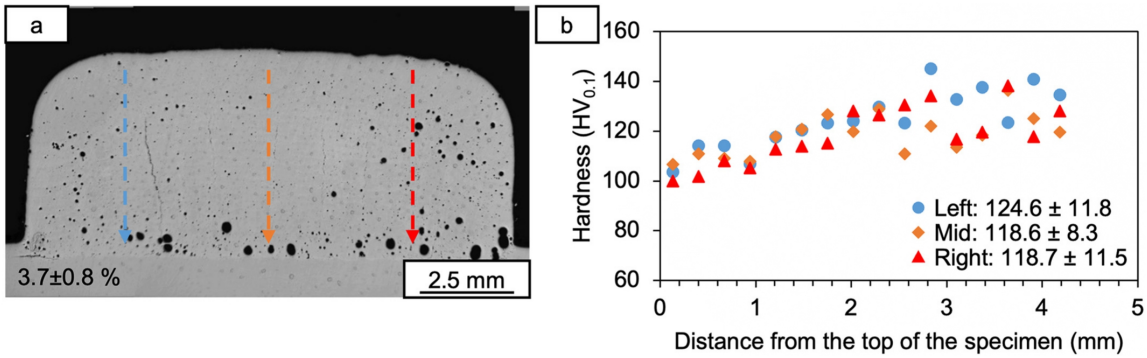

Fig. 15. (a) Cross-section of the specimen produced with the same parameters as in Fig. 14b, 24-layer-deposition. A porosity level is noted in the lower-left corner. (b) Hardness profile from the top to the bottom of the specimen along the direction of the arrows in (a). Specimens were cut by cutting plane 1.

also applied for the deposition of 24 layers.

3.4. Process stability and characterization of the 24-layer deposited specimens

As the geometry of built specimens becomes larger, the porosity level normally increases [40,41]. Process stability concerning the appearance of hot cracks and pores was investigated in the case of multi-layer L-DED up to 24 layers. In experiments accomplished within this study, the porosity level of L-DED-produced specimens under the same process parameters and robot programs is comparable between 12-layer deposited (3.5 ± 0.8 %, Fig. 14b) and 24-layer deposited (3.7 ± 0.8 %, Fig. 15a) specimens. The geometrical accuracy was also well maintained. However, hot cracks were observed in the cross-section of the 24-layer deposited specimen. The propagation direction of cracks is perpendicular to the substrate. As discussed above, these cracks might be eliminated by increasing laser power during laser pre-scan or employing a horizontal scanning strategy. However, as the number of cracks and porosity level cannot be reduced at the same time, the microstructure shown in Fig. 15 is a reasonable compromise.

The SEM images were captured from top to bottom of the specimen (Fig. 16). The chemical composition of the α-Al matrix, secondary phase, and grain boundary is listed in Table 5. Large grains grow crossing several deposition tracks and layers. Bright secondary phases are distributed on grain boundaries. Equiaxed grains are developed on the top of the specimen, while columnar grains dominate the mid and the bottom. Fig. 16a reveals material contrast between the α-Al matrix on the boundary and in the center of the melt pool. The matrix on the boundary (top: point 1, Table 5) has a lower Cu content than that in the center (top: point 3). Pitting corrosion prefers to initiate on the Cu-poor melt pool boundary [70]. The Cu content of the secondary phase on the melt pool boundary is significantly high (37.76 wt%, top: point 2), which could lead to the depletion of Cu in the surrounding matrix on the melt pool boundary. Although secondary phases inside grains (top: point 5, mid: point 4, bottom: point 3) and secondary phases on grain boundaries (top: point 4, mid: point 3, bottom: point 4) are both rich in Cu and Fe, the content of Cu and Fe of secondary phases on grain boundary is higher. In L-DED, previously solidified layers experience in-situ heat treatment during subsequent deposition. Zn- and Mg-rich phases are typical precipitates in 7XXX Al alloys during heat treatment [17,71]. However, no phase with higher content of Zn and Mg is detected. It was found that the precipitation sequence of Cu-rich precipitate (S phase) and (Zn, Mg)-rich precipitate (η phase) is: precipitation of η phase begins at 100–200 °C and precipitation of S-phase begins at 200–300 °C [14]. The temperature during processing might be significantly high, which can be confirmed by the loss of Zn in the α-Al

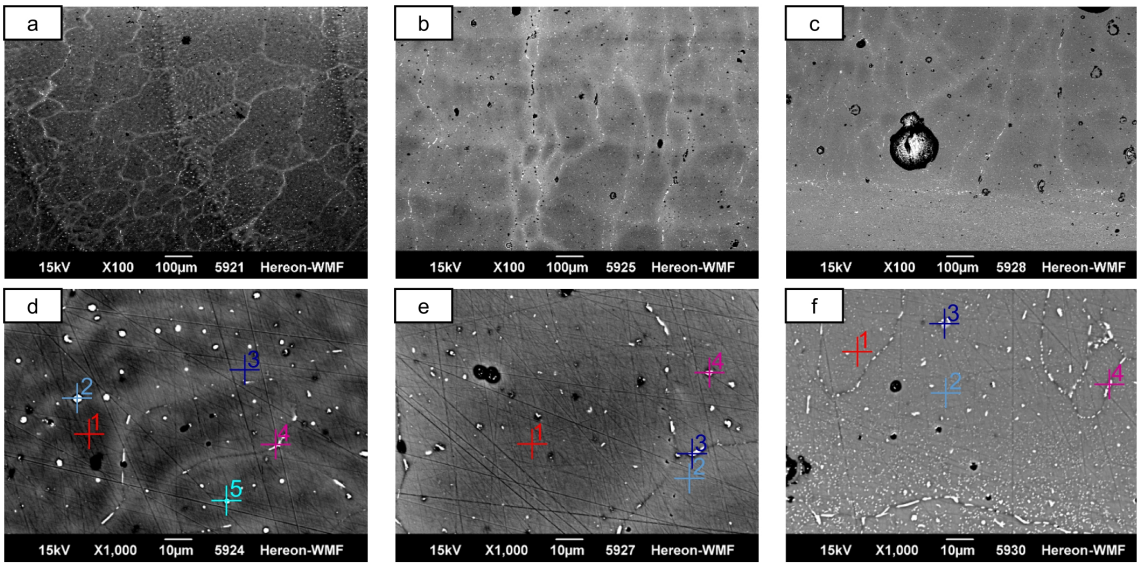

Fig. 16. SEM images of (a) top (b) mid (c) bottom of the middle area of the cross-section (Fig. 15a), 100×; (d) local magnification of (a), 1000×; (e) local magnification of (b), 1000×; (f) local magnification of (c) 1000×. The numbers in (d), (e), (f) represent the location of the EDX measurement. Specimens were cut by cutting plane 1.

Table 5
Chemical composition of the measuring locations in Fig. 16(d, e, f) (in wt%).

	Measuring points	Mg	Al	Si	Zr	Ti	Cr	Mn	Fe	Cu	Zn
Top	1	1.49	95.12	0.09	0.38	0.17	0.12	0.07	0.07	0.93	1.56
	2	3.47	54.90	0.50	0.15	0.01	0.05	0	2.21	37.76	0.93
	3	1.33	93.55	0.05	0.23	0.13	0.09	0.07	0.09	2.63	1.84
	4	1.26	87.50	0.11	0.14	0	0	0	2.55	6.92	1.52
	5	1.84	91.75	0.13	0.14	0.05	0.04	0.03	0.19	3.91	1.92
Mid	1	1.78	93.59	0.07	0.24	0.13	0.12	0.09	0.10	1.85	2.03
	2	1.46	92.66	0.33	0.19	0.12	0.12	0.08	0.07	2.68	2.29
	3	0.92	72.19	0.28	0.04	0.02	0	0.03	6.97	18.53	1.02
	4	2.85	88.91	0.10	0.55	0.10	0.04	0	1.15	4.34	1.96
Bottom	1	2.40	91.56	0.04	0.11	0.02	0.14	0	0.04	1.72	3.97
	2	2.46	91.45	0.06	0.09	0.04	0.07	0.02	0.03	1.70	4.06
	3	1.78	89.51	0.17	0.15	0.07	0.12	0.02	1.01	3.78	3.39
	4	1.83	84.04	0.08	0.17	0.03	0.12	0	2.69	8.20	2.84

matrix from the bottom to the top of the specimen (bottom: points 1 and 2; top: points 1 and 3). The η-phase might have been precipitated and then re-dissolved into a matrix resulting in the absence of the η-phase in the specimen.

The average microhardness at the left, mid, and right positions of the specimen is comparable (about 120 $HV_{0.1}$, Fig. 15b). A generally decreasing trend from the bottom to the top of the specimen is observed. The reduction of hardness might be attributed to the solute loss, as shown in Table 5. The bottom of the specimen experiences an in-situ heat treatment, which could also contribute to the higher hardness. Considering the re-dissolution of the η-phase into the matrix and the lower hardness than that of the peak-aged AA7050 specimen [71], this specimen might be located in the over-aged phase. In the present study, the visibility of melt pools and the mechanical properties are dependent on the process parameters and the associated in-situ heat treatment. The microstructure modification and the resultant enhancement of mechanical properties have been tailored in titanium alloy [72] and low-carbon steel [73] by in-situ heat treatment in AM. Similar improvements in L-DED-processed Al alloys should be also expected.

4. Conclusion

Effects of different robot programs and scanning strategies on the buildability, geometrical accuracy, visibility of the melt pool, and hot crack initiation were investigated in L-DED-processed AA7050 powder. In terms of porosity reduction and crack elimination, the appropriate process window was studied for each combination of the robot program and scanning strategy. Based on the present results, the following main conclusions can be drawn:

- The acceleration and the deceleration phases of the robot arm deteriorate the buildability and the geometrical accuracy. Heat accumulation results in the formation of bumps at the start and the end of deposition tracks. The optimal control strategy to avoid it is to reduce laser power on two sides of each track or adjust the time for switching on the laser and the powder feeder.
- Robot program and scanning strategy affect the initiation of hot cracks. Higher cracking resistance is observed if the laser stays switched on during deposition. In the case of switching on and off the laser at the start and the end of deposition tracks, a horizontal

scanning strategy exhibits higher cracking resistance than a vertical scanning strategy, which could be attributed to the various resistance to the crack propagation in different patterns of grain boundaries.

- The *modified VED* is introduced to represent the effects of process parameters. The robot program and scanning strategy do not affect the visibility of melt pools in as-built specimens. The visibility of melt pools exhibits a dependence on the powder feed rate and the *modified VED*. In the process regime with a high powder feed rate and high *modified VED*, the melt pool boundary can be easily recognized.
- The minimal achievable porosity level is different in various combinations of robot programs and scanning strategies. Even if processing with the same process parameters, e.g. laser power, laser scan speed, etc., a difference in porosity level is demonstrated. Besides the process parameters, the switching state of the laser and powder feeder changes the actual energy input and the thermal history during the deposition. In future publications, more experimental details should be reported to help readers to better understand and reproduce experiments.

Declaration of competing interest

The authors declare that they have no known competing financial interests or personal relationships that could have appeared to influence the work reported in this paper.

Acknowledgements

The authors would like to thank R. Dinse and S. Riekehr for their assistance during laser-direct energy deposition as well as F. Dorn and Dr. Ventzke for their support during metallographic preparation and microstructural characterization.

References

[1] Frazier WE. Metal additive manufacturing: a review. J Mater Eng Perform 2014;23:1917–28.
[2] Wong KV, Hernandez A. A review of additive manufacturing. Int Sch Res Notices 2012;2012:1–10.
[3] Akinlabi ET, Akinlabi SA. Advanced coating: laser metal deposition of aluminium powder on titanium substrate. In: Ao SI, Len G, David WH, Andrew H, K.A. M., editors. Proceedings of the World Congress on Engineering. London: Newswood Limited; 2016. p. 863–8.
[4] Gasser A, Backes G, Kelbassa I, Weisheit A, Wissenbach K. Laser metal deposition (LMD) and selective laser melting (SLM) in turbo-engine applications. Laser Technik J 2010;2:58–63.
[5] Gradl PR, Protz CS, Wammen T. Additive manufacturing and hot-fire testing of liquid rocket channel wall nozzles using blown powder directed energy deposition inconel 625 and JBK-75 alloys. In: Shih TI-P, editor. AIAA, editors. Propulsion and Energy 2019 Forum. Indianapolis: American Institute of Aeronautics and Astronautics; 2019. p. 4362.
[6] Lee W-S, Sue W-C, Lin C-F, Wu C-J. The strain rate and temperature dependence of the dynamic impact properties of 7075 aluminum alloy. J Mater Process Technol 2000;100:116–22.
[7] Lampman S, editor. Weld integrity performance: A source book adapted from ASM international handbooks, conference proceedings, and technical books. 1st ed. Materials Park: ASM International; 1997.
[8] Liu Y, Liu C, Liu W, Ma Y, Tang S, Liang C, et al. Optimization of parameters in laser powder deposition AlSi10Mg alloy using Taguchi method. Opt Laser Technol 2019;111:470–80.
[9] Dinda G, Dasgupta A, Mazumder J. Evolution of microstructure in laser deposited Al–11.28% Si alloy. Surf Coat Technol 2012;206:2152–60.
[10] Ding Y, Muñiz-Lerma J, Trask M, Chou S, Walker A, Brochu M. Microstructure and mechanical property considerations in additive manufacturing of aluminum alloys. MRS Bull 2016;41:745–51.
[11] Hirsch J. Recent development in aluminium for automotive applications. Trans Nonferrous Met Soc China 2014;24:1995–2002.
[12] Dursun T, Soutis C. Recent developments in advanced aircraft aluminium alloys. Mater Des 2014;56:862–71.
[13] Isadare AD, Aremo B, Adeoye MO, Olawale OJ, Shittu MD. Effect of heat treatment on some mechanical properties of 7075 aluminium alloy. Mater Res 2013;16:190–4.
[14] Godard D, Archambault P, Aeby-Gautier E, Lapasset G. Precipitation sequences during quenching of the AA 7010 alloy. Acta Mater 2002;50:2319–29.
[15] Yang W, Ji S, Wang M, Li Z. Precipitation behaviour of Al–Zn–Mg–Cu alloy and diffraction analysis from η' precipitates in four variants. J Alloys Compd 2014;610:623–9.
[16] Paulisch M, Wanderka N, Haupt M, Selve S, Driehorst I, Reimers W. The influence of heat treatments on the microstructure and the mechanical properties in commercial 7020 alloys. Mater Sci Eng A 2015;626:254–62.
[17] Wang F, Gong Y, Du Y, Song M. Microstructures and mechanical properties of an Al-Zn-Mg-Cu alloy processed by two-step aging treatment. J Mater Eng Perform 2020;29:4404–11.
[18] Chemingui M, Khitouni M, Jozwiak K, Mesmacque G, Kolsi A. Characterization of the mechanical properties changes in an Al–Zn–Mg alloy after a two-step ageing treatment at 70° and 135°C. Mater Des 2010;31:3134–9.
[19] Hebert RJ. Metallurgical aspects of powder bed metal additive manufacturing. J Mater Sci 2016;51:1165–75.
[20] Herzog D, Seyda V, Wycisk E, Emmelmann C. Additive manufacturing of metals. Acta Mater 2016;117:371–92.
[21] Toda H, Hidaka T, Kobayashi M, Uesugi K, Takeuchi A, Horikawa K. Growth behavior of hydrogen micropores in aluminum alloys during high-temperature exposure. Acta Mater 2009;57:2277–90.
[22] Harvey J-P, Chartrand P. Modeling the hydrogen solubility in liquid aluminum alloys. Metall Mater Trans B 2010;41:908–24.
[23] Susan D, Puskar J, Brooks J, Robino CV. Quantitative characterization of porosity in stainless steel LENS powders and deposits. Mater Charact 2006;57:36–43.
[24] Louvis E, Fox P, Sutcliffe CJ. Selective laser melting of aluminium components. J Mater Process Technol 2011;211:275–84.
[25] Tang M, Pistorius PC. Oxides, porosity and fatigue performance of AlSi10Mg parts produced by selective laser melting. Int J Fatigue 2017;94:192–201.
[26] Altıparmak SC, Yardley VA, Shi Z, Lin J. Challenges in additive manufacturing of high-strength aluminium alloys and current developments in hybrid additive manufacturing. Int J Lightweight Mater Manuf 2021;4:246–61.
[27] Cross C. On the origin of weld solidification cracking. In: Böllinghaus T, Herold H, editors. Hot Cracking Phenomena in Welds. Berlin, Heidelberg: Springer; 2005. p. 3–18.
[28] Stopyra W, Gruber K, Smolina I, Kurzynowski T, Kuźnicka B. Laser powder bed fusion of AA7075 alloy: influence of process parameters on porosity and hot cracking. Addit Manuf 2020;35:101270.
[29] Javidani M, Arreguin-Zavala J, Danovitch J, Tian Y, Brochu M. Additive manufacturing of AlSi10Mg alloy using direct energy deposition: microstructure and hardness characterization. J Therm Spray Technol 2017;26:587–97.
[30] Li Y, Gu D. Parametric analysis of thermal behavior during selective laser melting additive manufacturing of aluminum alloy powder. Mater Des 2014;63:856–67.
[31] Sargent N, Jones M, Otis R, Shapiro AA, Delplanque J-P, Xiong W. Integration of processing and microstructure models for non-equilibrium solidification in additive manufacturing. Metals 2021;11:570.
[32] Parry L, Ashcroft I, Wildman RD. Understanding the effect of laser scan strategy on residual stress in selective laser melting through thermo-mechanical simulation. Addit Manuf 2016;12:1–15.
[33] Chen W, Xu L, Han Y, Zhao L, Jing H. Control of residual stress in metal additive manufacturing by low-temperature solid-state phase transformation: an experimental and numerical study. Addit Manuf 2021;42:102016.
[34] Froend M, Ventzke V, Dorn F, Kashaev N, Klusemann B, Enz J. Microstructure by design: an approach of grain refinement and isotropy improvement in multi-layer wire-based laser metal deposition. Mater Sci Eng A 2020;772:138635.
[35] Zhang J, Gao J, Song B, Zhang L, Han C, Cai C, et al. A novel crack-free Ti-modified Al-Cu-Mg alloy designed for selective laser melting. Addit Manuf 2021;38:101829.
[36] Kaufmann N, Imran M, Wischeropp TM, Emmelmann C, Siddique S, Walther F. Influence of process parameters on the quality of aluminium alloy EN AW 7075 using selective laser melting (SLM). Phys Procedia 2016;83:918–26.
[37] Montero-Sistiaga ML, Mertens R, Vrancken B, Wang X, Van Hooreweder B, Kruth J-P, et al. Changing the alloy composition of Al7075 for better processability by selective laser melting. J Mater Process Technol 2016;238:437–45.
[38] Zhou S, Su Y, Wang H, Enz J, Ebel T, Yan M. Selective laser melting additive manufacturing of 7xxx series Al-Zn-Mg-Cu alloy: cracking elimination by co-incorporation of Si and TiB2. Addit Manuf 2020;36:101458.
[39] Li L, Li R, Yuan T, Chen C, Zhang Z, Li X. Microstructures and tensile properties of a selective laser melted Al–Zn–Mg–Cu (Al7075) alloy by Si and Zr microalloying. Mater Sci Eng A 2020;787:139492.
[40] Benoit M, Sun S, Brandt M, Easton M. Processing window for laser metal deposition of Al 7075 powder with minimized defects. J Manuf Process 2021;64:1484–92.
[41] Langebeck A, Bohlen A, Rentsch R, Vollertsen F. Mechanical properties of high strength aluminum alloy EN AW-7075 additively manufactured by directed energy deposition. Metals 2020;10:579.
[42] Singh A, Ramakrishnan A, Dinda G. Direct laser metal deposition of Al 7050 alloy. In: SAE Technical Paper; 2017. p. 0286.
[43] Pinkerton AJ, Li L. Modelling the geometry of a moving laser melt pool and deposition track via energy and mass balances. J Phys D Appl Phys 2004;37:1885.
[44] Peyre P, Aubry P, Fabbro R, Neveu R, Longuet A. Analytical and numerical modelling of the direct metal deposition laser process. J Phys D Appl Phys 2008;41:025403.
[45] Bi G, Gasser A, Wissenbach K, Drenker A, Poprawe R. Characterization of the process control for the direct laser metallic powder deposition. Surf Coat Technol 2006;201:2676–83.
[46] Pi G, Zhang A, Zhu G, Li D, Lu B. Research on the forming process of three-dimensional metal parts fabricated by laser direct metal forming. Int J Adv Manuf Technol 2011;57:841–7.
[47] DePond PJ, Guss G, Ly S, Calta NP, Deane D, Khairallah S, et al. In situ measurements of layer roughness during laser powder bed fusion additive manufacturing using low coherence scanning interferometry. Mater Des 2018;154:347–59.

[48] Dunbar A, Denlinger E, Heigel J, Michaleris P, Guerrier P, Martukanitz R, et al. Development of experimental method for in situ distortion and temperature measurements during the laser powder bed fusion additive manufacturing process. Addit Manuf 2016;12:25–30.
[49] Thijs L, Kempen K, Kruth J-P, Van Humbeeck J. Fine-structured aluminium products with controllable texture by selective laser melting of pre-alloyed AlSi10Mg powder. Acta Mater 2013;61:1809–19.
[50] Wu AS, Brown DW, Kumar M, Gallegos GF, King WE. An experimental investigation into additive manufacturing-induced residual stresses in 316L stainless steel. Metall Mater Trans A 2014;45:6260–70.
[51] Prashanth K, Scudino S, Eckert J. Defining the tensile properties of Al-12Si parts produced by selective laser melting. Acta Mater 2017;126:25–35.
[52] Song Y-A, Park S, Chae S-W. 3D welding and milling: part II—optimization of the 3D welding process using an experimental design approach. Int J Mach Tool Manuf 2005;45:1063–9.
[53] Touzé S, Rauch M, Hascoët J-Y. Flowability characterization and enhancement of aluminium powders for additive manufacturing. Addit Manuf 2020;36:101462.
[54] Nagulin KY, Iskhakov F, Shpilev A, Gilmutdinov AK. Optical diagnostics and optimization of the gas-powder flow in the nozzles for laser cladding. Opt Laser Technol 2018;108:310–20.
[55] Ng G, Jarfors A, Bi G, Zheng H. Porosity formation and gas bubble retention in laser metal deposition. Appl Phys A 2009;97:641–9.
[56] Zhao T, Wang Y, Xu T, Bakir M, Cai W, Wang M, et al. Some factors affecting porosity in directed energy deposition of AlMgScZr-alloys. Opt Laser Technol 2021;143:107337.
[57] Svetlizky D, Zheng B, Buta T, Zhou Y, Golan O, Breiman U, et al. Directed energy deposition of Al 5xxx alloy using laser engineered net shaping (LENS®). Mater Des 2020;192:108763.
[58] Toyserkani E, Khajepour A, Corbin SF. Laser cladding. 1st ed. Boca Raton: CRC Press; 2004.
[59] Uddin SZ, Espalin D, Mireles J, Morton P, Terrazas C, Collins S, et al. Laser powder bed fusion fabrication and characterization of crack-free aluminum alloy 6061 using in-process powder bed induction heating. Austin: Proceedings of SFF Symposium; 2017. p. 214–27.
[60] Yang J, Sun S, Brandt M, Yan W. Experimental investigation and 3D finite element prediction of the heat affected zone during laser assisted machining of Ti6Al4V alloy. J Mater Process Technol 2010;210:2215–22.
[61] Khamidullin B, Tsivilskiy I, Gorunov A, Gilmutdinov AK. Modeling of the effect of powder parameters on laser cladding using coaxial nozzle. Surf Coat Technol 2019;364:430–43.
[62] Neumann V. Focusing and optical imaging in applied laser technologies: beam characteristics of both methods. Laser Technik J 2012;9:41–4.
[63] Dinda G, Dasgupta A, Bhattacharya S, Natu H, Dutta B, Mazumder J. Microstructural characterization of laser-deposited Al 4047 alloy. Metall Mater Trans A 2013;44:2233–42.
[64] Zhang Z, Zhao Y, Shan J, Wu A, Sato YS, Tokita S, et al. Evolution behavior of liquid film in the heat-affected zone of laser cladding non-weldable nickel-based superalloy. J Alloys Compd 2021;863:158463.
[65] Tokita S, Kadoi K, Kanno Y, Inoue H. Microstructural evolution and solidification cracking susceptibility of grain boundary engineered fully austenitic stainless steel. Weld World 2020:1–8.
[66] Ahsan MN, Bradley R, Pinkerton AJ. Microcomputed tomography analysis of intralayer porosity generation in laser direct metal deposition and its causes. J Laser Appl 2011;23:022009.
[67] Froend M, Riekehr S, Kashaev N, Klusemann B, Enz J. Process development for wire-based laser metal deposition of 5087 aluminium alloy by using fibre laser. J Manuf Process 2018;34:721–32.
[68] Mahamood R, Akinlabi ET. Laser metal deposition of functionally graded Ti6Al4V/TiC. Mater Des 2015;84:402–10.
[69] Fu C, Guo Y. Three-dimensional temperature gradient mechanism in selective laser melting of Ti-6Al-4V. J Manuf Sci Eng 2014;136.
[70] Chong P, Liu Z, Skeldon P, Thompson G. Large area laser surface treatment of aluminium alloys for pitting corrosion protection. Appl Surf Sci 2003;208:399–404.
[71] Liu Y, Jiang D, Li W. The effect of multistage ageing on microstructure and mechanical properties of 7050 alloy. J Alloys Compd 2016;671:408–18.
[72] Li D, Huang H, Chen C, Liu S, Liu X, Zhang X, et al. Additive manufacturing of high strength near β titanium alloy Ti-55511 by engineering nanoscale secondary α laths via in-situ heat treatment. Mater Sci Eng A 2021;814:141245.
[73] Li Y, Wu S, Li H, Dong Y, Cheng F. Submerged arc additive manufacturing (SAAM) of low-carbon steel: effect of in-situ intrinsic heat treatment (IHT) on microstructure and mechanical properties. Addit Manuf 2021;46:102–24.

Paper 2: M. Wang, N. Kashaev, Investigation of process window for AA7075 considering effects of different wire feed directions in lateral Laser Metal Deposition, Procedia CIRP 111 (2022) 218-223.

This published paper was incorporated as Chapter 4.3 (with permission from Elsevier).

Available online at www.sciencedirect.com

ScienceDirect

Procedia CIRP 111 (2022) 218–223

www.elsevier.com/locate/procedia

12th CIRP Conference on Photonic Technologies [LANE 2022], 4-8 September 2022, Fürth, Germany

Investigation of process window for AA7075 considering effects of different wire feed directions in lateral Laser Metal Deposition

Mengjie Wang[a,*], Nikolai Kashaev[b]

[a]Helmholtz-Zentrum Hereon, Max-Planck-Straße 1, Geesthacht 21502, Germany
[b]Institute of Materials Mechanics, Department of Laser Processing and Structural Assessment

* Corresponding author. Tel.: +494152872618; fax: +4941528742536. *E-mail address:* mengjie.wang@hereon.de

Abstract

This work addresses the influences of the feed direction of AA7075 high-strength aluminum alloy in wire-based lateral laser metal deposition (LMD). The additive manufacturing process is investigated for the deposition of thin-walled structures. The interaction between wire and laser beam as well as the evolution of the melt pool are in-situ monitored by a high-speed camera. The consequences of different feed directions are analyzed in terms of processability, surface morphology, geometry, and porosity. Besides, the appropriate process parameters for AA7075 in lateral wire LMD are also studied. A maximal relative density level of about 99.7 % can be reached. No macro-cracks on the specimen surface or inside the specimen are observed. Optical microscopy, scanning electron microscopy, and energy-dispersive X-ray spectroscopy are employed to characterize the microstructure and measure the chemical composition of specimen produced with the optimal process parameters. The plateau-like distribution of the hardness evolution and the uniform layer thickness in the middle of the thin-walled structure indicate that a stable LMD-process can be achieved.

Keywords: AA7075 aluminum alloy; laser metal deposition; wire feed direction; relative density; hot cracking

1. Introduction

Additive manufacturing (AM) as new manufacturing technology has replaced conventional subtractive technologies in some aerospace and automotive industries [1]. In AM, parts with any complex geometries can be produced layer by layer using a CAD model. Laser metal deposition (LMD)/laser-directed energy deposition (L-DED) is one of the prevailing AM technologies. The feedstock is fed through a nozzle and melted by the laser. LMD has multiple application areas, such as coating [2], repairing, and building 3D parts [3]. LMD as an AM technology can be applied to produce thin-walled 3D parts, e.g. the channel wall nozzles that were fabricated by LMD in NASA [4]. According to the type of feedstock, LMD can be further divided into powder-based and wire-based techniques [5]. Compared with powder-based LMD, wire-based LMD has a higher deposition rate [6].

7XXX high-strength Al alloys are widely used in industries because of their high strength-to-density ratio [7]. However, processing 7XXX alloys is challenging in AM due to their high sensitivity to hot cracking [8]. Besides, the porosity is another challenge. 7XXX alloys are enriched in volatile alloying elements, such as Zn and Mg. The evaporation of these elements at high processing temperatures forms gas, which could get trapped inside parts forming pores. These challenges were reported by the investigation of the processability of 7XXX alloys in the case of powder-based LMD [9] and wire and arc additive manufacturing (WAAM) [10, 11]. Considering the

10.1016/j.procir.2022.08.053

advantages of 7XXX alloys and wire-based LMD, the development of an appropriate process window is necessary.

In wire-based LMD, the wire can be fed laterally or coaxially relative to the laser beam [6, 12]. The present study adopts a lateral LMD apparatus that can be easily reconstructed from a welding apparatus. According to the results of the current study, the interaction among laser beam, wire, and melt pools is dependent on the feed direction of wires. However, studies that address the impacts of the feed direction of the wire are scarce. Hence, this paper addresses the consequences of wire feed direction in lateral LMD and investigates the optimal process window for LMD processing AA7075 alloy.

2. Experimental

AA7075 wire has a diameter of 1.2 mm. The typical chemical composition of AA7075 is listed in Table 1. The wire was deposited on 15 mm thick AA7075 T651 substrates. The LMD apparatus is shown in Fig. 1. A CNC machine is programmed to control the motion of the table and the optic head during the deposition. The interaction among laser beam, wire, and melt pools was captured by a high-speed camera, which was mounted on the side of the optic. The TruDisk 4001 (TRUMPF SE + Co. KG) with a wavelength of 1030 nm is used as the heat source. The TruDisk 4001 has a ring-core profile. In the present study, a constant ring-core ratio of 15-85 was adopted. The laser spot diameter is 1.5 mm. During the process, argon as a shielding gas was fed through the wire nozzle with a flow rate of 5 l/min and the extra nozzle with a flow rate of 20 l/min to prevent oxidation.

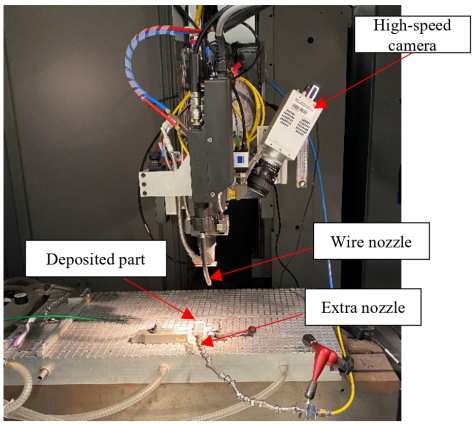

Fig. 1. Apparatus of the lateral wire-laser metal deposition.

Table 1. The chemical composition of AA7075 (in wt. %) [13].

Zn	Mg	Cu	Mn	Ti	Cr	Si	Fe	Al
5.2	2.1	1.5	0.3	0.2	0.2	0.2	0.2	Bal.

Four kinds of wire feed directions are illustrated in Fig. 2. The distance of the wire from the laser spot was kept constant in different wire feed directions. The terminology of the wire feed directions is borrowed from [14] and is further specified in this work. To investigate the effects of different wire feed directions, one single track was deposited on the substrate using each wire feed direction. In Fig. 2(a), the wire feed direction is almost opposite to the deposition direction (with an angle of about 135 °, hereinafter referred to as front feeding). In Fig. 2(b), the wire feed direction is almost parallel to the deposition direction (with an angle of about 45 °, hereinafter referred to as back feeding). In Fig. 2(c), the single track was deposited from left to right in the horizontal direction relative to the substrate (hereinafter referred to as side feeding (l-r)). In Fig. 2(d), the single track was deposited from right to left (hereinafter referred to as side feeding (r-l)).

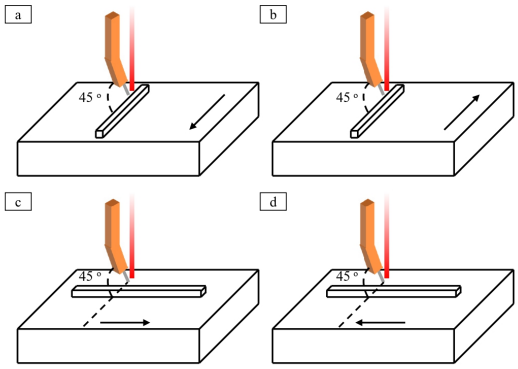

Fig. 2. Four kinds of wire feed directions: (a) front feeding; (b) back feeding; (c) side feeding (l-r); (d) side feeding (r-l).

As-deposited specimens were cut in the middle for the metallographic preparation. The specimens were ground, polished, and etched (Barker's etchant) for the microstructure characterization. The microstructure was analyzed using optical microscopy (OM, Leica DMI 5000M) and Jeol JSM-6490LV scanning electron microscopy (SEM). The chemical composition was characterized by energy-dispersive X-ray (EDX) analysis (EDAX Genesis). The hardness was measured in the middle of the as-deposited thin wall structures along the building direction.

3. Results and discussion

3.1. Effects of the wire feed direction

The effects of wire feed direction are investigated in two aspects, i.e. in-process and post-process. During LMD processing, the image of the wire and the melt pool is captured by the high-speed camera, as shown in Fig. 3. The surface morphology of the deposited single track is inserted on the left top corner.

In Fig. 3(a, b, c), the wire is located at the front of the melt pool, whereas the wire is located at the tail of the melt pool in Fig. 3d (the criterion for classifying the front and the tail of the melt pool is relative to the deposition direction). Despite the same process parameters, the wire is stuck in the solidified material and the process has to be aborted when

using the back feeding. As depicted in Fig. 4, it is assumed that the geometry of the melt pool generated by using front feeding and back feeding is the same when using the same process parameters. If the wire is located at the tail of the melt pool, the wire is further away from the laser beam than that located at the front of the melt pool. It experiences less irradiation or preheating by laser beam. Hence, the wire might be not sufficiently melted leading to being stuck in the track.

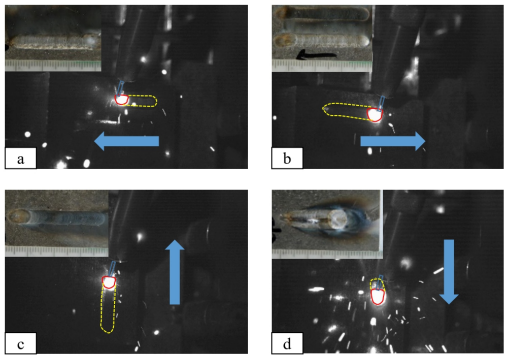

Fig. 3. Images captured during LMD process using (a) side feeding (l-r); (b) side feeding (r-l); (c) front feeding; (d) back feeding. The melt pool and the wire are marked with red and blue lines, respectively. The already deposited material is marked by yellow dashed lines. Images of deposited single track are inserted on the left top corner. Because of the mounting position of the high-speed camera, the left and the right sides in this figure are reversed as those illustrated in Fig. 2. Laser power: 4000 W, wire feed rate: 4 m/min, scan speed: 1 m/min.

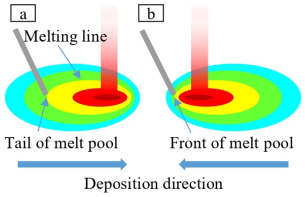

Fig. 4. Illustration of the interaction between wire and laser beam as well as the melt pool when the wire is (a) at the tail and (b) at the front of the melt pool. The elliptical geometry and the distribution of temperature field in melt pool are reported in [15].

The surface morphology of deposited tracks using different wire feed directions is inserted in Fig. 3. The single tracks in Fig. 3(a, b) have a comparable bright surface morphology, while the surface is covered by a dark film when using front feeding (Fig. 3c). The vaporized Zn and Mg are oxidized in air and fall onto the surface of the deposited track forming the powder-like dark film, which can be removed by interlayer cleaning. This is also observed in WAAM processing of AA7055 alloy [10]. Considering the flow direction of argon from the wire nozzle and the deposition direction, except using front feeding, the oxidized Zn and Mg particles are blown away from the deposited tracks, so the tracks exhibit a bright surface. It is noticed that a single dark line is located in the middle of the deposited track when using back feeding in Fig. 3d. The dark line cannot be removed by interlayer cleaning. The formation of this dark line might be attributed to the sinter of the oxidized Zn and Mg particles.

The cross-sections of the single tracks using different wire feed directions are shown in Fig. 5. The cross-section of the track deposited using back feeding is not prepared because the unmelted wire is stuck in the track. The three tracks are free of pores.

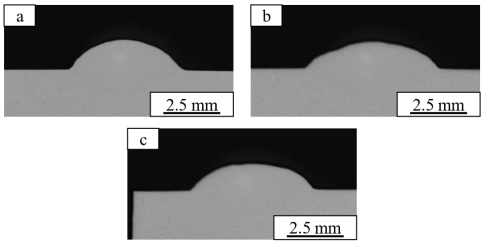

Fig. 5. Cross-sectional view of the single tracks using (a) wire feeding (l-r); (b) wire feeding (r-l); (c) front feeding. The process parameters are the same as in Fig. 3.

The cross-sectional geometries of single tracks slightly deviate from each other when using three wire feed directions (l-r, r-l, front) (Table. 2), while all the three tracks are free of pores. This indicates that the porosity level is mainly dependent on the process parameters. The wire feed direction has noticeable effects on the track geometry but no significant effect on the porosity level.

Table 2. Geometry of tracks deposited using different wire feed directions (mm).

	(l-r)	(r-l)	front
Width	4.95	5.70	5.29
Height	1.28	1.11	1.14
Depth	0.98	1.20	0.94

3.2. Single track deposition

The parameter study begins from the single track deposition to select the parameters for the fabrication of the thin-walled structure. The investigated parameter range is listed in Table. 3. The quality of the deposited tracks is evaluated by the geometric uniformity and the cross-sectional porosity level.

Table 3. Investigated process parameters for the single track deposition.

Laser power (W)	Scan speed (m/min)	Wire feed speed (m/min)
2000 - 4000	1 – 3.5	2 - 10

Three typical geometries are shown in Fig. 6: insufficient melting, uneven geometry, and uniform morphology. Fig. 7 demonstrates four classes of porosity level: low porosity, high porosity, crack, and poor wetting. The process parameters for tracks with uniform morphology and low porosity are chosen for building the thin-walled structure.

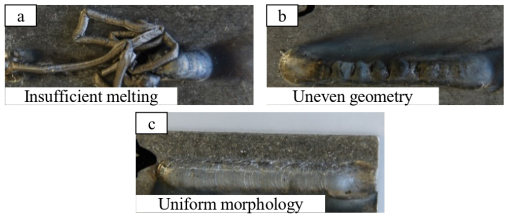

Fig. 6. Classification of different track geometries: (a) insufficient melting, laser power: 3500 W, wire feed rate: 9 m/min, scan speed: 1 m/min; (b) uneven geometry, laser power: 4000 W, wire feed rate: 10 m/min, scan speed: 1.5 m/min; (c) uniform morphology, laser power: 4000 W, wire feed rate: 4 m/min, scan speed: 1 m/min.

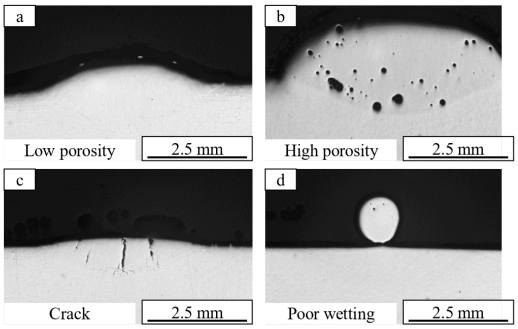

Fig. 7. Classification of different cross-sections: (a) low porosity, laser power: 4000 W, wire feed rate: 2 m/min, scan speed: 1 m/min; (b) high porosity, laser power: 4000 W, wire feed rate: 6 m/min, scan speed: 1 m/min; (c) crack, laser power: 3500 W, wire feed rate: 2 m/min, scan speed: 3 m/min; (d) poor wetting, laser power: 2000 W, wire feed rate: 2 m/min, scan speed: 2 m/min. Low porosity represents cross-sectional porosity level lower than 0.5 %.

The k value and the specific energy input E_M in wire-based LMD are adopted to represent the overall influences of process parameters, as shown in (1) and (2) [16]:

$$k = \frac{v_w}{v_s}, \tag{1}$$

where v_w is the wire feed speed and v_s is the scan speed.

$$E_M = \frac{P}{m}, \tag{2}$$

where P is the laser power. The parameter m is the mass flow of the wire (g/min) and it is calculated as

$$m = \frac{v_w \pi d_x^2 \rho}{4}, \tag{3}$$

where d_x is the wire diameter and ρ is the wire density (2.81 g/cm^3 [17]).

Fig. 8 reveals the influences of the process parameters on the cross-sectional porosity of single tracks. The single tracks with high porosity levels are deposited with lower specific energy. Most of the pores are spherical, so they might be gas pores rather than the lack of fusion pores [18]. The tracks with low porosity level and the tracks with hot cracks are distributed in the regime of higher energy input. The amount of fluid with low viscosity increases with higher energy input and the resultant higher temperature [19]. Hence, it is easier for the gas trapped in the melt pool to escape leading to a lower porosity level. Hot cracks tend to initiate in the tracks processed with lower k values. It is noticed that cross-sections with cracks also exhibit a low porosity level. However, the lower k value increases the sensitivity to hot cracking.

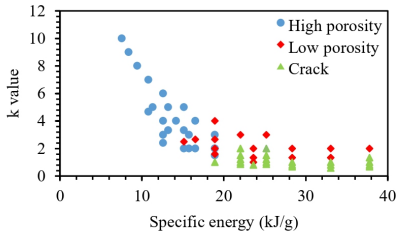

Fig. 8. Correlation among the specific energy, k value, and the cross-sectional porosity level.

3.3. Deposition of thin-walled structure

The thin-walled structures are bi-directionally deposited. The process parameters capable of producing crack-free single tracks with low porosity levels are selected for building the thin-walled structure. Three process strategies are employed to avoid heat accumulation as the deposition proceeds, which can cause uneven wall thickness along the building direction.

The three process strategies are: decreasing laser power with increasing number of layers and then processing with a constant laser power (continuous process); processing with constant laser power and interlayer cooling for 1.5 min (discontinuous process); processing with constant laser power and interlayer cooling to room temperature (discontinuous process, time interval about 10 min, the interlayer temperature is measured with a calibrated infrared pyrometer). In the first two strategies, the layer height set in the program is determined by averaging the height of a preliminary 30-layer-deposition. In the third strategy, the layer height is measured after each deposition and set in the program adaptively.

The specimen without hot cracks and with the lowest porosity level is achieved by using interlayer cooling to room temperature. The cross-section and the hardness evolution of this specimen are shown in Fig. 9. The cross-sectional porosity level is 0.29 % and no hot cracks are observed. The majority of pores are distributed in the lower part of the cross-section. With increasing number of deposited layers, the upper part is almost free of porosity. The deposition layers in the lower part have a higher cooling rate and a shorter lifetime of the melt pool because of the rapid heat conduction to the substrate, which could increase the possibility of the entrapment of gas pores. As the building height increases, the heat conduction conditions become

stable and the lifetime of the melt pool is extended resulting in lower porosity in the upper part. The wall thickness along the building direction is uniform. The layer boundaries can be observed on the etched cross-section (Fig. 9b). The layer height becomes stable after about 10 layers. Large columnar grains indicate epitaxial grain growth as also reported in [20].

The thin wall structure has an average hardness of 112.1 ± 6.2 $HV_{0.1}$ (Fig. 9c). From the top to the middle of the cross-section, the hardness first increases and then becomes stable. At the vicinity of the substrate, the first several deposition layers exhibit the highest hardness. At the top, the last layer does not experience partial remelting and heat treatment induced by subsequent deposition, which leads to the lowest hardness. The uniform distribution of hardness in the middle indicates a stable process. The first several layers are located in the dilution zone. The substrate in a peak-aged state in this area is remelted. Moreover, the heat conduction conditions differ from the layers away from the substrate [21]. The substrate can act as a heat sink causing a higher cooling rate and various precipitation dynamics of the second phase.

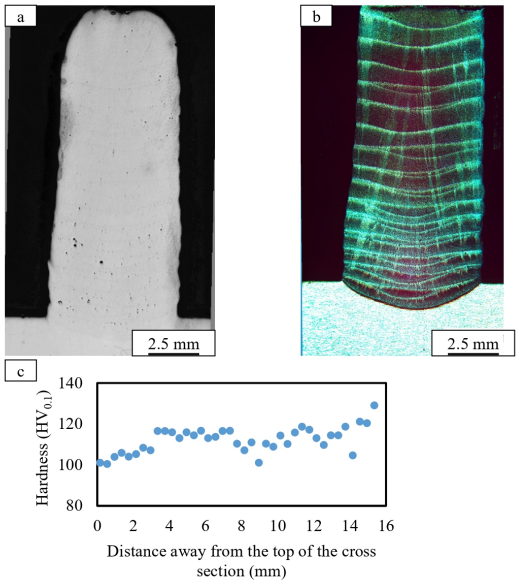

Fig. 9. Cross-section of the (a) non-etched and (b) etched thin-walled structure. (c) Hardness evolution along the building direction. The thin-walled structure is built with interlayer cooling to room temperature and constant laser power. Laser power: 4000 W; scan speed: 1.5 m/min; wire feed rate: 4 m/min; number of deposited layers: 31 layers. Layer thickness set in the program: 1st layer 1.1 mm; 2nd layer: 0.3 mm; 3rd layer: 0.7 mm; 4th and 5th layer: 0.6 mm; 6th – 31st layer: 0.5 mm.

The precipitates are distributed along grain boundaries and inside grains (Fig. 10). The segregation of secondary phases along grain boundaries could contribute to intergranular cracking [22]. Microcracks can be observed in Fig. 10a. The large columnar grains are aligned along the build direction, since grains prefer to grow along the heat flow direction during solidification [23]. It contribute to a strong texture and anisotropy in LMD-produced specimens [24]. The chemical composition of the matrix and the precipitates are listed in Table. 4. The precipitates are enriched with Mg, Cu, and Zn. The content of Mg, Cu, and Zn in precipitates increases first and then decreases along the build direction. Besides, the sight fluctuation of Si content is also observed. On the one hand, it could be correlated to the complicated thermal cycles during the LMD process. On the other hand, it could also be attributed to the measurement error. The content of the volatile elements Mg and Zn decreases in the matrix as the deposition proceeds. The high process temperature leads to slight evaporation of Mg and substantial evaporation of Zn.

Table 4. Chemical composition of the matrix (mat.) and precipitates (pre.) (in wt. %). The measuring locations correspond to that numbered in Fig. 9. Locations 1, 2 are matrix and locations 3, 4 are precipitates. The content of elements is averaged by the measurement in two locations.

		Al	Mg	Si	Ti	Cr	Fe	Cu	Zn
Top	Mat.	94.1	2.0	0.2	0.1	0.3	0.1	0.4	2.9
	Pre.	72.7	7.1	0.1	0	0.1	0.1	8.4	11.5
Mid	Mat.	92.6	2.3	0.4	0.1	0.2	0	0.6	3.7
	Pre.	55.3	11.5	0.2	0	0.1	0.9	14.9	17.2
Bot	Mat.	91.2	2.6	0.1	0.1	0.2	0	0.9	4.9
	Pre.	64.9	7.4	0.8	0	0.2	1.7	10.1	14.8

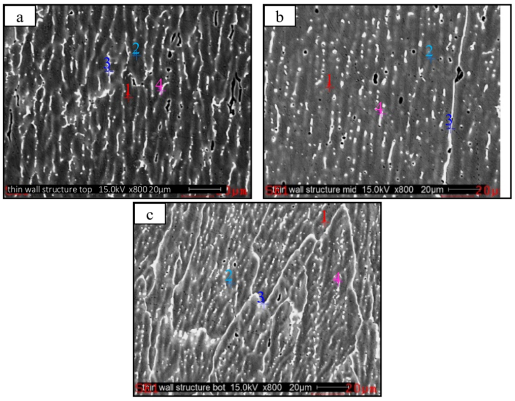

Fig. 10. SEM images at (a) the top, (b) the mid, and (c) the bottom of the thin-walled structure.

4. Conclusions

The effects of wire feed direction on the lateral LMD process and the properties of deposited single tracks are studied using the high-speed camera. The optimal process window of lateral LMD processing of AA7075 alloy is investigated. The following conclusions can be drawn:

- Under the same process parameters, the wire feed direction can affect the geometry of single tracks, but it does not influence the porosity level. An additional interlayer cleaning is required when using front feeding. The wire might be stuck in track causing the process aborted when using back feeding.
- The k value, which is the ratio of wire feed speed and scan speed, is a critical parameter affecting the initiation of

cracks in the LMD process. Setting the k value over a threshold has been proved as an effective method to prevent cracking.

- By the parameter optimization and the introduction of different process strategies, a thin-walled structure with a minimum porosity level of 0.29 % and without macrocracks can be produced. It has a uniform thickness along the building direction with the average hardness of 112.1 ± 6.2 $HV_{0.1.}$
- Mg-, Zn-, and Mg-rich secondary phases are distributed along grain boundaries and inside grains. Due to the high temperature during the process, the content of Mg and Zn decreases because of the evaporation of the volatile elements.

Acknowledgements

The authors would like to thank R. Dinse and S. Riekehr for their assistance during laser metal deposition as well as F. Dorn and Dr. V. Ventzke for their support during metallographic preparation and microstructural characterization.

References

[1] Wong, K.V., Hernandez, A., 2012. A review of additive manufacturing, International Scholarly Research Notices 2012, p. 208760.
[2] Akinlabi, E.T., Akinlabi, S.A., 2016. Advanced coating: Laser metal deposition of aluminium powder on titanium substrate, in "Proceedings of the World Congress on Engineering. Vol. II" S. I. Ao, L. Gelman, D. W. L. Hukins, A. Hunter, A. M. Korsunsky, Editors. Newswood Limited, London, p. 863-868.
[3] Gasser, A., Backes, G., Kelbassa, I., Weisheit, A., Wissenbach, K., 2010. Laser metal deposition (LMD) and selective laser melting (SLM) in turbo-engine applications, Laser Technik Journal 2, p. 58-63.
[4] Gradl, P.R., Protz, C.S., Wammen, T., 2019. Additive manufacturing and hot-fire testing of liquid rocket channel wall nozzles using blown powder directed energy deposition inconel 625 and JBK-75 Alloys, in "AIAA Propulsion and Energy 2019 Forum" T. I-P. Shih, Editor. American Institute of Aeronautics and Astronautics, Indianapolis, p. 4362.
[5] Bambach, M., Sizova, I., Silze, F., Schnick, M., 2018. Comparison of laser metal deposition of Inconel 718 from powder, hot and cold wire, Procedia CIRP 74, p. 206-209.
[6] Froend, M., Riekehr, S., Kashaev, N., Klusemann, B., Enz, J., 2018. Process development for wire-based laser metal deposition of 5087 aluminium alloy by using fibre laser, Journal of Manufacturing Processes 34, p. 721-732.
[7] Lee, W.-S., Sue, W.-C., Lin, C.-F., Wu, C.-J., 2000. The strain rate and temperature dependence of the dynamic impact properties of 7075 aluminum alloy, Journal of Materials Processing Technology 100, p. 116-122.
[8] Stopyra, W., Gruber, K., Smolina, I., Kurzynowski, T., Kuźnicka, B., 2020. Laser powder bed fusion of AA7075 alloy: Influence of process parameters on porosity and hot cracking, Additive Manufacturing 35, p. 101270.
[9] Benoit, M., Sun, S., Brandt, M., Easton, M., 2021. Processing window for laser metal deposition of Al 7075 powder with minimized defects, Journal of Manufacturing Processes 64, p. 1484-1492.
[10] Dong, B., Cai, X., Lin, S., Li, X., Fan, C., Yang, C., Sun, H., 2020. Wire arc additive manufacturing of Al-Zn-Mg-Cu alloy: microstructures and mechanical properties, Additive Manufacturing 36, p. 101447.
[11] Li, S., Zhang, L.-J., Ning, J., Wang, X., Zhang, G.-F., Zhang, J.-X., Na, S.-J., 2020. Microstructures and mechanical properties of Al–Zn–Mg aluminium alloy samples produced by wire+ arc additive manufacturing, Journal of Materials Research and Technology 9, p. 13770-13780.
[12] Kelbassa, J., Gasser, A., Bremer, J., Pütsch, O., Poprawe, R., Henrich Schleifenbaum, J., 2019. Equipment and process windows for laser metal deposition with coaxial wire feeding, Journal of Laser Applications 31, p. 022320.
[13] Zou, X.-L., Hong, Y., Chen, X.-H., 2017. Evolution of second phases and mechanical properties of 7075 Al alloy processed by solution heat treatment, Transactions of Nonferrous Metals Society of China 27, p. 2146-2155.
[14] Heralic, A., 2012. Monitoring and control of robotized laser metal-wire deposition. Doctoral Thesis. Chalmers University of Technology, Göteborg.
[15] Zhou, S., Su, Y., Wang, H., Enz, J., Ebel, T., Yan, M., 2020. Selective laser melting additive manufacturing of 7xxx series Al-Zn-Mg-Cu alloy: Cracking elimination by co-incorporation of Si and TiB2, Additive Manufacturing 36, p. 101458.
[16] Frönd, M., 2021. Process Development and Metallurgical Characterization of Wire-based Direct Energy Deposition for Aluminium-Magnesium Alloys. sierke VERLAG-Sierke WWS GmbH, Göttingen.
[17] Canakci, A., Varol, T., 2014. Microstructure and properties of AA7075/Al–SiC composites fabricated using powder metallurgy and hot pressing, Powder Technology 268, p. 72-79.
[18] Ng, G. K. L, Jarfors, A. E. W., Bi, G., Zheng, H. Z., 2009. Porosity formation and gas bubble retention in laser metal deposition, Applied Physics A 97, p. 641-649.
[19] Wang, L.-Z., Wang, S., Wu, J.-J., 2017. Experimental investigation on densification behavior and surface roughness of AlSi10Mg powders produced by selective laser melting, Optics & Laser Technology 96, p. 88-96.
[20] Thijs, L., Kempen, K., Kruth, J.-P., Van Humbeeck, J., 2013. Fine-structured aluminium products with controllable texture by selective laser melting of pre-alloyed AlSi10Mg powder, Acta Materialia 61, p. 1809-1819.
[21] Dinda, G., Dasgupta, A., Bhattacharya, S., Natu, H., Dutta, B., Mazumder, J., 2013. Microstructural characterization of laser-deposited Al 4047 alloy, Metallurgical and Materials Transactions A 44, p. 2233-2242.
[22] Yan, L., Fan, J., 2016. In-situ SEM study of fatigue crack initiation and propagation behavior in 2524 aluminum alloy 110, Materials & Design, p. 592-601.
[23] Wei, H., Mazumder, J., DebRoy, T., 2015. Evolution of solidification texture during additive manufacturing, Scientific Reports 5, p. 1-7.
[24] Froend, M., Ventzke, V., Dorn, F., Kashaev, N., Klusemann, B., Enz, J., 2020. Microstructure by design: An approach of grain refinement and isotropy improvement in multi-layer wire-based laser metal deposition, Materials Science and Engineering: A 772, p. 138635.

Paper 3: M. Wang, V. Ventzke, N. Kashaev, Wire-based laser directed energy deposition of AA7075: effect of process parameters on microstructure and mechanical properties, Journal of Materials Research and Technology 21 (2022) 388-403.

This published paper was incorporated as Chapter 4.4 (with permission from Elsevier).

JOURNAL OF MATERIALS RESEARCH AND TECHNOLOGY 2022;21:388–403

Available online at www.sciencedirect.com

jmr&t Journal of Materials Research and Technology

journal homepage: www.elsevier.com/locate/jmrt

Original Article

Wire-based laser directed energy deposition of AA7075: effect of process parameters on microstructure and mechanical properties

Mengjie Wang[*], *Volker Ventzke*, *Nikolai Kashaev*

Institute of Materials Mechanics, Department of Laser Processing and Structural Assessment, Helmholtz-Zentrum Hereon. Max-Planck-Str. 1, D-21502 Geesthacht, Germany

ARTICLE INFO

Article history:
Received 22 August 2022
Accepted 13 September 2022
Available online 17 September 2022

Keywords:
Laser directed energy deposition
AA7075 wire
Process development
Mechanical properties
Microstructure
Temperature field simulation

ABSTRACT

The process development for wire-based laser directed energy deposition of AA7075 is studied. Thin-wall structures are produced to investigate the process-microstructure-mechanical performance relationship. By optimizing the process parameters and building strategies, the minimal porosity level of 0.8% and 0.3% can be achieved in the continuous and discontinuous building strategies, respectively. The porosity level exhibits a primary dependence on the specific energy and a secondary dependence on the ratio between wire feed rate and laser scan speed. Thin-wall structures show an average hardness of 115 $HV_{0.1}$. In two optimized building strategies, the ultimate tensile strength of 400 MPa is achieved without the cost of ductility (fracture strain of 9.2%). Large columnar grains with preferential orientation and the distribution of secondary phases relative to the loading direction during tensile tests contribute to superior mechanical properties.

1. Introduction

Additive manufacturing (AM) as advanced technology has been academically researched for a long time. It is playing an increasingly important role in the automotive, aerospace, and medical fields [1]. Recent works concentrate on broadening applicable materials [2] and industrialization, such as improvement of productivity and building an automated production chain [3]. Laser powder bed fusion (LPBF) and directed energy deposition (DED) are two popular AM technologies in processing metals. In LPBF, powders as feedstock are spread in a building platform and selectively melted by the laser. It can produce parts with complex geometries. However, the space of the platform and processing chamber restricts the manufacturing of large parts [4]. In contrast to LPBF, there is no such limitation in DED. The feedstock is fed through a nozzle and melted by external energy input, such as laser beam (laser directed energy deposition, L-DED) and electric arc (wire and arc additive manufacturing, WAAM). Both powder and wire are optional feedstock in L-DED. Powder-based L-DED can produce high-precise parts with small size, while wire-based L-DED has an almost 100% material utilization rate [5] and can provide a high deposition rate [6].

* Corresponding author.
E-mail address: mengjie.wang@hereon.de (M. Wang).
https://doi.org/10.1016/j.jmrt.2022.09.051

Aluminum alloys are lightweight materials with a high density-strength ratio [7]. Although there are numerous available Al alloys designed for specific scenarios, such as casting and wrought Al alloys, the applicable material spectrum in AM is still limited [8]. Al alloys of 7XXX series as precipitation-strengthening Al alloys exhibit high strength [9]. The precipitation dynamics of 7XXX alloys during heat treatment are complicated. T6 heat treatment (solid solution + quenching + artificial ageing) is normally conducted to improve the properties of 7XXX alloys [10,11]. The main strengthening precipitate is $MgZn_2$ (also called the η phase) [12]. The precipitation consists of four phases during ageing: saturated solid solution, segregation and formation of solute clusters known as Guinier-Preston (GP) zone, precipitation as η' phase, growth and coarsening of η' phase to η phase [9]. GP zone and η' phase are formed at the early stage of ageing. As ageing proceeds, the GP zone can act as nuclei for the η' phase increasing the number density of the η' phase and enhancing the strength. Further extending the holding time at high temperatures leads to the transformation of the η' phase to the η phase and the deterioration of strength. The highest strength is reached at the peak-aged stage, while the resistance to stress corrosion cracking (SCC) is degraded [13]. Multi-stage ageing has been developed to improve corrosion resistance and maintain high strength [13].

Regardless of these advantages of 7XXX alloys, they are still not recognized as an applicable material in AM. There are several challenges in AM processing 7XXX alloys needed to be overcome, e.g. oxidation, porosity formation, and cracking susceptibility. Al and alloying elements in 7XXX alloys are sensitive to oxidation [14]. In AM, the oxidation could increase the possibility of porosity formation since the oxides cannot be sufficiently wetted by the liquid Al [15]. Besides, the oxide particles in the AM-produced parts could degrade the fatigue performance, especially when these particles are distributed on the surface or sub-surface regions [15,16]. In powder-based AM, the flowability of powder particles could be reduced because of oxidation [14].

Porosity in AM-produced parts can be classified into two types, i.e. gas pores and lack-of-fusion pores [17]. Gas pores exhibit a spherical morphology, while the morphology of lack-of-fusion pores is irregular. Lack-of-fusion pores are periodically located in parts, e.g. in the overlap area between adjacent deposition tracks. The formation of lack-of-fusion pores can be attributed to inappropriate process parameters, such as fast scanning speed and high powder feed rate [17]. The origins of gas pores can be summarized in several aspects. First, there are significant solubility differences between hydrogen in liquid and solid Al alloys [18]. Melted Al can react with moisture in the surrounding atmosphere generating hydrogen [19]. Due to the drop in solubility during solidification, supersaturated hydrogen is either stored in the lattice, dislocations, grain boundaries, etc., or precipitates as gas trapped in solidified materials [18]. Second, the evaporation of volatile elements of 7XXX alloys could be another factor [20]. If there is insufficient time for vapor to escape, it could be trapped in melt pools leading to the formation of gas pores. Third, in powder-based AM, gas pores could be retained inside powder particles during gas atomization [21], which are also potential origins of porosity in AM-produced parts. Moreover, the contamination of feedstock [22] or substrates [23] and the entrapment of shielding gas [17] are also possible reasons for the formation of gas pores. There is another type of porosity correlated to the evaporation of alloying elements, i.e. keyhole pores [24]. Under excessive energy input, as the recoil pressure caused by evaporation exceeds the surface tension and hydrostatic pressure in melt pools, keyhole-mode welding is activated [25]. Keyhole pores are normally characterized by large size and irregular geometry [26,27].

Cracking is one of the most common and difficult problems in AM processing 7XXX alloys. Cracks that occur in AM-produced parts can be categorized into solidification cracks and liquation cracks [28]. Solidification cracks are initiated during solidification caused by the insufficient backfilling of melt to the interdendritic regions [29]. In AM, previously solidified layers experience reheating during subsequent deposition. Eutectic phases with low melting points could be partially melted forming a liquid film along grain boundaries and broken under tensile residual stress resulting in liquation cracks [30]. 7XXX alloys have a large solidification range and the resultant long interdendritic region, which is difficult for melt to sufficiently backfill the shrinkage during solidification [31]. High energy density input in laser processing contributes to the formation of high-temperature gradient and residual stress [32], which further promotes the cracking in AM-produced parts. Two methods have been implemented trying to prevent and diminish cracking in AM processing 7XXX alloys, i.e. optimizing process strategies (preheating substrate, changing parameters, alternating scanning strategies, adopting hot isostatic pressing as post-treatment) [30] and modifying raw materials (blending additive into 7XXX alloys) [33,34]. Cracks can be eliminated only by modifying material composition in laser-based AM. Two kinds of mechanisms for eliminating cracks by additives are introduced: additives like Si can enhance the flowability of melt and improve the compensation for shrinkage during solidification, while additives like Zr and TiB_2 can act as nuclei for primary Al grains to refine grains enhancing the cracking resistance [33,34]. The appropriate process window and strategies for pure 7XXX alloys are still not established.

Previous researches in AM processing 7XXX alloys focus on LPBF, WAAM, and powder-based L-DED. The knowledge of wire-based L-DED in processing 7XXX alloys is still empty. Given the advantages of wire-based L-DED and 7XXX alloys, the appropriate process development is highly in demand. In the present paper, process parameters are optimized and different building strategies are used to reduce the porosity level and prevent cracking. The microstructure is characterized and the mechanical properties are tested. Thermal analysis is implemented via FEM simulation trying to better elaborate the microstructure formation. The correlation of process-microstructure-mechanical properties is revealed within this work.

2. Materials and methods

2.1. Experimental

2.1.1. Wire-based laser directed energy deposition

The feedstock is the AA7075 wire with a diameter of 1.2 mm supplied by Drahtwerk Elisental W. Erdmann GmbH & Co. The

chemical composition of AA7075 is listed in Table 1. Rolled AA7075 sheets with a geometry of 100 mm × 50 mm x 15 mm were used as substrates. During processing, the substrate was clamped on a working table made of AA5087. The feedstock was melted by the laser with a core-ring profile (TruDisk 4001, TRUMPF SE + Co. KG). According to the set of the core-ring ratio, the laser energy input is distributed in the core and ring area separately. The inner core and the outer ring have a diameter of 100 μm and 400 μm in the focal position. Preliminary study indicated that the core-ring ratio has no significant influence on the sufficient melting and the integrity of the produced specimens as long as the core-ring ratio exceeds a threshold. Hence, the core-ring ratio was kept constant at 15% in the present study. The laser beam spot diameter located on the substrate was 1.5 mm by a positively defocusing of 36.14 mm (laser focus above the substrate). The deposition path was controlled by a CNC machine. Argon as shielding gas was used to protect the material from oxidation and blow the volatilized metal elements away from the melt pool. The configuration of the apparatus is introduced in [35].

The process parameters for building thin-wall structures were selected by evaluating the integrity of single tracks in the previous study [37]. Two building strategies were adopted in the thin-wall structures, i.e. continuous and discontinuous processes. In the continuous process, the laser power declined with the increasing layer number, and no interlayer-cooling was inserted between two adjacent layers. However, to abort the process instantly in case of processing errors and adjust process parameters between layers, the process was paused after each layer deposition and the program was started again after inspecting whether the surface defects were present. It took about 40 s. In the discontinuous process, either an interlayer-cooling time of 1.5 min was set between layers, or the solidified layer was cooled to room temperature before the next deposition. The laser power was kept unchanged in the discontinuous process. The workflow for the process development is sketched in Fig. 1.

2.1.2. *Characterization*

L-DED-produced specimens were cut in the middle along the length direction and ground, as well as polished for the cross-sectional observation under an optical microscope (OM, Leica DMI 5000M). Barker's etchant was used to reveal the microstructure. Scanning electron microscope (SEM, Jeol JSM-6490LV) and connected energy-dispersive X-ray (EDX, EDAX Genesis) were employed to analyze the distribution and the chemical composition of the secondary phases in as-built specimens. Besides, the texture and the grain orientation as well as the grain size were determined by electron backscatter diffraction (EBSD) to disclose the internal process-microstructure-properties relationship (effective scan field area: 1875 μm × 1875 μm, working distance: 13 mm, acceleration voltage: 25 kV, tilt angle: 70°). The scanned area was located in the middle of the thin-wall structure, which corresponds to the gauge area of the tensile specimens.

Hardness measurement was conducted with a load of 100 g and a load time of 10 s. The indentation points were aligned from 10 mm to 18 mm away from the substrate surface with a distance increment of 0.4 mm. These indentations were placed in the gauge area of tensile bars, which ensures a plausible correlation between the hardness and the tensile properties. The tensile tests were implemented under the strain rate of 1/s. Three tensile specimens were extracted along the thickness direction in the middle of the thin-wall structures, as shown in Fig. 2a. The length direction of tensile specimens is parallel to the building direction. The geometry of the tensile specimens is sketched in Fig. 2b.

Table 1 – Chemical composition of AA7075 Al alloy provided in [36] (in wt. %).

Al	Zn	Mg	Cu	Mn	Ti	Cr	Si	Fe
Bal.	5.2	2.1	1.5	0.3	0.2	0.2	0.2	0.2

3. Results and discussion

3.1. *Process development*

The process parameters for building thin-wall structures in L-DED processing AA7075 were selected based on the single-track deposition. According to preliminary experiments [37], the porosity level and the cracking sensitivity were significantly dependent on the k value and specific energy. The k value is the ratio between wire feed rate and laser scan speed. Specific energy is the ratio between laser power and fed wire mass per unit time [35]. Defects in L-DED produced specimens are large obstacles hindering the wide application of high-strength Al alloy in AM. Porosity and cracks are detrimental to mechanical performances. By initially screening process parameters from single tracks, further optimization methods, such as changing building strategies and process parameters, were implemented to reduce the porosity level and prevent cracking.

Thin-wall structures with 30 layers were investigated to determine the decreasing gradient of laser power during the layer-by-layer deposition since the heat conduction conditions change as the deposition proceeds [38]. In the continuous building strategy, if the laser power is kept constant, the heat accumulation could increase the size of melt pools in higher deposition layers leading to non-uniform thickness along the building direction. Besides laser power (P), laser scan speed (v_s) and wire feed rate (v_w) are also optimized to reduce porosity level and prevent cracking. Specific energy and k value have been proven as effective indicators to represent the effects of process parameters on the porosity level in the single-track investigation. The laser power changes in the first several layers and then keeps constant (before the 10^{th} layer) in building thin-wall structures. Hence, specific energy is calculated for each layer in the first 10 layers and used to evaluate the effects on the porosity level in thin-wall structures. According to Fig. 3a, b, under the same k value, the lowest porosity level is achieved when processing is performed with the highest specific energy. If the specific energy keeps unchanged, increasing the k value can reduce the porosity level, see Fig. 3c. Comparing the thin-wall structures processed with different magnitudes of the specific energy and k value (Fig. 3d), the porosity level is dominantly affected by the specific energy. It suggests that in terms of the effects

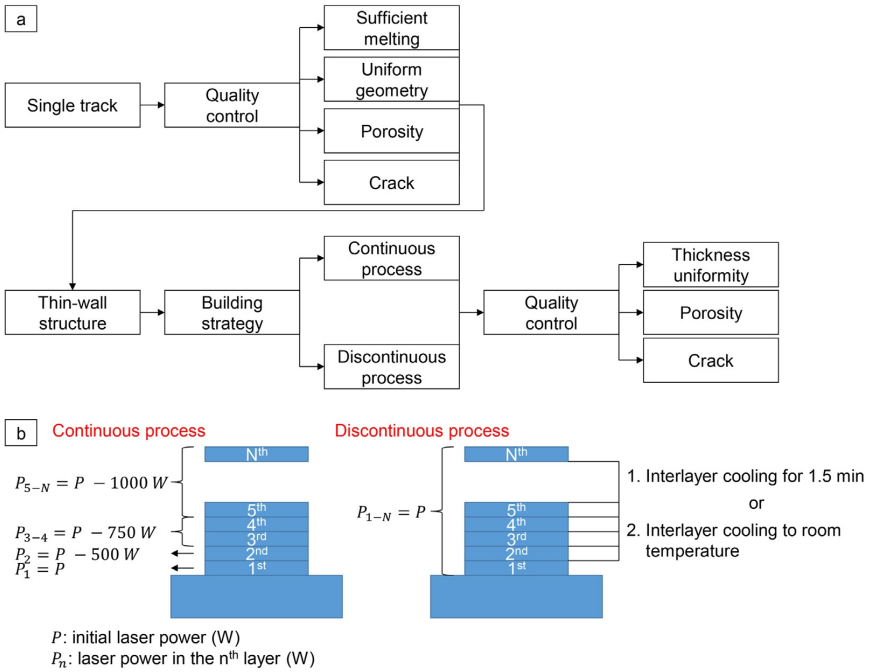

Fig. 1 – (a) Workflow of the process development. (b) Illustration of the continuous and discontinuous building strategies.

on porosity level, the specific energy is the primary factor, while the k value is the secondary factor.

In the continuous building strategy, three thin-wall structures with 30 layers produced with optimized parameters are shown in Fig. 4a, c, e. The minimum porosity level of 0.8% is achieved in the case of parameter set 1. The pores can be classified as gas pores because of the random distribution on the cross-section and the nearly spherical morphology [17]. No cracks and no lack-of-fusion pores are observed in the cross-sections. It is noticed that the porosity level increases as the deposited layer number increases from 30 layers to 60 layers using parameter sets 1 and 3, while specimens produced with parameter set 2 maintain a relatively stable porosity level. In Fig. 4f, a cluster of large pores is observed in the upper part. They are located near the side surface of the wall structure. During L-DED processing, the high-temperature gradient inside the melt pool leads to the spatial gradient of surface tension contributing to the formation of the Marangoni effect [39]. It drives the melt pool and bubbles to flow from the center toward the edges. The magnitude of the Marangoni-driven force is significantly higher than the buoyancy force of bubbles [17]. Hence, gas pores could be retained in the melt pool. Higher laser scan speed enhances the temperature gradient [40] leading to a more substantial Marangoni effect. As the distance from the substrate increases, the heat conduction is weakened leading to heat accumulation for a short time before reaching a stable process, which increases the possibility of the evaporation of volatile elements. In summary, the formation of large pores at the edges of wall structures in higher layers could be attributed to the combined effects of the Marangoni effect and heat accumulation.

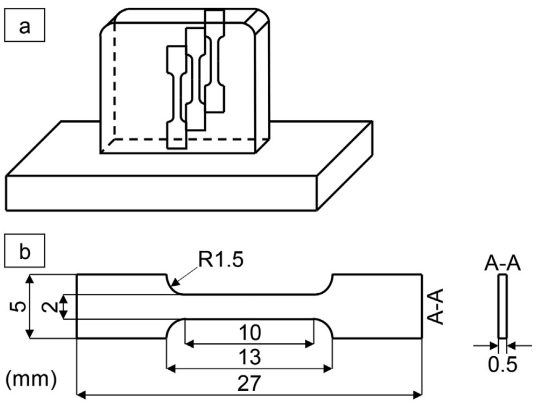

Fig. 2 – (a) Alignment of tensile specimens in the thin-wall structure. (b) Geometry of tensile specimens.

In the discontinuous building strategy, the minimal porosity of 0.3% can be realized in a crack-free specimen when the interlayer cooling to room temperature is applied, as shown in Fig. 4g. As the deposition proceeds to the 52nd layer, the specimen exhibits a porosity level of 1%. Moreover, some cracks are observed in the cross-section with a propagation direction along the building direction. In the single-track

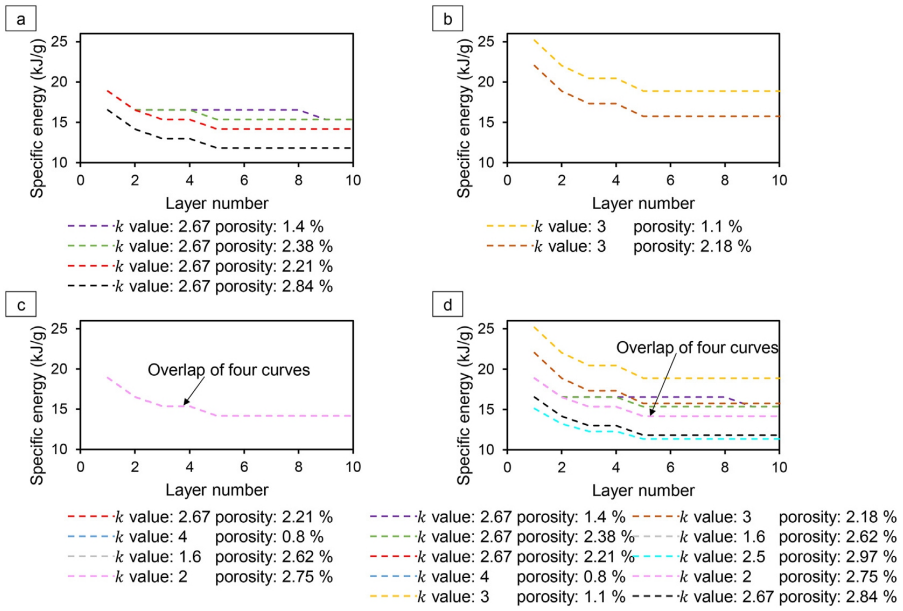

Fig. 3 – Correlation between specific energy and *k* value as well as porosity level: (a) porosity – specific energy relation under constant *k* value of 2.67; (b) porosity – specific energy relation under constant *k* value of 3; (c) porosity- *k* value relation under constant specific energy; (d) porosity – specific energy – *k* value relation under all parameter sets.

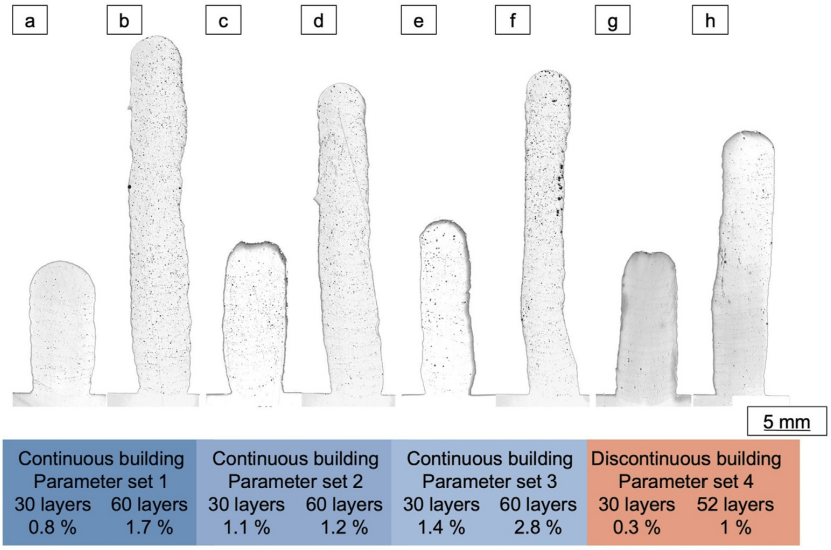

Fig. 4 – Cross-sectional views of specimens processed with optimized parameters. Porosity levels are noted below images. In the continuous building strategy, (a) and (b) were produced with parameter set 1 (P: 1st layer – 4000 W, 2nd layer – 3500 W, 3rd – 4th layer – 3250 W, remained layers – 3000 W; v_s: 1 m/min; v_w: 4 m/min). (c) and (d) were produced with parameter set 2 (P: 1st layer – 4000 W, 2nd layer – 3500 W, 3rd – 4th layer – 3250 W, remained layers – 3000 W; v_s: 1 m/min; v_w: 3 m/min). (e) and (f) were produced with parameter set 3 (P: 1st layer – 4000 W, 2nd – 8th layer – 3500 W, remained layers – 3250 W; v_s: 1.5 m/min; v_w: 4 m/min). In, the discontinuous building strategy, (g) and (h) were produced with parameter set 4 (P: 4000 W, v_s: 1.5 m/min; v_w: 4 m/min, interlayer cooling to room temperature).

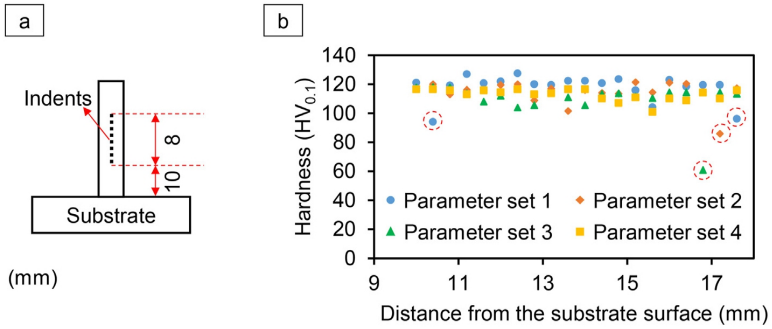

Fig. 5 – (a) Sketch of the position of indentation points in the cross-section. (b) Hardness profile of specimens produced with four parameter sets. Abnormal indents are marked with dotted circles.

investigation, some tracks are fully dense. Continuous processing could result in heat accumulation promoting the formation of pores. Using interlayer cooling aims to decline the temperature and try to repeat the same melting mode and solidification conditions. Indeed, the interlayer cooling succeeds in reaching a lower porosity level. However, 0.3% and 1% porosity levels cannot be eliminated. It indicates that the heat transfer conditions for building layers on a previously cooled deposition layer and a cooled substrate are different.

3.2. *Mechanical properties*

The hardness was measured in the middle of four thin-wall structures (Fig. 4b, d, f, h) along the building direction. 20 indentation points were located in the area of 10–18 mm away from the substrate, see Fig. 5a. Except for indentation points with abnormal low hardness values in each parameter set, which could be resulted from the pores underneath the indentations, the plateau-like hardness profiles along the building directions manifest a stable L-DED process (Fig. 5b). The average hardness values of parameter sets 1–4 are 118 ± 9 $HV_{0.1}$, 114 ± 8 $HV_{0.1}$, 110 ± 12 $HV_{0.1}$, and 113 ± 4 $HV_{0.1}$, respectively. Given the standard deviation, four specimens exhibit comparable hardness levels. Most of the indentation points of specimens processed parameter sets 1 and 2 are located above those processed with parameter sets 3 and 4 in Fig. 5. Laser scan speed (v_s) of parameter sets 1 and 2 is 1 m/min, while v_s of parameter sets 3 and 4 is 1.5 m/min. However, the laser power (P) of the first two parameter sets (3000 W in the measured area) is lower than that of the last two parameter sets (3250 W and 4000 W in the measured area). The process parameters P and v_s have contrary effects on the strengthening mechanisms. In terms of the grain refinement, higher P could cause excessive heat input promoting the grain growth and deteriorating the performance, whilst higher v_s could increase the cooling rate and diminish the solidification time restricting the grain growth [41]. Besides grain refinement, solid solution strengthening and precipitation strengthening in 7XXX Al alloys are also affected by the complex thermal history during deposition.

Tensile tests were performed to further characterize the mechanical performance of specimens. Fig. 6 shows the stress–strain curve of one representative test of specimens produced with each parameter set. The instability with an appearance of serrations in the stress–strain curves is observed in all four specimens, which is so-called the Portevin–Le Chatelier effect [42]. It is highly dependent on the testing temperature and strain rate. The Portevin-Le Chatelier effect has resulted from the interaction between solutes and dislocations. Specimens produced with parameter sets 2 and 4 are less ductile than those produced with parameter sets 1 and 3. Using parameter sets 2 and 3 it is possible to produce specimens with higher strength. If only a representative engineering stress–strain curve per each parameter set is analyzed (Fig. 6), it seems that parameter set 3 has the best compromise between strength and ductility. However, by averaging the results from different tests, as listed in Table 2, tensile test results of specimens produced with parameter sets 3 and 4 show the highest standard deviations considering the ultimate tensile strength values. On the contrary, using parameter sets 1 and 2 it is possible to produce specimens with more reproducible mechanical properties. The highest achievable yield strength (*YS*) and ultimate tensile strength (*UTS*) values are 271.8 ± 3.9 MPa and 401.6 ± 1.9 MPa, respectively (parameter set 2). The highest ductility (fracture strain A_f of 16.8 ± 1.9%) was achieved for the specimen produced with parameter set 1.

The stress–strain curve demonstrates a ductile fracture behavior of the specimens produced with parameter sets 1–4 (Fig. 6), while the mechanical properties of these specimens, i.e. *YS*, *UTS*, and A_f, are different (Table 2). This result is also reflected in the macroscopic fracture surfaces. The fracture surface shown in Fig. 7a exhibits two parts with a flat and a rough topography respectively, while the fracture surfaces shown in Fig. 7e, i, m are characterized by a comparatively more uniform topography and a more compact fracture surface. The plastic fracture strain of 7% and the tensile strength of 340 MPa of the tensile specimen produced with parameter set 4 could be explained by defects in the AM structure, which appear as cracks on the fracture surfaces (Fig. 7m). In addition to the cracks, pores can also be seen in Fig. 7b, f, j, n. However, the porosity did not seem to have exerted any influence on tensile properties when correlating Fig. 4 and Table 2. In all tensile specimens tested, transcrystalline ductile fracture

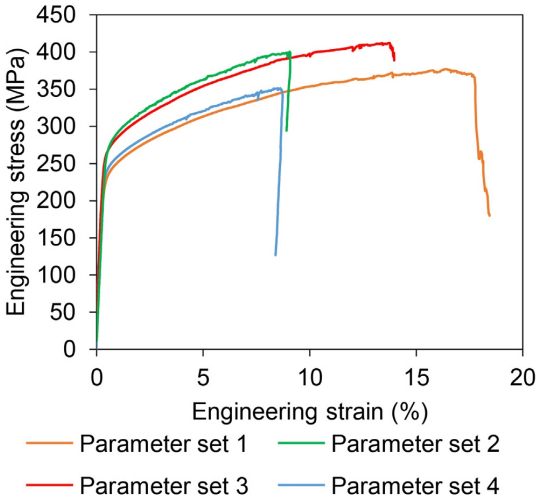

Fig. 6 – Stress–strain curve of specimens produced with four parameter sets. Only one representative specimen in each parameter set is illustrated here.

resulted in the formation of a dimple structure. During plastic deformation, microvoids are formed by the fracture of inclusion particles or the separation between the deformed matrix and inclusion particles. The yellow arrows in Fig. 7d, h, l, p indicate such inclusion particles, whose chemical composition and arrangement in the microstructure will be discussed in Section 3.3. The dimple structure is formed by the new formation and union of microvoids at certain critical strains, see Fig. 7c, g, k, o. Besides the dimple structure, smoother regions with shear lips can be seen, indicating that a multiaxial stress state was present in the AM structure during the tensile test [43], which resulted in a mixture of normal and shear fractures. The comparison between the tensile specimens fractured at 17% and 13% in Fig. 7d, l and the tensile specimens fractured at 9% and 7% in Fig. 7h, p shows that the higher the plastic fracture strain, the larger the mean dimple diameter and the mean dimple depth, respectively. The relationship between dimple size and microstructural parameters such as distance between inclusion particles, inclusion particle diameter, and deformation in the ductile fracture is described in [44].

Limited statistics of mechanical properties of AM processing 7XXX high-strength Al alloys can be collected so far. Fig. 8 compares the YS, UTS, and A_f of 7XXX alloys processed with LPBF, L-DED (wire and powder), and WAAM. Specimens produced with wire-based L-DED in this study exhibit superior strength and ductility compared with 7XXX alloys processed with other AM technologies. Two kinds of 7XXX alloys blended with other alloying elements have higher ultimate tensile strength but lower ductility. Only Al6Zn2Mg alloy blended with Sc and Zr processed with LPBF demonstrates better performance in terms of strength and ductility. A higher cooling rate during solidification can be reached in LPBF than in L-DED [45,46] developing finer grains in as-built specimens [47]. Moreover, Sc and Zr as alloying elements can act as nuclei for primary Al grains [48]. Nuclei promote grain refinement and inhibit the growth of large columnar grains. Based on the Hall–Petch relation and boundary strengthening, finer grains increase strength by imposing extra resistance to dislocation movement [49]. The propagation of microcracks during tensile tests can be branched and extended in refined microstructure leading to an enhancement of ductility [50]. Besides, adding alloying elements as nuclei can also diminish microstructure defects, such as porosity [23] and cracks [51]. Despite the advantages of material modification for processing, the price of Sc and Zr is expensive. Besides, blending material, both by mechanical alloying and metallurgical alloying, is time-consuming and needs extra cost. Concerning AM processing pure 7XXX alloys, the mechanical properties achieved here are competent.

Table 2 – Average mechanical properties of specimens. Yield strength (YS), ultimate tensile strength (UTS), fracture strain (A_f).

Specimens	YS (MPa)	UTS (MPa)	A_f (%)
Parameter set 1	238.3 ± 3.7	378.5 ± 2.4	16.8 ± 1.9
Parameter set 2	271.8 ± 3.9	401.6 ± 1.9	9.2 ± 1.1
Parameter set 3	257.6 ± 13.3	396.6 ± 22.1	12.6 ± 0.8
Parameter set 4	240.6 ± 2.6	339.6 ± 16.6	7.3 ± 1.0

3.3. *Microstructure characterization*

EBSD measurements were carried out in the middle area of the thin-wall structures produced with parameter sets 1–4. Microtexture and grain morphology were determined from single orientation measurements to assess the influence of L-DED process parameter variation. Ordinary pole figures ($h\ k\ l$) [$u\ v\ w$] were used to describe the microtexture. The building direction of thin-wall structures was parallel to the transverse direction TD and crystal direction [$u\ v\ w$]. RD is the thickness direction of thin-wall structures. RD-TD corresponds to the ground plane of the specimens. The normal direction ND is perpendicular to the ground plane and parallel to the wire feed direction. The grain morphology was described in terms of the long and short grain axes d_{max} and d_{min}, the aspect ratio d_{min}/d_{max}, and the orientation $\sphericalangle(d_{max}, hor.)$.

The crystal orientation images and the ordinary pole figures of the thin-wall structures produced with parameter sets 1–3 are shown in Fig. 9. The mean grain length d_{max} decreases in the order of specimens produced with parameter sets 1, 2, 3 and the mean grain width d_{min} decreases in the order of specimens produced with parameter sets 1, 3, 2. The thin-wall structure produced with parameter set 2 exhibits the finest grain structure with respect to d_{max} and d_{min}. The orientation of the grains of the three structures, expressed by the angle between the long grain axis d_{max} and a horizontal reference line ($\sphericalangle(d_{max}, hor.)$) ranges between 97° and 113° and is thus oriented almost parallel to the building direction. Therefore, the parameter variation shows no noticeable effect on the orientation. The microstructural refinement is accompanied in particular by an increase in yield strength and also in tensile strength, indicating that the Hall–Petch mechanism is effective. The highest values of yield strength and tensile

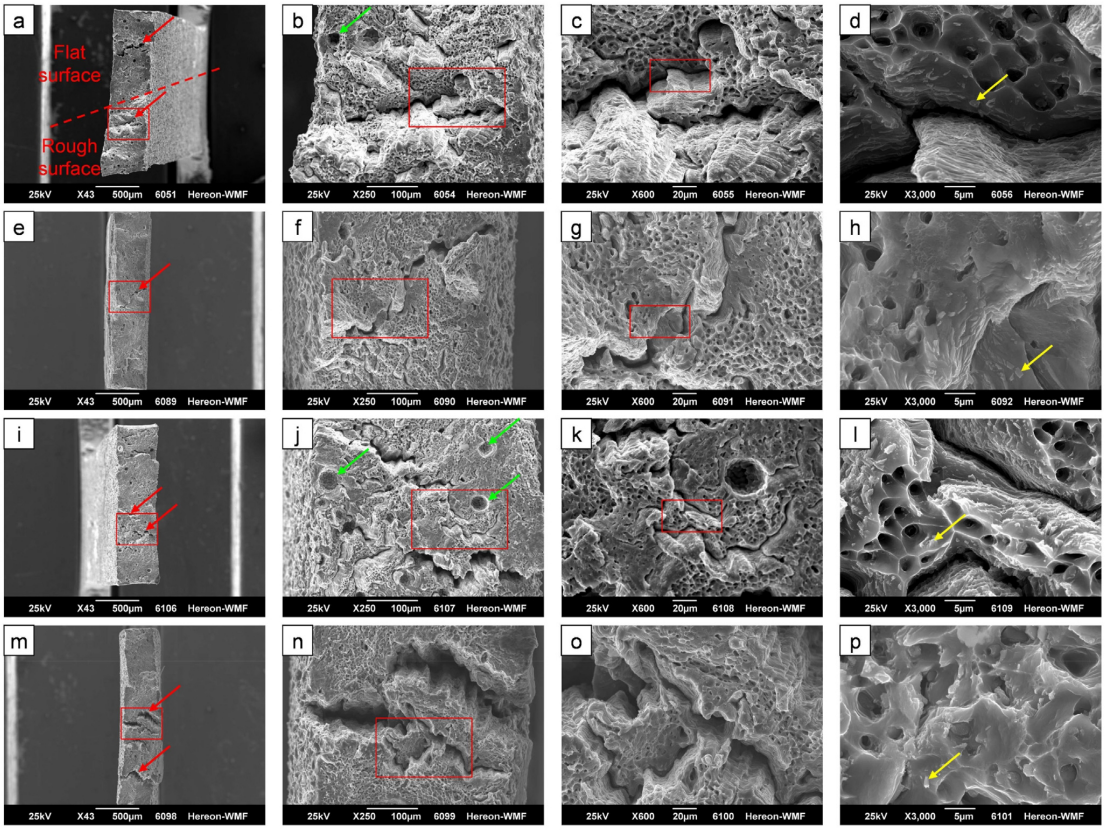

Fig. 7 – Fracture surface of tensile specimens produced with parameter set 1 (a–d), parameter set 2 (e–h), parameter set 3 (i–l), and parameter set 4 (m–p). Magnified areas are marked with red rectangular boxes. Red, green, and yellow arrows point at the cracks, pores, and secondary phases, respectively.

strength are determined on the tensile specimen produced with parameter set 2. Comparing the specimens produced with parameter sets 1 and 2, reducing the wire feed rate from 4.0 m/min to 3.0 m/min likely resulted in grain refinement. The ordinary (1 0 0) pole figures exhibit the occurrence of pole densities especially at TD, suggesting the presence of a <1 0 0>-fiber texture with local maxima in the form of the orientations (0 0 1)[1–6 0] in the specimen produced with parameter set 1, (1 1 0)[1–10 0] in the specimen produced with parameter set 2, and <1 0 0>-fiber in the specimen produced with parameter set 3. The orientation of the <1 0 0> crystal axis is thus nearly parallel to the long grain axis d_{max} and thus nearly parallel to the building direction TD. In the L-DED process, <1 0 0> was the preferred crystal growth direction, which is in agreement with the results in [39] that <1 0 0> is the preferred crystal direction for grain growth in face-centered cubic materials.

While thin-wall structures produced with parameter sets 1–3 were built up continuously, the buildup of the specimen produced with parameter set 4 was discontinuous. This specimen was investigated by EBSD in the interfacial region between the substrate and AM structure, at the mid and top of the structure to detect possible variations along the building direction. The crystal orientation images as well as the ordinary pole figures of this specimen are shown in Fig. 10.

The discontinuously built specimen is also characterized by <1 0 0>-fiber texture, with an additional (0 0 1)[1 0 0] component appearing with increasing height. Furthermore, it can be seen that grain coarsening occurs with increasing height (Note: The structure of the substrate was not taken into account when determining the average grain size). The coarseness of the AM structures is the reason why no closed orientation bands can be seen on the RD axis of the ordinary (1 0 0) pole figures. It should be further noted that in the tensile test, the load direction was nearly perpendicular to the {1 0 0} crystal planes, resulting in high shear stresses in the {1 1 1}<1 1 0> slip system. Table 3 summarizes the relevant data in the EBSD measurements.

All specimens investigated in this study exhibit significantly elongated columnar grains with typical epitaxial growth and superior mechanical properties, which are reported for the same material, see Fig. 8. In tensile tests,

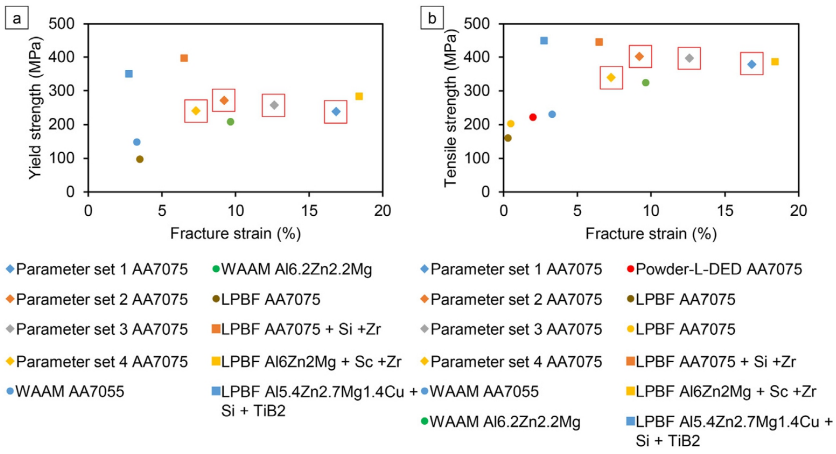

Fig. 8 – Mechanical properties of 7XXX Al alloys processed with different AM technologies. (a) Yield strength – fracture strain; (b) ultimate tensile strength – fracture strain. Specimens produced in the present study are marked with red square boxes. Ref.: WAAM AA7075 [52], WAAM Al6.2Zn2.2 Mg [53], powder-L-DED AA7075 [54], LPBF AA7075 [30,55], LPBF AA7075 + Si + Zr [34], LPBF Al6Zn2Mg + Sc + Zr [48], LPBF Al5.4Zn2.7Mg1.4Cu + Si + TiB2 [33].

loading directions have effects on the measured mechanical properties of AM-produced specimens. However, a clear dependence is not disclosed. For example, in [56], it is found that the specimen extracted parallel to the building direction demonstrates better properties than that extracted vertical to the building direction. Nevertheless, in [43], the strength of tensile specimens parallel to the building direction is inferior. The loading direction in this work is parallel to the building direction and nearly parallel to the major axis of columnar grains. Secondary phases formed during processing are considered weak positions under loading and are susceptible to cracking [57]. Tensile-stress bearing areas are distributed with fewer secondary phases leading to delayed initiation of primary cracks. Hence, the properties concerning the strength and fracture strain could be improved. Meanwhile, shear stress rips off the long grain boundaries initiating secondary cracking because of secondary phases, as illustrated in Fig. 11. Secondary cracks on fracture surfaces caused by shear stress verify the explanation. Fracture surfaces suggest a combined fracture mode as a combination of ductile and shear fracture.

Previously solidified layers are subjected to reheating during the building of subsequent layers. As precipitation-strengthening 7XXX alloys, the cyclic energy input could act as heat treatment and contribute to the precipitation. EDX mapping is conducted to the specimen produced with parameter set 2 to get an overview of possible precipitates and the enriched alloying elements (Fig. 12). Precipitates along grain boundaries are mainly enriched in Cu, Mg, and Zn. A small fraction of precipitates along grain boundaries also contains Fe and Si. The enrichment of these five alloying elements can also be detected in the precipitates inside grains. It is noticed that the element distribution maps of Cu and Mg closely coincide, while some precipitates are free of Zn. The presence of precipitates inside grains could be a factor contributing to higher strength in this study.

The chemical composition of six points, as marked in Fig. 12, is measured to determine the secondary phases. Points 1, 2, and 3 are Mg-, Zn-, and Cu-rich secondary phases, see Table 4. The secondary phase could be $Mg(Zn, Cu, Al)_2$, which is an eutectic phase along grain boundaries formed during casting [36]. Points 4 and 5 are enriched in Mg and Cu. S phase (Al_2CuMg) is a possible secondary phase, which could form during solidification or precipitate during the heat treatment of 2XXX alloys [47,58] and 7XXX alloys [59]. The phase of point 6 has the most complicated composition. The segregation of Mg, Si, Fe, Cu, and Zn is observed. The Fe-rich phase could be Al_7Cu_2Fe, which is also detected during WAAM deposition of 7XXX alloys [52].

Comparing parameter sets 2 and 3, laser power and laser scan speed are different. Line energy density is commonly used in L-DED to represent the laser energy input [60]. In the present study, laser power varies in different layers, so energy input should be calculated separately. Total energy input (*TEI*) is used to evaluate the energy input of parameter sets 2 and 3 during deposition, as defined in the following equations:

$$TEI = \sum_{n=1}^{60} \frac{P_n}{v_s} * l \qquad 1$$

where P_n is laser power in the n^{th} layer, v_s is laser scan speed (constant in the $1^{st} - 60^{th}$ layer), and l is track length (constant in the $1^{st} - 60^{th}$ layer). Parameter sets 1 and 2 have the same *TEI* of 327.6 kJ. The *TEI* of parameter set 3 is 237 kJ.

AA7075 contains volatile alloying elements, such as Zn and Mg. The evaporation of these elements could result in gas porosity in deposited specimens [23,53,61] and degrade the potential of precipitation strengthening. The chemical

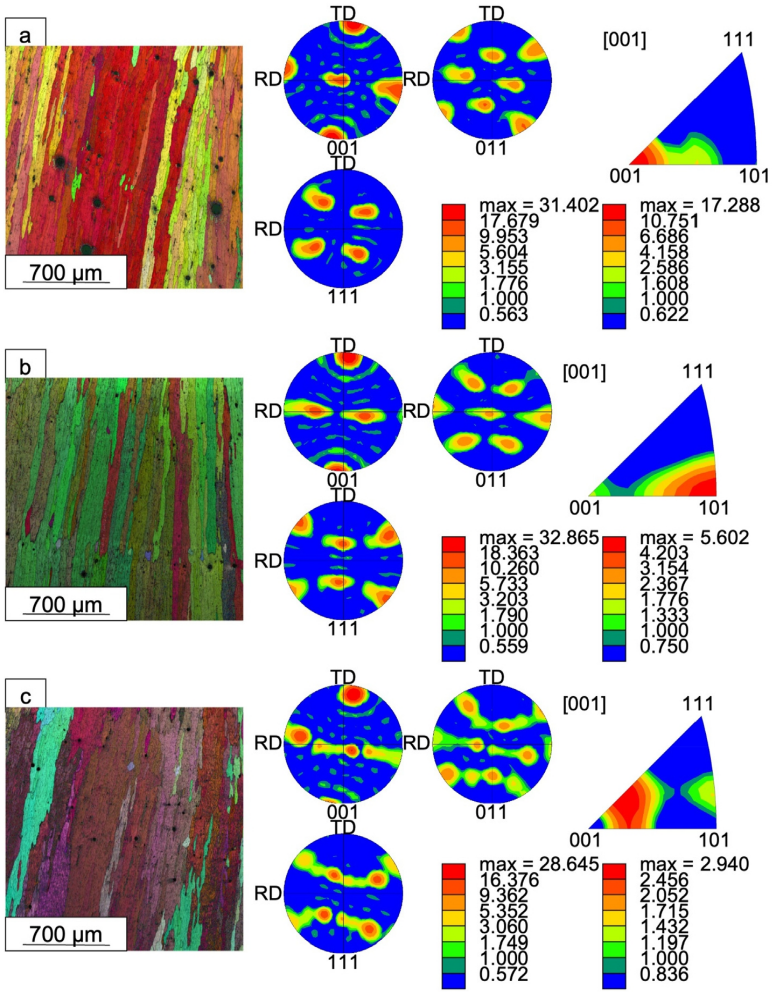

Fig. 9 – Crystal orientation maps and (*h k l*) pole figures: (a) parameter set 1, P_{max} = 31.4 mrd, <1 0 0> fibre as well as (0 0 1) [1–6 0], missorientation $\Delta\omega = 0.84°$; (b) parameter set 2, P_{max} = 32.9 mrd, <1 0 0> fibre as well as (1 1 0)[1–10 0], missorientation $\Delta\omega = 1.23°$; (c) parameter set 3, P_{max} = 28.6 mrd, <1 0 0> fibre, missorientation $\Delta\omega = 1.15°$.

composition of the matrix in specimens produced with parameter sets 1, 2, and 3 is measured. Table 5 indicates the element loss of Zn during deposition compared with the raw material. However, the content of Mg is comparable to the non-processed material. The boiling temperature of Zn and Mg is 907 °C [62] and 1090 °C [63], respectively. It means that the maximal temperature in melt pools is located in this temperature range. Parameter sets 1 and 2 provided more energy input than parameter set 3 leading to more element loss of Zn.

The three specimens investigated exhibit similar microstructure after etching. Besides, the grain size in the entire cross-section cannot be reasonably compared among these three specimens due to the small neighboring misorientation angle. Hence, only the specimen produced with parameter set 1 is shown in Fig. 13a. Columnar grains with epitaxial growth patterns dominate in the cross-section. The mixed microstructure of coarse equiaxed grains and columnar grains are distributed at the top of the thin-wall structure, while only columnar grains are observed in the middle. The last layer experience no remelting. Hence, the morphology of coarse equiaxed grains above columnar grains can be preserved. Fine grains can be observed near the substrate, which is attributed to the higher cooling rate caused by rapid heat conduction to the substrate and the initial low substrate temperature [64,65]. Three kinds of columnar grains with different growth directions are present in the middle of the thin-wall structure. At two edges, columnar grains are tiled toward the center, while the growth direction of columnar grains in the center is parallel to the building direction, as also observed in [66]. The

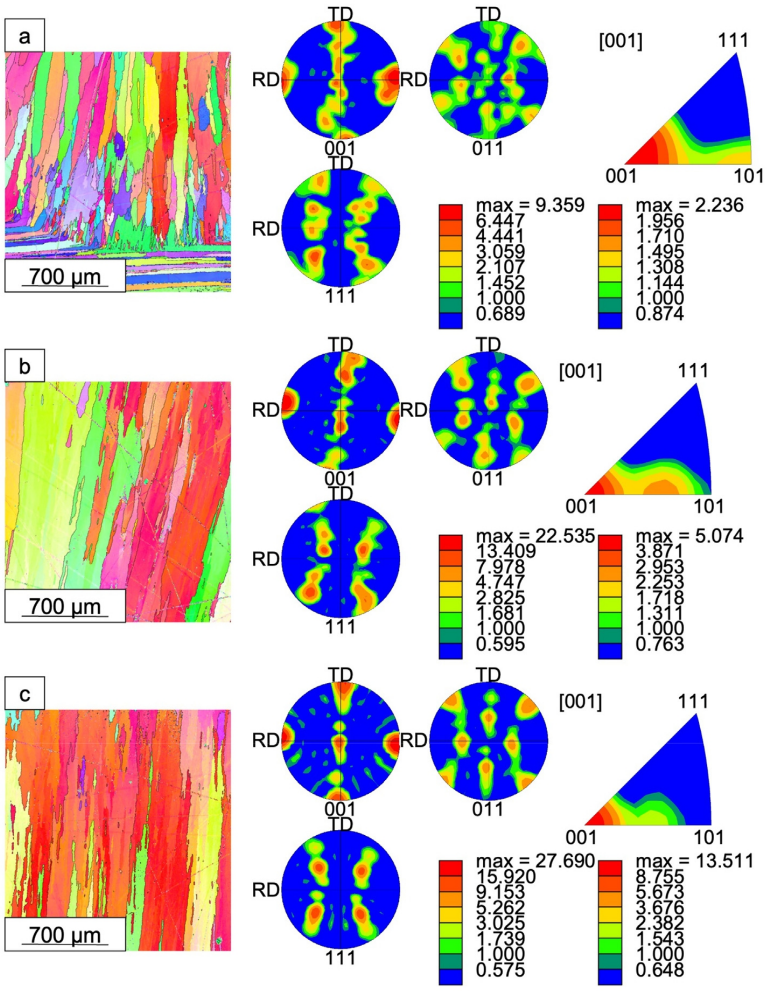

Fig. 10 – Crystal orientation maps and (*h k l*) pole figures of the specimen produced with parameter set 4: (a) bottom of the AM structure, $P_{max} = 9.4$ mrd, <1 0 0> fibre, missorientation $\Delta\omega = 0.80°$; (b) mid of the AM structure, $P_{max} = 22.5$ mrd, <1 0 0> fibre, missorientation $\Delta\omega = 0.83°$; (c) top of the AM structure, $P_{max} = 27.7$ mrd, <1 0 0> fibre, missorientation $\Delta\omega = 1.03°$.

Table 3 – Grain morphology, missorientation and pole density of specimens produced with parameter sets 1–4 (used images for analysis, see Figs. 9 and 10).

Specimen	d_{max} [µm]	d_{min} [µm]	d_{min}/d_{max}	$\sphericalangle(d_{max}$, hor.) [°]	$\Delta\omega$ [°]	P_{max} [mrd]
Parameter set 1	977.03	231.41	0.22	113.43	0.84	31.4
Parameter set 2	830.81	96.06	0.12	96.90	1.23	32.9
Parameter set 3	793.22	186.01	0.22	111.16	1.15	28.6
Parameter set 4 bottom	372.52	48.04	0.15	101.08	0.80	9.4
Parameter set 4 mid	820.81	152.09	0.18	107.21	0.83	22.5
Parameter set 4 top	889.25	183.01	0.20	105.80	1.03	27.7

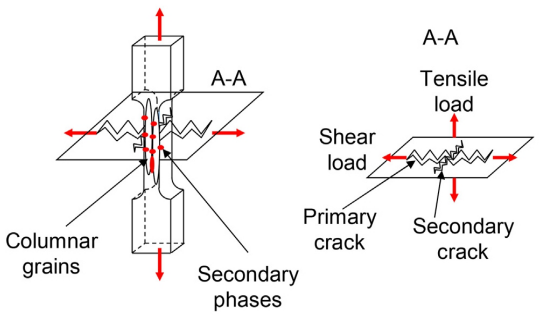

Fig. 11 – Illustration for an explanation of the fracture mechanism in a tensile specimen during tensile test. A–A cross-section corresponds to the fracture surface.

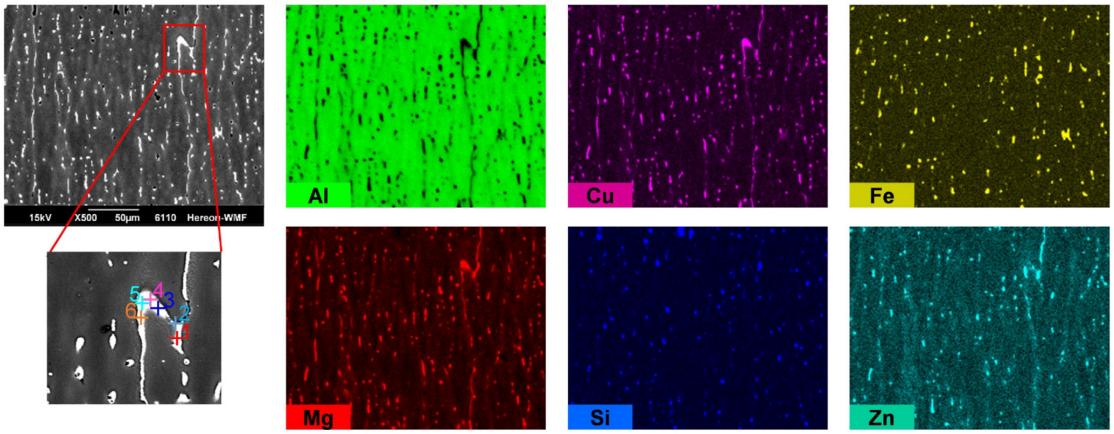

Fig. 12 – EDX mapping and point measurement of the specimen produced with parameter set 2. The measured area is in the middle of the thin-wall structure.

Table 4 – Chemical composition of six points marked in Fig. 12 (in wt. %).

Point	Al	Mg	Si	Fe	Cu	Zn
1	60.2	10.4	0.3	0.1	9.5	19.4
2	55.4	10.6	0.3	0.1	11.3	22.4
3	77.6	4.9	0.4	0.2	5.6	11.3
4	65	9.1	0.4	0.1	21.6	3.9
5	54.8	12.3	0.4	0	27.6	4.8
6	76.2	4	1	7.6	4.8	6.5

maximal heat flux direction is perpendicular to the interface of melt pools [67], as sketched in Fig. 13b. Dendrites with preferential orientation along heat flux direction can succeed in the growing competition with other grains [66]. Consequently, columnar grains with three morphologies are formed.

The simulated maximal temperature during depositing each layer and the simulated cooling rate in the middle of each layer (where specimens were cut for metallographic preparation) are listed in Table A. 1. The maximal temperature in melt pools exceeds the boiling point of Zn but is still below the boiling point of Mg. It is consistent with the observation of EDX measurement, i.e. no evaporation of Mg and element loss of Zn. The cooling rate decreases as the distance from the substrate surface increases. In the 1st layer, the cooling rate can reach about 358 K/s promoting the formation of equiaxed grains. A lower cooling rate in further deposition cannot effectively inhibit the epitaxial growth of columnar grains.

Table 5 – Chemical composition of the matrix in three specimens. The content of Mg and Zn is listed (in wt. %).

Specimen	Mg	Zn
Parameter set 1	2.30 ± 0.27	3.16 ± 0.15
Parameter set 2	2.30 ± 0.39	3.45 ± 0.35
Parameter set 3	2.40 ± 0.04	3.58 ± 0.21

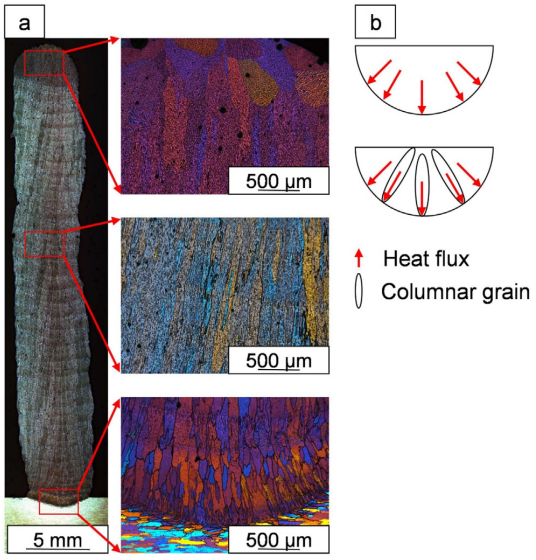

Fig. 13 – (a) Cross-sectional view of the etched specimen produced with parameter set 1. (b) Illustration of columnar grain formation in melt pools.

4. Conclusions

In this work, the processability of AA7075 in L-DED was investigated. The process parameters and building strategies were optimized to produce crack-free specimens with low porosity levels. The microstructure was characterized by different methods and the mechanical properties of

specimens were tested. FEM simulation was conducted to better understand the correlation between process and microstructure as well as mechanical properties. Based on the results, the following conclusions can be drawn:

- The specific energy and k value are two effective indicators to reveal the overall effects of process parameters on the integrity of single tracks and thin-wall structures. The porosity level is negatively correlated to the magnitude of specific energy and k value. A stronger dependence of the porosity level on the specific energy is observed.
- By the process optimization to a 30-layer deposition, the porosity level can be reduced to 0.8% in the continuous processing, whereby a further reduction to 0.3% is possible in the discontinuous processing. However, the porosity level deteriorates with further deposition to 60 layers in the both building strategies.
- The hardness is nearly constant in the middle of thin-wall structures suggesting stable processing. The average hardness of thin-wall structures produced with four parameter sets is comparable (about 115 $HV_{0.1}$). Fracture surfaces disclose a mixed fracture mode of ductile fracture and shear fracture. The specimen produced with the discontinuous building strategy has the lowest strength, which could be attributed to the presence of large pores and cracks inside the specimen. The highest strength is achieved in the specimen produced with parameter set 2 (*YS*: 271.8 MPa, *UTS*: 401.6 MPa, A_f: 9.2%), while the specimen produced with parameter set 1 exhibits the highest ductility (*YS*: 238.3 MPa, *UTS*: 378.5 MPa, A_f: 16.8%).
- Large columnar grains with epitaxial growth dominate the cross-sections of specimens. The growth direction is perpendicular to the interface of melt pools and nearly parallel to the building directions. All specimens exhibit a fibre texture despite the different process parameters and building strategies. Various precipitates are present in as-built specimens because of the reheating of previously solidified layers when building subsequent layers.
- The superior mechanical properties of these specimens could be resulted from the orientation of long grain boundaries and the distribution of secondary phases. In tensile tests, the tensile stress is nearly parallel to the long grain boundaries, where the secondary phases are distributed. Secondary phases are assumed as the preferential sites for cracking initiation. Since they are not subjected to a high tensile stress in this work, it could lead to a "delayed" fracture.
- With the calibrated transient heat analysis, the maximal temperature in the melt pool of is in the range of 900–1080 °C leading to the evaporation of Zn and no loss of Mg, which is in agreement with the EDX measurement. The epitaxial growth cannot be inhibited by the decreasing cooling rate with the increasing building height resulting in the dominant columnar grains.

Declaration of Competing Interest

The authors declare that they have no known competing financial interests or personal relationships that could have appeared to influence the work reported in this paper.

Acknowledgments

The authors would like to thank R. Dinse and S. Riekehr for their assistance during laser directed energy deposition as well as F. Dorn for the support during metallographic preparation and microstructural characterization.

Appendices

Temperature field evolution assisted by finite element model

The transient temperature evolution during deposition was monitored and documented using two type K thermocouples. The thermocouples were inserted into the holes of 2 mm depth as shown in Fig. A.1. To calibrate the numerical model of L-DED process, the temperature measurements were performed during the deposition of a thin-wall structure with four layers.

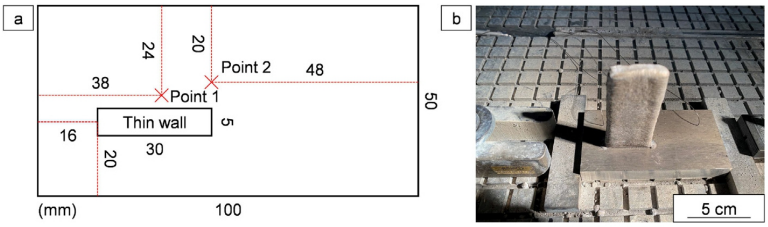

Fig. A.1 – (a) Illustration of positions of thermocouples and thin-wall structure on the substrate. (b) Photo of a deposited thin-wall structure with thermocouples inserted into the holes on the substrate.

Finite element (FE) simulation was implemented in ABAQUS CAE with a plug-in called AM Modeler. AM Modeler has a toolpath-mesh intersection module, which provides easy activation of death elements and ensures the synchronous path control of laser beam and deposited material.

Heat transfer in the form of heat conduction, convection, and radiation can be calculated by the heat equations, as described in [32,68]. The density (ρ) of AA7075 was estimated

as 2.81 g/cm^3 [69] and considered temperature-independent. Another two heat-analysis-related material properties, i.e. thermal conductivity (h) and specific heat capacity (c) were assumed as temperature-dependent and were determined using the following equations [70]:

$$h = 25.22 + 0.3978T \quad \text{A.1}$$

$$c = 929.3 - 0.627T + 0.00187T^2 \quad \text{A.2}$$

where T is the temperature. The material properties of AA5087 used in the simulation were taken from [68].

A good agreement between the simulated and the measured temperature evolution can be achieved in a transient heat transfer analysis without considering the phase transformation during the L-DED process [68]. Hence, the same strategy was adopted in the present FEM simulation to simplify the model. The model of laser heat source was established using the double ellipsoidal power density distribution [71]. Calculation indicated that the temperature gradient on the front side is steeper than that on the rear side of the heat source. Hence, the power density distribution is separately considered in two ellipsoids, as shown in Fig. A.2. It has been proven that the most accurate results can be achieved assuming an identical geometry between the double ellipsoid heat source and the melt pool. Based on this conclusion, the magnitude of the depth and the width of melt pools measured under the microscope were set as input in FEM simulation as the half-width (a) and the penetration depth (b) of the heat source. A high-speed camera was used to capture the images of melt pools for the measurement of the length (c_1 and c_2).

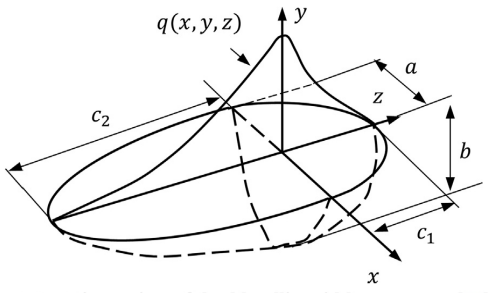

Fig. A.2 – Dimension of double ellipsoid heat source [71]: half-width (a), penetration depth (b), front length (c_1), and rear length (c_2) of the heat source. Laser moves along the positive z-direction.

Equation A.3 introduces how the power density is distributed [71] in the local xyz-coordinates:

$$q(x, y, z, t) = \frac{6\sqrt{3}f_x P\alpha}{abc\pi\sqrt{\pi}} e^{-3\left(\frac{x^2}{a^2}+\frac{y^2}{b^2}+\frac{z^2}{c^2}\right)} \quad \text{A.3}$$

where α is the laser absorption coefficient ($\alpha = 0.65$ in the present work [72]), P is the laser power, and f_x is the scaling factor (the percentage of laser heat input allocated to the front and the rear side (f_f, f_r, $f_f + f_r = 2$).

At the beginning of the L-DED process, the deposited layer height could significantly fluctuate due to the changing heat transfer conditions [21]. Hence, the height of the first 4 layers is measured and set as a variable in simulation.

Simulation results are validated by calibrating the temperature evolution of point A and point B (Fig. A.1) in the substrate with the results measured by thermocouples in the 4-layer deposition. As shown in Fig. A.3a, the maximal, minimal temperature, heating, and cooling behaviors of point A measured by thermocouple and simulated by the FE-Model demonstrate a good agreement. However, the thermal history in point B deviates in the third layer (Fig. A.3b). The maximal temperature in the experiment is higher than that in the simulation. Point B is located farther from the melt pool than point A. The various distance between measurement points and deposited layers could lead to inaccuracy in predicting temperature evolution, as observed in [73,74]. It is noticed that a rapid temperature drop is observed before deposition, as circled in Fig. A.3. Compressed air flows through the optic system to protect from contamination due to fume. Before scanning each layer, the valve of compressed air is switched on. During stabilizing the gas flow to set-value, a strong gas flow is conveyed onto the deposited structure causing a rapid temperature drop. Overall, the FE-model can be adopted to predict the thermal history of deposited layers and used to elaborate on the correlation between processing and microstructure.

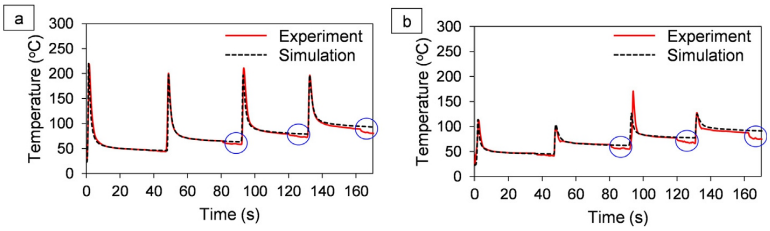

Fig. A.3 – Temperature evolution of (a) point A and (b) point B in the substrate from experiment and simulation.

Table A.1 – Temperature peaks and cooling rates in the first 4 layers.

	Maximal temperature (°C)	Cooling rate (K/s)
1st layer	956	358
2nd layer	969	241
3rd layer	919	124
4th layer	1080	49

REFERENCES

[1] Schmidt M, Merklein M, Bourell D, Dimitrov D, Hausotte T, Wegener K, et al. Laser based additive manufacturing in industry and academia. Cirp Annals 2017;66(2):561–83.

[2] Seifi M, Salem A, Beuth J, Harrysson O, Lewandowski JJ. Overview of materials qualification needs for metal additive manufacturing. JOM (J Occup Med) 2016;68(3):747–64.

[3] Mazzucato F, Avram O, Valente A, Carpanzano E. Recent advances toward the industrialization of metal additive manufacturing. Systems Engineering in the Fourth Industrial Revolution 2019:273–319.

[4] Gasser A, Backes G, Kelbassa I, Weisheit A, Wissenbach K. Laser additive manufacturing: laser metal deposition (LMD) and selective laser melting (SLM) in turbo-engine applications. Laser Technik Journal 2010;7(2):58–63.

[5] Medrano A, Folkes J, Segal J, Pashby I. Fibre laser metal deposition with wire: parameters study and temperature monitoring system. In: XVII international symposium on gas flow, chemical lasers, and high-power lasers. SPIE; 2009. p. 539–45.

[6] Froend M, Ventzke V, Riekehr S, Kashaev N, Klusemann B, Enz J. Microstructure and hardness evolution of laser metal deposited AA5087 wall-structures. Procedia CIRP 2018;74:131–5.

[7] Lee W-S, Sue W-C, Lin C-F, Wu C-J. The strain rate and temperature dependence of the dynamic impact properties of 7075 aluminum alloy. J Mater Process Technol 2000;100(1–3):116–22.

[8] Ding Y, Muñiz-Lerma J, Trask M, Chou S, Walker A, Brochu M. Microstructure and mechanical property considerations in additive manufacturing of aluminum alloys. MRS Bull 2016;41(10):745–51.

[9] Wang F, Gong Y, Du Y, Song M. Microstructures and mechanical properties of an Al-Zn-Mg-Cu alloy processed by two-step aging treatment. J Mater Eng Perform 2020;29(7):4404–11.

[10] Engdahl T, Hansen V, Warren P, Stiller K. Investigation of fine scale precipitates in Al–Zn–Mg alloys after various heat treatments. Mater Sci Eng, A 2002;327(1):59–64.

[11] Yang W, Ji S, Wang M, Li Z. Precipitation behaviour of Al–Zn–Mg–Cu alloy and diffraction analysis from η′ precipitates in four variants. J Alloys Compd 2014;610:623–9.

[12] Paulisch M, Wanderka N, Haupt M, Selve S, Driehorst I, Reimers W. The influence of heat treatments on the microstructure and the mechanical properties in commercial 7020 alloys. Mater Sci Eng, A 2015;626:254–62.

[13] Azarniya A, Taheri AK, Taheri KK. Recent advances in ageing of 7xxx series aluminum alloys: a physical metallurgy perspective. J Alloys Compd 2019;781:945–83.

[14] Hebert RJ. Metallurgical aspects of powder bed metal additive manufacturing. J Mater Sci 2016;51(3):1165–75.

[15] Tang M, Pistorius PC. Oxides, porosity and fatigue performance of AlSi10Mg parts produced by selective laser melting. Int J Fatig 2017;94:192–201.

[16] Xue Y, El Kadiri H, Horstemeyer M, Jordon J, Weiland H. Micromechanisms of multistage fatigue crack growth in a high-strength aluminum alloy. Acta Mater 2007;55(6):1975–84.

[17] Ng G, Jarfors A, Bi G, Zheng H. Porosity formation and gas bubble retention in laser metal deposition. Appl Phys A 2009;97(3):641–9.

[18] Toda H, Hidaka T, Kobayashi M, Uesugi K, Takeuchi A, Horikawa K. Growth behavior of hydrogen micropores in aluminum alloys during high-temperature exposure. Acta Mater 2009;57(7):2277–90.

[19] Harvey J-P, Chartrand P. Modeling the hydrogen solubility in liquid aluminum alloys. Metall Mater Trans B 2010;41(4):908–24.

[20] Herzog D, Seyda V, Wycisk E, Emmelmann C. Additive manufacturing of metals. Acta Mater 2016;117:371–92.

[21] Susan D, Puskar J, Brooks J, Robino CV. Quantitative characterization of porosity in stainless steel LENS powders and deposits. Mater Char 2006;57(1):36–43.

[22] Bambach M, Sizova I, Silze F, Schnick M. Comparison of laser metal deposition of Inconel 718 from powder, hot and cold wire. Procedia CIRP 2018;74:206–9.

[23] Zhao T, Wang Y, Xu T, Bakir M, Cai W, Wang M, et al. Some factors affecting porosity in directed energy deposition of AlMgScZr-alloys. Opt Laser Technol 2021;143:107337.

[24] Aboulkhair NT, Everitt NM, Ashcroft I, Tuck C. Reducing porosity in AlSi10Mg parts processed by selective laser melting. Addit Manuf 2014;1:77–86.

[25] Qi T, Zhu H, Zhang H, Yin J, Ke L, Zeng X. Selective laser melting of Al7050 powder: melting mode transition and comparison of the characteristics between the keyhole and conduction mode. Mater Des 2017;135:257–66.

[26] King WE, Barth HD, Castillo VM, Gallegos GF, Gibbs JW, Hahn DE, et al. Observation of keyhole-mode laser melting in laser powder-bed fusion additive manufacturing. J Mater Process Technol 2014;214(12):2915–25.

[27] Yang KV, Rometsch P, Jarvis T, Rao J, Cao S, Davies C, et al. Porosity formation mechanisms and fatigue response in Al-Si-Mg alloys made by selective laser melting. Mater Sci Eng, A 2018;712:166–74.

[28] Altıparmak SC, Yardley VA, Shi Z, Lin J. Challenges in additive manufacturing of high-strength aluminium alloys and current developments in hybrid additive manufacturing. Int J Lightweight Mater Manuf 2021;4(2):246–61.

[29] Cross C. On the origin of weld solidification cracking, Hot cracking phenomena in welds. Springer; 2005. p. 3–18.

[30] Stopyra W, Gruber K, Smolina I, Kurzynowski T, Kuźnicka B. Laser powder bed fusion of AA7075 alloy: influence of process parameters on porosity and hot cracking. Addit Manuf 2020;35:101270.

[31] Martin JH, Yahata BD, Hundley JM, Mayer JA, Schaedler TA, Pollock TM. 3D printing of high-strength aluminium alloys. Nature 2017;549(7672):365–9.

[32] Parry L, Ashcroft I, Wildman RD. Understanding the effect of laser scan strategy on residual stress in selective laser melting through thermo-mechanical simulation. Addit Manuf 2016;12:1–15.

[33] Zhou S, Su Y, Wang H, Enz J, Ebel T, Yan M. Selective laser melting additive manufacturing of 7xxx series Al-Zn-Mg-Cu alloy: cracking elimination by co-incorporation of Si and TiB2. Addit Manuf 2020;36:101458.

[34] Li L, Li R, Yuan T, Chen C, Zhang Z, Li X. Microstructures and tensile properties of a selective laser melted Al–Zn–Mg–Cu (Al7075) alloy by Si and Zr microalloying. Mater Sci Eng, A 2020;787:139492.

[35] Froend M, Riekehr S, Kashaev N, Klusemann B, Enz J. Process development for wire-based laser metal deposition of 5087 aluminium alloy by using fibre laser. J Manuf Process 2018;34:721–32.

[36] Zou X-l, Hong Y, Chen X-h. Evolution of second phases and mechanical properties of 7075 Al alloy processed by solution heat treatment. Trans Nonferrous Metals Soc China 2017;27(10):2146–55.
[37] Wang M, Kashaev N. Investigation of process window for AA7075 considering effects of different wire feed directions in lateral metal deposition. Procedia CIRP 2022;111:218–23.
[38] Heilemann M, Möller M, Emmelmann C, Burkhardt I, Riekehr S, Ventzke V, et al. Laser metal deposition of Ti-6Al-4V structures: new building strategy for a decreased shape deviation and its influence on the microstructure and mechanical properties. Laser Manuf Conf Proc 2017.
[39] Wei H, Mazumder J, DebRoy T. Evolution of solidification texture during additive manufacturing. Sci Rep 2015;5(1):1–7.
[40] Li Y, Gu D. Thermal behavior during selective laser melting of commercially pure titanium powder: numerical simulation and experimental study. Addit Manuf 2014;1:99–109.
[41] Bertoli US, Guss G, Wu S, Matthews MJ, Schoenung JM. In-situ characterization of laser-powder interaction and cooling rates through high-speed imaging of powder bed fusion additive manufacturing. Mater Des 2017;135:385–96.
[42] Yilmaz A. The Portevin–Le Chatelier effect: a review of experimental findings. Sci Technol Adv Mater 2011.
[43] Froend M, Ventzke V, Dorn F, Kashaev N, Klusemann B, Enz J. Microstructure by design: an approach of grain refinement and isotropy improvement in multi-layer wire-based laser metal deposition. Mater Sci Eng, A 2020;772:138635.
[44] Schmidt V. Microprocess of fracture, electronmicroscopy in the solid state physics (in German). In: Bethge H, Heydenreich J, editors. Berlin, Heidelberg, New York: Springer-Publisher; 1982. p. 321–40.
[45] Javidani M, Arreguin-Zavala J, Danovitch J, Tian Y, Brochu M. Additive manufacturing of AlSi10Mg alloy using direct energy deposition: microstructure and hardness characterization. J Therm Spray Technol 2017;26(4):587–97.
[46] Li Y, Gu D. Parametric analysis of thermal behavior during selective laser melting additive manufacturing of aluminum alloy powder. Mater Des 2014;63:856–67.
[47] He C, Yu W, Li Y, Wang Z, Wu D, Xu G. Relationship between cooling rate, microstructure evolution, and performance improvement of an Al–Cu alloy prepared using different methods. Mater Res Express 2020;7(11):116501.
[48] Zhou L, Pan H, Hyer H, Park S, Bai Y, McWilliams B, et al. Microstructure and tensile property of a novel AlZnMgScZr alloy additively manufactured by gas atomization and laser powder bed fusion. Scripta Mater 2019;158:24–8.
[49] Hansen N. Hall–Petch relation and boundary strengthening. Scripta Mater 2004;51(8):801–6.
[50] Mukai T, Higashi K. Ductility enhancement of ultra fine-grained aluminum under dynamic loading. Scripta Mater 2001;44(8–9):1493–6.
[51] Tang Z, Vollertsen F. Influence of grain refinement on hot cracking in laser welding of aluminum. Weld World 2014;58(3):355–66.
[52] Dong B, Cai X, Lin S, Li X, Fan C, Yang C, et al. Wire arc additive manufacturing of Al-Zn-Mg-Cu alloy: microstructures and mechanical properties. Addit Manuf 2020;36:101447.
[53] Li S, Zhang L-J, Ning J, Wang X, Zhang G-F, Zhang J-X, et al. Microstructures and mechanical properties of Al–Zn–Mg aluminium alloy samples produced by wire+ arc additive manufacturing. J Mater Res Technol 2020;9(6):13770–80.
[54] Langebeck A, Bohlen A, Rentsch R, Vollertsen F. Mechanical properties of high strength aluminum alloy EN AW-7075 additively manufactured by directed energy deposition. Metals 2020;10(5):579.
[55] Reschetnik W, Brüggemann J-P, Aydinöz M, Grydin O, Hoyer K-P, Kullmer G, et al. Fatigue crack growth behavior and mechanical properties of additively processed EN AW-7075 aluminium alloy. Procedia Struct Integr 2016;2:3040–8.
[56] Karg MCH, Ahuja B, Wiesenmayer S, Kuryntsev SV, Schmidt M. Effects of process conditions on the mechanical behavior of aluminium wrought alloy EN AW-2219 (AlCu6Mn) additively manufactured by laser beam melting in powder bed. Micromachines 2017;8(1):23.
[57] Pineau A, Benzerga AA, Pardoen T. Failure of metals I: brittle and ductile fracture. Acta Mater 2016;107:424–83.
[58] Wang S, Starink M. Two types of S phase precipitates in Al–Cu–Mg alloys. Acta Mater 2007;55(3):933–41.
[59] Godard D, Archambault P, Aeby-Gautier E, Lapasset G. Precipitation sequences during quenching of the AA 7010 alloy. Acta Mater 2002;50(9):2319–29.
[60] Lee Y, Kim ES, Park S, Park JM, Seol JB, Kim HS, et al. Effects of laser power on the microstructure evolution and mechanical properties of Ti–6Al–4V alloy manufactured by direct energy deposition. Met Mater Int 2022;28(1):197–204.
[61] Zhao T, Dahmen M, Cai W, Alkhayat M, Schaible J, Albus P, et al. Laser metal deposition for additive manufacturing of AA5024 and nanoparticulate TiC modified AA5024 alloy composites prepared with balling milling process. Opt Laser Technol 2020;131:106438.
[62] Murray J. The Ti-Zn (Titanium-Zinc) system. Bulletin of alloy phase diagrams 1984;5(1):52–6.
[63] Liu S, Liu X, Liu B, Liu L, Jin W, Hu X. Effect of some alloying elements on boiling point of magnesium. Mater Sci Technol 2005;21(6):735–8.
[64] Gudur S, Nagallapati V, Pawar S, Muvvala G, Simhambhatla S. A study on the effect of substrate heating and cooling on bead geometry in wire arc additive manufacturing and its correlation with cooling rate. Mater Today Proc 2021;41:431–6.
[65] Yi H-J, Kim J-W, Kim Y-L, Shin S. Effects of cooling rate on the microstructure and tensile properties of wire-arc additive manufactured Ti–6Al–4V alloy. Met Mater Int 2020;26(8):1235–46.
[66] Vrancken B, Thijs L, Kruth J-P, Van Humbeeck J. Microstructure and mechanical properties of a novel β titanium metallic composite by selective laser melting. Acta Mater 2014;68:150–8.
[67] Fernandez-Zelaia P, Kirka MM, Dryepondt SN, Gussev MN. Crystallographic texture control in electron beam additive manufacturing via conductive manipulation. Mater Des 2020;195:109010.
[68] Bock FE, Herrnring J, Froend M, Enz J, Kashaev N, Klusemann B. Experimental and numerical thermo-mechanical analysis of wire-based laser metal deposition of Al-Mg alloys. J Manuf Process 2021;64:982–95.
[69] Aherwar A, Patnaik A, Pruncu CI. Effect of B4C and waste porcelain ceramic particulate reinforcements on mechanical and tribological characteristics of high strength AA7075 based hybrid composite. J Mater Res Technol 2020;9(5):9882–94.
[70] Tang J, Shen Y. Numerical simulation and experimental investigation of friction stir lap welding between aluminum alloys AA2024 and AA7075. J Alloys Compd 2016;666:493–500.
[71] Goldak J, Chakravarti A, Bibby M. A new finite element model for welding heat sources. Metall Trans A B 1984;15(2):299–305.
[72] Pierron N, Sallamand P, Matteï S. Study of magnesium and aluminum alloys absorption coefficient during Nd: YAG laser interaction. Appl Surf Sci 2007;253(6):3208–14.
[73] Chiumenti M, Lin X, Cervera M, Lei W, Zheng Y, Huang W. Numerical simulation and experimental calibration of additive manufacturing by blown powder technology. Part I: thermal analysis. Rapid Prototyp J 2017;23/2:448–63.
[74] Ren K, Chew Y, Fuh J, Zhang Y, Bi G. Thermo-mechanical analyses for optimized path planning in laser aided additive manufacturing processes. Mater Des 2019;162:80–93.

Paper 4: Unravelling the cracking mechanism in laser-directed energy deposition processing high-strength aluminum alloy (under preparation for submission)

This paper was under preparation for submission and incorporated as Chapter 4.5.

Unravelling the cracking mechanism in laser-directed energy deposition processing high-strength aluminum alloy

Mengjie Wang [a,*], Nowfal Al-Hamdany [a], Yujie Deng [b], Emad Maawad [c], Shengnian Luo [b], Nikolai Kashaev [a]

[a] Institute of Materials Mechanics, Department of Laser Processing and Structural Assessment, Helmholtz-Zentrum Hereon, Max-Planck-Str. 1, D-21502 Geesthacht, Germany
[b] School of Materials Science and Engineering, Southwest Jiaotong University, Chengdu, Sichuan 610031, People's Republic of China
[c] Institute of Materials Physics, X-Ray Diffraction with Synchrotron Radiation, Helmholtz-Zentrum Hereon, Max-Planck-Str. 1, D-21502 Geesthacht, Germany

*Corresponding author: mengjie.wang@hereon.de (M. Wang)

Abstract

High-strength aluminum alloys exhibit high cracking susceptibility in laser-based additive manufacturing. Understanding the mechanisms behind cracking and identifying the primary factors are crucial to preventing cracking, especially when dealing with difficult-to-process materials. Therefore, it is necessary to uncover the cracking mechanisms during successive deposition. In this study, the cracking mechanism is investigated in laser-directed energy deposition processing AA7075 alloy in terms of solidification conditions, microstructure, and residual stress. Based on the results, the cracking phenomenon observed during successive deposition is induced by insufficient backfilling to solidification shrinkage leading to solidification cracking. The melt-pool lifetime and the maximum melt-pool temperature are the primary factors determining the solidification cracking susceptibility. After the initiation, the cracks grow in two directions parallel to the building direction. The growth downwards is attributed to the liquation cracking mechanism, while the growth upwards results from the solidification cracking mechanism. The delayed cracking (cracking after a certain number of layers have been deposited) is identified as the consequence of the competitive growth between grains with preferential growth direction and highly misaligned grains.

Keywords

Laser-directed energy deposition; high-strength Al alloy; cracking mechanism; residual stress; microstructural analysis; solidification conditions.

1. Introduction

Hot cracking in welding can be categorized into three subgroups according to the formation mechanisms, i.e. solidification cracking, liquation cracking, and ductility-dip cracking [1]. The three cracking mechanisms differentiate from each other in terms of crack nucleation.

The solidification cracking occurs in the last phase of solidification [2]. In the semisolid state, the grains have grown and the liquid left needs to feed the area between grain boundaries. Otherwise, the shrinkage initiates after solidification and could act as nucleation sites for cracks and propagate under tensile stress until fracture. The solidification cracks initiate in the welds and could propagate along grain boundaries toward the weld surface center [3]. The heat transferred from the welds to the heat-affected zone (HAZ) could result in the partial remelting of secondary phases with low boiling points distributed along grain boundaries in the HAZ and the formation of liquid film [4]. Subsequently, the liquid film is torn apart from the solid under the tensile stress contributing to the formation of the liquation cracks. The liquation cracks are generated in the HAZ and could propagate either in the HAZ or to the fusion zone [5, 6]. The ductility-dip cracking exhibits no specific nucleation sites. According to the cracking mechanism, ductility-dip cracking is attributed to the ductility loss at the homologous temperature between 0.4 and 0.9 [7]. The cracks can initiate in the welds or HAZ, if the threshold of the temperature and tensile stress can be reached [8, 9]. The tensile stress is an essential ingredient for the propagation of the cracks in the three cracking mechanisms and is also important for the initiation of ductility-dip cracks.

Laser-based additive manufacturing (AM) is a rapid prototyping technology that employs laser as the energy source to melt material and produce structures. The physical mechanisms of laser beam welding and laser-based AM demonstrate similar characteristics in terms of rapid melting and solidification. Laser powder bed fusion (LPBF) and laser-directed energy deposition (L-DED) are two common technologies within laser-based AM. Regarding the processing differences between the two technologies, the feedstock is spread in a powder bed in LPBF, whilst the feedstock is fed through a nozzle coaxially or laterally to the laser beam in L-DED [10]. Additionally, the material in L-DED can be in the form of powder or wire, in contrast to LPBF, which uses only powder [10]. LPBF is able to produce structures with complex geometries, whereas L-DED is limited in terms of the variety of geometry [11]. Despite the distinctions between L-DED and LPBF, both technologies have limitations on the types of applicable materials due to the cyclic rapid melting and solidification as well as the high processing temperature, which could induce the formation of defects such as cracks and porosity [12].

Different types of materials manifest different degrees of cracking susceptibility in laser-based AM. There are also significant differences in cracking resistance even within a single alloy system such as Al alloys due to

the variation in the type or content of alloying elements [13]. Cast Al alloys with a high content of Si are suitable for AM. The addition of Si increases the melt-pool flowability and decreases the solidification temperature range improving the processability [13, 14]. Unlike cast Al alloys, wrought Al alloys such as 7XXX alloys are considered difficult to process. 7XXX alloys contain a lower content of Si and exhibit a large solidification temperature range contributing to high susceptibility for solidification cracking [14]. Besides, there is a substantial content of volatile elements such as Zn and Mg in 7XXX alloys, which could be evaporated at elevated temperatures and form porosity in as-built parts [15, 16]. Despite the processing difficulties, 7XXX as ageing-hardening alloy can be applied in the automotive [17] and aircraft industries [18], where high strength and lightweight are simultaneously in demand. Consequently, attempts to relieve the cracking susceptibility and improve the processability have been made by researchers.

The methods to improve the processability of difficult-to-process materials can be arranged into three phases: pre-processing preparation, in-process actions, and post-processing treatments. Before processing, the material can be modified by pre-alloying (different materials are mixed in a metallurgical manner) and material blending (different materials are mixed without melting and re-solidification). In terms of material blending for powders, the cracking-susceptible material can be modified by doping other materials via mechanical blending. By doping TiC [19] or ZrH_2 [20] particles into AA7075 alloy using the ball milling method, the hot cracking can be prevented during L-DED processing, which is attributed to the grain refinement caused by the dope particles as heterogeneous nuclei for α-Al matrix. A significant reduction of porosity level is also achieved by mechanically incorporating the TiC nanoparticles into Al-Mg-Sc-Zr alloys for L-DED processing [21]. However, it is challenging to achieve a homogeneous distribution of dope particles in the microstructure via mechanical blending [19]. By utilizing a bonding agent, a novel satelliting method enables the blending of materials through the decoration of larger parent particles with finer particles [22], which demonstrates less elemental segregation compared with the mechanical blending method [23]. Alternatively, the chemical composition of raw powders can be adjusted and pre-alloyed before atomization to avoid uneven dispersion of dope particles [24]. In wire-based L-DED, the chemical composition of feedstock can be modified by simultaneously feeding the cracking-susceptible wire material and additional wire materials. The feed speed of various wires and the adjustment of process parameters as well as the alignment of the experimental setup are critical for a smooth deposition [25, 26]. The achieved better processability and properties of as-built structures are explained by the enhanced laser absorption and the alleviated solidification shrinkage as well as the grain refinement [27, 28].

The actions adopted during processing concern the parameter adjustment and the optimization of building strategy [16, 29]. The appropriate process window should be investigated in terms of minimizing the defects and fulfilling geometrical requirements without sacrificing properties. Besides the parameter optimization, additional process control can be adopted to further assist the production. Preheating the substrate before deposition can reduce the cooling rate, temperature gradient, and the resultant residual stress leading to a lower cracking susceptibility [30]. The island scanning strategy can be used to reduce cracking susceptibility due to lower residual stress induced using shorter deposition lengths [31, 32]. This approach has been conducted in LPBF but has not been implemented in L-DED. A novel methodology is proposed by employing interlayer laser shock peening (LSP) during layer-by-layer deposition in L-DED processing AlSi10Mg alloy [33]. The interlayer LSP reduces the tensile residual stress in as-built structures, refines the grains, and improves mechanical properties. However, this methodology demands more advanced equipment. After the production of parts, hot isostatic pressing (metallic parts are simultaneously subjected to thermal annealing and pressure) is widely conducted to heal small cracks and porosity [34].

There are some experimental studies to investigate the origins of porosity formation in laser-based AM [35-37]. Research to analyze the cracking mechanism is based on simulation and analytics [38, 39]. Some premises are assumed for the simplification in simulation, which could contribute to high deviation compared with experiments. In fact, a great agreement between the thermal simulation and experimentally recorded temperature can be achieved [40]. Nevertheless, the calibration for the mechanical simulations with the experimentally obtained data such as the residual stress is either not reported [38, 40] or exhibits high deviation [39].

While several investigations have been carried out to analyze the cracking observed in AM, it remains challenging to fully comprehend the significance of various factors that contribute to cracking due to the complex physical processes involved in AM. A systematic analysis of the cracking mechanisms in laser-based AM is yet to be established. It is crucial to understand the cracking mechanisms and identify the primary factors in order

to effectively prevent cracking. Therefore, it is necessary to reveal the cracking mechanisms in laser-based AM processes, especially when dealing with difficult-to-process materials. This study aims to experimentally analyze the initiation and growth mechanisms of cracks observed during the successive deposition considering various factors that affect the cracking susceptibility of high-strength Al alloys in L-DED, such as solidification conditions, microstructure, and residual stress.

2. Experimental

2.1. Laser-directed energy deposition

2.1.1 Material

The material used in this study is AA7075 alloy in wire form with a diameter of 1.2 mm. The chemical composition was measured using an SEM (Jeol JSM-6490LV) equipped with energy-dispersive X-ray analysis (EDX, EDAX Genesis) and listed in Table 1. The material was melted by the laser (TruDisk 4001, TRUMPF SE and Co. KG) and layer-by-layer deposited on a 100 mm × 50 mm × 15 mm AA7075 substrate. Both sides of the substrate were clamped. The laser energy of this system is distributed in a core-ring profile. A constant core-ring ratio of 15 % was adopted throughout the study. The diameter of the core and ring is 100 μm and 400 μm, respectively. A laser spot diameter of 1.5 mm was maintained constant on the surface to be processed during the multi-layer deposition. Argon was adopted as a shielding gas to prevent oxidation and protect the melt pool.

Table 1. The chemical composition of AA7075 wire (in wt. %).

Zn	Mg	Cu	Mn	Ti	Cr	Si	Fe	Al
5.7	2.5	1.3	0.1	0.1	0.2	0.4	0.2	Bal.

2.1.2 Building strategy

Thin-wall structures with single track and multiple layers were built with a bi-directional scanning strategy, i.e., the deposition direction is rotated with an angle of 180 ° between adjacent layers. Three kinds of process parameters were adopted to build thin-wall structures, as illustrated in Figure 1. Besides the process parameters (laser power and laser scanning speed), three deposition lengths (30 mm, 50 mm, and 70 mm) were also used to investigate the effects of deposition length on the processing and properties of structures. The designation for these samples is $S1^N$ to $S5^N$. N is the number of deposited layers. A delayed cracking was observed in this study. When more than 30 layers were deposited, macro-cracks were observed in some samples with deposition lengths of 50 mm and 70 mm, see Figure 4(d, f). To analyze the property evolution during successive deposition and the resultant cracking susceptibility, samples with different deposition layers were built and characterized.

In building samples $S1^N$ to $S3^N$, the laser scanning speed remained constant, while the laser power decreased from 4000 W to 3000 W and then stayed unchanged. The difference among samples $S1^N$, $S2^N$, and $S3^N$ is the deposition length, i.e. the length of thin-wall structures ($S1^N$: 30 mm, $S2^N$: 50 mm, $S3^N$: 70 mm). The deposition length of samples $S4^N$ and $S5^N$ is the same as sample $S3^N$. Line energy density is the ratio of laser power and laser scanning speed [41]. It is proposed to represent the laser energy input in L-DED. The laser power and laser scanning speed were simultaneously reduced to keep the same line energy density in building sample $S4^N$. As a control group, sample $S5^N$ was also deposited with the same constant line energy density as sample $S4^N$. However, the laser power and laser scanning speed remain unchanged during deposition. The process parameters for each sample are listed in Table 2.

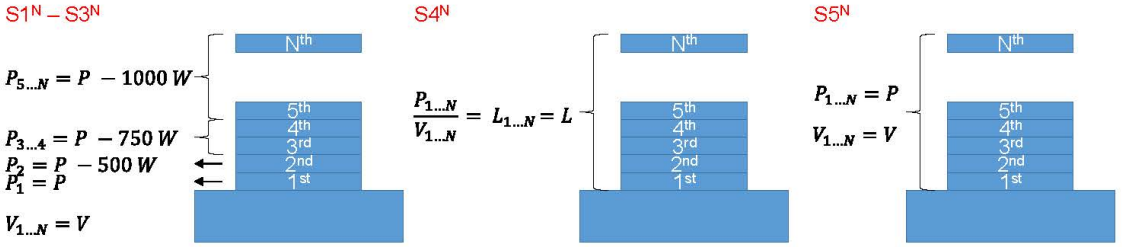

P: initial laser power (W)
P_n: laser power in the n^{th} layer (W)
V: initial laser scanning speed (W)
V_n: laser scanning speed in the n^{th} layer (W)
L: initial line energy density (J/mm, $L = P/V$)
L_n: line energy density in the n^{th} layer (W)

Figure 1. Illustration of the adjustment for laser power, laser scanning speed, and line energy density in building thin-wall structures named samples $S1^N$ to $S5^N$. N is the number of deposited layers.

Table 2. Detailed process parameters depending on the layer number in building samples $S1^N$ to $S5^N$. N is the number of deposited layers. In building sample $S4^N$, if the number of deposited layers exceeds 37, the laser power and laser scanning speed are only reduced to 2560 W and 640 mm/s, respectively, since a further reduction leads to insufficient melting.

Sample name	Deposition length (mm)	Layer number/ laser power (W)	Layer number/ laser scanning speed (mm/s)	Wire feed speed (mm/min)	Number of deposited layers
$S1^N$	30	1st layer: 4000 2nd layer: 3500 3rd-4th layers: 3250 5th-Nth layers: 3000	1st-Nth layers: 1000		
$S2^N$	50				
$S3^N$	70				
$S4^N$	70	1st layer: 4000 2nd layer: 3960 3rd layer: 3920 … 37th layer: 2560 38th – Nth layer: 2560	1st layer: 1000 2nd layer: 990 3rd layer: 980 … 37th layer: 640 38th – Nth layer: 640	4000	N
$S5^N$	70	1st-Nth layers: 4000	1st-Nth layers: 1000		

2.1.3 Process monitoring

The thermal history of different samples was recorded during the L-DED processing by an infrared camera (Optris PI400). The resolution, frequency, and spectral range are 382 × 288 pixels, 27 Hz, and 7.5 – 13 µm, respectively. The infrared camera was focused at the center of thin-wall structures, as shown in Figure 2(d-f). The used technology shows the highest accuracy in the temperature range of 150 – 900 °C according to the manufacturer's specification. However, the maximum measurable temperature range can be expanded to 20 – 1500 °C, where the temperature range beyond the recommendation exhibits a relatively lower accuracy. The emissivity is dependent on many factors such as material and surface roughness as well as the current temperature [42]. The emission coefficient of AA7075 during L-DED was calibrated by using thermocouples. The thermocouples were inserted at the calibration point on the substrate and located 0.5 mm below the substrate surface, as illustrated in Figure 2b. The calibration was conducted in a single-track deposition. During the deposition, the temperature evolution was recorded by the infrared camera and thermocouples. A good agreement was achieved between the infrared camera and thermocouples when the emission coefficient was set at 0.32. Despite the fluctuation of emissivity in various temperature ranges, a constant emission coefficient

was assumed in this study, since temperature evolutions of different samples during processing were compared in the same temperature range.

The building direction and the longitudinal direction for deposition are sketched in Figure 2a. The thermal history in the cooling phase during the deposition of the 30th layer was extracted and analyzed from samples S1^{30} to S5^{30} (reasons for selecting the 30th layer can be referred to in Section 4.3.1). It is difficult to explicitly find the position of the last layer in the height building direction from the thermography images. Hence, the following workflows were conducted: in the 30 mm sample (S1^{30}), a matrix consisting of 40 points was selected, which covers the entire last layer in the building direction and the middle part of the last layer in the longitudinal direction (8 rows, 5 columns, the size of each point and the matrix is 0.48 mm × 0.48 mm and 19.2 mm × 3.8 mm, respectively. As shown in Figure 2d, each white dot corresponded to a measuring point). The point in each column exhibits the highest maximum temperature during the last-layer deposition among the 8 points was considered the position of melt pools. Subsequently, 5 points were selected along the longitudinal direction, and the temperature evolution of the 5 points in the 30th layer was used to represent the cooling conditions of sample S1^{30}. The same workflow was also applied for samples S2^{30} to S5^{30}. A matrix with more columns in the longitudinal direction was employed to cover the middle part of the last layer and reflect the overall cooling conditions. In a short conclusion, 5, 7, and 11 cooling curves were extracted and analyzed along the longitudinal direction in the 30th layer from the processing of thin-wall structures with deposition lengths of 30 mm (Figure 2d), 50 mm (Figure 2e), and 70 mm (Figure 2f), respectively.

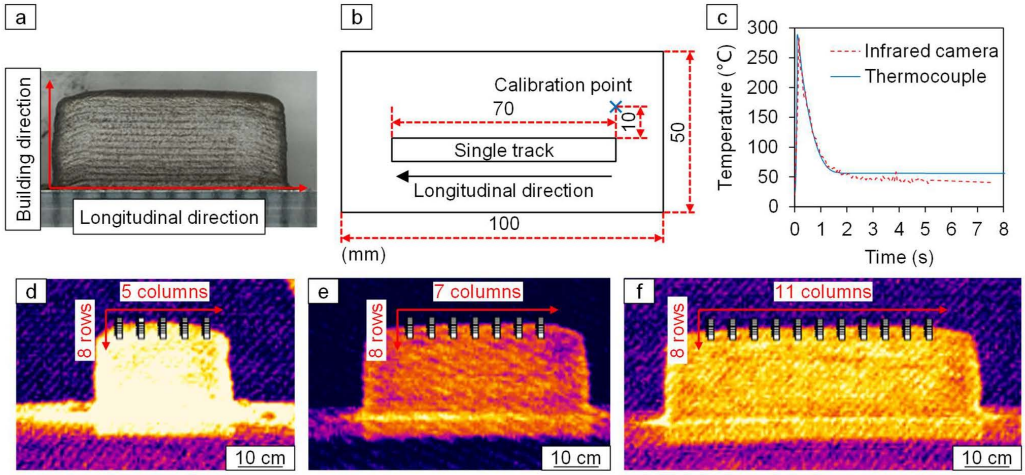

Figure 2. (a) Building direction and longitudinal direction for deposition. (b) Illustration for the setup to calibrate the emission coefficient. (c) Temperature evolution at the calibration point as shown in (b) captured by thermocouples and an infrared camera with the setting of emission coefficient at 0.32. (d)-(f) Thermography images while building samples S1^{30} to S3^{30}, where the points to extract the temperature evolution are also marked with white dots. The temperature evolution of (d) 40 points (8 rows, 5 columns), (e) 56 points (8 rows, 7 columns), and (f) 88 points (8 rows, 11 columns) are extracted and analyzed from the processing of thin-wall structures with deposition lengths of 30 mm, 50 mm, and 70 mm, respectively.

2.2. Post-process characterization

2.2.1 Residual stress analysis

The residual stress was calculated based on the experimental diffraction data acquired at the High Energy Materials Science beamline P07b (EH1) at DESY [43]. Experimental setups are presented in Figure 3a and the measuring pattern for sample S1^{N} is exemplarily depicted in Figure 3b. The thin-wall structure was mounted on the sample stage so that the building direction of the structure is parallel to the z axis (in the direction of σ_{yy}) and the longitudinal direction of the structure is parallel to the x axis (in the direction of σ_{xx}), as shown in Figure

3b. An x-ray beam of energy 87.1 keV (wavelength of 0.142353 Å) with a size of 0.5×0.5 mm^2 was used for the measurement of residual strain along the building direction. The distance between the thin-wall structure and the two-dimensional detector type Perkin Elmer XRD 1621 (PE) was 1200 mm. Debye Scherrer rings for several reflections was recorded and the (3 1 1) reflection was used to calculate the residual stresses since the grains with the (3 1 1) planes exhibit the smallest influence from residual intergranular stress and lower influence from the crystallographic texture [44]. Due to the large grain size, the sample was oscillated for each measurement point in the direction of σ_{xx} with ± 2.5 mm to obtain better statistics. For each measuring point, the exposure time was 10 s. To characterize the variation of residual stress along the building direction, the residual strain measurements along the building direction started from 0.5 mm from the top surface with a moving step of 2 mm until it reached the substrate, as shown in Figure 3b. The measurement of residual strain along the building direction was performed at different locations starting from the middle of the structure to both edges with a moving step ± 5 mm (Figure 3b). For the thin-wall structures with deposition lengths of 50 mm and 70 mm, 5 and 7 measuring sequences with the same setting as for sample S1^N were utilized to determine the residual stress in the middle parts.

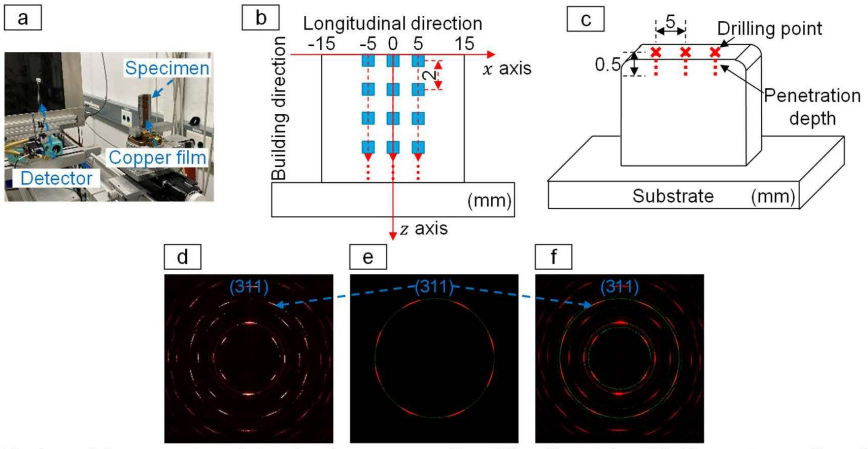

Figure 3. (a) Photos of the experimental setup to measure the diffraction data. (b) Measuring pattern for the thin-wall structure with a deposition length of 30 mm. (c) Sketch showing the position of drilling points in the hole-drilling measurement. (d) Measured partial diffraction rings. (e) Complete (3 1 1) diffraction ring after data recovery using ellipse fitting; (f) Full diffraction rings after data recovery. The solid red lines are the diffraction patterns experimentally measured. The dotted green lines are the recovered diffraction patterns.

To avoid any misalignment effect that arose from the sample geometry on the residual stress calculation, a thin layer of copper powder was coated on the sample surface and a correction factor based on shifting of a copper reflection close to (3 1 1) from Al was utilized.

The residual stress was calculated from the measured strain based on the fundamental equation of strain (Equation 1 to 3) and by using the elastic constant E311: 69.39 GPa and the poison's ratio v_{311}:0.35 of Al obtained from XEC software [45]. Since cracks observed in this study grew along the building direction and perpendicular to the longitudinal direction, see Figure 4 and Figure 6, the residual stress along the longitudinal direction (σ_{xx}) exhibits pronounced impacts on the crack growth. Hence, the residual stress along the longitudinal direction is considered and analyzed in the following parts.

To measure the d_0, a stress-free sample is required. Therefore, a pin from the middle of a second thin-wall structure with comparable process parameters was cut. A pin with a cross-section of 3×3 mm^2 and a height comparable to samples S1^N to S5^N was cut using electrical discharge machining (EDM).

$$\varepsilon_{hkl} = \frac{(d_{hkl} - d^0_{hkl})}{d^0_{hkl}} = \frac{\sin\theta^0_{hkl}}{\sin\theta_{hkl}} - 1 \qquad \text{Equation 1}$$

$$\sigma_{Long.} = \frac{E_{hkl}}{1 - {v_{hkl}}^2}(\varepsilon_x + v_{hkl}\varepsilon_y) \quad \text{Equation 2}$$

$$\sigma_{Build.} = \frac{E_{hkl}}{1 - {v_{hkl}}^2}(\varepsilon_y + v_{hkl}\varepsilon_x) \quad \text{Equation 3}$$

The two-dimensional diffraction pattern measured for L-DED-processed Al alloys is incomplete due to the lack of information, such as the (3 1 1) crystal plane as shown in Figure 3d, which is attributed to the intrinsic characteristics of the microstructure such as coarse grains and strong texture, respectively. Hence, the partial diffraction patterns were recovered by employing ellipse fitting (Figure 3e and f), which has been validated as a reliable methodology for completing the partial diffraction rings [46]. Afterward, the complete diffraction patterns were employed to calculate the strains for the (3 1 1) crystal plane and the corresponding residual stress. The residual stress was also analyzed on the top surface of samples along the longitudinal direction by the hole-drilling method using PRISM system (Stresstech GmbH). A hole with a 1.0-mm diameter was incrementally drilled to a maximum depth of 0.5 mm using a drill made of high-speed steel Co 5 with a TiAlN solid carbide insert. The drilling depth was increased in 0.025 mm increments. Three holes were drilled on the top surface with a distance of 5 mm along the longitudinal direction for each sample, as sketched in Figure 3c.

2.2.2 Microstructural characterization

Cross-sectional images of samples were captured by an optical microscope (OM, Leica DMI 5000M) to reveal the porosity level and global microstructure. Samples were cut in the middle parts of thin-wall structures to ensure comparability. The electron backscatter diffraction (EBSD) measurements were conducted for the determination of grain size. The area fraction and distribution of secondary phases were observed under a scanning electron microscope (SEM, FEI Nova 200). To analyze the macro-crack observed in this study, the thin-wall structure was ground and polished along the transverse direction, see Figure 5a. Besides, the fracture surface of the macro-cracks was also analyzed using a digital microscope (VHX-7000, Keyence). Barker's reagent was used as an etchant for as-built and heat-treated samples to expose grain structures.

2.2.3 Thermodynamic simulation

A Pandat 2020 software and Al database PanAluminum were employed to implement thermodynamic simulations. The PanPhaseDiagram module and a simple Scheil solidification model were adopted. The maximum temperature step size was set at 4 K. The solidification path was obtained from the simulations. The solute diffusion in solid is not considered in this Scheil solidification model.

3. Results

3.1. Cracking phenomenon

Based on our previous studies investigating the optimal process parameters for producing thin-wall structures with a deposition length of 30 mm [47, 48], it was found that L-DED processing AA7075 alloy exhibited a narrow appropriate process window regarding the minimization of internal defects such as porosity and cracks. By using the optimal process parameter, a porosity level of approx. 2 % and a crack-free microstructure can be achieved in the as-built thin-wall structures. The processing remained stable and the deterioration of properties was not observed with the increase of deposition layers.

The deposition length was not previously considered as a variable in [47, 48]. However, the current study has discovered that the deposition length is an important parameter that significantly impacts the processability. As the deposition length of thin-wall structures increases, the processability is significantly damaged despite using the same process parameter (samples $S1^N$ to $S3^N$). As shown in Figure 4(a, b), the structural integrity of thin-wall structures with a deposition length of 30 mm can be well maintained from 30 to 100 layers. No visible defects are present on the structure's surface and the L-DED processing proceeds without any noticeable anomaly. As the deposition length increases from 30 mm to 50 mm, a crack-free thin-wall structure with 30 layers can be successfully produced. Nevertheless, macro-cracks are observed on the surface of the structure with 51

layers, see Figure 4d. The length of the macro-crack is 8.1 mm. Increasing the deposition length to 70 mm still enables the production of crack-free structures with 30 layers (Figure 4e). Yet, two visible macro-cracks, measuring 11.4 mm and 10.6 mm in length, appear on the surface of the thin-wall structure with 51 layers, see Figure 4f.

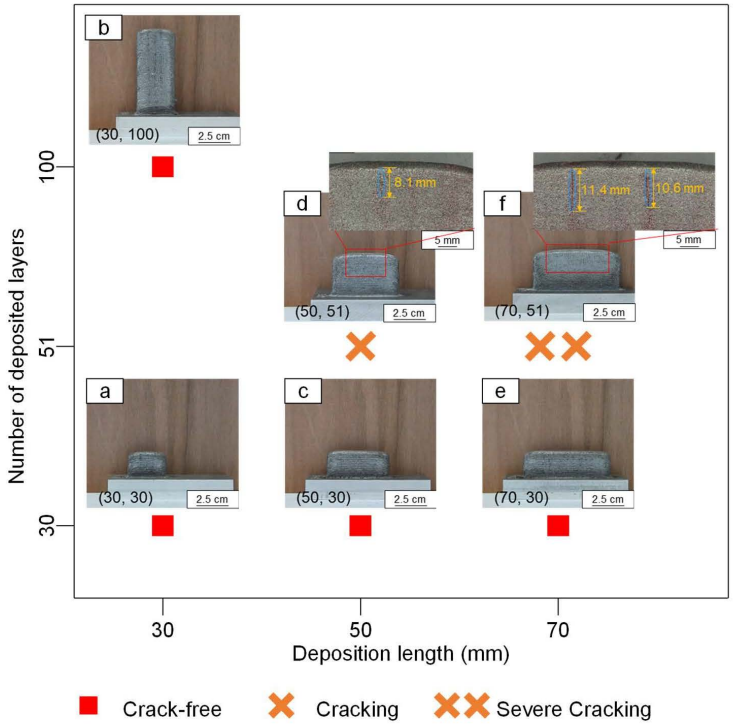

Figure 4. Dependence of cracking susceptibility on deposition length and number of deposited layers. Images of as-built thin-wall structures: (a) $S1^{30}$ (deposition length of 30 mm and 30 deposited layers); (b) $S1^{100}$ (deposition length of 30 mm and 100 deposited layers); (c) $S2^{30}$ (deposition length of 50 mm and 30 deposited layers); (d) $S2^{51}$ (deposition length of 50 mm and 51 deposited layers); (e) $S3^{30}$ (deposition length of 70 mm and 30 deposited layers); (f) $S3^{51}$ (deposition length of 70 mm and 51 deposited layers). The Deposition length and the number of deposited layers are also noted as (x, y) in the left bottom corner of each image. The same process parameter set was used to build the structures (a) – (f). Laser power in 1st layer: 4000 W, 2nd layer: 3500 W, 3rd – 4th layers: 3250 W, from the 5th layer: 3000 W; laser scanning speed: 1000 mm/s, wire feed speed: 4000 mm/min. Visible macro-cracks are circled with blue ellipses and the corresponding length is measured. The layer number of structures is noted in the corner of the images.

Sample $S3^{51}$ from Figure 4f is ground and polished along the transverse direction. The macro-crack with a length of 11.4 mm is observed under the optical microscope after etching, see Figure 5(a-e). Columnar grains epitaxially grow across several layers and dominate the microstructure. The macro-crack initiates and grows during processing along two directions parallel to the building direction. The macro-crack exhibits an intergranular growth, as observed at the bottom of the macro-crack (Figure 5e). It is noticed that large pores with regular morphology are distributed around the macro-crack. However, these large pores are present in the upper part of the macro-crack (noted as area A), while they are absent in the lower part (area B and C). In addition to large pores, some transgranular micro-cracks initiate and grow across several grains in the upper part of the macro-crack.

The macro-crack is also analyzed from the view of the fracture surface (B-B cross-section as shown in Figure 5f). The fracture surface is also categorized into areas $A - C$, the same as in Figure 5a. The upper part (area A) of the fracture surface exhibits rougher and darker surface compared with the lower part (area C). In

locally magnified images of the areas A and C, the intergranular fracture surface is noticed exhibiting smooth grain facets. Area C demonstrates a higher area fraction of liquid film. The oxidation in area A is more severe than that in area C.

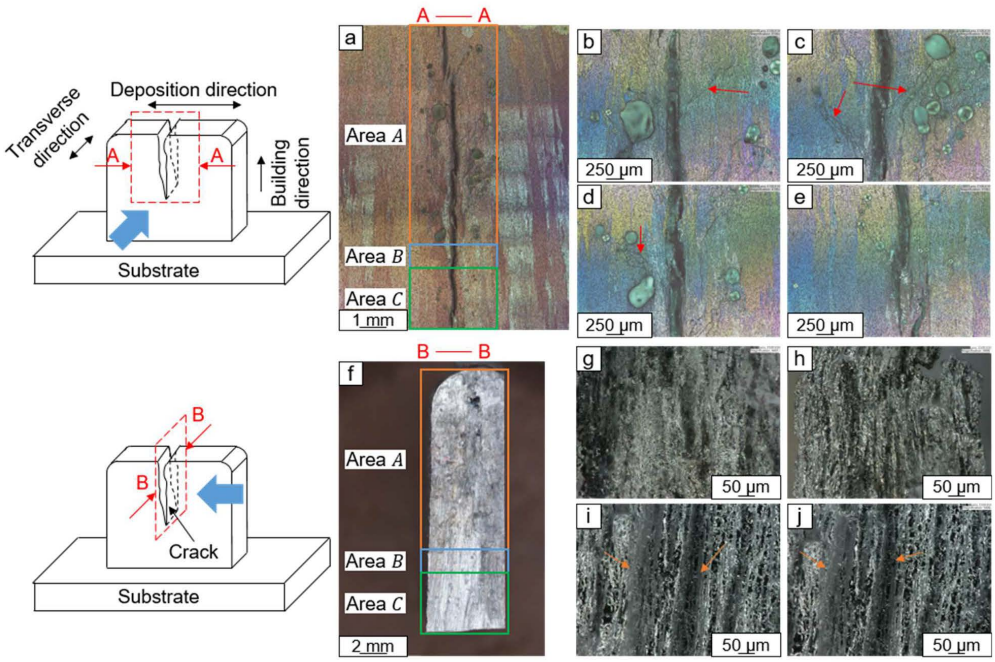

Figure 5. Metallographic observation of macro-cracks with a length of 11.4 mm in sample S3[51]. (a) A-A Cross-sectional microstructure after ground, polishing, and etching. The viewing point is along the transverse direction of the thin-wall structure, as illustrated on the left of (a). (b-d) Locally magnified images in area A. (e) Locally magnified image in area C. (f) B-B Cross-sectional view of the fractured surface without any metallographic preparation. The viewing point is along the deposition direction of the thin-wall structure, as illustrated on the left of (f). (g-h) Locally magnified images in area A. (i-j) Locally magnified image in area C. Micro transgranular cracks are pointed by red arrows in (b, c, d). Liquid film on grain boundaries is pointed by orange arrows in (i, j).

The parameter optimization is conducted in thin-wall structures with a deposition length of 70 mm to investigate whether an appropriate parameter set is available to build crack-free structures without layer-number limits. The laser power and laser scanning speed decrease by the same percentage as the deposition layer increases to maintain a constant line energy density. The 30-layer sample built with this process parameter is named sample S4[30]. As a control group, the laser power and laser scanning speed as well as the line energy density remain constant simultaneously. The 30-layer sample built with this process parameter is named sample S5[30]. Samples S4[30] and S5[30] exhibit no macro-cracks on the surface (Figure 6a and c). Nevertheless, serious cracking occurs in the 51-layer sample S5[51], as shown in Figure 6b. Crack-free sample S4[100] with 100 layers can be successfully produced.

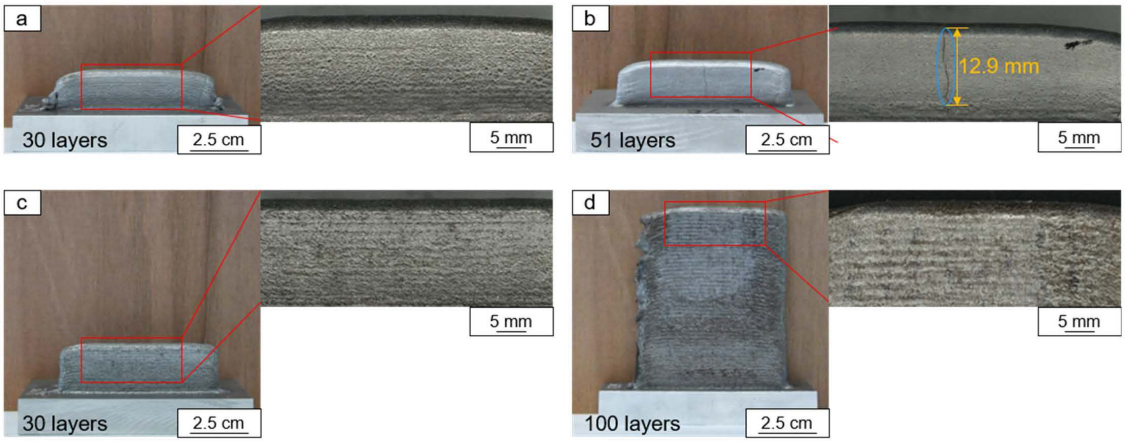

Figure 6. Images of as-built thin-wall structures with a deposition length of 70 mm (a, b) samples $S5^{30}$ and $S5^{51}$ built with constant laser power and laser scanning speed of 4000 W and 1000 mm/s. (c, d) samples $S4^{30}$ and $S4^{100}$ built with constant line density but decreasing laser power and laser scanning speed. Laser power and laser scanning speed are reduced by 40 W and 10 mm/s per layer starting with 4000 W and 1000 mm/s in the 1st layer. In the 100-layer thin-wall structures, laser power and laser scanning speed are reduced until 2560 W and 640 mm/s and then kept constant, since further reduction leads to insufficient melting. Visible macro-cracks are circled with blue ellipses and the corresponding length is measured. The layer number of structures is noted in the corner of the images.

In addition to parameter optimization, the concept of using the island scanning strategy to prevent cracking in LPBF is also attempted in L-DED processing in this study. However, it failed. The results and analysis can be referred to in Section A.3.

3.2. Microstructure

The three thin-wall structures with 30 layers, i.e. samples $S1^{30}$ to $S3^{30}$ (Figure 4(a, c, e)) are investigated under an optical microscope to examine the microstructure and the presence of micro-cracks. Figure 7a exemplarily exhibits the cross-sectional image of sample $S1^{30}$ and the etched microstructure in the middle. Sample $S1^{30}$ with the shortest deposition length exhibits the highest cross-sectional porosity level. A comparable cross-sectional porosity level is observed in samples $S2^{30}$ and $S3^{30}$, as shown in Figure 7b. As the deposition length increases from 30 mm to 70 mm, the average thickness of thin-wall structures increases from 6.21 mm to 6.44 mm, which indicates the widening of melt pools and could be attributed to heat accumulation during processing. The porosity is homogeneously distributed in the cross-sections of three samples. The spherical morphology [49] and the random distribution [50] of pores are considered the typical characteristics of gas pores. The formation of gas pores could be attributed to the evaporation of volatile elements due to excessive process temperature [51] and hydrogen entrapment in the melt pools [49]. Strong textured microstructure can be observed in the etched microstructure. The large columnar grains grow along the heat flow direction [14]. No micro-crack can be detected neither in the cross-sectional images nor the locally magnified microstructure. It indicates that the crack-free 30-layer thin-wall structures with different deposition lengths can be produced using the same process parameter. However, the formation and solidification of melt pools exhibit some discrepancies deduced from the wall thickness and the cross-sectional porosity level. The threshold layer number from which the macro-crack initiates and grows has not been reached in the 30-layer samples $S2^{30}$ to $S3^{30}$.

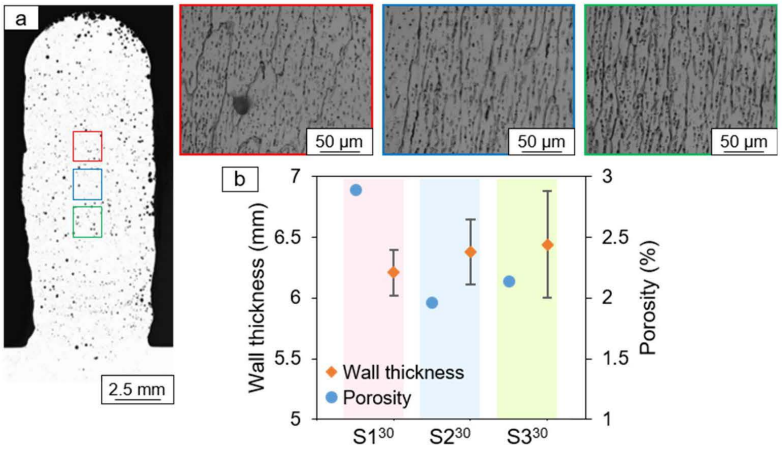

Figure 7. (a) Cross-sectional images of as-built sample $S1^{30}$ and its corresponding etched microstructure at the middle of the cross-sections. The magnified etched microstructure is placed in the right of the global cross-sections. (b) Cross-sectional porosity level and wall thickness of samples $S1^{30}$ to $S3^{30}$. The wall thickness is calculated by averaging the 10 measurements of the thickness from the top to the bottom of the wall.

Due to the large grain size of L-DED processing AA7075 alloy, the dimension of the maximum field of view in conventional EBSD measurement is less than the length of a grain leading to a high measuring deviation of grain size [48]. In this study, the grain size is represented by the primary dendrite spacing for the large columnar grains in the middle of thin-wall structures, as suggested in [52], and the average grain area of the equiaxed grains at the top of the last deposition layer. The area of equiaxed grains is measured in the images of the etched microstructure captured under OM. As shown in Table 3, the average grain area increases with increased deposition length ($S1^{30}$ to $S3^{30}$). The primary dendrite spacing is determined using EBSD measurement in the middle of thin-wall structures. Misorientation over 5 degrees is considered to be at grain boundaries. The dependence of primary dendrite spacing on the deposition length is not noticed.

Table 3. Average grain area and corresponding aspect ratio of the equiaxed grains on the top of the last deposition layer and the primary dendrite spacing of the large columnar grains in the middle of thin-wall structures.

	$S1^{30}$	$S2^{30}$	$S3^{30}$
Average grain area (mm^2)	0.14 ± 0.07	0.15 ± 0.06	0.19 ± 0.06
Aspect ratio	1.82 ± 0.69	1.94 ± 0.76	2.21 ± 0.97
Primary dendrite spacing (µm)	38.62 ± 4.32	41.32 ± 5.65	39.40 ± 4.41

Table 4 shows the correlation between the area fraction of secondary phases inside grains and along grain boundaries with the deposition length (an illustration showing the workflow for calculating the area fraction of secondary phases is inserted in Section A.2). Given the standard deviation between the measurements, the average area fraction of secondary phases in samples $S1^{30}$ to $S3^{30}$ is considered comparable.

Table 4. The average area fraction of secondary phases of samples $S1^{30}$ to $S3^{30}$.

	$S1^{30}$	$S2^{30}$	$S3^{30}$
Average area fraction (%)	2.55 ± 0.31	3.21 ± 0.47	3.14 ± 0.49

3.3. Residual stress

The residual stress in Figure 8(a-b) is analyzed using the hole-drilling method with a drill diameter of 1 mm and a drilled depth of 0.5 mm. Analysis is conducted on the top surface of as-built samples $S3^{20}$ with 20 layers and $S3^{30}$ with 30 layers, respectively. The magnitude of residual stress at each depth is averaged based on

three measuring points along the longitudinal direction. Figure 8a and Figure 8b illustrate that the magnitude of residual stress is not correlated with the number of deposited layers as the process has stabilized, i.e., as the heat transfer is less dependent on the substrate. With the increase of deposited layer number from 20 to 30, a stress accumulation is not noticed at the top of thin-wall structures.

The residual stress in Figure 8(d-e) is analyzed using the synchrotron X-ray diffraction. In Figure 8e, despite a higher standard deviation, the average and maximum tensile residual stress of sample $S1^{100}$ with 100 layers, are comparable to those of sample $S1^{30}$ with 30 layers. This finding further supports the conclusion that stress accumulation is not noticed at the top of thin-wall structures as the processing has stabilized.

Figure 8d depicts the distribution of residual stress in sample $S4^{100}$ with 100 layers. The upper part of the thin-wall structure exhibits tensile residual stress, whereas the compressive residual stress is generated in the lower part. The maximum tensile residual stress is observed in the last several deposition layers. This stress distribution is consistent with the simulation results in [53] and the experimental measurements obtained from X-ray diffraction patterns in [54]. To statistically compare the magnitude of the tensile residual stress of different samples, measurements from the top three rows, as marked in Figure 8d, are averaged for each sample and noted as the average residual tensile stress. The maximum tensile residual stress represents the highest value among these measurements. As shown in Figure 8e, samples $S1^{30}$ to $S3^{30}$, processed with the same process parameter but different deposition lengths, exhibit a comparable magnitude of average tensile residual stress ($S1^{30}$: 63.2 MPa, $S2^{30}$: 66 MPa, $S3^{30}$: 65.3 MPa). However, the maximum residual tensile stress in samples $S3^{30}$ (98.1 MPa) and $S2^{30}$ (96.6 MPa) is higher than that in samples $S1^{30}$ (83.3 MPa).

As the deposition proceeds and stabilizes, the heat transfer becomes less dependent on the substrate leading to a comparable magnitude of residual stress in the upper part of samples with different numbers of deposited layers, as confirmed by the hole-drilling method and the synchrotron radiation. In sample $S4^{100}$ with 100 layers, the maximum tensile residual stress and the average tensile residual stress have reached 152.1 MPa and 86.8 MPa, respectively, which are significantly higher than those obtained in samples $S1^{30}$, $S2^{30}$, $S3^{30}$, and $S1^{100}$.

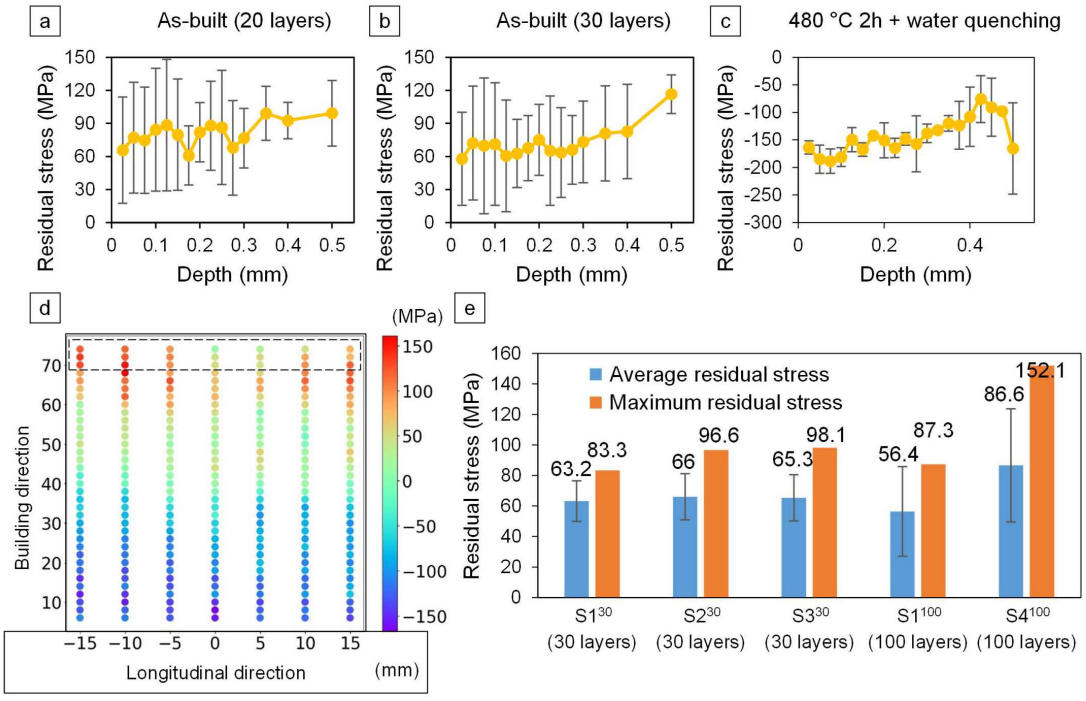

Figure 8. Residual stress analysis: (a) residual stress of as-built sample $S3^{20}$ with 20 layers; (b) residual stress of as-built sample $S3^{30}$ with 30 layers; (c) residual stress of sample $S3^{30}$ with 30 layers heat-treated at 480 °C for 2 h and water-quenched; (d) distribution of residual stress of sample $S4^{100}$ with 100 layers; (e) average and maximum residual stress of samples $S1^{30}$ to $S3^{30}$ with 30 layers and two samples $S1^{100}$ and $S4^{100}$ with 100 layers, respectively. The residual stress shown in (a-c) and (d-e) was analyzed by the hole-drilling method and synchrotron X-ray diffraction, respectively. The residual stress compared here is σ_{xx}, which is along the longitudinal direction of thin-wall structures, see Figure 3b.

4. Discussion

4.1. Growth of cracks

The macro-crack initiates from a certain layer and grows in two directions along the building direction. The large pores are distributed around the flank of the macro-crack. However, the macro-crack and the large pores are not connected. There should be a correlation between the initiations of them.

Under the assumption that the macro-crack is induced by the large pores, it is acknowledged that the stress concentration around the large pores could contribute to the initiation of cracks [55] and the cracks further grow under tensile residual stress. If this is the case, the growth of cracks should start from the location of large pores. However, the macro-crack has no contact with large pores. In addition, the large pores are regularly distributed around the macro-crack. Therefore, it is more reasonable that the large pores are generated attributed to the presence of the macro-crack.

The pores with regular morphology are considered gas pores [50], which could escape from the melt pools before the melt pools solidify [37]. The macro-crack could initiate in the transition area B between area A and area C, as marked in Figure 5. The macro-crack grows downwards to the lower part (area C, similar to the growth to the heat-affected zone in welding) and upwards to the upper part (area A, similar to the growth to the welds) of the structure. With further deposition after the crack has been initiated, in the upper part (area A), the material undergoes melting and solidification. As the macro-crack is present, it provides an additional cooling channel for melt pools near the crack and thus decreases the time that the liquid melt pools exist. The flow of a gas bubble in melt pools is determined by gravity, buoyancy, and Marangoni convection [50]. The larger the gas bubble size the more likely it is to be trapped in melt pools [50]. Therefore, the large gas bubble cannot escape from melt pools leading to the entrapment of gas bubbles around the macro-crack in as-built samples. At the lower part (area C), the macro-crack does not influence the solidification of melt pools since this area has already solidified before the initiation of the crack. Therefore, no large pores are observed around the macro-crack in the area C. In other words, the growth of the macro-crack in area C is a consequence of liquation cracking, whereas the growth of the macro-crack in area A is a consequence of solidification cracking. A higher area fraction of liquid film in area C supports this assumption. The morphological difference and the oxidation degree in these two areas, as shown in Figure 5f, could also be evidence of the different cracking mechanisms. Nevertheless, the reason for the initiation of the macro-crack needs to be further analyzed as follows.

4.2. Initiation of cracks - Liquation cracking analysis

4.2.1 Dependence of liquation cracking susceptibility on deposition length

The susceptibility of liquation cracking is analyzed by considering the remelting of eutectic phases and the magnitude of tensile residual stress. The secondary phases are eutectic phases with low melting points, which could be remelted forming a liquid film in the heat-affected zone and leading to cracking under tensile residual stress, so-called liquation cracking [56]. As the area fraction of eutectic phases or the magnitude of tensile residual stress increases, the susceptibility of liquation cracking should be enhanced.

The content of eutectic phases is comparable in as-built samples $S1^{30}$ to $S3^{30}$ (Table 4), while the magnitude of the maximum tensile residual stress of sample $S1^{30}$ is lower than those of samples $S2^{30}$ and $S3^{30}$ (Figure 8e, $S1^{30}$: 83.3 MPa, $S2^{30}$: 96.6 MPa, $S3^{30}$: 98.6 MPa). Given that no distinct difference in grain size is noticed between these samples (Table 3), it can be inferred that sample $S1^{30}$ with the shortest deposition length of 30 mm should have the least cracking susceptibility, which is in agreement with the observations during

deposition. However, the cracking susceptibility of samples S2[30] (deposition length: 50 mm) and S3[30] (deposition length: 70 mm) should be similar, which does not correspond to the experimental observations.

It cannot be determined based on the above-mentioned results whether there is a dependence of liquation cracking susceptibility on the deposition length and whether the initiation of the macro-cracks observed in this study is a consequence of liquation cracking.

4.2.2 Evaluation of the heating effects during successive deposition to previous layers

No dependence between the two factors determining the liquation cracking susceptibility (eutectic phase and tensile residual stress) and the deposition length can be noticed. However, it is not plausible to exclude that the liquation cracking mechanism is not the reason for the initiation of macro-cracks observed in this study.

Heat treatment conducted here is designed to analyze the heating effects during successive deposition to the eutectic phases in previously solidified layers. The temperature of heat treatment is set at 480 °C since it is reported that the maximal melting point of different eutectic phases in AA7075 alloy is around 480 °C [57, 58], which can also be supported by the thermodynamic simulation conducted in this study, see Figure 12a. The phase diagram calculated based on the Scheil solidification model indicates that the eutectic phases present after solidification have a maximal liquidus temperature of around 480 °C. The holding time for 2 h ensures the dissolution of eutectic phases into the α-Al matrix. Water quenching follows after the heating to prevent the re-precipitation of eutectic phases.

The building process for the thin-wall structure (Figure 9a) first starts with the deposition of the lower part. Subsequently, the lower part is artificially heat-treated at 480 °C for 2 h followed by water-quenching. Eventually, the upper part is further deposited on the top of the lower part.

The upper part and the lower part of this thin-wall structure exhibit different microstructures. The grain morphology in the lower part can be distinguished, whereas the grain morphology in the upper part is ambiguous. The visual discrepancy of the grain morphology is caused by the dispersively distributed eutectic phases. Substantial coarse eutectic phases dispersively distributed can be observed in the upper part (Figure 9b), whereas the small precipitates in the nanometer scale cannot be detected (Figure 9c). The number density of coarse eutectic phases is significantly reduced in the lower part (Figure 9g), while the nanometer-size precipitates are present (Figure 9h). The precipitates manifest a rod-like shape, which is typical η phase in Al-Zn-Mg alloys as reported in [59]. In the transition zone between the upper and lower parts (Figure 9d), the discrepancy of phases is more pronounced. A higher number density of the η phase is present in the area of the transition zone, which is artificially heat-treated (Figure 9f). The absence of η phase is noticed in the upper area of the transition zone. In the lower part of the thin-wall structure, the coarse eutectic phase dissolves into the matrix during the heat treatment at 480 °C for 2 h.

For the lower part, the cyclic heating imposed from building the successive layers in the upper part provides the driving force for the precipitation of the η phase. However, for the upper part itself, the cyclic heating during successive deposition exhibits no significant influence on the dissolution of coarse eutectic phases to the matrix in the previous layers of the upper part. It indicates a weaker heating effect of successive deposition compared with the artificial heat treatment at 480 °C for 2 h. According to [60], the high cooling rate induced by water quenching could increase the solubility of solutes in the α-Al matrix and suppress the precipitation of eutectic phases after heating at 480 °C. Conversely, it could be possible that the cyclic heating during successive deposition could provide sufficient heating effects and driving force to dissolve eutectic phases. However, the relatively slow cooling rate cannot suppress the precipitation of eutectic phases during air cooling after deposition. Therefore, a thin-wall structure is heat-treated at 480 °C and cooled in the air to compare with the thin-wall structures under two different conditions (heat-treated at 480 °C and water-quenched, not heat-treated/as-built). As shown in Fig. A. 4 of Section A.4, the grain morphology of the sample cooled in the air after heat treatment (Fig. A. 4b) can also be distinguished, which has been confirmed as the consequence of the absence of eutectic phases. In contrast, the as-built sample exhibits an ambiguous grain morphology (Fig. A. 4c). This observation

supports the conclusion that the heat treatment at 480 °C for 2 h demonstrates a stronger heating effect than the cyclic heating induced by successive deposition.

In this study, the driving force provided by the heating effects during successive deposition is confirmed insufficient to affect the dynamics of eutectic phases in previous layers including precipitation and dissolution. The eutectic phases inside the α-Al matrix and along grain boundaries are formed during solidification.

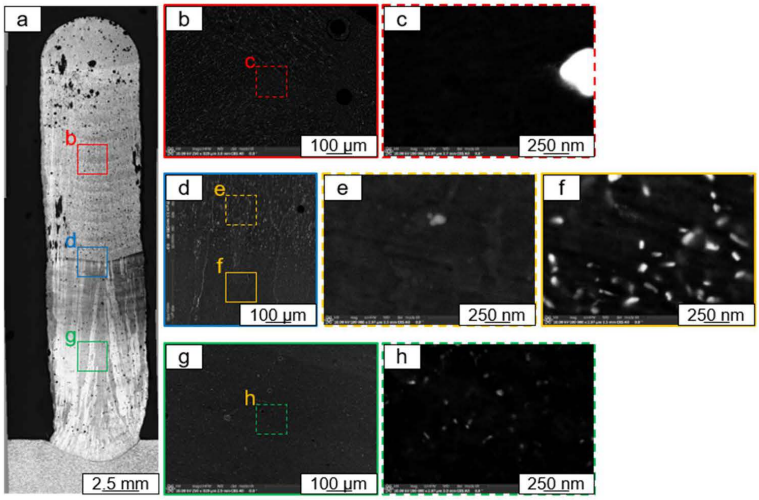

Figure 9. Effects of artificial heat treatment and the cyclic heating from successive deposition on the microstructure: (a) cross-sectional image captured under OM after etching; (b-h) locally magnified images captured under SEM. The location for magnification is marked with colored solid and dotted frames. The thin-wall structure consists of 40 layers. After building the first 20 layers, the sample is heat-treated at 480 °C for 2 h followed by water quenching. Afterwards, 20 layers are further deposited on the top of the first 20 layers. The process parameter and the deposition length are the same as in sample $S3^{N}$, see Table 2.

Liquation of the eutectic phases occurs over the eutectic temperature [61]. The driving force for liquation cannot be derived based on the driving force for precipitation and dissolution. The formation of the existing liquid film, as can be observed in Figure 5(i, j), could be the synergetic results of non-equilibrium solidification and successive heating. Two possibilities are given:

- Possibility 1 (the laser energy input for building samples $S2^{30}$ and $S3^{30}$ is insufficient to result in the partial remelting of eutectic phases): Two premises for the liquation cracking are the partially remelted eutectic phases and the tensile residual stress. The maximum of tensile residual stress is detected near the top of samples and a stress accumulation is not noticed as the process has stabilized after 20 deposition layers, see Figure 8. Nevertheless, the cracks are initiated after 30 deposition layers. Given that the tensile residual stress is not accumulated and the quantity of eutectic phases in previous layers is not dependent on the successive deposition, the initiation of cracks observed in this study is less likely to be the consequence of the liquation cracking.
- Possibility 2 (the laser energy input for building samples $S2^{30}$ and $S3^{30}$ is sufficient to result in the partial remelting of eutectic phases): The area fraction of eutectic phases in $S4^{30}$ is significantly higher than that in samples $S1^{30}$ – $S3^{30}$, see Table 4 and Table 5. EDX measurements indicate that the chemical composition of the eutectic phases is comparable in these samples. The process parameter of sample $S4^{100}$ exhibits higher laser line energy input than that of sample $S3^{30}$ (Table 2), which means that the successive deposition in building sample $S4^{100}$ should result in more severe partial remelting of eutectic phases. In addition, the tensile residual stress in the as-built $S4^{100}$ is significantly higher than that in the as-built sample $S3^{30}$ or $S3^{51}$. Given the potential of forming liquid film and the higher residual stress, no cracking observed in sample

$S4^{100}$ confirms that the liquation cracking is not the reason for the initiation of the macro-cracks observed in this study.

Table 5. The average area fraction of eutectic phases of samples $S4^{30}$ and $S5^{30}$

	$S4^{30}$	$S5^{30}$
Average area fraction (%)	6.73 ± 1.27	3.65 ± 0.78

The ductility-dip cracking is mainly investigated for nickel alloys [9] and austenitic steels [62]. According to the rare reports on the ductility dip of Al alloy from high temperature to room temperature, the ductility dip is observed at about 300 °C and the magnitude of the ductility at 300 °C is comparable or even higher to that at room temperature [63, 64]. Since the sample during the water quenching from 480 °C to room temperature experiences the ductility dip point and no cracking is noticed, the ductility-dip cracking can also be excluded.

4.3. Initiation of cracks - Solidification cracking analysis

4.3.1 Solidification conditions

The solidification cracking is attributed to insufficient backfilling to shrinkage during solidification. To analyze the solidification conditions of different samples, the temperature evolution needs to be recorded during deposition. The visible macro-cracks can be observed on the surface of samples with 51 layers. It might be possible that cracks initiate during the deposition of previous layers. The cooling phase of the 30th layer is recorded by the infrared camera and used to analyze the cracking mechanisms in thin-wall structures with higher deposition length for the following reasons: no crack is detected in the cross-sectional images of samples $S1^{30}$ to $S3^{30}$ with 30 layers; the 30th layer is far away from the substrate, therefore, the cooling phase is less dependent on the heat conduction to the substrate and should be representative for the specific solidification conditions determined by different deposition lengths.

The melting temperature of 660 ºC for pure Al is considered the liquidus temperature for AA7075 in this study [65]. The raw temperature data recorded by the infrared camera exhibits fluctuation and some abnormal points (Fig. A. 1b and c), which could be attributed to the oxidation [66] as well as the changing gas atmosphere [67], where the metal vapor and fumes, as well as spatter, were noticed during processing in this study. To alleviate the data abnormality and ensure the same standard for temperature analysis, the raw temperature data is processed using polynomial fitting to obtain a smooth cooling curve for each sample. As the temperature approaches the room temperature, the cooling rate rapidly decreases. The cooling curve tends to be flat at the last stage increasing the difficulty in fitting raw data and leading to the substantial loss of information at the early stage of cooling. Besides, the used technique shows the highest accuracy in the temperature range of 200 ºC – 900 ºC, and the material starts to solidify from the liquidus temperature (660 ºC). Hence, to analyze the solidification conditions of different samples, the raw temperature in the range of 200 ºC – 660 ºC captured by the infrared camera is selected and fitted using the polynomial fitting. The workflow for the data fitting is introduced in Fig. A. 1d of Section A.1 shows the processed cooling curve after the polynomial fitting from Fig. A. 1c.

The following indicators are proposed in this study to represent the solidification characteristics:

$$v_{cool,N,t} = \frac{T_{N,t} - T_{N,t+0.037}}{0.037} \quad \text{Equation 4}$$

$$v_{cool,max,N} = \max_{t-t_{200}} v_{cool,N,t} \quad \text{Equation 5}$$

$$v_{cool,average} = \frac{1}{N_{total}} \sum_{N=1}^{N=N_{total}} v_{cool,max,N} \quad \text{Equation 6}$$

$$v_{cool,max} = \max_{N-N_{total}} v_{cool,max,N} \quad \text{Equation 7}$$

$$TG_{N,N+1,t} = \frac{T_{N,t} - T_{N+1,t}}{d_{N,N+1}} \quad \text{Equation 8}$$

$$TG_{max,N,N+1} = \max_{t-t_{200}} TG_{N,N+1,t} \quad \text{Equation 9}$$

$$TG_{average} = \frac{1}{N_{total}-1} \sum_{N=1}^{N=N_{total}-1} TG_{max,N,N+1} \quad \text{Equation 10}$$

$$TG_{max} = \max_{N-N_{total-1}} TG_{max,N,N+1} \quad \text{Equation 11}$$

where $T_{N,t}$ is the temperature of the N^{th} column of the 30th layer at the time point of t, 0.037 s is the time interval between two consecutive temperature recordings, t_{200} is the time point when the temperature reaches 200 °C during cooling, N_{total} is the total number of columns recorded in the 30th layer, as shown in Figure 2(d-f); $v_{cool,N,t}$ and $v_{cool,max,N}$ are the cooling rate at the time point of t and the maximum cooling rate during the entire cooling phase in the N^{th} column of the 30th layer; $v_{cool,average}$ and $v_{cool,max}$ are the average cooling rate and the maximum cooling rate among the N_{total} columns in the 30th layer. The variable $d_{N,N+1}$ is the distance between two neighboring columns, which is 4.8 mm here; $TG_{N,N+1,t}$ and $TG_{max,N,N+1}$ are the temperature gradient at the time point of t and the maximum temperature gradient during the entire cooling phase between the N^{th} and $(N+1)^{th}$ column; $TG_{average}$ and TG_{max} are the average temperature gradient and the maximum temperature gradient among the N_{total} columns in the 30th layer.

Figure 10a exhibits a downward trend of maximum cooling rate and average cooling rate with increased deposition length from 30 mm to 70 mm. A large gap is observed between sample $S1^{30}$ and the other two samples ($S2^{30}$, $S3^{30}$). The maximum and average temperature gradients of samples $S1^{30}$ to $S3^{30}$ manifest a comparable magnitude. No obvious dependence of the temperature gradient on the deposition length can be noticed.

It was reported in [68] that the top center position of melt pools exhibited the highest temperature. Hence, the temperature evolution recorded and analyzed in this study corresponds to the top center of melt pools, as referred to in the experimental description for Figure 2. The melt-pool lifetime is defined here as the time taken to cool down from the maximum temperature to the liquidus temperature in the melt-pool top center. The solidification starts from the melt-pool boundary [69]. Within the melt-pool lifetime defined here, the liquid on the top of melt pools has the chance to backfill solidification shrinkage near the boundary of melt pools. The temperature data used to calculate the maximum temperature and melt-pool lifetime is the raw temperature data recorded by the infrared camera without any data fitting. The average maximum temperature of melt pools and the average melt-pool lifetime decrease with the increased deposition length (Figure 10b). The viscosity of liquid Al alloy is negatively proportional to the temperature [70]. It indicates that sample $S1^{30}$ (deposition length 30 mm) has the lowest viscosity and enhanced flowability, while sample $S3^{30}$ manifests the highest viscosity and the worst flowability. As for building sample $S3^{30}$, it is difficult for the flowing melt pools to backfill the shrinkage generated during the solidification. Furthermore, the shorter duration of the melt-pool lifetime cannot provide a sufficient chance for the flowing liquid to backfill the shrinkage in previously solidified parts. Hence, considering the cooling conditions during the deposition, the cracking susceptibility increases with the increased deposition length, which could be attributed to the decreased flowability of melt pools and the inadequate ability to backfill the solidification shrinkage.

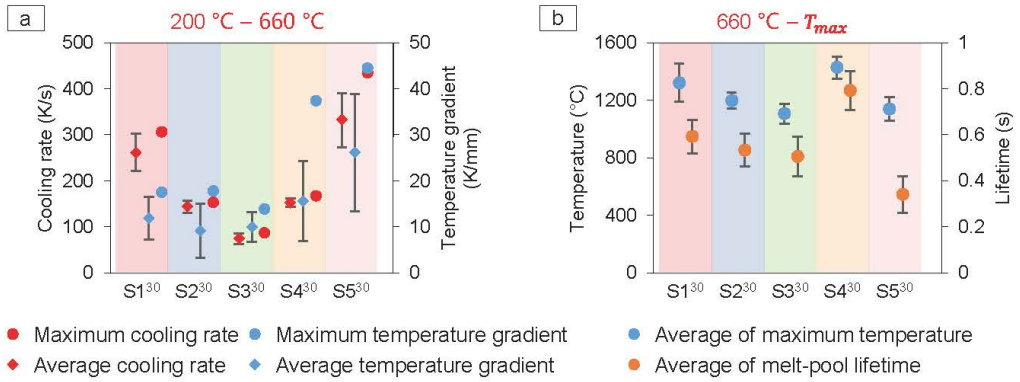

Figure 10. Solidification characteristics in the 30th layer of samples $S1^{30}$ to $S5^{30}$: (a) cooling rate and temperature gradient. The temperature used for analysis is in the range of 200°C – 660 °C. (b) Average of maximum temperature and melt-pool lifetime, which represents the average value of the maximum temperature and the melt-pool lifetime of all recorded positions in the 30th layer. The temperature used for analysis is in the range of 660 °C – T_{max} °C.

Based on the analysis of the solidification conditions, the initiation of the macro-cracks observed in Figure 4(d, f) is identified as the consequence of solidification cracking due to shrinkage and insufficient backfilling during solidification.

The solidification conditions of samples $S4^{30}$ and $S5^{30}$ are also analyzed in terms of the cooling curve of the 30th layer (Figure 10b) to validate the cracking mechanism. Sample $S4^{30}$ demonstrates a longer melt-pool lifetime than sample $S1^{30}$, whereas the melt-pool lifetime of sample $S5^{30}$ is the shortest among samples $S1^{30}$ to $S5^{30}$. Furthermore, the maximum temperature of melt pools in sample $S4^{30}$ also reduces the viscosity and improves the flowability promoting better backfilling, since the viscosity of liquid Al alloy is negatively proportional to the temperature [70]. It indicates that sample $S4^{30}$ demonstrates a lower solidification cracking susceptibility, whereas sample $S5^{30}$ is susceptible to solidification cracking, which is in agreement with the experimental observations in Figure 6. A delayed cracking is noticed in $S5^{51}$, whereas no cracking is observed in $S4^{100}$.

4.3.2 Solute-related solidification cracking susceptibility

The content of Mg and Zn is measured in the α-Al matrix from the top of the last layer to the bottom of samples $S1^{30}$ to $S3^{30}$, see Figure 11a. The content of Zn and Mg is lower than that in the feedstock due to the evaporation caused by high processing temperatures exceeding the boiling points of the alloying elements, as confirmed by the infrared camera. However, the element content in different positions of the samples is comparable except for the top of the last layer (Figure 11b and c). At the top of the last layer, a more serious element loss is observed. During the deposition of each layer, the temperature decreases from the top of the melt-pool center to the melt-pool boundary [68]. Hence, the top of the last layer demonstrates the least content of Mg and Zn content, whereas the bottom of the last layer compensates Mg and Zn to the top of the previous layer by partially remelting achieving a stable distribution of the content of alloying elements through the samples.

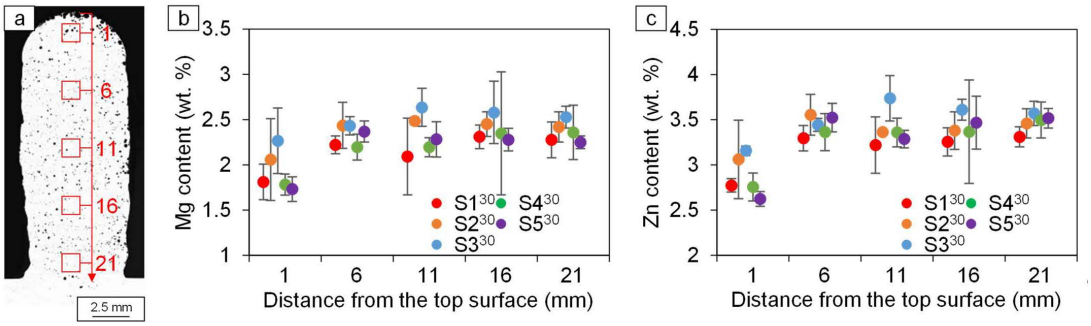

Figure 11. Results of EDX measurements for the content of Mg and Zn in α-Al matrix of samples $S1^{30}$ – $S5^{30}$. (a) Locations for measuring the content of Mg and Zn. Five measurements are done from the top to the bottom of the structures according to distance from the top surface: 1 mm, 6 mm, 11 mm, 16 mm, 21 mm. (b) Content of Mg. (c) Content of Zn.

An index for the cracking susceptibility during solidification is proposed in [71]:

$$\left|dT/d(f_s)^{1/2}\right| \text{ near } (f_s)^{1/2} = 1 \qquad \text{Equation 12}$$

where T is the temperature and f_s is the fraction of solid. The resistance against solidification cracking decreases with a higher index for cracking susceptibility, since the neighboring columnar grains slowly grow toward each other in the lateral direction and the intergranular channel is prolonged, which promotes the formation of shrinkage and increases the difficulty for liquid to backfill [71]. The dependence of the cracking susceptibility index on the content of alloying elements is investigated in binary Al alloys such as Al-Zn and Al-Mg alloys [72]. It is also validated in multiple Al alloying systems [2]. The cracking susceptibility index is the maximum steepness $\left|dT/d(f_s)^{1/2}\right|$ of the T-$(f_s)^{1/2}$ [72].

The content of alloying elements (Mg, Zn) in the last layer, as shown in Figure 11 (at a 1 mm distance from the top surface) is used for the thermodynamic simulation. The content of Cu measured is also included. Figure 12a demonstrates the solidification path of samples $S1^{30}$ to $S5^{30}$ in the last layer. Samples $S1^{30}$, $S4^{30}$, and $S5^{30}$ exhibit a similar solidification path due to the comparable content of alloying elements. The solidification path of sample $S3^{30}$ with the highest content of Mg and Zn is located underneath that of other samples. The steepness in the range of ${f_s}^{1/2}$ over 0.99 is not considered since continuous grain-boundary liquid films cannot be formed to cause cracking [2]. According to the cracking susceptibility index in Figure 12b (the maximum steepness $\left|dT/d(f_s)^{1/2}\right|$ of the T-$(f_s)^{1/2}$), using process parameters of samples $S1^{30}$, $S4^{30}$, and $S5^{30}$ should exhibit higher cracking susceptibility than using process parameters of samples $S2^{30}$ and $S3^{30}$. Nevertheless, the cracked samples, as shown in Figure 4(d, f) and Figure 6b, are built using process parameters of samples $S2^{30}$, $S3^{30}$, and $S5^{30}$, respectively.

It indicates that the index for solidification cracking susceptibility calculated by using the Scheil solidification model considering no solid-state diffusion exhibits limitation. As reported in [2, 72], the back diffusion of Mg in solid Al can decrease the steepness of $T - {f_s}^{1/2}$. Different factors such as the melt-pool lifetime and the maximum temperature, as analyzed in Section 4.3.1, could be considered as alternative factors determining the solidification cracking susceptibility in specific cases.

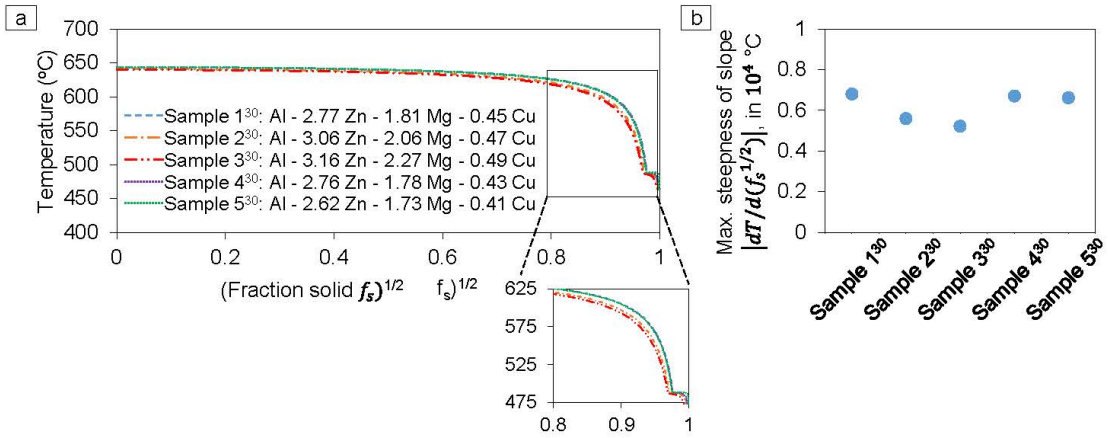

Figure 12. (a) Solidification path of samples S1^{30} to S5^{30}. (b) Maximum steepness of slop $|dT/d(f_s^{1/2})|$ in the range of $f_s^{1/2}$ < 0.99.

The viscosity of liquid Al alloys decreases with the reduction of the Mg content, whereas it increases with the reduction of the Zn content [73]. Since the content difference of Zn and Mg on the top of the last layer between different samples is comparable, the effects of the concentration of Mg and Zn on the viscosity of the melt pools are considered counteracted.

4.3.3 "Delayed cracking"

The above-analyzed results demonstrate that the initiation of the macro-cracks is attributed to solidification cracking rather than liquation cracking and ductility-dip cracking. However, the solidification cracking is not observed in the thin-wall structures with fewer layers but in those with more layers.

It is worth noting that the dependence of maximum tensile residual stress on process parameters and deposition length is consistent with the dependence of the maximum temperature gradient on process parameters and deposition length, as shown in Figure 8 and Figure 10a. This validates a strong correlation between the tensile residual stress and the thermal fields during solidification. The stress accumulation was reported during the deposition of the first several layers, particularly in the area near the substrate [39, 53]. In this study, as the process becomes stable (after 20 layers), the magnitude of tensile residual stress near the top of samples has been proven not related to the number of deposited layers indicating a stable thermal field.

In addition, the two factors determining the solidification cracking susceptibility, i.e. the melt-pool lifetime and the melt-pool maximum temperature, exhibit no significant dependence on the number of deposited layers after the deposition exceeding 20 layers, as shown in Figure 13(a, b). The maximum temperature demonstrates the same dependence on the process parameter and the deposition length in the 20th layer and the 30th layer. Despite the standard deviation, the maximum temperature of melt pools is comparable in the 20th layer and the 30th layer during building samples. In terms of the melt-pool lifetime, the dependence on the deposition length between S2^{30} and S3^{30} is different in the 20th layer and the 30th layer. However, the temperature data extracted from the 20th layer during building samples still support the conclusion regarding the impact of the melt-pool lifetime on the solidification cracking susceptibility: S2^{30}, S3^{30}, and S5^{30} with the shorter melt-pool lifetime exhibit higher solidification cracking susceptibility. The noticeable variation of the melt-pool lifetime is observed as the deposition has stabilized. The stabilization of thermal fields including the maximum temperature and the melt-pool lifetime could also be supported by the homogeneous content of volatile alloying elements (Figure 11) and porosity distribution (Figure 7) along the building direction since the evaporation of volatile elements and the escape of gas bubbles from the melt pools are determined by the thermal fields. Hence, the analysis for "delayed cracking" is focused on microstructural variation with deposition layers rather than the thermal fields.

The etched microstructure, as shown in Figure 13c, reveals the epitaxial growth of columnar grains through several layers and the converging boundaries between grains with different growth directions. The brightness contrast of grains with different orientations can be noticed after etching. In L-DED, the direction of heat flow is nearly parallel to the building direction (BD) of thin-wall structures [74, 75]. The strong <001>//BD texture is observed in the microstructure of L-DED processed Al alloys [48, 76]. When the growth direction of grains is closely aligned with the building direction, the growth is preferentiated. As the deposition proceeds, the grains with preferential growth direction dominate the cross section by suppressing the growth of highly misaligned grains. This phenomenon is also confirmed by the phase field simulation that the misaligned grains are continuously eliminated as the processing proceeds [76]. The cumulative solutes released from the well-aligned dendrite tip through the dendritic channel impeded the continued growth of misaligned dendrites by increasing the level of constitutional undercooling before attaining the state of steady growth [76].

The highly misaligned grains are eliminated by the growth of two neighboring well-aligned grains with faster growth rates, e.g. the elimination of grain 3 by the widening and growth as well as merge of grains 1 and 2 and the elimination of grain 6 by the widening and growth as well as merge of the grains 4 and 5 (Figure 13c). The grain size of misaligned grain 6 is larger than that of misaligned grain 3 before elimination since those misaligned grains not eliminated in time also grow simultaneously leading to an increased contact area during the merge of two well-aligned grains to eliminate the misaligned grains, as marked by the red line. The increased contact area contributes to poorer permeability and promotes the formation of shrinkage as well as leads to an enhanced cracking susceptibility. This assumption is supported by the microstructure in area B, as marked in Figure 5, where the macro-crack could initiate. Large columnar grains with different growth directions are noticed around the macro-crack.

In thin-wall structures with a deposition length of 30 mm, the maximum temperature of melt pools enhances the flowability and the longer melt-pool lifetime provides the melt pools sufficient time to backfill shrinkage. The solidification cracking occurs as the thin-wall structures with deposition lengths of 50 mm and 70 mm reach a certain height. The flowability of melt pools and the melt-pool life cannot ensure adequate backfilling during the elimination of misaligned coarse grains in higher layers.

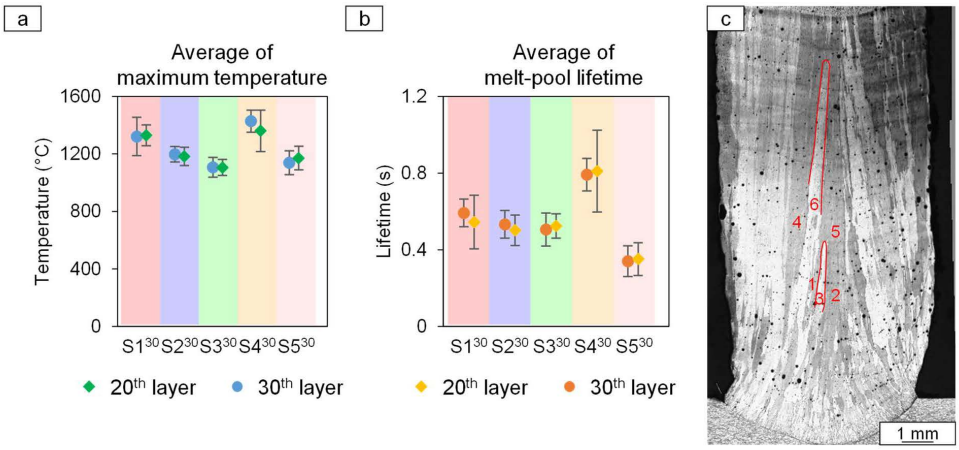

Figure 13. (a) Average of maximum temperature and (b) average of melt-pool lifetime in the 20th layer and the 30th layer during building samples S1^{30} to S5^{30}. (c) Elimination of misaligned grains by the growth of grains with preferential growth direction.

5. Conclusions

In the present study, the cracking mechanism of the macro-cracks observed during successive deposition during L-DED processing high-strength AA7075 alloy is experimentally investigated considering the solidification conditions, microstructure, and residual stress. The cracking mechanism deduced in this study is further

validated by a crack-free thin-wall structure processed with optimized parameters. The following conclusions can be drawn based on the experimental results:

- The cracking susceptibility increases with increased deposition length under the same process parameter. The cracking phenomenon occurs after the deposited layer reaches a threshold number during the building of structures with longer deposition lengths.
- The cracks initiate and grow in two directions parallel to the building direction during successive deposition. The initiation of cracks is induced by insufficient backfilling to shrinkage leading to solidification cracking. After the initiation of cracks, the growth of cracks downwards is attributed to the consequence of the liquation cracking. The growth of cracks upwards results from the solidification cracking. A crack-free thin-wall structure with the longest deposition length is produced with optimized process parameters. The mechanism for the initiation of cracks deduced in this study is also validated.
- The reason why the cracking does not occur until a certain number of layers is deposited, so-called "delayed cracking", is attributed to the competitive growth between grains with different growth directions. As the deposition proceeds, the grains with preferential growth directions eliminate the highly misaligned grains. The later the highly misaligned grains are eliminated, the larger the size of these grains, which prolongs the channel for backfilling shrinkage and deteriorates the permeability as well as enhances the cracking susceptibility.

Appendices

A.1. Data processing for the temperature recorded by infrared camera

To alleviate the data abnormality and ensure the same standard for temperature analysis, the raw temperature data is processed using polynomial fitting and least square fitting to obtain a smooth cooling curve for each sample. The data deviation between the raw temperature data and the data fitted by polynomial fitting and least square fitting is shown in Fig. A. 1a and Tab. A. 1. Using polynomial fitting can clean the raw temperature data with high fluctuation and abnormal points at less loss of information than using the least square fitting. Consequently, the raw temperature data is cleaned by using polynomial fitting. Fig. A. 1d shows the processed cooling curve after the polynomial fitting from Fig. A. 1c.

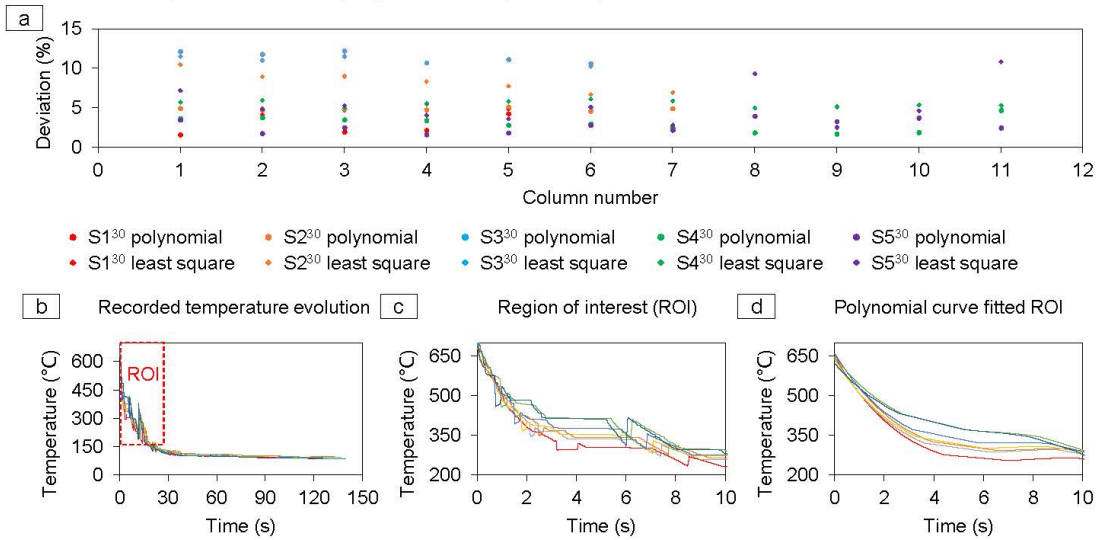

Fig. A. 1. Data fitting for the raw temperature data recorded by the infrared camera during the cooling phase of the 30th layer. (a) Deviation of the processed data using polynomial fitting and least square fitting, respectively, and the experimental data recorded by the infrared camera. The column number is consistent with the positions in the 30th layer from Figure 2(d-f). (b) Raw temperature data of different positions in the 30th layer of sample S2^{30} during the cooling phase. Columns are

counted from left to right in the 30th layer. (c) Locally magnified raw temperature data in the range of 200 °C – 660 °C. (d) Temperature data fitted from (c) using polynomial fitting.

Tab. A. 1. The average deviation between the processed data using polynomial fitting and least square fitting, respectively, and the raw temperature data recorded by the infrared camera. For each sample, the deviation of all positions in the 30th layer is averaged.

Sample	Averaged deviation of the fitted data (%)	
	Polynomial	Least square
$S1^{30}$	2.3	4.5
$S2^{30}$	4.8	8.3
$S3^{30}$	11.4	11
$S4^{30}$	2.9	5.5
$S5^{30}$	2.7	5.4

A.2. Calculation of the average area fraction of secondary phases

Three SEM images (magnification 500x) were captured at the top, mid, and bottom of the thin-wall structure, as shown in Fig. A. 2a. Subsequently, the SEM images are binarized using the Otsu's thresholding method to identify the secondary phases and the α-Al matrix (Fig. A. 2c). Ultimately, the area percentages of the secondary phases at the top, mid, and bottom of the thin-wall structure are averaged to represent the area fraction of the secondary phases for each sample.

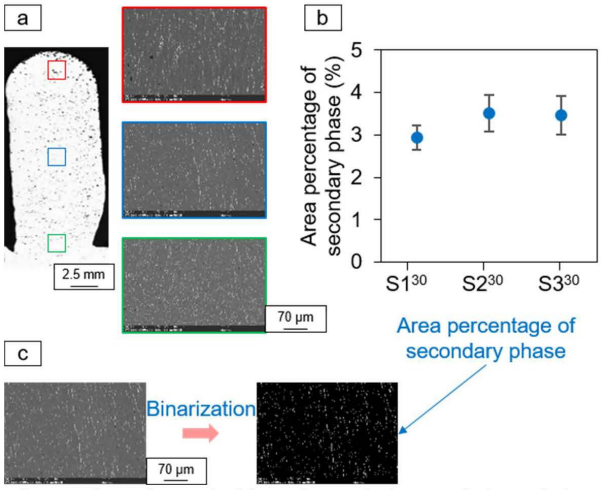

Fig. A. 2. The area fraction of secondary phases inside grains and along grain boundaries: (a) locations for measuring the area fraction of secondary phases; (b) the average area fraction of secondary phases of samples $S1^{30}$ to $S3^{30}$; (c) process of how to calculate the area fraction of secondary phases.

A.3. Attempt to suppress cracking via island scanning in L-DED

The dependence of cracking susceptibility is mostly investigated with a focus on process parameters in L-DED [77, 78]. Inappropriate parameter sets can lead to the formation of visible macro-cracks on the structure surface [77] and intergranular or transgranular micro-cracks observed under a microscope [79]. Regarding the scanning strategy, the same deposition direction throughout all layers and the alternating deposition directions are adopted to modify the microstructure and mechanical properties [80, 81], whereas the optimization of the scanning strategy to alleviate cracking susceptibility is rarely reported due to the insufficient processing flexibility compared to LPBF. In LPBF, various scanning strategies such as island scanning are applied to reduce the cracking susceptibility [16]. No such attempt has been reported in L-DED processed thin-wall structures.

In this study, the island scanning strategy is conducted to build thin-wall structures with a deposition length of 50 mm. The deposition length of 50 mm is considered the linkage of two deposition sequences with a length of 25 mm. This methodology failed due to the processing characteristics of L-DED: the accelerating and decelerating phases in one deposition sequence as well as the essence of material feeding in L-DED result in the formation of bumps and macro-cracks in the middle of the 50-mm deposition track. The bumps and cracks initiating in the middle of the thin-wall structures can be observed in Fig. A. 3. Using the island scanning strategy, macro-cracks become visible before the 15th layer. In contrast to the crack-free 30-layer structure built with conventional bi-directional scanning, island scanning enhances the cracking susceptibility. Hence, instead of optimizing the scanning strategy, the current process parameters are optimized to prevent cracking when building thin-wall structures with a deposition length of 70 mm without the cost of other properties.

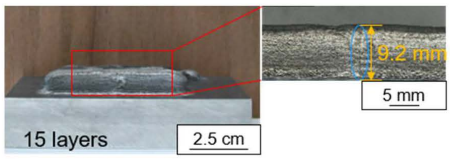

Fig. A. 3. Sample built with island scanning strategy. Laser power in 1st layer: 4000 W, 2nd layer: 3500 W, 3rd – 4th layers: 3250 W, 5th – 15th layers: 3000 W; laser scanning speed: 1000 mm/s, wire feed speed: 4000 mm/min.

A.4. Dominant reason for the elimination of eutectic phases

Fig. A. 4a and b exhibit the grain morphology of samples heat-treated at 480 °C for 2 h and followed by water-quenching and air-cooling, respectively. Compared with the as-built sample (Fig. A. 4c), both grain morphologies can be distinguished indicating the absence of coarse eutectic phases. Hence, the dominant reason for the absence of eutectic phases in heat-treated samples is the dissolution of them at high temperatures rather than the increased solubility under rapid cooling suppressing the precipitation of eutectic phases.

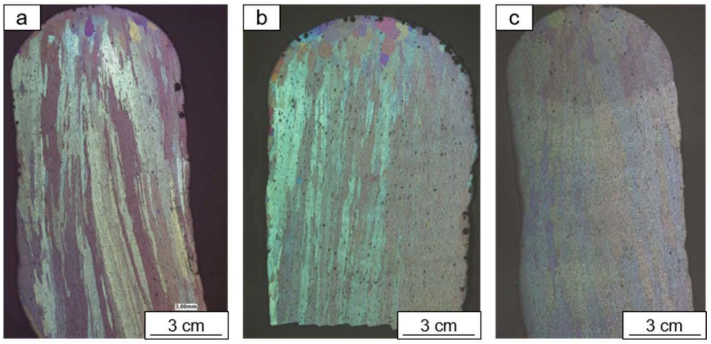

Fig. A. 4. Cross-sectional photos of etched samples S3^{20} after different treatments: (a) heat-treated at 480 ^{o}C for 2 h and followed by water quenching; (b) heat-treated at 480 ^{o}C for 2 h and followed by air cooling; (c) as-built (not heat treated).

Acknowledgments

The authors would like to thank R. Dinse and S. Riekehr for their assistance during laser-directed energy deposition as well as F. Dorn for the support during metallographic preparation and microstructural characterization. The authors would like to thank Dr. V. Ventzke for the discussion of the results. The authors would like to thank Prof. Qun Luo and Yufei Zhang from Shanghai University for their support and discussion regarding the thermodynamic simulation. We acknowledge DESY (Hamburg, Germany), a member of the Helmholtz Association HGF, for the provision of experimental facilities. Parts of this research were carried out at P07b @ PETRA III.

Reference

[1] T. Böllinghaus, H. Herold, C.E. Cross, J.C. Lippold, Hot cracking phenomena in welds II, first ed., Springer Science & Business Media, Berlin. 2008.
[2] S. Kou, A simple index for predicting the susceptibility to solidification cracking, Weld. J. 94 (2015) 374-388.
[3] X. Zhang, Z. Cao, P. Zhao, Investigation on solidification cracks in pulsed laser spot welding of an AZ31 magnesium alloy, Opt. Laser Technol. 126 (2020) 106132.
[4] H. Zhang, J. Senkara, Resistance welding: fundamentals and applications, second ed., CRC press, Boca Raton, 2011.
[5] F.M. Ghaini, M. Sheikhi, M. Torkamany, J. Sabbaghzadeh, The relation between liquation and solidification cracks in pulsed laser welding of 2024 aluminium alloy, Mater. Sci. Eng. A 519 (2009) 167-171.
[6] Y. Chen, K. Zhang, J. Huang, S.R.E. Hosseini, Z. Li, Characterization of heat affected zone liquation cracking in laser additive manufacturing of Inconel 718, Mater. Des. 90 (2016) 586-594.
[7] G. Young, T. Capobianco, M. Penik, B. Morris, J. McGee, The mechanism of ductility dip cracking in nickel-chromium alloys, Weld. J. 87 (2008) 31-43.
[8] C. Fink, An investigation on ductility-dip cracking in the base metal heat-affected zone of wrought nickel base alloys—part I: metallurgical effects and cracking mechanism, Weld. World 60 (2016) 939-950.
[9] A. Ramirez, J. Lippold, High temperature behavior of Ni-base weld metal: Part II–Insight into the mechanism for ductility dip cracking, Mater. Sci. Eng. A 380 (2004) 245-258.
[10] D. Herzog, V. Seyda, E. Wycisk, C. Emmelmann, Additive manufacturing of metals, Acta Mater. 117 (2016) 371-392.
[11] B. Graf, M. Schuch, R. Kersting, A. Gumenyuk, M. Rethmeier, Additive process chain using selective laser melting and laser metal deposition, in: T. Graf, C. Emmelmann, L. Overmeyer, F. Vollertsen (Eds.) Lasers in Manufacturing Conference, Wissenschaftliche Gesellschaft Lasertechnik e.V., Munich, 2015, pp. 59-64.
[12] C. Donate-Buendia, D. Gu, M. Schmidt, S. Barcikowski, A.M. Korsunsky, B. Goekce, On the selection and design of powder materials for laser additive manufacturing, Mater. Des. 204 (2021).
[13] Y. Ding, J. Muñiz-Lerma, M. Trask, S. Chou, A. Walker, M. Brochu, Microstructure and mechanical property considerations in additive manufacturing of aluminum alloys, MRS Bull. 41 (2016) 745.
[14] J.H. Martin, B.D. Yahata, J.M. Hundley, J.A. Mayer, T.A. Schaedler, T.M. Pollock, 3D printing of high-strength aluminium alloys, Nature 549 (2017) 365-369.
[15] M. Benoit, S. Sun, M. Brandt, M. Easton, Processing window for laser metal deposition of Al 7075 powder with minimized defects, J. Manuf. Process. 64 (2021) 1484-1492.
[16] W. Stopyra, K. Gruber, I. Smolina, T. Kurzynowski, B. Kuźnicka, Laser powder bed fusion of AA7075 alloy: Influence of process parameters on porosity and hot cracking, Addit. Manuf. 35 (2020) 101270.
[17] J. Hirsch, Recent development in aluminium for automotive applications, Trans. Nonferrous Met. Soc. 24 (2014) 1995-2002.
[18] T. Dursun, C. Soutis, Recent developments in advanced aircraft aluminium alloys, Mater. Des. 56 (2014) 862-871.
[19] L.C. Gonzalez, J. Tuominen, S. Ahmed, M. Patnamsetty, P. Peura, Directed energy deposition of AA7075-Effect of TiC nanoparticles on microstructure, Results Mater. 16 (2022) 100341.
[20] H. Xu, W. Ren, C. Ma, L. Xu, Y. Han, L. Zhao, K. Hao, Laser-directed energy deposition of ZrH2 particles reinforced Al7075 alloy: Cracks elimination and strength enhancement, Addit. Manuf. 78 (2023) 103877.
[21] T. Zhao, Y. Wang, T. Xu, M. Bakir, W. Cai, M. Wang, M. Dahmen, Q. Zheng, X. Wei, C. Hong, Some factors affecting porosity in directed energy deposition of AlMgScZr-alloys, Opt. Laser Technol. 143 (2021) 107337.
[22] M.H. Mosallanejad, B. Niroumand, A. Aversa, A. Saboori, In-situ alloying in laser-based additive manufacturing processes: A critical review, J. Alloys Compd. 872 (2021) 159567.
[23] M. Simonelli, N.T. Aboulkhair, P. Cohen, J.W. Murray, A.T. Clare, C. Tuck, R.J. Hague, A comparison of Ti-6Al-4V in-situ alloying in Selective Laser Melting using simply-mixed and satellited powder blend feedstocks, Mater. Charact. 143 (2018) 118-126.
[24] Q. Li, G. Li, X. Lin, D. Zhu, J. Jiang, S. Shi, F. Liu, W. Huang, K. Vanmeensel, Development of a high strength Zr/Sc/Hf-modified Al-Mn-Mg alloy using Laser Powder Bed Fusion: Design of a heterogeneous microstructure incorporating synergistic multiple strengthening mechanisms, Addit. Manuf. 57 (2022) 102967.

[25] C. Ma, Y. Yan, Z. Yan, Y. Liu, X. Wu, D. Li, L. Zhao, P. Liu, H. Jin, Investigation of bypass-coupled double-pulsed directed energy deposition of Al–Mg alloys, Addit. Manuf. 58 (2022) 103058.
[26] P. Jiang, X. Li, X. Zong, X. Wang, Z. Chen, H. Yang, C. Liu, N. Gao, Z. Zhang, Multi-wire arc additive manufacturing of Ti basic heterogeneous alloy: Effect of deposition current on the microstructure, mechanical property and corrosion-resistance, J. Alloys Compd. 920 (2022) 166056.
[27] J. Zhang, Y. Liu, G. Sha, S. Jin, Z. Hou, M. Bayat, N. Yang, Q. Tan, Y. Yin, S. Liu, Designing against phase and property heterogeneities in additively manufactured titanium alloys, Nat. Commun. 13(1) (2022) 4660.
[28] S. Zhou, Y. Su, H. Wang, J. Enz, T. Ebel, M. Yan, Selective laser melting additive manufacturing of 7xxx series Al-Zn-Mg-Cu alloy: Cracking elimination by co-incorporation of Si and TiB2, Addit. Manuf. 36 (2020) 101458.
[29] P. Wang, H. Li, K. Prashanth, J. Eckert, S. Scudino, Selective laser melting of Al-Zn-Mg-Cu: Heat treatment, microstructure and mechanical properties, J. Alloys Compd. 707 (2017) 287-290.
[30] J. Xiong, Y. Lei, R. Li, Finite element analysis and experimental validation of thermal behavior for thin-walled parts in GMAW-based additive manufacturing with various substrate preheating temperatures, Appl. Therm. Eng. 126 (2017) 43-52.
[31] L. Mugwagwa, D. Dimitrov, S. Matope, I. Yadroitsev, Evaluation of the impact of scanning strategies on residual stresses in selective laser melting, Int. J. Adv. Manuf. Technol. 102 (2019) 2441-2450.
[32] P. Bian, J. Shi, Y. Liu, Y. Xie, Influence of laser power and scanning strategy on residual stress distribution in additively manufactured 316L steel, Opt. Laser Technol. 132 (2020) 106477.
[33] J. Zhou, X. Zhou, H. Li, J. Hu, X. Han, S. Liu, In-situ laser shock peening for improved surface quality and mechanical properties of laser-directed energy-deposited AlSi10Mg alloy, Addit. Manuf. 60 (2022) 103177.
[34] C. Ye, C. Zhang, J. Zhao, Y. Dong, Effects of post-processing on the surface finish, porosity, residual stresses, and fatigue performance of additive manufactured metals: a review, J. Mater. Eng. Perform. 30 (2021) 6407-6425.
[35] A. Wang, Q. Wei, Z. Tang, P. Ren, X. Zhang, Y. Wu, H. Wang, A. Du Plessis, J. Huang, K. Hu, Effects of processing parameters on pore defects in blue laser directed energy deposition of aluminum by in and ex situ observation, J. Mater. Process. Technol. 319 (2023) 118068.
[36] Y. Huang, T.G. Fleming, S.J. Clark, S. Marussi, K. Fezzaa, J. Thiyagalingam, C.L.A. Leung, P.D. Lee, Keyhole fluctuation and pore formation mechanisms during laser powder bed fusion additive manufacturing, Nat. Commun. 13 (2022) 1170.
[37] C.L.A. Leung, S. Marussi, M. Towrie, R.C. Atwood, P.J. Withers, P.D. Lee, The effect of powder oxidation on defect formation in laser additive manufacturing, Acta Mater. 166 (2019) 294-305.
[38] P. Promoppatum, S.-C. Yao, Influence of scanning length and energy input on residual stress reduction in metal additive manufacturing: Numerical and experimental studies, J. Manuf. Process. 49 (2020) 247-259.
[39] H. Zhao, G. Zhang, Z. Yin, L. Wu, Three-dimensional finite element analysis of thermal stress in single-pass multi-layer weld-based rapid prototyping, J. Mater. Process. Technol. 212 (2012) 276-285.
[40] F.E. Bock, J. Herrnring, M. Froend, J. Enz, N. Kashaev, B. Klusemann, Experimental and numerical thermo-mechanical analysis of wire-based laser metal deposition of Al-Mg alloys, J. Manuf. Process. 64 (2021) 982-995.
[41] J. Ye, A. Bab-Hadiashar, R. Hoseinnezhad, N. Alam, A. Vargas-Uscategui, M. Patel, I. Cole, Predictions of in-situ melt pool geometric signatures via machine learning techniques for laser metal deposition, Int. J. Comput. Integr. Manuf. 36 (2022) 1-17.
[42] Z. Lanc, M. Zeljković, B. Štrbac, A. Živković, I. Drstvenšek, M. Hadžistević, The determination of the emissivity of aluminum alloy AW 6082 using infrared thermography, J. Prod. Eng. 18 (2015) 23-26.
[43] N. Schell, A. King, F. Beckmann, T. Fischer, M. Müller, A. Schreyer, The high energy materials science beamline (HEMS) at PETRA III, Mater. Sci. Forum 772 (2014), 57-61.
[44] M.T. Hutchings, P. J. Withers, T. M. Holden, T. Lorentzen, Introduction to the characterization of residual stress by neutron diffraction, first ed., CRC press, Boca Raton, 2005.
[45] H. Wern, R. Johannes, H. Walz, Dependence of the X - ray elastic constants on the diffraction plane, Phys. Status Solidi (B) 206 (1998) 545-557.
[46] M. Tang, J. Huang, Y. Zhang, S. Luo, Full strain tensor measurements with X-ray diffraction and strain field mapping: a simulation study, J. Synchrotron Radiat. 27 (2020) 646-652.
[47] M. Wang, N. Kashaev, Investigation of process window for AA7075 considering effects of different wire feed directions in lateral Laser Metal Deposition, Procedia CIRP 111 (2022) 218-223.

[48] M. Wang, V. Ventzke, N. Kashaev, Wire-based laser directed energy deposition of AA7075: effect of process parameters on microstructure and mechanical properties, J. Mater. Res. Technol. 21 (2022) 388-403.
[49] C. Weingarten, D. Buchbinder, N. Pirch, W. Meiners, K. Wissenbach, R. Poprawe, Formation and reduction of hydrogen porosity during selective laser melting of AlSi10Mg, J. Mater. Process. Technol. 221 (2015) 112-120.
[50] G. Ng, A. Jarfors, G. Bi, H. Zheng, Porosity formation and gas bubble retention in laser metal deposition, Appl. Phys. A 97 (2009) 641-649.
[51] D. Svetlizky, B. Zheng, T. Buta, Y. Zhou, O. Golan, U. Breiman, R. Haj-Ali, J.M. Schoenung, E.J. Lavernia, N. Eliaz, Directed energy deposition of Al 5xxx alloy using Laser Engineered Net Shaping (LENS®), Mater. Des. 192 (2020) 108763.
[52] R. Geng, J. Du, Z. Wei, S. Xu, N. Ma, Modelling and experimental observation of the deposition geometry and microstructure evolution of aluminum alloy fabricated by wire-arc additive manufacturing, J. Manuf. Process. 64 (2021) 369-378.
[53] T. Mukherjee, W. Zhang, T. DebRoy, An improved prediction of residual stresses and distortion in additive manufacturing, Comput. Mater. Sci. 126 (2017) 360-372.
[54] Y. Liu, Y. Yang, D. Wang, A study on the residual stress during selective laser melting (SLM) of metallic powder, Int. J. Adv. Manuf. Technol. 87 (2016) 647-656.
[55] G. Meng, J. Zhang, J. Li, Z. Jiang, Y. Gong, J. Zhao, Impact of pore defects on laser additive manufacturing of Inconel 718 alloy based on a novel finite element model: Thermal and stress evaluation, Opt. Laser Technol. 167 (2023) 109782.
[56] F. Yan, S. Liu, C. Hu, C. Wang, X. Hu, Liquation cracking behavior and control in the heat affected zone of GH909 alloy during Nd: YAG laser welding, J. Mater. Process. Technol. 244 (2017) 44-50.
[57] N. Nayan, S. Narayana Murty, Gotvind, M. Mittal, P. Sinha, Optimization of homogenizing mode for aluminum alloy AA7075 using calorimetric and microstructural studies, Met. Sci. Heat Treat. 51 (2009) 330-337.
[58] M. Xu, S. Chen, T. Yuan, X. Jiang, H. Zhang, Effect of thermal cycles on the microstructure and properties of the Al–Zn–Mg–Cu alloy during wire-arc additive manufacturing, J. Alloys Compd. 928 (2022) 167172.
[59] J. Liu, J. Chen, X. Yang, S. Ren, C. Wu, H. Xu, J. Zou, Revisiting the precipitation sequence in Al–Zn–Mg-based alloys by high-resolution transmission electron microscopy, Scripta Mater. 63(11) (2010) 1061-1064.
[60] J. Mazumder, A. Kar, Solid solubility in laser cladding, JOM 39 (1987) 18-23.
[61] C. Huang, S. Kou, Partially melted zone in Aluminum welds-liquation mechanism and directional soldification, Weld. J. 79 (2000) 113-s.
[62] K. Han, J. Yoo, B. Lee, I. Han, C. Lee, Effect of Ni on the hot ductility and hot cracking susceptibility of high Mn austenitic cast steel, Mater. Sci. Eng. A 618 (2014) 295-304.
[63] E. Bouchaud, L. Kubin, H. Octor, Ductility and dynamic strain aging in rapidly solidified aluminum alloys, Metall. Trans. A 22 (1991) 1021-1028.
[64] S. Bahl, A. Plotkowski, K. Sisco, D.N. Leonard, L.F. Allard, R.A. Michi, J.D. Poplawsky, R. Dehoff, A. Shyam, Elevated temperature ductility dip in an additively manufactured Al-Cu-Ce alloy, Acta Mater. 220 (2021) 117285.
[65] L. Ci, Z. Ryu, N.Y. Jin-Phillipp, M. Rühle, Investigation of the interfacial reaction between multi-walled carbon nanotubes and aluminum, Acta Mater. 54 (2006) 5367-5375.
[66] A. Da Silva, J. Frostevarg, A.F. Kaplan, Thermal monitoring for directed energy deposition of stainless steel, bronze, and cobalt-based alloy, Surf. Coat. Technol. 451 (2022) 129078.
[67] A. Ashby, G. Guss, R.K. Ganeriwala, A.A. Martin, P.J. DePond, D.J. Deane, M.J. Matthews, C.L. Druzgalski, Thermal history and high-speed optical imaging of overhang structures during laser powder bed fusion: A computational and experimental analysis, Addit. Manuf. 53 (2022) 102669.
[68] A.B. Spierings, K. Dawson, T. Heeling, P.J. Uggowitzer, R. Schäublin, F. Palm, K. Wegener, Microstructural features of Sc-and Zr-modified Al-Mg alloys processed by selective laser melting, Mater. Des. 115 (2017) 52-63.
[69] F. He, H. Zhou, K. Li, Y. Zhu, Z. Wang, Numerical Analysis and Experimental Verification of Melt Pool Evolution During Laser Cladding of 40CrNi2Si2MoVA Steel, J. Therm. Spray Technol. 32 (2023) 1416-1432.
[70] R. Brooks, A. Dinsdale, P. Quested, The measurement of viscosity of alloys—a review of methods, data and models, Meas. Sci. Technol. 16 (2005) 354.
[71] S. Kou, A criterion for cracking during solidification, Acta Mater. 88 (2015) 366-374.

[72] J. Liu, S. Kou, Crack susceptibility of binary aluminum alloys during solidification, Acta Mater. 110 (2016) 84-94.
[73] A. Dinsdale, P. Quested, The viscosity of aluminium and its alloys--A review of data and models, J. Mater. Sci. 39 (2004) 7221-7228.
[74] H. Wei, J. Mazumder, T. DebRoy, Evolution of solidification texture during additive manufacturing, Sci. Rep. 5 (2015) 16446.
[75] T. Gu, B. Chen, C. Tan, J. Feng, Microstructure evolution and mechanical properties of laser additive manufacturing of high strength Al-Cu-Mg alloy, Opt. Laser Technol. 112 (2019) 140-150.
[76] J. Park, J.-H. Kang, C.-S. Oh, Phase-field simulations and microstructural analysis of epitaxial growth during rapid solidification of additively manufactured AlSi10Mg alloy, Mater. Des. 195 (2020) 108985.
[77] S. Chen, M. Xu, T. Yuan, X. Jiang, H. Zhang, X. Zheng, Thermal–microstructural analysis of the mechanism of liquation cracks in wire-arc additive manufacturing of Al–Zn–Mg–Cu alloy, J. Mater. Res. Technol. 16 (2022) 1260-1271.
[78] M. Froend, V. Ventzke, F. Dorn, N. Kashaev, B. Klusemann, J. Enz, Microstructure by design: An approach of grain refinement and isotropy improvement in multi-layer wire-based laser metal deposition, Mater. Sci. Eng. A 772 (2020) 138635.
[79] M. Froend, S. Riekehr, N. Kashaev, B. Klusemann, J. Enz, Process development for wire-based laser metal deposition of 5087 aluminium alloy by using fibre laser, J. Manuf. Process. 34 (2018) 721-732.
[80] G. Dinda, A. Dasgupta, J. Mazumder, Texture control during laser deposition of nickel-based superalloy, Scr. Mater. 67 (2012) 503-506.
[81] A. Pandey, V. Gaur, Effect of dwell time on fatigue properties of wire-arc additively manufactured IN718 alloy, Int. J. Fatigue 176 (2023) 107863.

Paper 5: M. Wang, N. Kashaev, On the maintenance of processing stability and consistency in laser-directed energy deposition via machine learning, Journal of Manufacturing Systems 73 (2024) 126-142.

This published paper was incorporated as Chapter 4.6 (with permission from Elsevier).

Journal of Manufacturing Systems 73 (2024) 126–142

Contents lists available at ScienceDirect

Journal of Manufacturing Systems

journal homepage: www.elsevier.com/locate/jmansys

Technical paper

On the maintenance of processing stability and consistency in laser-directed energy deposition via machine learning

Mengjie Wang *, Nikolai Kashaev

Institute of Materials Mechanics, Department of Laser Processing and Structural Assessment, Helmholtz-Zentrum Hereon, Max-Planck-Str. 1, D-21502 Geesthacht, Germany

ARTICLE INFO

Keywords:
Laser-directed energy deposition
Processing stability and consistency
Geometrical accuracy
Porosity level
Convolutional neural network
In-situ process monitoring and adjustment

ABSTRACT

In lateral wire-based laser-directed energy deposition, conveying shielding gas through the wire feed nozzle devastates the processing stability, which results in a geometrical deviation and an increase in porosity level. In the present study, an extra nozzle is installed to convey shielding gas to balance the gas flow from the wire feed nozzle. It is confirmed that the installation of the extra nozzle sustains the processing stability, achieves geometrical accuracy, and reduces the porosity level. However, finding an appropriate flow rate for the extra shielding gas is time- and material-consuming. In order to efficiently find the flow rate, a convolutional neural network is used to simplify this process by analyzing the processing images and receiving guidance from the outputs to adjust the current flow rate to save time and material cost. In addition, a novel methodology is proposed to in-situ monitor and in-situ adjust process parameters during laser-directed energy deposition by adopting a convolutional neural network. The processing characteristics such as melt pools, plume, and spatter can be well maintained, which contributes to a consistent geometry and porosity of deposition layers. Results indicate that the methodology proposed in this study is promising to be transferred to other laser-beam-melting processes both in additive manufacturing and coating.

1. Introduction

Additive manufacturing (AM) exhibits advantages over conventional subtractive manufacturing technologies such as casting with respect to design freedom and material saving, etc [1]. 3D parts can be built according to the deposition path coded in a program or designed in a 3D model. However, the geometry of as-built parts could be inconsistent with that as designed even though following the path. The reasons can be divided into two specific aspects, i.e. hyperparameters (hardware- and technology-related) [2–6] and operator-adjustable parameters (material- and processing-related) [7,8].

In terms of the hardware, despite the flexibility of robots, the movement commands executed by the industrial robots exhibit a lower path accuracy compared with the movement in conventional CNC machines, which results in the geometry deviation in as-built parts [2]. The geometrical inaccuracy can also be caused due to the unsuitable CAD file [3]. Besides, the type of laser and the wavelength need to be appropriately selected for a certain AM technology [4]. Regarding AM technologies, laser powder bed fusion (LPBF) can produce parts with better precision compared with laser-directed energy deposition (L-DED) [5]. According to the type of feedstock, L-DED can be classified into powder- and wire-based L-DED. A better precision can be achieved in powder-based L-DED than in wire-based L-DED [6]. However, wire-based L-DED has its irreplaceability compared with powder-based L-DED such as a near 100% material utilization rate [9]. Both L-DED processes can be applied in some scenarios where LPBF is not suitable, such as the production of large-size parts and the scenario with a requirement for a high deposition rate [10].

In wire-based L-DED, the wire can be either laterally [11] or coaxially [12] fed relative to the laser beam. During processing, the shielding gas is utilized to create an inert gas atmosphere and protect deposited layers from oxidation. In coaxially wire-based L-DED, the shielding gas can be conveyed through the optic head to protect the deposition from the top. The lateral L-DED apparatus can be modified from a laser welding apparatus [13], where the flexibility of the path direction is not highly in demand. In this case, the shielding gas is conveyed through the wire feed nozzle as in a welding apparatus [14]. According to the previous study, the wire should be fed by using the side-feeding strategy to avoid the wire getting stuck in the track in back feeding and oxidized metal vapor falling on the track surface in front feeding [15]. In this

* Corresponding author.
E-mail address: mengjie.wang@hereon.de (M. Wang).

https://doi.org/10.1016/j.jmsy.2024.01.005
Received 31 July 2023; Received in revised form 17 October 2023; Accepted 12 January 2024
Available online 3 February 2024

case, Ar is conveyed through the wire feed nozzle and toward one side of the built thin-wall structures, which is asymmetrical to the melt pools during processing. The effects of shielding gas on the direct energy deposition (DED) process and the properties of as-built specimens (e.g. geometry and porosity level) have been studied with a focus on the flow rate of shielding gas [16–18]. In most of the DED processes, the shielding gas is coaxially conveyed through the optic head and symmetrically blows from the top to the melt-pool surface [16,19]. To realize the symmetrical blowing direction in a modified laser welding apparatus, extra components need to be purchased to enable the coaxial conveying of shielding gas through the optic head. Given the existed effects of blowing directions in single-track deposition [15], it is meaningful to comprehensively study the influences of the asymmetrical blowing of shielding gas on the L-DED process and the properties of as-built specimens. If the negative effects exist, it is worth investigating whether there is an economic solution to tackle them rather than purchasing extra components to enable the coaxial conveying through the optic head.

Concerning operator-adjustable parameters, the possible factors affecting the geometrical accuracy of as-built specimens also cover the material selection and process parameters being used. In L-DED, the relative positions between laser focus, powder focus, and melt pools affect the surface quality of deposited tracks [7]. Adjustment of the laser beam irradiance reduces the size of surface grooves in thin-wall structures [20]. Residual stress is formed during AM because of the rapid heating and cooling characteristics, which could lead to distortion [21]. Heat transfer and fluid flow models are developed to estimate the dependence of residual stress and distortion on process parameters [22]. The distortion can also be predicted by a mathematical model before processing and prevented by exerting geometry compensation in the path design step [23]. Heat accumulation caused by changing heat transfer conditions and delayed parameter adaption contribute to the geometry deviation [8]. Hence, the parameters or the processing strategies should be adjusted depending on the situation, such as adopting inter-layer cooling [24] and developing advanced algorithms to update process parameters [25].

Machine learning (ML) has been widely employed to assist manufacturing processes. In AM, the application of ML can be categorized into three phases, i.e. prior process, in-situ process, and post-process [26]. Before processing, ML can be adopted to select and develop suitable material composition [27]. In the phase of design for AM, ML aids the topology improvement [28]. There are numerous controllable process variables in AM, which increases the difficulty of searching for the optimal process window. ML algorithms such as neural networks [29–31] are applied to shorten the parameter study. Several researchers have investigated the possibility of using ML to predict the geometry of as-built single tracks [32] and multiple layers [33]. To lessen the cost in the experimental characterization for as-built specimens, some works have been implemented to integrate the microstructure and mechanical properties with process-related factors by using ML. The process parameters and microstructural features can be correlated to realize the prediction and tailoring of microstructure [34]. By extracting thermal histories during AM process, the quasi-static tensile properties can be predicted in the local region of a thin-wall structure [35]. The process-and-analysis chain is constructed by using ML in terms of parameter adjustment to achieve high-density parts and the prediction of strength based on microstructure [36].

ML algorithms are also able to support the in-situ process monitoring and control. Convolutional neural network (CNN) is a prevailing algorithm to conduct in-situ monitoring and defect detection based on image recognition since it exhibits higher accuracy and lower requirements for feature extraction than conventional ML algorithms [26]. Images captured during AM process for the CNN model contain melt pools [37–39], plume and spatter [40], and layer surface [41,42]. All the information enclosed in the images belongs to the processing characteristics. The images can be either utilized to quantitatively characterize the properties, such as the prediction of porosity level [43] and surface roughness [44], or used to qualitatively evaluate the processing, such as the presence of defects and processing anomalies [38,40]. Nevertheless, the aforementioned works can predict defects and diagnose the processing anomaly, while a simultaneous correction is not possible. An in-situ adjustment of process parameters is essential to avoid the deterioration of present anomalies and the waste of material.

In this study, the characteristics of lateral conveying of shielding gas and its effects on the L-DED processing stability and the properties (geometrical accuracy and porosity level) of as-built specimens are addressed. The feasibility of adopting ML algorithms for in-situ monitoring and in-situ adjustment of process parameters is investigated with the assistance of a high-speed camera to maintain processing stability and consistency.

2. Methods

2.1. Laser-directed energy deposition

The material used in the present study is AA7075 wire. Details regarding the laser system and material were introduced in the previous work of the authors [13]. Thin-wall structures were built by using a bi-directional scanning strategy. A high-speed camera is fixed to the side of the optic head by an extension bracket (Fig. 1a). It is focused at the tip of the wire, which enables the capture of sharp images of the processing characteristics during deposition. The focus plane of the camera is parallel to the cross-sectional plane of the thin-wall structures, as illustrated in Fig. 1d. Hence, the processing images taken during deposition correspond to the cross-sections in the direction of the melt-pool width. The shielding gas Ar is coaxially conveyed through the wire feed nozzle to the melting area to protect it from oxidation. Besides, an extra nozzle conveying Ar is installed and located mirror-symmetrically to the wire feed nozzle relative to the thin-wall structure, as shown in Fig. 1b. The side facing the wire feed nozzle is defined as the front side of the wall and the other side facing the extra nozzle is referred to as the back side of the wall, as illustrated in Fig. 1c.

Thin-wall structures were built with two processing strategies, i.e. continuous and discontinuous processing. In the continuous processing, no interlayer cooling is adopted, while each layer is cooled to room temperature before the subsequent deposition in the discontinuous processing. The identical interlayer temperature could build a similar heat transfer condition in different layers.

2.2. Material characterization

Thin-wall structures were cut in the middle along the width direction and prepared for microstructural observation under an optical microscope (OM, Leica DMI 5000 M). The prepared specimens were ground and polished three times to gain three cross-sections and the cross-sectional porosity level is averaged. Specimens were etched with Barker's etchant for 15 s to disclose the grain morphology.

A 3D profile of the built structures was created with a digital microscope (VHX-7000, Keyence), see Fig. 2a. Maximum roughness R_{max} (vertical distance from peak to valley according to German standard DIN4768) is adopted to represent the surface roughness of the back side of thin-wall structures. The reference x-y plane/zero point in the height direction (z-axis) cannot be set as the same for all thin-wall structures. Hence, the color bar on the left upper corner can only represent the height fluctuation on the back side (Fig. 2b). The values next to the color bar are not comparable between different specimens. The two points

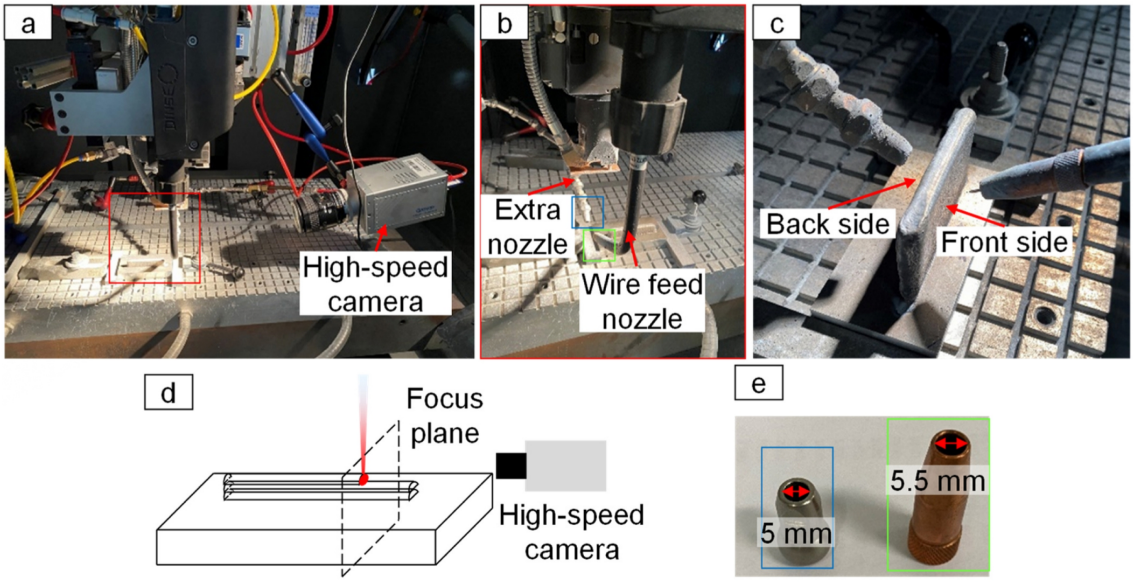

Fig. 1. (a) Experimental setup in the L-DED process. (b) Locally magnified area showing the position of extra shielding gas nozzle. The geometry of the wire feed nozzle and the extra nozzle is also shown. (c) The illustration shows the relative position of the front side and back side of thin-wall structures and wire feed nozzle and extra nozzle. (d) Position of the focus plane of the high-speed camera relative to the thin-wall structure. (e) The geometry of two nozzles.

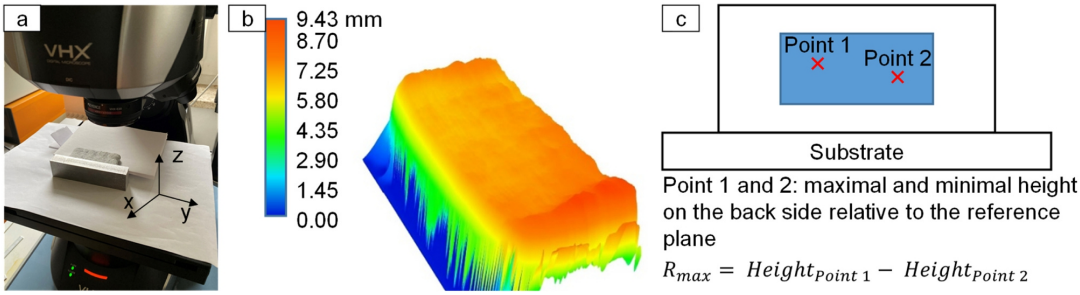

Fig. 2. (a) Placement of specimen during 3D scanning and (b) 3D profile of the back side of the thin-wall structure. (c) Illustration of how the maximum roughness R_{max} is calculated.

with maximal height and minimal height on the back side relative to the reference plane can be detected in a selected region by the microscope. The parameter R_{max} is then calculated as shown in Fig. 2c.

Hardness was measured with Falcon 5000 microhardness tester (INNOVATEST Europe BV, load: 100 g, loading time: 10 s). The indentation points were aligned along the building direction from the thin-wall structure surface with a distance increment of 2.7 mm to the dilution area with the substrate.

2.3. Image processing

Grayscale images were captured by the high-speed camera at a frame rate of 2000 frames per second (FPS) and an exposure time of 100 μs. Raw images with a size of 1280 × 860 pixels contain different information, such as melt pool, plume, and spatter. In this study, the images are resized to 640 × 430 to save computation time and then used for two scenario analyses: evaluation of the processing stability during deposition and input in a neural network model. Plume and spatter are noises in the first analysis since only the geometry and the area of melt pools need to be analyzed. Hence, raw images were processed by a Python script to extract the melt-pool profile. A threshold value of 190 was selected for binary raw images before further contour detection.

2.4. Architecture of convolutional neural network

Three CNN models with different architectures were constructed to solve various tasks as shown in Fig. 3 and Table A.3. The architecture of models shown in Fig. 3 exhibits the best performance in terms of accuracy and generalization. The design and optimization of the CNN models can be referred to in Appendix A.2. Model 1 and model 2 were applied to identify processing images during deposition with different shielding gas flow rates. Model 1 with one output can only recognize the right or wrong answer (appropriate and inappropriate gas flow rate), while model 2 with three outputs can separate the wrong answers into more specific groups. Model 3 was used to classify the processing images during deposition with different laser powers. With 5 outputs, it can finely categorize the images into various groups according to the magnitude of laser power.

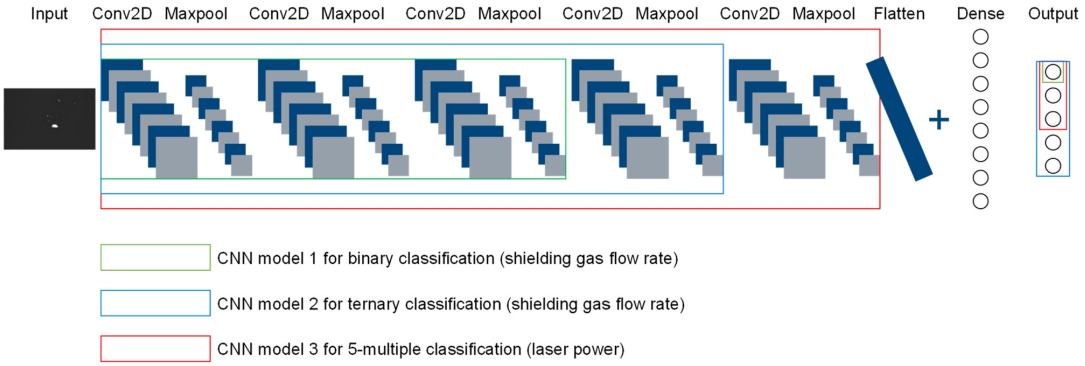

Fig. 3. Illustration of the architecture of three CNN models. The size of images does not correspond to the actual size of images in pixels after processing by convolutional and maxpool layers.

Labeling the images and random data division for train data, validation data, and test data are introduced in the following specific parts. Besides resizing the raw images from 1280 × 860 pixels to 640 × 430 pixels, all input images are randomly panned by N pixels ($N \in [-150, 150]$) in the width and length directions before feeding into the CNN model. Thereby, the CNN model focuses on the relative spatial locations of the melt pool and the plume as well as the spatter rather than their absolute positions in the 640 × 430 images.

Given the process parameters introduced in this study, such as gas flow rates and laser power, the prediction for the two parameters can be also approached as a regression problem. The comparison and discussion for both the classification and regression CNN can be referred to in Appendix A.3.

3. Results and discussion

3.1. Processing stability

In the previous works, the process window for AA7075 in L-DED was investigated in [13,15]. The optimal process window has been found considering the porosity level and cracking sensitivity. However, it is noticed that the maximum roughness on the front side and the back side of the as-built thin-wall structures exhibit a significant discrepancy. The initial L-DED apparatus is not equipped with an extra shielding gas nozzle. Ar is conveyed coaxially with wire and blows only the front side of the structure during deposition with a flow rate of 10 l/min. It is assumed that the blowing direction of Ar is the key factor causing the

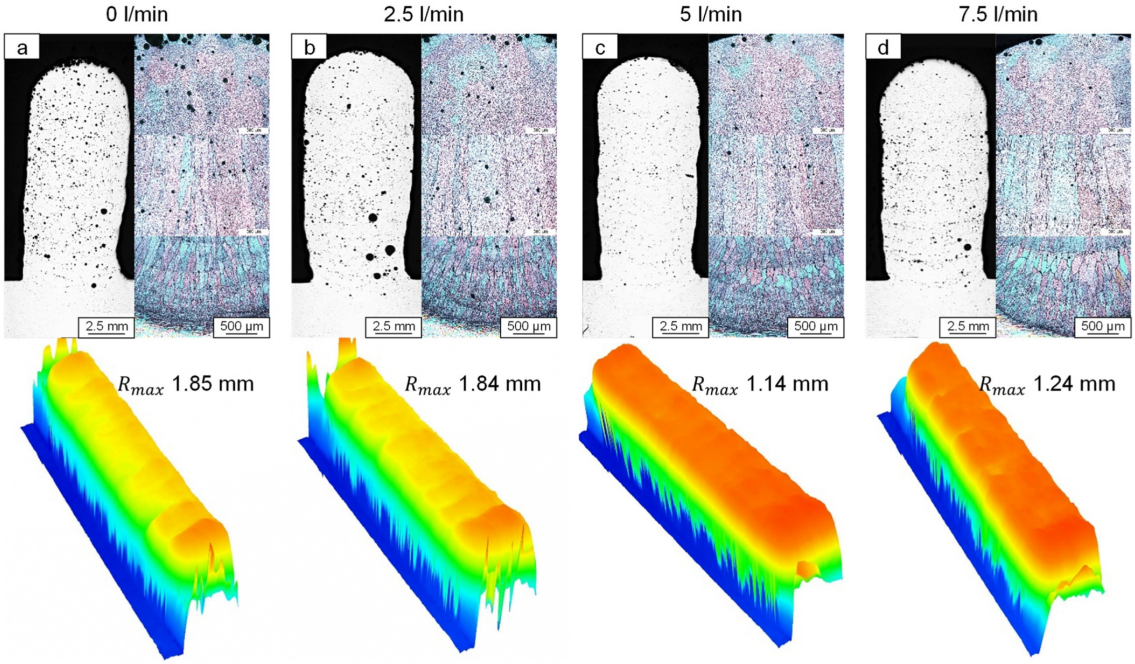

Fig. 4. Cross-sectional views and 3D-reconstructed back sides of 20-layer specimens produced with various extra shielding gas flow rates of (a) 0 l/min, (b) 2.5 l/min, (c) 5 l/min, and (d) 7.5 l/min. Other process-related parameters kept constant (Laser power: 1st layer 4000 W, 2nd layer 3500 W, 3rd – 4th layer 3250 W, 5th–20th layer 3000 W. Laser scan speed: 1 m/min. Wire feed speed: 4 m/min, no inter-layer cooling is adopted).

difference in maximum roughness on the two sides of thin-wall structures. Under this consideration, an extra nozzle is installed attempting to create balanced fluid dynamic conditions for the entire structure.

Thin-wall structures with 20-layers are built in lateral L-DED with various Ar flow rates of the extra nozzle, i.e. 0 l/min, 2.5 l/min, 5 l/min, and 7.5 l/min, whilst the Ar flow rate from the wire feed nozzle keeps constant at 10 l/min in all experiments. As-built specimens are characterized and investigated in terms of porosity level, microstructure, and maximum roughness R_{max} on the back side, see Fig. 4. The microstructure at the top, mid, and bottom sides of four specimens exhibit the typical coarse equiaxed, large columnar, and fine equiaxed grain morphology. The hardness is measured from the top to the bottom of as-built structures and averaged. No noticeable difference in hardness can be identified from the four specimens as shown in Table 1. The cross-sectional porosity level of specimens from Fig. 4(a) to (d) is 4.0 ± 1.0%, 3.7 ± 1.2%, 1.4 ± 0.3%, and 2.6 ± 1.1%, respectively. Using a flow rate of 5 l/min for the extra gas nozzle can significantly increase the relative density of as-built specimens. The porosity level decreases with increasing flow rate until 5 l/min and then deteriorates with excessive flow rate.

It is also noticed that a fraction of pores is distributed in the subsurface region in the specimen without conveying extra Ar during deposition (Fig. 4a). The subsurface porosity is reduced in specimens processed with extra Ar. Most of the pores exhibit a spherical morphology and a non–periodical dispersion [18]. The last layer experiences no remelting. Consequently, the gas pores trapped on the top of the melt pool cannot float to the upper layers or escape to the air as in the previous layers. The potential sources of gas porosity in as-built specimens contain the evaporation of alloying elements [45], retention of shielding gas [18], and absorption of moisture from ambient temperature [46,47]. The peak temperature in the melt pool is mainly dependent on the intrinsic material properties and the energy input. Under this consideration, the reasons for the reduction of subsurface porosity could be attributed to either absorbing less moisture from the atmosphere or extending the melt-pool lifetime, which provides more chances for the gas pores to escape.

The specimen processed with an extra Ar flow rate of 5 l/min manifests the least color contrast, which indicates the most homogeneous height distribution on the back side (Fig. 4c). The workflow to calculate R_{max} is introduced in Fig. 2. The maximum roughness in the back side varies with the flow rate of extra Ar in the same trend as the porosity level. The minimum R_{max} of 1.14 mm is achieved by using 5 l/min flow rate. In the other three specimens, the shrinkage can be observed in different positions on the back side without any regularity. The effects of inappropriate gas flow are strengthened with increasing layer numbers. Compared with no extra Ar, the back-side maximum roughness of a 100-layer structure is decreased from 6.26 mm to 1.02 mm by adopting an extra nozzle with 5 l/min flow rate Fig. 5(a, b). The top view of as-built thin-wall structures also qualitatively demonstrates the improvement, see Fig. 5(c, d).

In the initial L-DED apparatus, the melt pool is blown by Ar only on one side, which creates uneven cooling conditions for the entire melt pool. Different cooling rates on the melt-pool surface lead to forming an inhomogeneous distribution of temperature gradient and surface tension. The Marangoni convection drives the melt from the high-temperature region to the low-temperature region [48]. The surface tension is negatively proportional to the temperature:

$$\sigma(T) = 3.282 - 8.9e^{-4}T \quad (1)$$

where σ is the surface tension and T is the temperature in Kelvin [49]. Therefore, the points with high temperature and low surface tension on the melt-pool surface can be considered weak points from the perspective of maintaining the integrity of the melt pool.

When the temperature during L-DED exceeds the boiling point of metal elements, the vapor recoil pressure is generated as a counteracting force for evaporation and imposed on the melt-pool surface [49]. The evaporation-induced recoil pressure is enhanced with increasing temperature on the melt-pool surface [50]. Hence, the weak points with low surface tension withstand higher recoil pressure. The back side of melt pools has a slower cooling rate and a resultant higher temperature compared with the front side in case of no extra Ar. Under the combined effects of surface tension and recoil pressure, the rupture of the melt-pool surface and the formation of droplets occur as shown in Fig. 6. The increase in maximum roughness caused by dispersive melt-pool spatter is also confirmed by experimental and modeling results [51].

Both insufficient and excessive flow rates of extra Ar result in unstable melt-pool dynamics. The occasional explosion of the melt pool promotes the formation of defects. It results in the fluctuation of melt-pool geometry and the geometrical inaccuracy in L-DED-produced specimens. Both one-side blowing and two-side blowing with inappropriate gas flow rates create melt pools with asymmetrical geometry.

The stability of melt pools during deposition is analyzed based on the melt-pool images in the first layer. The indicator for evaluating the stability of melt pools is the fluctuation of melt-pool area and shape. All grayscale images are binarized with a threshold value of 190. The threshold value is determined to accurately capture the melt-pool profile while avoiding any misleading information from the illuminated area surrounding the melt pools. The detailed workflow on how to determine the threshold value can be referred to in Appendix A.1. As-built single tracks exhibit various surface morphologies. In Fig. 7(a, b), using an Ar flow rate of 0 l/min and 2.5 l/min produces tracks with a bright surface, whilst the tracks are covered by dark films at one side of the track in Fig. 7c (5 l/min) and in the middle of the track in Fig. 7d (7.5 l/min), which is the oxide film. Under a low flow rate of extra Ar, the oxidized vapor is blown onto the surface of the substrate instead of falling on the track surface. The extracted contour of melt pools can represent its characteristics in raw images.

To accurately evaluate the processing stability, it is important to consider the geometrical fluctuation of melt pools. Even if two melt pools have the same area, they can exhibit different geometries. The variation in geometry can be influenced by gas flow, leading to property variations, as reported in [52]. After binarization, all pixel points in the processing image corresponding to the melt pool are assigned a grayscale value of 1, whereas other pixel points corresponding to non-melt-pool areas are assigned a grayscale value of 0. To compare the geometrical deviation of melt pools in different images, it is necessary to compare the grayscale values of each pixel point representing the location of melt pools pixel by pixel between images. To statistically represent this geometrical fluctuation of melt pools during processing, the *dHash* value and *dHash* difference are adopted. These metrics allow us to quantify and analyze the differences in geometry between melt pools in different images.

The *dHash* value is a parameter to compare the grayscale values in two neighboring pixel points in an image row by row. The workflow to calculate the *dHash* value of one image and the *dHash* difference between two images is illustrated in Fig. 8. If the grayscale value of the left pixel is higher than that of the right pixel, the character "1" is recorded. Otherwise, the character "0" is recorded. Subsequent to the comparison of all pixel points, a long string consisting of "1" and "0" is arranged for each image. In this study, since the raw images are firstly binarized to extract the contour of melt pools, the pixel points exhibit either black or

Table 1
Average hardness of 20-layer thin-wall structures processed with various extra Ar feed rates.

Shielding gas flow rate (l/min)	0	2.5	5	7.5
Hardness ($HV_{0.1}$)	75.0 ± 6.5	77.4 ± 5.8	76.8 ± 7.7	74.0 ± 8.3

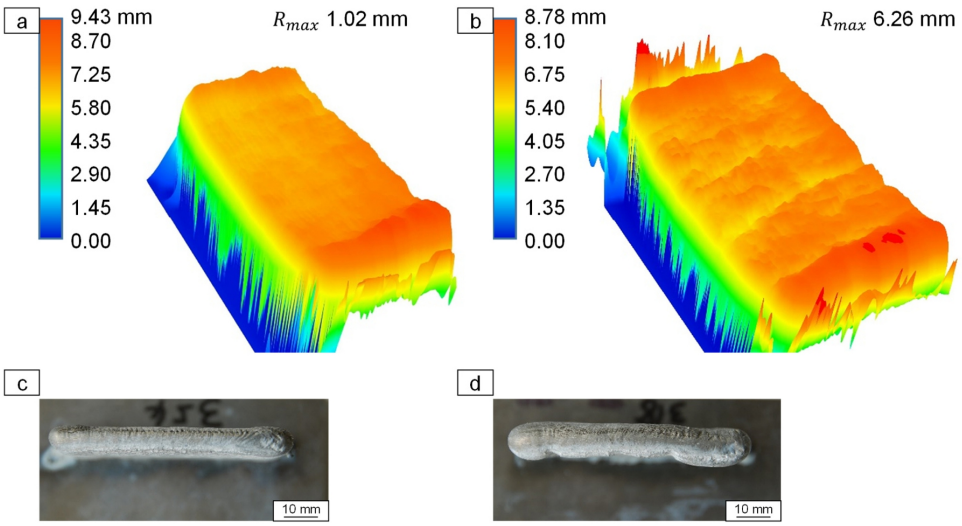

Fig. 5. (a, b) Back sides reconstructed by digital microscope and (c, d) top views captured by optical camera of 100-layer specimens produced with extra shielding gas flow rates of (a, c) 5 l/min and (b, d) 0 l/min.

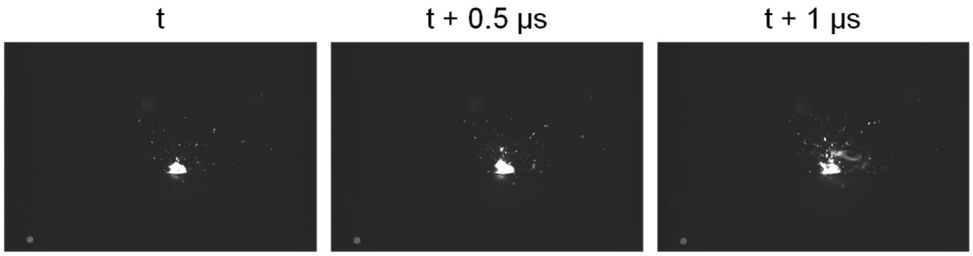

Fig. 6. An explosion of melt pool during processing with shielding gas flow rate of 10 l/min.

white. Characters in the string are considered binary numbers. To save computational time while maintaining the sensitivity to detect subtle differences, every two characters in the string from the first to the last are converted to decimal numbers and stored as a new string. The fully converted string corresponds to the *dHash* value of the image. All the images have the same length of strings because of the same image size. The *dHash* difference is the total number of characters that differ in the identical position in two strings converted from two images.

In each group, 4751 images are evaluated. The 1st image is considered a reference. The initial *Area* difference and *dHash* difference are calculated relative to the 1st image. The area and the shape of the 1st image might not be representative of each group. Hence, after the first calculation phase, the *Area* difference and the *dHash* difference of the 2nd – 4751st images are averaged as the new reference value. Afterward, the new difference is calculated by subtracting the new reference value using the initial difference.

The distribution and statistic results of indicators of 4750 images in each group are shown in Fig. 9 and Table 2. In terms of *Area* difference, the melt pools processed without extra Ar exhibit a larger average *Area* difference (3.90) than those processed with 2.5 l/min (3.70) and 5 l/min (3.07) but a lower average difference than those processed with 7 l/min (4.77). The maximum *Area* difference of 46.87 is observed in the group of 0 l/min, while other groups show a lower maximum of *Area* difference. Hence, the flow rate of 2.5 l/min and 5 l/min can stabilize melt pools during processing considering the *Area* difference. Regarding the shape variation of melt pools, the group of 5 l/min demonstrates the lowest value of the average *dHash* difference (36.69) and the maximum *dHash* difference (116.56). As the extra Ar flow rate of 5 l/min is employed, all the indicators are significantly improved in comparison with no extra nozzle. The stable processing can also be verified with the least fluctuation of melt-pool area and shape according to the standard deviation. The investigation regarding the melt-pool stability is consistent with the observation of the back-side maximum roughness that using a 5 l/min flow rate can effectively balance the gas flow from the wire feed nozzle and maintain the melt-pool stability during deposition as well as further increase the geometrical accuracy. The porosity level of as-built specimens exhibits the same downward and upward trend with increasing extra shielding gas flow rate as the two indicators for the stability of melt pools, i.e. *dHash* and *Area* difference, as shown in Fig. 10. The stability of melt pools is directly determined by the flow rate of extra Ar, which subsequently affects the porosity level of the solidified material. A similar correlation has been observed in [51,53]. The unstable melt flow favors melt splashing and the formation of pores.

3.2. Determination of processing stability via machine learning

3.2.1. CNN model for binary classification

It has been confirmed that the extra shielding gas can improve the quality of as-built specimens. However, the shielding gas flow rate must be properly adjusted to achieve the best processing stability. The quality

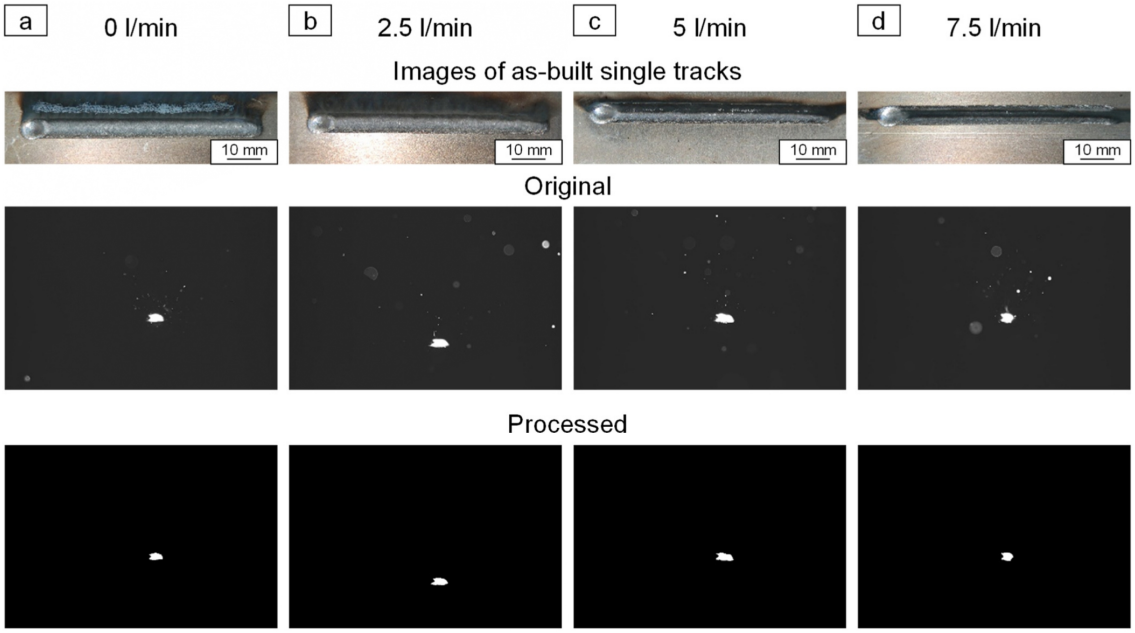

Fig. 7. As-built single tracks and corresponding original images as well as processed images of melt pools processed with different extra Ar flow rates. Except for the extra Ar flow rate, other process parameters for the single-track deposition are the same: laser power 4000 W, laser scan speed 1 m/min, and wire feed speed 4 m/min.

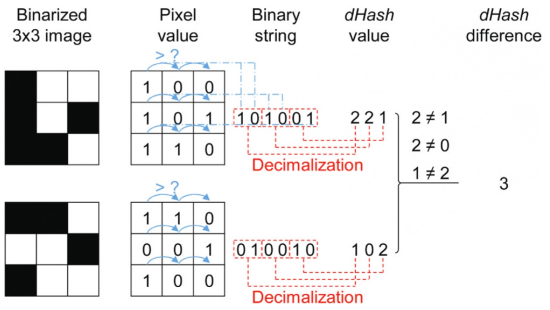

Fig. 8. Illustration shows the workflow to calculate *dHash* difference between two 3 × 3 pixel images.

of thin-wall structures is evaluated based on the back-side maximum roughness and the cross-sectional porosity level. To measure the maximum roughness on the back side, at least 15–20 layers need to be deposited to reflect the maximum roughness, which is time- and material-consuming. The subsequent 3D scanning or metallography preparation also takes time. Therefore, it is beneficial if the process chain to find the optimal gas flow rate can be simplified.

Given the distinct characteristics of melt pools and plume as well as spatter under different process conditions and the image identification of the CNN model, a CNN model for binary classification is built to classify the images captured during processing into the appropriate and inappropriate groups based on their characteristics and adherence to the desired processing conditions. The appropriate group consists of processing images captured when using an extra shielding gas flow rate of 5 l/min. This gas flow rate has been found to enhance the processing stability and improve the properties of specimens. These images are labeled as 1 in the binary classification. The inappropriate group comprises processing images captured when using extra shielding gas flow rates of 0, 2.5, and 7.5 l/min. These gas flow rates do not achieve the desired processing stability. The images in this group are labeled as 0 in the binary classification.

The CNN model is named model 1 in this study and its architecture is shown in Fig. 3 and Table A.3. Over 8000 images are stored during the image acquisition for a single-track deposition by the high-speed camera. A total of 4571 images are selected from the middle of the image sequence and used in the CNN model since the L-DED process reaches a stable state in the middle of a deposition. Before feeding the data to model 1, 4751 images are randomly selected from the 14253 images of the inappropriate group to ensure the same size for the dataset in the two groups. The training set and the validation set are randomly divided in a ratio of 0.5. A dropout of 0.1 is added before the last fully-connected layer to avoid overfitting. Accuracy is selected for the metrics during training.

The performance of the last epoch in model 1 is shown in Table 3. To further evaluate the CNN model, a testing dataset and suitable metrics should be arranged. A total of 2000 images are selected from the initial image acquisition for each flow rate. There is no overlap between the images used in training, validation, and testing. The same operation is conducted in the testing dataset. A total of 2000 images are randomly selected from the 6000 images of the inappropriate group to ensure the same size for the testing dataset in two groups. The metrics for judging the performance of classification neural networks contain accuracy, precision, recall, and F1-score. Accuracy is the simplest metric and is defined as the ratio of the number of correctly classified images and the total number of images. In the case of the other three metrics, a confusion matrix needs to be created and used to calculate the metrics. Compared with accuracy, the other three metrics provided a more convincing evaluation when the testing dataset in different groups exhibits a size difference. Nevertheless, given the same size of the testing dataset in two groups, accuracy should be also representative. Model 1 classifies the testing dataset with an accuracy rate of 100%.

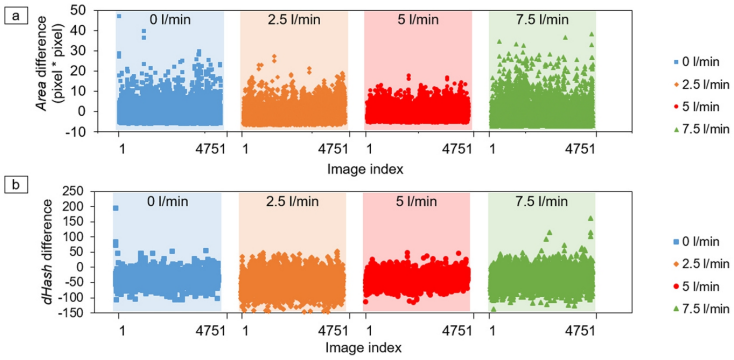

Fig. 9. Evaluation of the melt-pool stability under different extra Ar flow rates in terms of the fluctuation of *Area* difference and *dHash* difference.

Table 2
Statistic results of the *Area* difference (pixel * pixel) and *dHash* difference of melt-pool images. AVE: average value, STD: standard deviation; MAX (ABS): maximum of absolute values.

Extra Ar flow rate	Indicator	AVE	STD	MAX (ABS)
0 l/min	*Area* difference	3.90	3.38	46.87
	dHash value	53.49	16.61	194.44
2.5 l/min	*Area* difference	3.70	2.76	27.48
	dHash value	50.18	27.78	145.82
5 l/min	*Area* difference	3.07	2.17	17.84
	dHash value	36.69	17.73	116.56
7.5 l/min	*Area* difference	4.77	4.03	38.39
	dHash value	39.02	23.58	162.32

3.2.2. CNN model for ternary classification

Model 1 for binary classification confirms that the CNN model can forecast in the 1st layer whether the current gas flow can maintain the processing stability and avoid geometrical deviation during deposition. However, model 1 cannot guide the operator on how the inappropriate gas flow should be adjusted. Consequently, it still takes time to find a suitable gas flow. Using a multiple-classification model not only identifies input images as right or wrong but also divides the wrong images into specific groups.

A ternary classification model (model 2) is built to finely forecast processing images captured during L-DED. Three input groups of 0 l/min, 5 l/min, and 7.5 l/min are labeled as [0 1 0], [1 0 0], and [0 0 1], respectively. The preparation for the training dataset and validation dataset is the same as in the binary classification. The architecture of model 2 is listed in Fig. 3 and Table A.3. Model 2 consists of five convolutional layers and five maxpooling layers. A fully connected layer is inserted between the convolutional network and the output layer with three outputs. A dropout of 0.1 is applied before feeding data to the output layer. The training performance is established in Fig. 11. The accuracy increases and the loss decreases rapidly in the first 6 epochs. The best accuracy in the training dataset and validation dataset is 0.9317 and 0.9777, respectively. The lower accuracy in the training dataset is attributed to the addition of dropout in the network. Further increasing the number of training epochs does not significantly increase the accuracy.

The testing dataset in model 2 contains the images captured in the same deposition track as the training dataset and validation dataset. An accuracy of 0.9893 can be achieved. Besides, the reproducibility and the generalization of model 2 are also validated. A new single-track processed with an extra Ar flow rate of 5 l/min is deposited. Model 2 can correctly classify 4741 images out of 4751 images from the new track with an accuracy rate of 99.8%. One image from the 5 l/min track and the newly deposited 5 l/min track is selected to visually and statistically compare, see Fig. 12. Exclusively considering the melt pool, the *Area* difference and the *dHash* difference of these two melt pools are 65.5 and 91, respectively. The *Area* difference is higher than the maximum difference of 4750 processing images in the same 5 l/min group (17.84, see Table 2). The geometry of the two melt pools exhibits a moderate deviation. The processing images captured during processing with different Ar flow rates shown in Fig. 7 are also compared with the 5 l/min track in terms of *Area* difference and *dHash* difference. The newly deposited track processed with 5 l/min manifests a higher discrepancy in the geometry and a lower discrepancy in the area compared with the tracks processed with 0 l/min, 2.5 l/min, and 7.5 l/min, see Table 4. One image selected from each group might not be representative. However, it at least verifies that the *Area* and *dHash* difference of melt pools can be used to evaluate the stability of the L-DED process rather than determining whether the processing conditions are identical. In the 1st filter of the 1st convolutional layer in model 2, the melt pool, plume, and spatter are marked with color as shown in Fig. 12. Besides the melt pool, the CNN model learns various information in the raw image, such as the map of grayscale values in the image and the spatial distribution of spatter and plume relative to the melt pool. The images through

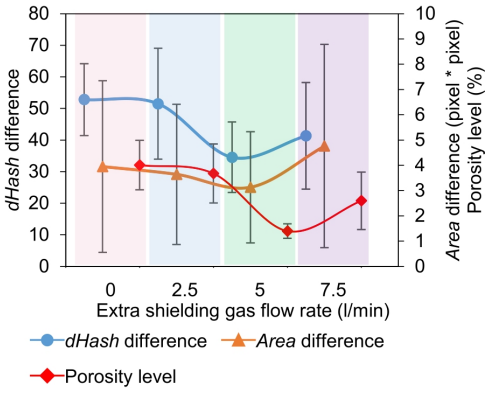

Fig. 10. The dependence of *dHash* difference, *Area* difference, and porosity level of as-built specimens on the extra shielding gas flow rate.

Table 3
Performance of CNN model 1 for binary classification.

	Train loss	Train accuracy	Validation loss	Validation accuracy	Test accuracy
Model 1	0.0374	0.9945	0.0096	0.9968	1

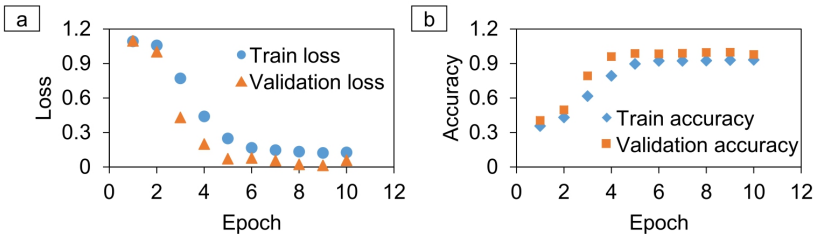

Fig. 11. Training performance of model 2.

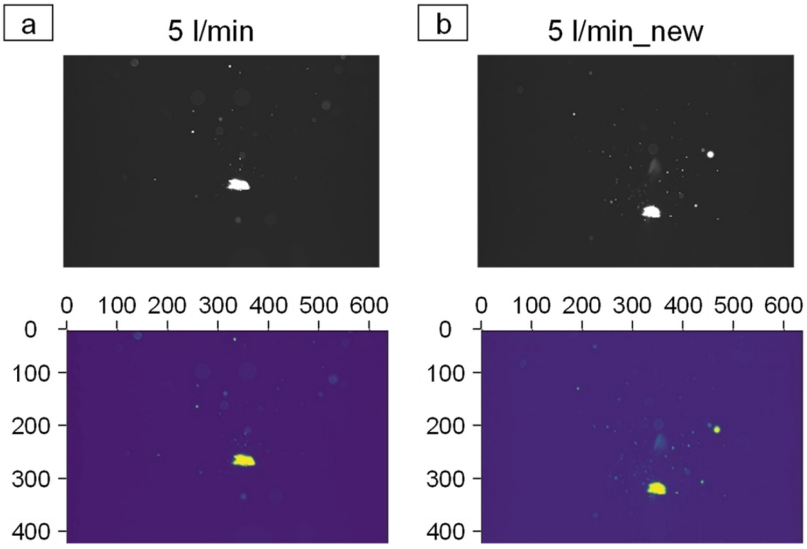

Fig. 12. Visualization of what the 1st convolutional layer has learned in CNN model 2. Pixel is used as a unit in the spatial description of melt pools. 5 l/min_new is one of the processing images captured during the deposition of a new track under an extra shielding gas flow rate of 5 l/min to validate the generalization of the CNN model.

Table 4
Area difference and *dHash* difference compared with the melt-pool processed with 5 l/min from Fig. 12a.

	Area difference	*dHash* difference
5 l/min_new (Fig. 12b)	65.5	46
0 l/min (Fig. 7a)	171	41
2.5 l/min (Fig. 7b)	79	44
7.5 l/min (Fig. 7d)	168	43

deeper layers become abstract and unexplainable.

3.2.3. *Verification of potential application in real manufacturing*

L-DED can be applied as AM technology and coating technology. The aforementioned investigations are based on single-track deposition. Nevertheless, thin-wall structures, which normally consist of multiple layers [20], and coatings, which normally consist of multiple tracks [54], are built for the two application scenarios. Hence, the possibility of using such a CNN model for image identification should be examined. The components in the image contain the melt pool, plume, spatter, etc. The characteristics of these components are correlated to the current processing environment [55]. Heat transfer conditions vary with increasing layers or tracks during L-DED [56]. Heat accumulation occurs leading to the formation of larger melt pools [57], which increases the difficulty to classify processing images in multiple layers or multiple tracks into the image group of single tracks processed with nominally identical parameters. Therefore, each layer or each track is cooled to room temperature before the next deposition attempting to create a similar heat transfer condition as in the single-track deposition.

A 9-layer thin-wall structure and a 3-track coating are produced as representative specimens in AM and coating technology, respectively. Images are captured in the 9th layer and the 3rd track, respectively. Photos of as-built specimens and the corresponding images are shown in Fig. 13. The thin-wall structure with 9 layers is produced with the optimal extra Ar flow rate (5 l/min). The geometrical accuracy and no processing-induced shrinkage along the length direction are attributed to the processing stability during L-DED. The optimal extra Ar flow rate determined with the process parameters from Fig. 4 and Fig. 5 applies also here, which confirms its generalization. The coating produced with a hatch distance of 4.5 mm exhibits adequate overlap and acceptable surface morphology. Hence, the two building jobs can represent real manufacturing scenarios. The similarity between the processing images of the 9th layer and the 3rd track as well as the single track is difficult to statistically disclose. Nevertheless, model 2 can classify the images of the 9th layer with a 100% accuracy rate and the images of the 3rd track with a 96.4% accuracy rate into the single-track image group processed with 5 l/min flow rate.

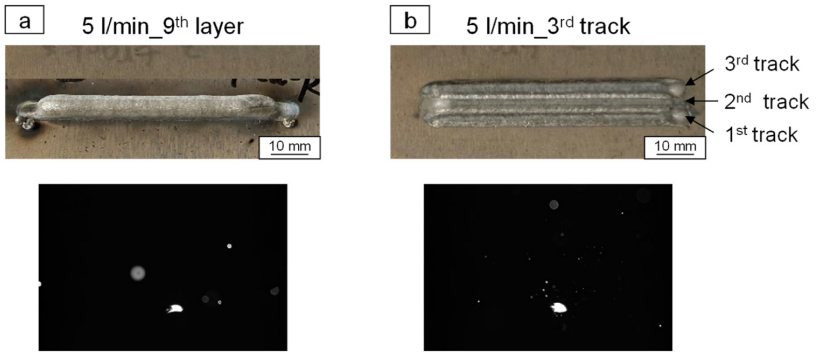

Fig. 13. Photos of as-built (a) thin-wall structure and (b) coating as well as correspondent images taken by a high-speed camera during deposition. 9 layers and 3 tracks are built with the same process parameters as in the single-track deposition, see Fig. 7. The hatch distance for the 3-track deposition is 4.5 mm. The extra shielding gas flow rate is 5 l/min.

3.3. Realization of processing consistency via machine learning and in-situ parameter adjustment

The envisionment of using the CNN model to predict and adjust shielding gas flow rate in single-track depositions has been validated. Furthermore, it is applicable in real manufacturing scenarios i.e. additive manufacturing and coating. A further step is to use the CNN model to in-situ adjust process parameters such as laser power. In laser-based additive manufacturing, the energy input is dependent on the laser power, laser scan speed, hatch distance, etc. If the same process parameters are used in building 3D structures without control for interlayer- or intertrack-temperature, the varied heat transfer conditions lead to heat accumulation. Hence, the energy input should be decreased depending on the current process state. The volumetric energy density (*VED*,((2)) [58] and the line energy density (*LED*,((3)) [59] are indicators to represent the energy input in LPBF and L-DED, respectively:

$$VED = \frac{P}{v^{*}h^{*}s} \tag{2}$$

$$LED = \frac{P}{v} \tag{3}$$

where P: laser power; v: laser scan speed; h: hatch distance; s: layer height.

The energy density is calculated by considering several independent variables, which makes the determination of the parameter to be adjusted difficult. Some research works treat laser power as a variable while keeping other parameters constant [2,12]. However, various process parameters impose different influences on the processing characteristics and the properties of as-built specimens [60]. Under this consideration, a systematical approach with the aid of the CNN model is proposed in this study. As shown in Fig. 14, using this paradigm and logistics, it can be systematically deduced which parameter should be adjusted and how to be adjusted. The optimal parameters are determined in the 1st single track based on the analysis of defects and processing stability. These images are labeled and set as input group 1 for the CNN model. The input groups contain other enormous databases, which cover the images taken during processing with inappropriate parameters, such as excessive and insufficient laser power (with finer distribution), higher and lower laser scan speed (with finer distribution), etc. A CNN model is trained by using this database. As an in-situ adjustment methodology, a sequence of the processing image is captured at point 1 and fed into the CNN model. If these images are classified as group 1, the process parameters are maintained. Otherwise, the images are classified into a specific group with improper process parameters. It indicates that the processing images currently being processed are equivalent to the processing images processed with the wrong process parameters as in the 1st single track. Subsequently, the current parameters can be relatively adjusted based on the forecasted parameters. After a preset period, a new sequence of images can be taken and analyzed again to ensure a stable process throughout the entire process.

In the present study, laser power is selected as the single variable to be adjusted. Two thin-wall structures with 3 layers are built as representative specimens. No interlayer cooling is adopted. The in-situ control has a strict requirement for computer-machine interaction.

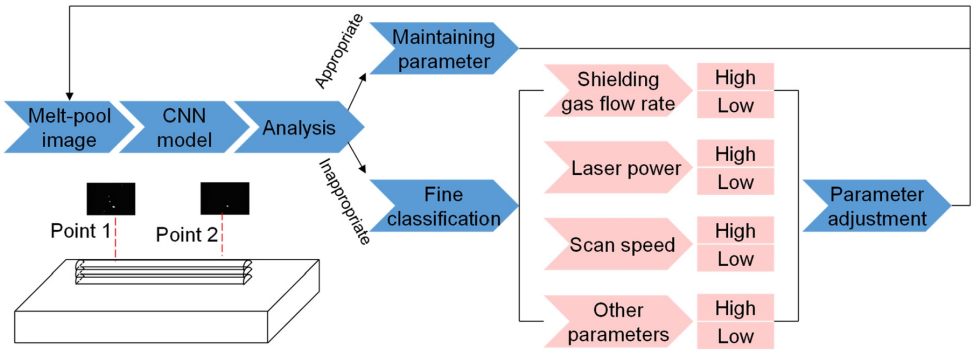

Fig. 14. Workflow of using the CNN model to in-situ adjust process parameters.

Therefore, processing images taken from the 3rd layer of the first specimen are used to analyze the current process state (step 1). According to the prediction of the CNN model, laser power is correspondently adjusted in the 3rd layer of the second specimen (step 2). Eventually, the images captured in the 3rd layer using adjusted laser power are fed into the CNN model again to validate the process state (step 3). The described logistic is shown in Fig. 15. There are two reasons for adjusting laser power in the 3rd layer and comparing it with the first two layers rather than changing laser power in the 2nd layer and comparing it with the 1st layer. First, the thickness of the thin-wall structure/the width of the melt pool does not increase in the 2nd layer compared with the 1st layer [24,61]. Second, two layers with a higher height are more intuitive than one layer to reveal the effects of parameter adjustment on the thickness.

The training dataset consists of the processing images taken during processing with 3000 W, 3250 W, 3500 W, 3750 W, and 4000 W in the single-track deposition. Each group has 4751 images. According to previous studies [15], the optimal laser power is 4000 W considering the minimum porosity level. However, 4000 W is the maximal laser power that the laser can provide. If a constant laser power of 4000 W is used in the 2nd and 3rd layers, the equivalent laser power in terms of the processing characteristics could be much higher than 4000 W. However, the training dataset cannot include such images. Consequently, to validate the proposed methodology, 3000 W is selected as the laser power in the 1st layer and assumed as the optimal process state. The characteristics of images and the porosity level in the 3rd layer should be adjusted to the state of 3000 W in the 1st layer.

The architecture of the CNN model (model 3) is introduced in Fig. 3 and Table A.3. The training dataset and validation dataset are divided with a ratio of 7:3. Fig. 16(a, b) reveals the training performance with an accuracy rate of 91.94% for the train data and 99.09% for the validation data. The accuracy difference is attributed to the application of a dropout of 0.2 before the output layer in model 3. As illustrated in Fig. 15, 96.7% of the images taken from the 3rd layer using 3000 W are equivalent to the images taken from the single track using 3750 W. It indicates that the laser power in the 3rd layer should be reduced by 750 W to 2250 W. In the last step, the images taken from the 3rd layer using 2250 W are fed into the model. 93.4% of the images can be correctly classified to the group corresponding to using 3000 W in the single track.

Excessive energy input and heat accumulation increase the size of melt pools and lead to the widening of deposition layers. The thickness of thin-wall structures is reduced with CNN model-assisted parameter adjustment by maintaining the consistency of melt pools in different layers, see Fig. 16c. The cross-sectional views of two representative specimens confirm the processing consistency, see Fig. 16(d, e). It has been proved that porosity is correlated to processing characteristics such as the formation of melt pools [43]. At the bottom of the two specimens corresponding to the first 2 layers, the high porosity level could be attributed to insufficient energy input and temperature. At the top of the specimen processed with 3000 W in the 3rd layer, the heat accumulation increases the temperature and changes the melt-pool characteristics, which could be the reason for the reduction of porosity level. However,

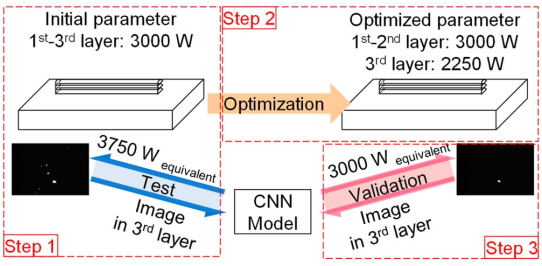

Fig. 15. Example of the process control in the case of laser power.

the high porosity level still exists at the top of the specimen processed with 2250 W in the 3rd layer. The average cross-sectional porosity level in the first 2 layers is 4.9% and the 3rd layer exhibits a comparable porosity level of 4.5%.

Besides the quantity of porosity, the pores in the 3rd layer and the first two layers exhibit a high similarity with respect to the distribution along the width direction of melt pools. Two masks are manually selected to separate the areas of the 1st – 2nd layers and the 3rd layer based on the etched microstructure. The distribution information of pores is extracted by a self-developed algorithm. The position of pores is normalized based on the maximal width of the mask to which they belong. Fig. 17 reveals the porosity length in pixels along the width of melt pools. The porosity evolution with an identical trend can be observed in the 1st – 2nd layers and the 3rd layer. The maximal porosity length is reached on the left side of melt pools. Furthermore, the left side demonstrates a higher porosity length overall compared with the right side. In the middle of the melt pools, the 1st – 2nd layers and the 3rd layer manifest a lower porosity length than the two sides.

The development of pores is significantly correlated with the instability of melt flow and the spatter of melt pools [51]. In addition to the shielding gas flow that can affect the stability of melt pools, other process parameters (e.g. laser scan speed and layer thickness) can also stabilize or destabilize the melt flow [51]. With the adjustment of laser power via the CNN model, the melt flow in the 3rd layer is consistent with the first two layers. Furthermore, it has been verified that the porosity level and the distribution of pores in melt tracks can be predicted according to the melt-pool images [43], which also indicates a strong relationship between the melt pools and the formation of pores. Since the comparable quantity and spatial distribution of pores are reached in this study, the adjustment of process parameters via ML is achievable to pursue the processing consistency regarding melt pools, plume, and spatter in various layers.

3.4. Novelty of the proposed methodology

Compared with conventional image processing algorithms or machine learning algorithms, CNN models offer several advantages, including higher accuracy and reduced requirements for feature extraction [26]. Previous studies have primarily focused on using CNN models for quantitative property prediction [43,44] or qualitative evaluation [38,40] as a post-processing method in additive manufacturing. However, in this work, a novel approach is proposed by utilizing CNN models to enable in-situ adjustment of process parameters. This is achieved by leveraging the capabilities of image classification to identify different processing states.

Regarding in-situ adjustment of process parameters, the commonly used method involves utilizing an infrared thermal camera to capture the processing temperature. The recorded temperature can then be used for a PID controller to adjust a single process parameter, typically laser power [62]. Another approach is to use the temperature data to identify the melt-pool geometry and subsequently adjust the process parameter, as demonstrated by the company Prima Additive [63]. However, both of these methods have limitations. Only one single process parameter can be adjusted at a time. Besides, both approaches rely on infrared cameras for temperature measurements. In additive manufacturing, these measurements can be affected by deviations caused by unstable emissivity due to surface roughness [64], oxide formation, and atmosphere change during processing [65]. In contrast, the proposed methodology of using CNN models to identify processing states offers several advantages. It provides the possibility of simultaneously controlling multiple process parameters since different processing states and properties of as-built specimens exhibit varying dependencies on parameters like laser power and scan speed [66]. Additionally, CNN models learn information about processing characteristics under different states, such as spatter and plume, which can aid in accurately identifying the current processing state instead of leading to the generation of deviations during the

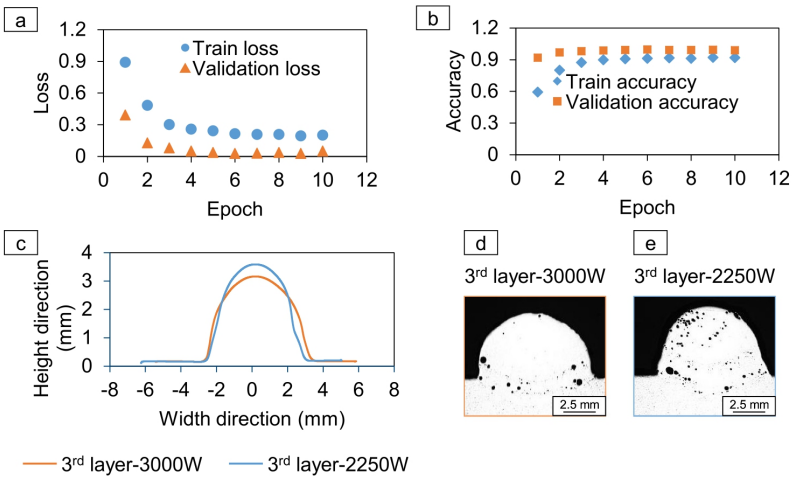

Fig. 16. (a, b) Training performance of CNN model 3. (c) Thickness and (d, e) cross-sectional images of two thin-wall structures along the building direction produced with initial parameter and adjusted parameter. Laser scan speed: 1 m/min, wire feed speed: 4 m/min.

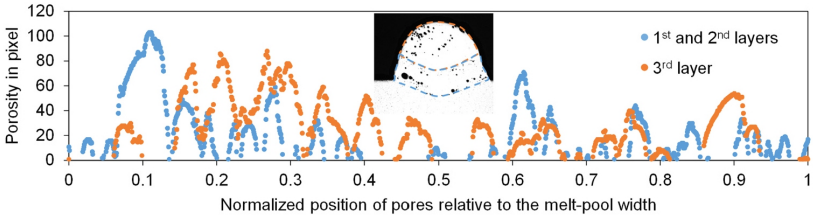

Fig. 17. Distribution of pores along the width direction of melt pools in the 1st – 2nd layers and the 3rd layer in the reference to the cross-sectional image in Fig. 16e.

temperature measurements.

Considering these advantages, the adoption of CNN models for identifying processing images represents a promising approach for in-situ adjustment of process parameters and maintaining a stable processing state.

4. Conclusions

In the present study, an extra lateral nozzle conveying shielding gas is installed to balance the shielding gas conveyed through the wire feed nozzle. Its effects on the dynamics of melt pools and geometrical accuracy as well as the properties of as-built specimens are investigated with thin-wall structures built by L-DED. Besides, CNN models are developed to efficiently find the optimal shielding gas flow rate. In the end, a methodology of CNN model-assisted process monitoring and parameter adjustment is proposed. Based on the experimental results, the following points can be concluded:

- In L-DED, the one-side blowing of shielding gas through the wire feed nozzle contributes to the processing instability during deposition, which results in the occasional explosion of melt pools and geometrical deviation. The installation of an extra shielding gas nozzle can balance the negative influences of one-side blowing. An appropriate flow rate for conveying the extra Ar needs to be determined. Otherwise, the processing stability can still not be reached. The processing stability not only improves the geometrical accuracy but also reduces the porosity level of as-built specimens.
- The back-side maximum roughness can be reflected until several layers are deposited. The process of finding the optimal gas flow rate is time- and material-consuming. The processing during deposition with different flow rates exhibits unique characteristics. CNN models using the images captured during deposition as input are developed to assist the parameter investigation. Even though an inappropriate flow rate is applied, the CNN model can instruct how to adjust the flow rate based on the current flow rate. With the CNN model, the appropriate gas flow rate can be identified based on the images in the first layer. CNN models classify images based on the information on melt pools, spatter, plume, and distribution of grayscale values in the image.
- A methodology by integrating the CNN model and L-DED process has been successfully verified. By learning from the images captured during the deposition in the single tracks processed with different laser power, the images in higher layers can be categorized to the equivalent process state as in the 1st layer from the training group. Subsequently, the laser power is adjusted to avoid heat accumulation and reach the process state as it is in the initial 1st layer, which ensures a consistent process state throughout the whole manufacturing. The specimen produced with the adjusted parameter demonstrates a thinner wall thickness. The porosity level and the correspondent pore distribution along the width direction of melt pools in the 3rd layer exhibit a high similarity as in the 1st - 2nd layers. The proposed methodology in this study could be universally applied in other laser-beam-melting-related processes not only to in-situ monitoring but also to in-situ adjust parameters.

Declaration of Competing Interest

The authors declare that they have no known competing financial

interests or personal relationships that could have appeared to influence the work reported in this paper.

Acknowledgments

The authors would like to thank R. Dinse and S. Riekehr for their assistance during laser-directed energy deposition as well as F. Dorn for the support during metallographic preparation and microstructural characterization.

Appendices

A.1. Determination of threshold value for binarizing processing images

The threshold value is utilized to binarize the processing images and extract the melt-pool profile. Before determining the threshold value, it is important to note that the processing images consist of three distinct areas in terms of the grayscale value: the dark area with a lower grayscale value, the illuminated areas surrounding the melt pool or spatter with a moderate grayscale value, and the melt pool with a higher grayscale value, see Fig. A.1(a, b). To ensure accurate binarization, it is crucial to exclude the illuminated areas from being considered as part of the melt pool. It can be observed that the grayscale value of these illuminated areas typically falls within the range of 150 – 200. To determine the grayscale value of the illuminated areas, pixel points in the processing image with a grayscale value lower than 190 are set to 190, which corresponds to the violet color, as depicted in Fig. A.1c. This adjustment allows for easy identification of the illuminated areas, which exhibit a violet color indicating a grayscale value equal to or lower than 190. By setting the threshold at 190, the melt-pool profile can be effectively preserved indicating a grayscale value higher than 190.

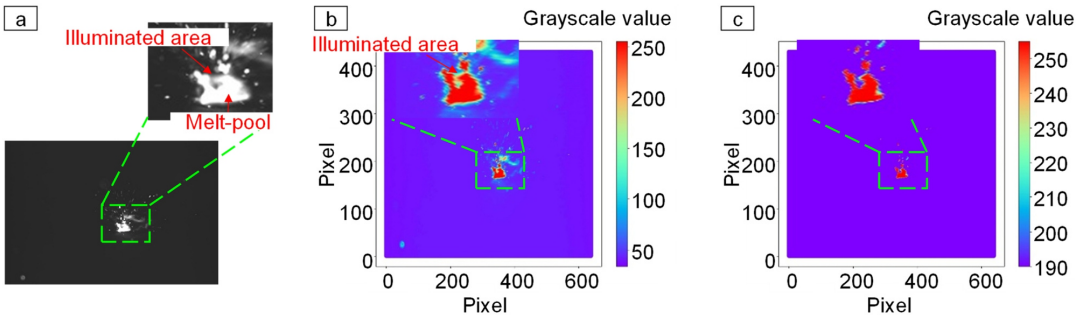

Fig. A.1. (a) Original processing image. (b) Distribution of grayscale value in each pixel point of the processing image in (a). (c) Distribution of grayscale value in each pixel point after setting the grayscale value lower than 190 to 190.

.

To ensure statistical reliability, different threshold values (180, 185, 190, 195, and 200) are applied to binarize processing images and analyze the processing stability. By conducting binarization using these various threshold values, the corresponding *Area* differences and *dHash* differences under different gas flow rates are listed in Table A.1. Different threshold values (180, 185, 195, 200) exhibit the same correlation between gas flow rate and processing stability as the threshold value of 190.

Table A.1
Area and *dHash* differences of melt pools in processing images captured under different gas flow rates after setting the threshold value to 180, 185, 190, 195, and 200.

Threshold value	Gas flow rate (l/min)	*Area* difference	*dHash* difference
180	0	3.76 ± 3.21	55.05 ± 12.82
	2.5	3.70 ± 2.72	53.89 ± 18.31
	5	3.14 ± 2.18	34.47 ± 11.23
	7.5	4.84 ± 4.11	41.09 ± 16.52
185	0	3.80 ± 3.23	54.42 ± 12.14
	2.5	3.68 ± 2.73	54.21 ± 18.19
	5	3.13 ± 2.19	34.79 ± 11.47
	7.5	4.89 ± 4.13	41.36 ± 16.93
190	0	53.49 ± 16.61	3.90 ± 3.38
	2.5	50.18 ± 27.78	3.70 ± 2.76
	5	36.69 ± 17.73	3.07 ± 2.17
	7.5	39.02 ± 23.58	4.77 ± 4.03
195	0	52.80 ± 11.41	3.95 ± 3.40
	2.5	51.48 ± 17.54	3.64 ± 2.78
	5	34.53 ± 11.16	3.13 ± 2.20
	7.5	41.32 ± 16.88	4.76 ± 4.02

(*continued on next page*)

Table A.1 (*continued*)

Threshold value	Gas flow rate (l/min)	*Area* difference	*dHash* difference
200	0	59.20 ± 10.91	3.94 ± 3.33
	2.5	52.75 ± 17.14	3.70 ± 2.81
	5	35.48 ± 11.60	3.14 ± 2.20
	7.5	42.63 ± 17.35	5.28 ± 4.28

A.2. Design and optimization of CNN models

The workflow in a supervised machine learning model is to achieve a satisfying prediction for a group of inputs by iteratively adjusting the weights and reducing the error between predicted and artificially given results. The backpropagation algorithm is a typical algorithm used in a multi-layer neural network to calculate the error in the hidden layers of the neural network since it was proposed [67]. In a multi-layer neural network, the activation function in the hidden layers must be nonlinear, otherwise, the effects of the hidden layer would be neglected [68]. In this study, the rectified linear unit (*ReLu*) function was selected as the activation function between the hidden layers and the fully connected layers. Compared with "*Sigmoid*", "*ReLu*" does not limit the magnitude of the output in nodes and it is a solution to the vanishing gradient, see Eqs. (4) and (5) [68]. The activation function in the output layer is "*Sigmoid*" in binary classification (model 1) and "*Softmax*" in multiple classification (models 2 and 3). The "*Softmax*" function calculates not only the weighted sum of inputs but also the weighted sum of inputs at other output nodes, see Eq. (6).

$$Sigmoid \quad (x) = \frac{1}{1+e^{-x}} \tag{4}$$

$$ReLU(x) = \begin{cases} x & x > 0 \\ 0x \leq 0 \end{cases} \tag{5}$$

$$Softmax(x) = \varphi(v_i) = \frac{e^{v_i}}{\sum_{k=1}^{M} e^{v_k}} \tag{6}$$

where v_i is the weighted sum in the i-th output node and M is the number of the node in the output layer.

Loss functions selected for the binary classification and multiple classifications are binary cross-entropy and categorical cross-entropy as suggested in [69]. The initial architecture of the CNN models is derived from the CNN model proposed in [43]. The choice of activation function and loss function for these CNN models is referred to in [69], which provides specific recommendations for different classification problems. The performance of the CNN models is evaluated by the prediction accuracy on both the training and validation datasets, as well as the generalization ability for the test dataset. The optimization principle is to maximize the generalization while avoiding overfitting of the models. The following optimizations are implemented:

1. According to the previous studies regarding the application of CNN models in additive manufacturing for image identification [70,71], the choice of optimizer for the CNN models is between "*Adam*" and "*RMSprop*". Based on the training results, the model trained with the "*Adam*" optimizer achieves higher accuracy compared to "*RMSprop*". This finding is consistent with the previous studies [70,71].
2. To prevent overfitting and improve the generalization of models, the magnitudes of "Dropout" and the "Hidden Layer" numbers are adjusted.

Since the trained models show no signs of underfitting due to the sufficient training data, there is no need to implement techniques such as data augmentation or *k*-fold validation to increase the size of the dataset. Additionally, since the adoption of "Dropout" and adjustments in network size effectively prevent overfitting and improve the generalization of models, regularization methods like adding weight regularization are not necessary.

The performance of different architectures for the ternary classification in terms of accuracy and generalization is listed in Table A.2.

Table A.2
Performance (prediction accuracy) of CNN models with different architectures for the ternary classification. 0 l/min, 5 l/min, 7.5 l/min represent the training and validation dataset used during training. 5 l/min_new, 5 l/min_9th layer, 5 l/min_3rd track are datasets decribed in Section 3.2.2 to test the generalization of the trained models.

Optimizer	Dropout	Epoch	Hidden layer number	0 l/min (%)	5 l/min (%)	7.5 l/min (%)	5 l/min new (%)	5 l/min 9th layer (%)	5 l/min 3rd track (%)
RMSprop	no	10	3	58.30	76.60	38.40	77	75.70	57.40
Adam	no	10	3	67.60	72.40	82.30	78.90	35.10	57.20
Adam	0.1	20	3	98.80	99.60	100	93.30	95	75
Adam	0.1	10	4	92.10	100	90	96.50	55	89
Adam	no	10	4	98.80	98.50	98.30	82.20	99	98.20
Adam	0.1	15	5	99.30	99.90	100	97.40	81.30	70
Adam	0.1	10	5	98	100	98.80	99.80	100	96.40
Adam	no	10	5	99.90	99.90	98.70	82.50	76.90	8.10

The optimized architecture of CNN models for the binary, ternary, and multiple classifications in this study is listed in Table A.3.

Table A.3
The architecture of CNN models with the best performance for the binary, ternary, and multiple classfications in this study.

	Application	Layer name	Operation	Number of filters	Filter size
Model 1	Binary classification	*conv2D_1*	*Convolution + ReLU*	16	3 × 3
		MaxPool_1	*Maxpooling*	1	2 × 2
		conv2D_2	*Convolution + ReLU*	64	3 × 3
		MaxPool_2	*Maxpooling*	1	2 × 2
		conv2D_3	*Convolution + ReLU*	128	3 × 3
		MaxPool_3	*Maxpooling*	1	2 × 2
		Fully connected_1	*ReLU*	8 output channels	
		Fully connected_2	*Sigmoid*	1 output channel for classification	
Model 2	Ternary classification	*conv2D_1*	*Convolution + ReLU*	16	3 × 3
		MaxPool_1	*Maxpooling*	1	2 × 2
		conv2D_2	*Convolution + ReLU*	64	3 × 3
		MaxPool_2	*Maxpooling*	1	2 × 2
		conv2D_3	*Convolution + ReLU*	64	3 × 3
		MaxPool_3	*Maxpooling*	1	2 × 2
		conv2D_4	*Convolution + ReLU*	128	3 × 3
		MaxPool_4	*Maxpooling*	1	2 × 2
		conv2D_5	*Convolution + ReLU*	128	3 × 3
		MaxPool_5	*Maxpooling*	1	2 × 2
		Fully connected_1	*ReLU*	8 output channels	
		Fully connected_2	*Softmax*	3 output channels for classification	
Model 3	5-multiple classification	*conv2D_1*	*Convolution + ReLU*	16	3 × 3
		MaxPool_1	*Maxpooling*	1	2 × 2
		conv2D_2	*Convolution + ReLU*	64	3 × 3
		MaxPool_2	*Maxpooling*	1	2 × 2
		conv2D_3	*Convolution + ReLU*	64	3 × 3
		MaxPool_3	*Maxpooling*	1	2 × 2
		conv2D_4	*Convolution + ReLU*	128	3 × 3
		MaxPool_4	*Maxpooling*	1	2 × 2
		Fully connected_1	*ReLU*	8 output channels	
		Fully connected_2	*Softmax*	5 output channels for classification	

A.3. Analysis of the potential of classification and regression CNN models

In this study, a regression model is also implemented to predict laser power. To modify the architecture of model 3, which is initially designed for multiple classifications, two changes are made. Firstly, the activation function in the last layer is changed from "*Softmax*" to "*Sigmoid*". Secondly, the number of nodes in the last layer is reduced to 1.

For the regression model, five groups of laser powers (3000, 3250, 3500, 3750, 4000 W) are normalized to a range of (0, 1). Each group consists of 4751 processing images. 10% of the total 23755 images are selected as the test dataset. The remaining images are divided into a training dataset and a validation dataset with a ratio of 7:3.

The regression model is initially trained for 10 epochs to ensure the comparability with the multiple-classification problem for laser power. As shown in Fig. A.2, although the validation loss is low, the training loss does not reach a stable value after 10 epochs. Using this trained model to predict the test dataset yielded an *R*-square (R^2) score of 0.89. To improve the performance of the model, the number of epochs is increased from 10 to 30. The training loss reaches a stable value and the validation loss further decreases. With more training epochs, the prediction performance improves, achieving an R^2 score of 0.98. The processing states can be successfully identified for a single process parameter (laser power) by the regression model. However, compared to multiple classifications, training the regression model requires more epochs to achieve optimal performance.

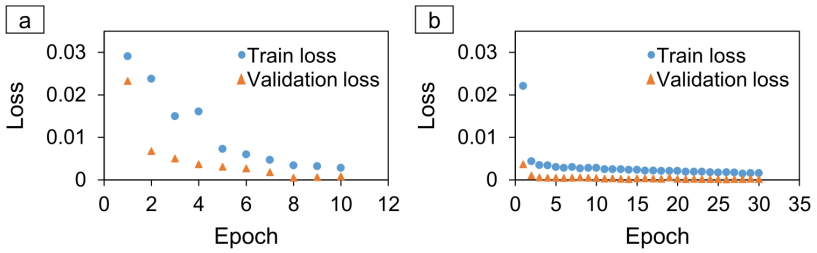

Fig. A.2. Training history of the regression model after training for (a) 10 epochs and (b) 30 epochs.

.

One objective of this study is to propose a methodology for achieving in-situ parameter adjustment to maintain processing stability. Considering the application potential of CNN models for classification and regression, the classification model can realize the parameter adjustment for multiple parameters by adding classification groups. However, given the different magnification scales of parameters, such as laser power (3000 – 4000 W) and gas flow rate (0 – 7.5 l/min), the regression model can only adjust one parameter at a time.

To address this limitation, the in-situ adjustment for multiple parameters using a regression model could be realized in conjunction with another classification model, as shown in the workflow illustrated in Fig. A.3. The first classification model predicts which parameter should be adjusted, while the second regression model predicts how to adjust that parameter. Alternatively, two classification models can also be combined to achieve parameter adjustment. The first classification model serves the same function, while the second classification model predicts the appropriate parameter set, as confirmed in this study.

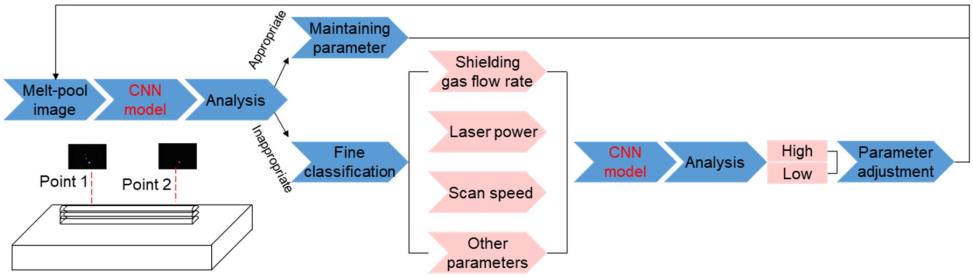

Fig. A.3. Workflow of using two tandem CNN models to in-situ adjust process parameters.

.

It is important to note that the methodologies involving two tandem CNN models introduce significant complexity, as the second CNN model must be properly selected based on the predictions from the first CNN model. This means that there should be different options for the second CNN model to match the prediction from the first CNN model. For example, if the prediction from the first CNN model indicates that the laser power needs to be adjusted, the second CNN model corresponding to the adjustment for laser power must be used rather than the CNN models corresponding to other process parameters. Fig. 14 illustrates the methodology proposed in this study, which utilizes a single classification model. The outputs of this classification model represent different processing images, each corresponding to different processing states. These states can include situations where the laser power is appropriate or inappropriate, the scan speed is appropriate or inappropriate, etc. By analyzing these predicted processing states, the model can provide valuable information about the current state of the process and identify any deviations from optimal parameter settings. This enables real-time monitoring and adjustment of process parameters to ensure stability and achieve desired outcomes.

In future work, the in-situ parameter adjustment for multiple parameters will be implemented using these three possible workflows. The evaluation criteria should include training difficulty, training performance (accuracy and R^2 score), and computational time for prediction. By comparing these criteria, the most effective approach for achieving accurate and efficient parameter adjustment in real-time processing scenarios can be determined.

References

[1] Ford S, Despeisse M. Additive manufacturing and sustainability: An exploratory study of the advantages and challenges. J Clean Prod 2016;137:1573–87.
[2] Bremer J, Walderich P, Pirch N, Schleifenbaum JH, Gasser A, Schopphoven T. Effects of path accuracy on additively manufactured specimens by laser material deposition using six-axis robots. J Laser Appl 2021;33(1):012045.
[3] Umaras E, Tsuzuki MS. Additive manufacturing-considerations on geometric accuracy and factors of influence. IFAC-PapersOnLine 2017;50(1):14940–5.
[4] H. Pil, H. Ch, W. Sang, K. Jeonghan, Review: dimensional accuracy in additive manufacturing processes, in: T. Costabile (Ed), Proceedings of the ASME 2014 International Manufacturing Science and Engineering Conference collocated with the JSME 2014 International Conference on Materials and Processing and the 42nd North American Manufacturing Research Conference, Society of Manufacturing Engineers, Detroit, 2014, MSEC2014-4037.
[5] Kotoban D, Nazarov A, Shishkovsky I. Comparative study of selective laser melting and direct laser metal deposition of Ni_3Al intermetallic alloy. Procedia IUTAM 2017;23:138–46.
[6] Shaikh MO, Chen C-C, Chiang H-C, Chen J-R, Chou Y-C, Kuo T-Y, Ameyama K, Chuang C-H. Additive manufacturing using fine wire-based laser metal deposition. Rapid Prototyp J 2019;26(3):473–83.
[7] Zhu G, Li D, Zhang A, Pi G, Tang Y. The influence of laser and powder defocusing characteristics on the surface quality in laser direct metal deposition. Opt Laser Technol 2012;44(2):349–56.
[8] Möller M, Ewald A, Weber J, Heilemann M, Herzog D, Emmelmann C. Characterization of the anisotropic properties for laser metal deposited Ti-6Al-4 V. J Laser Appl 2017;29(2):022308.
[9] Demir AG. Micro laser metal wire deposition for additive manufacturing of thin-walled structures. Opt Lasers Eng 2018;100:9–17.
[10] Frazier WE. Metal additive manufacturing: a review. J Mater Eng Perform 2014;23(6):1917–28.
[11] Wu Q, Lu J, Liu C, Shi X, Ma Q, Tang S, Fan H, Ma S. Obtaining uniform deposition with variable wire feeding direction during wire-feed additive manufacturing. Mater Manuf Process 2017;32(16):1881–6.
[12] Odermatt AE, Dorn F, Ventzke V, Kashaev N. Coaxial laser directed energy deposition with wire of thin-walled duplex stainless steel parts: Process discontinuities and their impact on the mechanical properties. CIRP J Manuf Sci Technol 2022;37:443–53.
[13] Wang M, Ventzke V, Kashaev N. Wire-based laser directed energy deposition of AA7075: effect of process parameters on microstructure and mechanical properties. J Mater Res Technol 2022;21:388–403.
[14] Yu Y, Huang W, Wang G, Wang J, Meng X, Wang C, Yan F, Hu X, Yu S. Investigation of melting dynamics of filler wire during wire feed laser welding. J Mech Sci Technol 2013;27(4):1097–108.
[15] Wang M, Kashaev N. Investigation of process window for AA7075 considering effects of different wire feed directions in lateral Laser Metal Deposition. Procedia CIRP 2022;111:218–23.
[16] Hauser T, Reisch RT, Breese PP, Nalam Y, Joshi KS, Bela K, Kamps T, Volpp J, Kaplan AF. Oxidation in wire arc additive manufacturing of aluminium alloys. Addit Manuf 2021;41:101958.
[17] Zhao T, Wang Y, Xu T, Bakir M, Cai W, Wang M, Dahmen M, Zheng Q, Wei X, Hong C. Some factors affecting porosity in directed energy deposition of AlMgScZr-alloys. Opt Laser Technol 2021;143:107337.
[18] Ng G, Jarfors A, Bi G, Zheng H. Porosity formation and gas bubble retention in laser metal deposition. Appl Phys A 2009;97(3):641–9.
[19] Benoit M, Sun S, Brandt M, Easton M. Processing window for laser metal deposition of Al 7075 powder with minimized defects. J Manuf Process 2021;64:1484–92.
[20] Froend M, Ventzke V, Kashaev N, Klusemann B, Enz J. Thermal analysis of wire-based direct energy deposition of Al-Mg using different laser irradiances. Addit Manuf 2019;29:100800.
[21] Li C, Liu Z, Fang X, Guo Y. Residual stress in metal additive manufacturing. Procedia CIRP 2018;71:348–53.
[22] Mukherjee T, Zhang W, DebRoy T. An improved prediction of residual stresses and distortion in additive manufacturing. Comput Mater Sci 2017;126:360–72.
[23] Afazov S, Okioga A, Holloway A, Denmark W, Triantaphyllou A, Smith S-A, Bradley-Smith L. A methodology for precision additive manufacturing through compensation. Precis Eng 2017;50:269–74.
[24] Dong B, Cai X, Xia Y, Lin S, Fan C, Chen F. Effects of interlayer temperature on the microstructures of wire arc additive manufactured Al-Zn-Mg-Cu alloy: Insights into texture responses and dynamic precipitation behaviors. Addit Manuf 2021;48:102453.
[25] Heilemann M, Jothi Prakash V, Beulting L, Emmelmann C. Effect of heat accumulation on the single track formation during laser metal deposition and development of a framework for analyzing new process strategies. J Laser Appl 2021;33(1):012003.

[26] Qin J, Hu F, Liu Y, Witherell P, Wang CC, Rosen DW, Simpson T, Lu Y, Tang Q. Research and application of machine learning for additive manufacturing. Addit Manuf 2022:102691.

[27] Johnson N, Vulimiri P, To A, Zhang X, Brice C, Kappes B, Stebner A. Invited review: Machine learning for materials developments in metals additive manufacturing. Addit Manuf 2020;36:101641.

[28] Ko H, Witherell P, Lu Y, Kim S, Rosen DW. Machine learning and knowledge graph based design rule construction for additive manufacturing. Addit Manuf 2021;37:101620.

[29] Rong-Ji W, Xin-Hua L, Qing-Ding W, Lingling W. Optimizing process parameters for selective laser sintering based on neural network and genetic algorithm. Int J Adv Manuf Technol 2009;42(11):1035–42.

[30] Silbernagel C, Aremu A, Ashcroft I. Using machine learning to aid in the parameter optimisation process for metal-based additive manufacturing. Rapid Prototyp J 2020;26(4).

[31] Zhang Y, Yang S, Dong G, Zhao YF. Predictive manufacturability assessment system for laser powder bed fusion based on a hybrid machine learning model. Addit Manuf 2021;41:101946.

[32] Caiazzo F, Caggiano A. Laser direct metal deposition of 2024 Al alloy: trace geometry prediction via machine learning. Mater 2018;11(3):444.

[33] Wacker C, Köhler M, David M, Aschersleben F, Gabriel F, Hensel J, Dilger K, Dröder K. Geometry and distortion prediction of multiple layers for wire arc additive manufacturing with artificial neural networks. Appl Sci 2021;11(10):4694.

[34] Han Y, Griffiths RJ, Hang ZY, Zhu Y. Quantitative microstructure analysis for solid-state metal additive manufacturing via deep learning. J Mater Res 2020;35(15):1936–48.

[35] Xie X, Bennett J, Saha S, Lu Y, Cao J, Liu WK, et al. Mechanistic data-driven prediction of as-built mechanical properties in metal additive manufacturing. NPJ Comput Mater 2021;7(1):1–12.

[36] Wang C, Chandra S, Huang S, Tor SB, Tan X. Unravelling process-microstructure-property correlations in powder-bed fusion additive manufacturing through information-rich surface features with deep learning. J Mater Process Technol 2022:117804.

[37] Cho H-W, Shin S-J, Seo G-J, Kim DB, Lee D-H. Real-time anomaly detection using convolutional neural network in wire arc additive manufacturing: Molybdenum material. J Mater Process Technol 2022;302:117495.

[38] Fathizadan S, Ju F, Lu Y. Deep representation learning for process variation management in laser powder bed fusion. Addit Manuf 2021;42:101961.

[39] Yang Z, Lu Y, Yeung H, Krishnamurty S. Investigation of deep learning for real-time melt pool classification in additive manufacturing. In: Reveliotis SS, editor. IEEE 15th International Conference on Automation Science and Engineering. IEEE; 2019. p. 640–7.

[40] Zhang Y, Hong GS, Ye D, Zhu K, Fuh JY. Extraction and evaluation of melt pool, plume and spatter information for powder-bed fusion AM process monitoring. Mater Des 2018;156:458–69.

[41] Scime L, Beuth J. A multi-scale convolutional neural network for autonomous anomaly detection and classification in a laser powder bed fusion additive manufacturing process. Addit Manuf 2018;24:273–86.

[42] Snow Z, Diehl B, Reutzel EW, Nassar A. Toward in-situ flaw detection in laser powder bed fusion additive manufacturing through layerwise imagery and machine learning. J Manuf Syst 2021;59:12–26.

[43] Zhang B, Liu S, Shin YC. In-Process monitoring of porosity during laser additive manufacturing process. Addit Manuf 2019;28:497–505.

[44] Gerdes N, Hoff C, Hermsdorf J, Kaierle S, Overmeyer L. Hyperspectral imaging for prediction of surface roughness in laser powder bed fusion. Int J Adv Manuf Technol 2021;115(4):1249–58.

[45] Herzog D, Seyda V, Wycisk E, Emmelmann C. Additive manufacturing of metals. Acta Mater 2016;117:371–92.

[46] Toda H, Hidaka T, Kobayashi M, Uesugi K, Takeuchi A, Horikawa K. Growth behavior of hydrogen micropores in aluminum alloys during high-temperature exposure. Acta Mater 2009;57(7):2277–90.

[47] Harvey J-P, Chartrand P. Modeling the hydrogen solubility in liquid aluminum alloys. Metall Mater Trans B 2010;41(4):908–24.

[48] Zou S, Xiao H, Ye F, Li Z, Tang W, Zhu F, Chen C, Zhu C. Numerical analysis of the effect of the scan strategy on the residual stress in the multi-laser selective laser melting. Results Phys 2020;16:103005.

[49] Khairallah SA, Anderson AT, Rubenchik A, King WE. Laser powder-bed fusion additive manufacturing: Physics of complex melt flow and formation mechanisms of pores, spatter, and denudation zones. Acta Mater 2016;108:36–45.

[50] Semak V, Matsunawa A. The role of recoil pressure in energy balance during laser materials processing. J Phys D 1997;30(18):2541.

[51] Qiu C, Panwisawas C, Ward M, Basoalto HC, Brooks JW, Attallah MM. On the role of melt flow into the surface structure and porosity development during selective laser melting. Acta Mater 2015;96:72–9.

[52] Reijonen J, Revuelta A, Riipinen T, Ruusuvuori K, Puukko P. On the effect of shielding gas flow on porosity and melt pool geometry in laser powder bed fusion additive manufacturing. Addit Manuf 2020;32:101030.

[53] Qiu C, Yue S, Adkins NJ, Ward M, Hassanin H, Lee PD, Withers PJ, Attallah MM. Influence of processing conditions on strut structure and compressive properties of cellular lattice structures fabricated by selective laser melting. Mater Sci Eng A 2015;628:188–97.

[54] Carrullo JCZ, Falcón JCP, Borrás VA. Influence of process parameters and initial microstructure on the oxidation resistance of Ti48Al2Cr2Nb coating obtained by laser metal deposition. Surf Coat Technol 2019;358:114–24.

[55] Wang C, Tan X, Tor S, Lim C. Machine learning in additive manufacturing: State-of-the-art and perspectives. Addit Manuf 2020;36:101538.

[56] Ghanavati R, Naffakh-Moosavy H, Moradi M. Additive manufacturing of thin-walled SS316L-IN718 functionally graded materials by direct laser metal deposition. J Mater Res Technol 2021;15:2673–85.

[57] Ocylok S, Alexeev E, Mann S, Weisheit A, Wissenbach K, Kelbassa I. Correlations of melt pool geometry and process parameters during laser metal deposition by coaxial process monitoring. Phys Procedia 2014;56:228–38.

[58] Zhou S, Su Y, Wang H, Enz J, Ebel T, Yan M. Selective laser melting additive manufacturing of 7xxx series Al-Zn-Mg-Cu alloy: Cracking elimination by co-incorporation of Si and TiB_2. Addit Manuf 2020;36:101458.

[59] Ye J, Bab-Hadiashar A, Hoseinnezhad R, Alam N, Vargas-Uscategui A, Patel M, Cole I. Predictions of in-situ melt pool geometric signatures via machine learning techniques for laser metal deposition. Int J Comput Integr Manuf 2022:1–17.

[60] Keshavarzkermani A, Marzbanrad E, Esmaeilizadeh R, Mahmoodkhani Y, Ali U, Enrique PD, Zhou NY, Bonakdar A, Toyserkani E. An investigation into the effect of process parameters on melt pool geometry, cell spacing, and grain refinement during laser powder bed fusion. Opt Laser Technol 2019;116:83–91.

[61] Froend M, Ventzke V, Riekehr S, Kashaev N, Klusemann B, Enz J. Microstructure and microhardness of wire-based laser metal deposited AA5087 using an Ytterbium fibre laser. Mater Charact 2018;143:59–67.

[62] Bi G, Gasser A, Wissenbach K, Drenker A, Poprawe R. Characterization of the process control for the direct laser metallic powder deposition. Surf Coat Technol 2006;201(6):2676–83.

[63] Prima Additive. Melting Pool Monitoring, https://www.primaadditive.com/en/technologies/direct-energy-deposition/melting-pool-monitoring (Accessed 16 October 2023).

[64] Lanc Z, Zeljković M, Štrbac B, Živković A, Drstvenšek I, Hadžistević M. The determination of the emissivity of aluminum alloy AW 6082 using infrared thermography. J Prod Eng 2015;18:23–6.

[65] Ashby A, Guss G, Ganeriwala RK, Martin AA, DePond PJ, Deane DJ, Matthews MJ, Druzgalski CL. Thermal history and high-speed optical imaging of overhang structures during laser powder bed fusion: A computational and experimental analysis. Addit Manuf 2022;53:102669.

[66] Bertoli US, Wolfer AJ, Matthews MJ, Delplanque J-PR, Schoenung JM. On the limitations of volumetric energy density as a design parameter for selective laser melting. Mater Des 2017;113:331–40.

[67] Rumelhart DE, Hinton GE, Williams RJ. Learning representations by back-propagating errors. Nature 1986;323(6088):533–6.

[68] Kim P. In: Spahr W, Green T, Anglin S, Moodie M, Lissner J, Powers M, Endsley K, editors. Matlab deep learning with machine learning, neural networks and artificial intelligence. New York: Springer; 2017.

[69] Chollet F. In: Arritola T, Gaines J, Dragosavljevic A, Taylor T, Tennant K, Ott A, Tobias R, Marsico D, Tudor M, editors. Deep learning with Python. Shelter Island: Manning Publications; 2021.

[70] Han F, Zou J, Ai Y, Xu C, Liu S. Image classification and analysis during the additive manufacturing process based on deep convolutional neural networks. In: Wong SF, editor. 20th International Conference on Electronic Packaging Technology. Hong Kong: IEEE; 2019. p. 1–4.

[71] Li Y, Mu H, Polden J, Li H, Wang L, Xia C, Pan Z. Towards intelligent monitoring system in wire arc additive manufacturing: A surface anomaly detector on a small dataset. Int J Adv Manuf Technol 2022;120(7-8):5225–42.

Bibliography

[1] W.E. Frazier, Metal additive manufacturing: a review, J. Mater. Eng. Perform. 23 (2014) 1917-1928.
[2] K.V. Wong, A. Hernandez, A review of additive manufacturing, Int. Sch. Res. Notices 2012 (2012) 1-10.
[3] W. S. Lee, W. C. Sue, C. F. Lin, C. J. Wu, The strain rate and temperature dependence of the dynamic impact properties of 7075 aluminum alloy, J. Mater. Process. Technol. 100 (2000) 116-122.
[4] Y. Ding, J. Muñiz-Lerma, M. Trask, S. Chou, A. Walker, M. Brochu, Microstructure and mechanical property considerations in additive manufacturing of aluminum alloys, MRS Bull. 41 (2016) 745-751.
[5] Z. Zhu, Z. Hu, H.L. Seet, T. Liu, W. Liao, U. Ramamurty, S.M.L. Nai, Recent progress on the additive manufacturing of aluminum alloys and aluminum matrix composites: Microstructure, properties, and applications, Int. J. Mach. Tools Manuf. 190 (2023) 104047.
[6] J. Hirsch, Recent development in aluminium for automotive applications, Trans. Nonferrous Met. Soc. China 24 (2014) 1995-2002.
[7] R. Wanhill, Aerospace applications of aluminum-lithium alloys, in: N. E. Prasad, A. A. Gokhale, R. Wanhill (Eds.), Aluminum-lithium Alloys Processing, Properties, and Applications, Butterworth-Heinemann, Boston, 2014, pp. 503-535.
[8] F. Wang, Y. Gong, Y. Du, M. Song, Microstructures and Mechanical Properties of an Al-Zn-Mg-Cu Alloy Processed by Two-Step Aging Treatment, J. Mater. Eng. Perform. 29 (2020) 4404-4411.
[9] E.T. Akinlabi, S.A. Akinlabi, Advanced coating: Laser metal deposition of aluminium powder on titanium substrate, in: S. I. Ao, L. Gelman, D. Hukins, A. Hunter, A. M. Korsunsky (Eds.), Proceedings of the World Congress on Engineering, Newswood Limited, London, 2016, pp. 863-868.
[10] A. Gasser, G. Backes, I. Kelbassa, A. Weisheit, K. Wissenbach, Laser metal deposition (LMD) and selective laser melting (SLM) in turbo-engine applications, Laser Tech. J. 2 (2010) 58-63.
[11] P.R. Gradl, C.S. Protz, T. Wammen, Additive manufacturing and hot-fire testing of liquid rocket channel wall nozzles using blown powder directed energy deposition inconel 625 and JBK-75 Alloys, in: L. Teague (Ed.), AIAA Propulsion and Energy Forum, American Institute of Aeronautics and Astronautics, Indianapolis, 2019, p. 4362.
[12] A.J. Pinkerton, L. Li, Modelling the geometry of a moving laser melt pool and deposition track via energy and mass balances, J. Phys. D: Appl. Phys. 37 (2004) 1885.
[13] P. Peyre, P. Aubry, R. Fabbro, R. Neveu, A. Longuet, Analytical and numerical modelling of the direct metal deposition laser process, J. Phys. D: Appl. Phys. 41 (2008) 025403.
[14] G. Bi, A. Gasser, K. Wissenbach, A. Drenker, R. Poprawe, Characterization of the process control for the direct laser metallic powder deposition, Surf. Coat. Technol. 201 (2006) 2676-2683.
[15] G. Pi, A. Zhang, G. Zhu, D. Li, B. Lu, Research on the forming process of three-dimensional metal parts fabricated by laser direct metal forming, Int. J. Adv. Manuf. Technol. 57 (2011) 841-847.
[16] P.J. DePond, G. Guss, S. Ly, N.P. Calta, D. Deane, S. Khairallah, M.J. Matthews, In situ measurements of layer roughness during laser powder bed fusion additive manufacturing using low coherence scanning interferometry, Mater. Des. 154 (2018) 347-359.
[17] A. Dunbar, E. Denlinger, J. Heigel, P. Michaleris, P. Guerrier, R. Martukanitz, T. Simpson, Development of experimental method for in situ distortion and temperature measurements

during the laser powder bed fusion additive manufacturing process, Addit. Manuf. 12 (2016) 25-30.
[18] L. Thijs, K. Kempen, J.-P. Kruth, J. Van Humbeeck, Fine-structured aluminium products with controllable texture by selective laser melting of pre-alloyed AlSi10Mg powder, Acta Mater. 61 (2013) 1809-1819.
[19] Q. Wu, J. Lu, C. Liu, X. Shi, Q. Ma, S. Tang, H. Fan, S. Ma, Obtaining uniform deposition with variable wire feeding direction during wire-feed additive manufacturing, Mater. Manuf. Process. 32 (2017) 1881-1886.
[20] A.E. Odermatt, F. Dorn, V. Ventzke, N. Kashaev, Coaxial laser directed energy deposition with wire of thinwalled duplex stainless steel parts: Process discontinuities and their impact on the mechanical properties, CIRP J. Manuf. Sci. Technol. 37 (2022) 443-453.
[21] M. Wang, V. Ventzke, N. Kashaev, Wire-based laser directed energy deposition of AA7075: effect of process parameters on microstructure and mechanical properties, J. Mater. Res. Technol. 21 (2022) 388-403.
[22] Y. Yu, W. Huang, G. Wang, J. Wang, X. Meng, C. Wang, F. Yan, X. Hu, S. Yu, Investigation of melting dynamics of filler wire during wire feed laser welding, J. Mech. Sci. Technol. 27 (2013) 1097-1108.
[23] M. Wang, N. Kashaev, Investigation of process window for AA7075 considering effects of different wire feed directions in lateral Laser Metal Deposition, Procedia CIRP 111 (2022) 218-223.
[24] T. Hauser, R.T. Reisch, P.P. Breese, Y. Nalam, K.S. Joshi, K. Bela, T. Kamps, J. Volpp, A.F. Kaplan, Oxidation in wire arc additive manufacturing of aluminium alloys, Addit. Manuf. 41 (2021) 101958.
[25] T. Zhao, Y. Wang, T. Xu, M. Bakir, W. Cai, M. Wang, M. Dahmen, Q. Zheng, X. Wei, C. Hong, Some factors affecting porosity in directed energy deposition of AlMgScZr-alloys, Opt. Laser Technol. 143 (2021) 107337.
[26] G. Ng, A. Jarfors, G. Bi, H. Zheng, Porosity formation and gas bubble retention in laser metal deposition, Appl. Phys. A 97 (2009) 641-649.
[27] M. Benoit, S. Sun, M. Brandt, M. Easton, Processing window for laser metal deposition of Al 7075 powder with minimized defects, J. Manuf. Process. 64 (2021) 1484-1492.
[28] N.T. Aboulkhair, N.M. Everitt, I. Ashcroft, C. Tuck, Reducing porosity in AlSi10Mg parts processed by selective laser melting, Addit. Manuf. 1 (2014) 77-86.
[29] T. Qi, H. Zhu, H. Zhang, J. Yin, L. Ke, X. Zeng, Selective laser melting of Al7050 powder: Melting mode transition and comparison of the characteristics between the keyhole and conduction mode, Mater. Des. 135 (2017) 257-266.
[30] W.E. King, H.D. Barth, V.M. Castillo, G.F. Gallegos, J.W. Gibbs, D.E. Hahn, C. Kamath, A.M. Rubenchik, Observation of keyhole-mode laser melting in laser powder-bed fusion additive manufacturing, J. Mater. Process. Technol. 214 (2014) 2915-2925.
[31] K.V. Yang, P. Rometsch, T. Jarvis, J. Rao, S. Cao, C. Davies, X. Wu, Porosity formation mechanisms and fatigue response in Al-Si-Mg alloys made by selective laser melting, Mater. Sci. Eng. A 712 (2018) 166-174.
[32] S. Kou, A simple index for predicting the susceptibility to solidification cracking, Weld. J. 94 (2015) 374-388.
[33] H. Zhang, J. Senkara, Resistance welding: fundamentals and applications, second ed., CRC press, 2011.
[34] A. Wang, Q. Wei, Z. Tang, P. Ren, X. Zhang, Y. Wu, H. Wang, A. Du Plessis, J. Huang, K. Hu, Effects of processing parameters on pore defects in blue laser directed energy deposition of aluminum by in and ex situ observation, J. Mater. Process. Technol. 319 (2023) 118068.
[35] Y. Huang, T.G. Fleming, S.J. Clark, S. Marussi, K. Fezzaa, J. Thiyagalingam, C.L.A. Leung, P.D. Lee, Keyhole fluctuation and pore formation mechanisms during laser powder bed fusion additive manufacturing, Nat. Commun. 13 (2022) 1170.

[36] C.L.A. Leung, S. Marussi, M. Towrie, R.C. Atwood, P.J. Withers, P.D. Lee, The effect of powder oxidation on defect formation in laser additive manufacturing, Acta Mater. 166 (2019) 294-305.
[37] P. Promoppatum, S.-C. Yao, Influence of scanning length and energy input on residual stress reduction in metal additive manufacturing: Numerical and experimental studies, J. Manuf. Process. 49 (2020) 247-259.
[38] H. Zhao, G. Zhang, Z. Yin, L. Wu, Three-dimensional finite element analysis of thermal stress in single-pass multi-layer weld-based rapid prototyping, J. Mater. Process. Technol. 212 (2012) 276-285.
[39] F.E. Bock, J. Herrnring, M. Froend, J. Enz, N. Kashaev, B. Klusemann, Experimental and numerical thermomechanical analysis of wire-based laser metal deposition of Al-Mg alloys, J. Manuf. Process. 64 (2021) 982-995.
[40] J. Qin, F. Hu, Y. Liu, P. Witherell, C.C. Wang, D.W. Rosen, T. Simpson, Y. Lu, Q. Tang, Research and application of machine learning for additive manufacturing, Addit. Manuf. 52 (2022) 102691.
[41] H.-W. Cho, S.-J. Shin, G.-J. Seo, D.B. Kim, D.-H. Lee, Real-time anomaly detection using convolutional neural network in wire arc additive manufacturing: Molybdenum material, J. Mater. Process. Technol. 302 (2022) 117495.
[42] S. Fathizadan, F. Ju, Y. Lu, Deep representation learning for process variation management in laser powder bed fusion, Addit. Manuf. 42 (2021) 101961.
[43] Z. Yang, Y. Lu, H. Yeung, S. Krishnamurty, Investigation of deep learning for real-time melt pool classification in additive manufacturing, in: D. Cappelleri, D. V. Dimarogonas, M. Dotoli, M. P. Fanti, P. Lutz, C. Seatzu, X. L. Xie (Eds.), IEEE 15th international conference on automation science and engineering (CASE), IEEE, Vancouver, 2019, pp. 640-647.
[44] Y. Zhang, G.S. Hong, D. Ye, K. Zhu, J.Y. Fuh, Extraction and evaluation of melt pool, plume and spatter information for powder-bed fusion AM process monitoring, Mater. Des. 156 (2018) 458-469.
[45] L. Scime, J. Beuth, A multi-scale convolutional neural network for autonomous anomaly detection and classification in a laser powder bed fusion additive manufacturing process, Addit. Manuf. 24 (2018) 273-286.
[46] Z. Snow, B. Diehl, E.W. Reutzel, A. Nassar, Toward in-situ flaw detection in laser powder bed fusion additive manufacturing through layerwise imagery and machine learning, J. Manuf. Syst. 59 (2021) 12-26.
[47] B. Zhang, S. Liu, Y.C. Shin, In-Process monitoring of porosity during laser additive manufacturing process, Addit. Manuf. 28 (2019) 497-505.
[48] N. Gerdes, C. Hoff, J. Hermsdorf, S. Kaierle, L. Overmeyer, Hyperspectral imaging for prediction of surface roughness in laser powder bed fusion, Int. J. Adv. Manuf. Technol. 115 (2021) 1249-1258.
[49] A. Da Silva, F. Belelli, G. Lupi, F. Bruzzo, B. Brandau, L. Maier, A. Pesl, J. Frostevarg, R. Casati, E. Lopez, Influence of aluminium powder aging on Directed Energy deposition, Mater. Des. 218 (2022) 110677.
[50] A. Da Silva, J. Volpp, A.F. Kaplan, The effects of laser irradiation on an aluminium powder stream in Directed Energy Deposition, Addit. Manuf. 41 (2021) 101968.
[51] S. Dietrich, M. Wunderer, A. Huissel, M. Zaeh, A new approach for a flexible powder production for additive manufacturing, Procedia Manuf. 6 (2016) 88-95.
[52] H. Dobbelstein, E.L. Gurevich, E.P. George, A. Ostendorf, G. Laplanche, Laser metal deposition of a refractory TiZrNbHfTa high-entropy alloy, Addit. Manuf. 24 (2018) 386-390.
[53] C. Weingarten, D. Buchbinder, N. Pirch, W. Meiners, K. Wissenbach, R. Poprawe, Formation and reduction of hydrogen porosity during selective laser melting of AlSi10Mg, J. Mater. Process. Technol. 221 (2015) 112-120.

[54] C. Meier, R. Weissbach, J. Weinberg, W.A. Wall, A.J. Hart, Critical influences of particle size and adhesion on the powder layer uniformity in metal additive manufacturing, J. Mater. Process. Technol. 266 (2019) 484-501.
[55] A.S. Wu, D.W. Brown, M. Kumar, G.F. Gallegos, W.E. King, An experimental investigation into additive manufacturing-induced residual stresses in 316L stainless steel, Metall. Mater. Trans. A 45 (2014) 6260-6270.
[56] W. Stopyra, K. Gruber, I. Smolina, T. Kurzynowski, B. Kuźnicka, Laser powder bed fusion of AA7075 alloy: Influence of process parameters on porosity and hot cracking, Addit. Manuf. 35 (2020) 101270.
[57] K. Prashanth, S. Scudino, J. Eckert, Defining the tensile properties of Al-12Si parts produced by selective laser melting, Acta Mater. 126 (2017) 25-35.
[58] Y.-A. Song, S. Park, S.-W. Chae, 3D welding and milling: part II—optimization of the 3D welding process using an experimental design approach, Int. J. Mach. Tools Manuf. 45 (2005) 1063-1069.
[59] N. Kalentics, N. Sohrabi, H.G. Tabasi, S. Griffiths, J. Jhabvala, C. Leinenbach, A. Burn, R.E. Loge, Healing cracks in selective laser melting by 3D laser shock peening, Addit. Manuf. 30 (2019) 100881.
[60] C.S. Montross, T. Wei, L. Ye, G. Clark, Y.-W. Mai, Laser shock processing and its effects on microstructure and properties of metal alloys: a review, Int. J. Fatigue 24 (2002) 1021-1036.
[61] M. Awd, J. Tenkamp, M. Hirtler, S. Siddique, M. Bambach, F. Walther, Comparison of microstructure and mechanical properties of Scalmalloy® produced by selective laser melting and laser metal deposition, Mater. 11 (2017) 17.
[62] T. Schopphoven, A. Gasser, G. Backes, EHLA: Extreme High-Speed Laser Material Deposition: Economical and effective protection against corrosion and wear, Laser Tech. J. 14 (2017) 26-29.
[63] T. Zhao, T. Chen, Y. Wang, M. Wang, M. Bakir, M. Dahmen, W. Cai, C. Hong, T. Schopphoven, N. Pirch, Laser Directed Energy Deposition of an AlMgScZr-Alloy in High-Speed Process Regimes, Mater. 15 (2022) 8951.
[64] M. Javidani, J. Arreguin-Zavala, J. Danovitch, Y. Tian, M. Brochu, Additive manufacturing of AlSi10Mg alloy using direct energy deposition: microstructure and hardness characterization, J. Therm. Spray Technol. 26 (2017) 587-597.
[65] A. Medrano, J. Folkes, J. Segal, I. Pashby, Fibre laser metal deposition with wire: parameters study and temperature monitoring system, in: A. B. Utkin (Ed.), XVII International Symposium on Gas Flow, Chemical Lasers, and High-Power Lasers, SPIE, Bellingham, 2008, pp. 539-545.
[66] M. Froend, V. Ventzke, S. Riekehr, N. Kashaev, B. Klusemann, J. Enz, Microstructure and hardness evolution of laser metal deposited AA5087 wall-structures, Procedia CIRP 74 (2018) 131-135.
[67] M. Froend, S. Riekehr, N. Kashaev, B. Klusemann, J. Enz, Process development for wire-based laser metal deposition of 5087 aluminium alloy by using fibre laser, J. Manuf. Process. 34 (2018) 721-732.
[68] J. Kelbassa, A. Gasser, J. Bremer, O. Pütsch, R. Poprawe, J. Henrich Schleifenbaum, Equipment and process windows for laser metal deposition with coaxial wire feeding, J. Laser Appl. 31 (2019) 022320.
[69] A. Heralic, Monitoring and control of robotized laser metal-wire deposition, ProQuest Dissertations Publishing, Chalmers University of Technology, 2012.
[70] C. Leyens, E. Beyer, Innovations in laser cladding and direct laser metal deposition, in: J. Lawrence (Ed.), Laser surface engineering. Processes and applications, Woodhead Publishing, Cambridge, 2015, pp. 181-192.
[71] B. Dong, X. Cai, S. Lin, X. Li, C. Fan, C. Yang, H. Sun, Wire arc additive manufacturing of Al-Zn-Mg-Cu alloy: microstructures and mechanical properties, Addit. Manuf. 36 (2020) 101447.

[72] S. Li, L. J. Zhang, J. Ning, X. Wang, G. F. Zhang, J. X. Zhang, S. J. Na, Microstructures and mechanical properties of Al–Zn–Mg aluminium alloy samples produced by wire+ arc additive manufacturing, J. Mater. Res. Technol. 9 (2020) 13770-13780.
[73] A. Langebeck, A. Bohlen, R. Rentsch, F. Vollertsen, Mechanical properties of high strength aluminum alloy EN AW-7075 additively manufactured by directed energy deposition, Metals 10(5) (2020) 579.
[74] B. Wu, Z. Pan, S. van Duin, H. Li, Thermal behavior in wire arc additive manufacturing: characteristics, effects and control, in: S. Chen, Y. Zhang, Z. Feng (Eds.), Transactions on Intelligent Welding Manufacturing, Springer, Singapore, 2019, pp. 3-18.
[75] C. He, W. Yu, Y. Li, Z. Wang, D. Wu, G. Xu, Relationship between cooling rate, microstructure evolution, and performance improvement of an Al–Cu alloy prepared using different methods, Mater. Res. Express 7 (2020) 116501.
[76] G. Zhang, X. Lu, J. Li, J. Chen, X. Lin, M. Wang, H. Tan, W. Huang, In-situ grain structure control in directed energy deposition of Ti6Al4V, Addit. Manuf. 55 (2022) 102865.
[77] M. Easton, D. StJohn, Grain refinement of aluminum alloys: Part I. the nucleant and solute paradigms—a review of the literature, Metall. Mater. Trans. A 30 (1999) 1613-1623.
[78] D.G. McCartney, Grain refining of aluminium and its alloys using inoculants, Int. Mater. Rev. 34 (1989) 247-260.
[79] T. Chandrashekar, M. Muralidhara, K. Kashyap, P.R. Rao, Effect of growth restricting factor on grain refinement of aluminum alloys, Int. J. Adv. Manuf. Technol. 40 (2009) 234-241.
[80] D.M. Stefanescu, R. Ruxanda, Fundamentals of solidification, first ed., ASM International, Almere, 2004.
[81] X. Liu, Heterogeneous nucleation or homogeneous nucleation?, J. Chem. Phys. 112 (2000) 9949-9955.
[82] A. Cibula, The mechanism of grain refinement of sand castings in aluminum alloys, J. Inst. Met 76 (1949) 1950.
[83] Z. Fan, Y. Wang, Y. Zhang, T. Qin, X. Zhou, G. Thompson, T. Pennycook, T. Hashimoto, Grain refining mechanism in the Al/Al–Ti–B system, Acta Mater. 84 (2015) 292-304.
[84] D. Zhou, F. Qiu, Q. Jiang, The nano-sized TiC particle reinforced Al–Cu matrix composite with superior tensile ductility, Mater. Sci. Eng. A 622 (2015) 189-193.
[85] K. Hyde, A. Norman, P. Prangnell, The effect of cooling rate on the morphology of primary Al_3Sc intermetallic particles in Al–Sc alloys, Acta Mater. 49 (2001) 1327-1337.
[86] K. Yan, Z. Chen, Y. Zhao, C. Ren, W. Lu, A. Aldeen, Morphological characteristics of Al_3Sc particles and crystallographic orientation relationships of Al_3Sc/Al interface in cast Al-Sc alloy, J. Alloys Compd. 861 (2021) 158491.
[87] Z. Chen, K. Yan, Grain refinement of commercially pure aluminum with addition of Ti and Zr elements based on crystallography orientation, Sci. Rep. 10 (2020) 16591.
[88] M. Johnsson, L. Backerud, G.K. Sigworth, Study of the mechanism of grain refinement of aluminum after additions of Ti-and B-containing master alloys, Metall. Trans. A 24 (1993) 481-491.
[89] X. Yao, S. McDonald, A. Dahle, C. Davidson, D. StJohn, Modeling of grain refinement: Part III. Al–7Si–0.3 Mg aluminum alloy, J. Mater. Res. 23 (2008) 1301-1306.
[90] Y. Birol, Effect of solute Mg on grain size of aluminium alloys, Mater. Sci. Technol. 28 (2012) 924-927.
[91] Y. Birol, Effect of solute Si and Cu on grain size of aluminium alloys, Int. J. Cast Met. Res. 26 (2013) 22-27.
[92] M. Mousavi, C. Cross, Ø. Grong, Effect of scandium and titanium–boron on grain refinement and hot cracking of aluminium alloy 7108, Sci. Technol. Weld. Join. 4 (1999) 381-388.
[93] Z. Tang, F. Vollertsen, Influence of grain refinement on hot cracking in laser welding of aluminum, Weld. World 58 (2014) 355-366.

[94] K. Kendig, D. Miracle, Strengthening mechanisms of an Al-Mg-Sc-Zr alloy, Acta Mater. 50 (2002) 4165-4175.
[95] S. Zhou, Y. Su, H. Wang, J. Enz, T. Ebel, M. Yan, Selective laser melting additive manufacturing of 7xxx series Al-Zn-Mg-Cu alloy: Cracking elimination by co-incorporation of Si and TiB_2, Addit. Manuf. 36 (2020) 101458.
[96] N. Hansen, Hall–Petch relation and boundary strengthening, Scripta Mater. 51 (2004) 801-806.
[97] Y. J. Kwon, I. Shigematsu, N. Saito, Mechanical property improvements in aluminum alloy through grain refinement using friction stir process, Mater. Trans. 45 (2004) 2304-2311.
[98] K. Basavakumar, P. Mukunda, M. Chakraborty, Influence of grain refinement and modification on microstructure and mechanical properties of Al–7Si and Al–7Si–2.5 Cu cast alloys, Mater. Charact. 59 (2008) 283-289.
[99] T. Engdahl, V. Hansen, P. Warren, K. Stiller, Investigation of fine scale precipitates in Al–Zn–Mg alloys after various heat treatments, Mater. Sci. Eng. A 327 (2002) 59-64.
[100] W. Yang, S. Ji, M. Wang, Z. Li, Precipitation behaviour of Al–Zn–Mg–Cu alloy and diffraction analysis from η' precipitates in four variants, J. Alloys Compd. 610 (2014) 623-629.
[101] M. Paulisch, N. Wanderka, M. Haupt, S. Selve, I. Driehorst, W. Reimers, The influence of heat treatments on the microstructure and the mechanical properties in commercial 7020 alloys, Mater. Sci. Eng. A 626 (2015) 254-262.
[102] D. Godard, P. Archambault, E. Aeby-Gautier, G. Lapasset, Precipitation sequences during quenching of the AA 7010 alloy, Acta Mater. 50 (2002) 2319-2329.
[103] A. Azarniya, A.K. Taheri, K.K. Taheri, Recent advances in ageing of 7xxx series aluminum alloys: a physical metallurgy perspective, J. Alloys Compd. 781 (2019) 945-983.
[104] M. Chemingui, M. Khitouni, K. Jozwiak, G. Mesmacque, A. Kolsi, Characterization of the mechanical properties changes in an Al–Zn–Mg alloy after a two-step ageing treatment at 70° and 135°C, Mater. Des. 31 (2010) 3134-3139.
[105] Y. Li, D. Gu, Parametric analysis of thermal behavior during selective laser melting additive manufacturing of aluminum alloy powder, Mater. Des. 63 (2014) 856-867.
[106] F. Fazeli, W. Poole, C. Sinclair, Modeling the effect of Al3Sc precipitates on the yield stress and work hardening of an Al–Mg–Sc alloy, Acta Mater. 56 (2008) 1909-1918.
[107] E. Huskins, B. Cao, K. Ramesh, Strengthening mechanisms in an Al–Mg alloy, Mater. Sci. Eng. A 527 (2010) 1292-1298.
[108] Ø. Ryen, B. Holmedal, O. Nijs, E. Nes, E. Sjölander, H. E. Ekström, Strengthening mechanisms in solid solution aluminum alloys, Metall. Mater. Trans. A 37 (2006) 1999-2006.
[109] J.L. Murray, The Al−Mg (aluminum− magnesium) system, J. Phase Equilibria 3 (1982) 60-74.
[110] A. McAlister, J. Murray, The (Al−Mn) aluminum-manganese system, J. Phase Equilibria 8 (1987) 438-447.
[111] T. Uesugi, K. Higashi, First-principles studies on lattice constants and local lattice distortions in solid solution aluminum alloys, Comput. Mater. Sci. 67 (2013) 1-10.
[112] K. Youssef, R. Scattergood, K. Murty, C. Koch, Nanocrystalline Al–Mg alloy with ultrahigh strength and good ductility, Scripta Mater. 54 (2006) 251-256.
[113] B. Hu, B. Quan, D. Li, X. Wang, Z. Li, X. Zeng, Solid solution strengthening mechanism in high pressure die casting Al–Ce–Mg alloys, Mater. Sci. Eng. A 812 (2021) 141109.
[114] R.J. Hebert, Metallurgical aspects of powder bed metal additive manufacturing, J. Mater. Sci. 51 (2016) 1165-1175.
[115] M. Tang, P.C. Pistorius, Oxides, porosity and fatigue performance of AlSi10Mg parts produced by selective laser melting, Int. J. Fatigue 94 (2017) 192-201.
[116] Y. Xue, H. El Kadiri, M. Horstemeyer, J. Jordon, H. Weiland, Micromechanisms of multistage fatigue crack growth in a high-strength aluminum alloy, Acta Mater. 55 (2007) 1975-1984.

[117] E. Louvis, P. Fox, C.J. Sutcliffe, Selective laser melting of aluminium components, J. Mater. Process. Technol. 211 (2011) 275-284.
[118] M. Gieseke, C. Noelke, S. Kaierle, V. Wesling, H. Haferkamp, Selective laser melting of magnesium and magnesium alloys, Magnes. Technol. 2013 (2016) 65-68.
[119] H. Toda, T. Hidaka, M. Kobayashi, K. Uesugi, A. Takeuchi, K. Horikawa, Growth behavior of hydrogen micropores in aluminum alloys during high-temperature exposure, Acta Mater. 57 (2009) 2277-2290.
[120] J. P. Harvey, P. Chartrand, Modeling the hydrogen solubility in liquid aluminum alloys, Metall. Mater. Trans. B 41 (2010) 908-924.
[121] D. Herzog, V. Seyda, E. Wycisk, C. Emmelmann, Additive manufacturing of metals, Acta Mater. 117 (2016) 371-392.
[122] D. Susan, J. Puskar, J. Brooks, C.V. Robino, Quantitative characterization of porosity in stainless steel LENS powders and deposits, Mater. Charact. 57 (2006) 36-43.
[123] M. Bambach, I. Sizova, F. Silze, M. Schnick, Comparison of laser metal deposition of Inconel 718 from powder, hot and cold wire, Procedia CIRP 74 (2018) 206-209.
[124] C. Zhong, A. Gasser, T. Schopphoven, R. Poprawe, Experimental study of porosity reduction in high deposition-rate Laser Material Deposition, Opt. Laser Technol. 75 (2015) 87-92.
[125] O. Fergani, F. Berto, T. Welo, S. Liang, Analytical modelling of residual stress in additive manufacturing, Fatigue Fract. Eng. Mater. Struct. 40 (2017) 971-978.
[126] P. Mercelis, J.P. Kruth, Residual stresses in selective laser sintering and selective laser melting, Rapid Prototyp. J. 12 (2006) 254-265.
[127] Y. Liu, Y. Yang, D. Wang, A study on the residual stress during selective laser melting (SLM) of metallic powder, Int. J. Adv. Manuf. Technol. 87 (2016) 647-656.
[128] M. Shiomi, K. Osakada, K. Nakamura, T. Yamashita, F. Abe, Residual stress within metallic model made by selective laser melting process, CIRP Ann. 53 (2004) 195-198.
[129] J. Fang, S. Li, S. Dong, Y. Wang, H. Huang, Y. Jiang, B. Liu, Effects of phase transition temperature and preheating on residual stress in multi-pass & multi-layer laser metal deposition, J. Alloys Compd. 792 (2019) 928-937.
[130] S. Zou, H. Xiao, F. Ye, Z. Li, W. Tang, F. Zhu, C. Chen, C. Zhu, Numerical analysis of the effect of the scan strategy on the residual stress in the multi-laser selective laser melting, Results Phys. 16 (2020) 103005.
[131] M. Froend, F.E. Bock, S. Riekehr, N. Kashaev, B. Klusemann, J. Enz, Experimental investigation of temperature distribution during wire-based laser metal deposition of the Al-Mg alloy 5087, Mater. Sci. Forum 941 (2019) 988-994.
[132] T. Böllinghaus, H. Herold, C.E. Cross, J.C. Lippold, Hot cracking phenomena in welds II, first ed., Springer Science & Business Media, Berlin, 2008.
[133] X. Zhang, Z. Cao, P. Zhao, Investigation on solidification cracks in pulsed laser spot welding of an AZ31 magnesium alloy, Opt. Laser Technol. 126 (2020) 106132.
[134] F.M. Ghaini, M. Sheikhi, M. Torkamany, J. Sabbaghzadeh, The relation between liquation and solidification cracks in pulsed laser welding of 2024 aluminium alloy, Mater. Sci. Eng. A 519 (2009) 167-171.
[135] Y. Chen, K. Zhang, J. Huang, S.R.E. Hosseini, Z. Li, Characterization of heat affected zone liquation cracking in laser additive manufacturing of Inconel 718, Mater. Des. 90 (2016) 586-594.
[136] G. Young, T. Capobianco, M. Penik, B. Morris, J. McGee, The mechanism of ductility dip cracking in nickelchromium alloys, Weld. J. 87(2) (2008) 31.
[137] C. Fink, An investigation on ductility-dip cracking in the base metal heat-affected zone of wrought nickel base alloys—part I: metallurgical effects and cracking mechanism, Weld. World 60 (2016) 939-950.
[138] A. Ramirez, J. Lippold, High temperature behavior of Ni-base weld metal: Part II–Insight into the mechanism for ductility dip cracking, Mater. Sci. Eng. A 380 (2004) 245-258.

[139] J.H. Martin, B.D. Yahata, J.M. Hundley, J.A. Mayer, T.A. Schaedler, T.M. Pollock, 3D printing of highstrength aluminium alloys, Nature 549 (2017) 365-369.
[140] L. Parry, I. Ashcroft, R.D. Wildman, Understanding the effect of laser scan strategy on residual stress in selective laser melting through thermo-mechanical simulation, Addit. Manuf. 12 (2016) 1-15.
[141] T. Dursun, C. Soutis, Recent developments in advanced aircraft aluminium alloys, Mater. Des. 56 (2014) 862-871.
[142] T. C. Lin, C. Cao, M. Sokoluk, L. Jiang, X. Wang, J.M. Schoenung, E.J. Lavernia, X. Li, Aluminum with dispersed nanoparticles by laser additive manufacturing, Nat. Commun. 10 (2019) 4124.
[143] J. Zhang, Y. Liu, G. Sha, S. Jin, Z. Hou, M. Bayat, N. Yang, Q. Tan, Y. Yin, S. Liu, Designing against phase and property heterogeneities in additively manufactured titanium alloys, Nat. Commun. 13 (2022) 4660.
[144] Q. Li, G. Li, X. Lin, D. Zhu, J. Jiang, S. Shi, F. Liu, W. Huang, K. Vanmeensel, Development of a high strength Zr/Sc/Hf-modified Al-Mn-Mg alloy using Laser Powder Bed Fusion: Design of a heterogeneous microstructure incorporating synergistic multiple strengthening mechanisms, Addit. Manuf. 57 (2022) 102967.
[145] C. Ma, Y. Yan, Z. Yan, Y. Liu, X. Wu, D. Li, L. Zhao, P. Liu, H. Jin, Investigation of bypass-coupled doublepulsed directed energy deposition of Al–Mg alloys, Addit. Manuf. 58 (2022) 103058.
[146] P. Jiang, X. Li, X. Zong, X. Wang, Z. Chen, H. Yang, C. Liu, N. Gao, Z. Zhang, Multi-wire arc additive manufacturing of Ti basic heterogeneous alloy: Effect of deposition current on the microstructure, mechanical property and corrosion-resistance, J. Alloys Compd. 920 (2022) 166056.
[147] P. Wang, H. Li, K. Prashanth, J. Eckert, S. Scudino, Selective laser melting of Al-Zn-Mg-Cu: Heat treatment, microstructure and mechanical properties, J. Alloys Compd. 707 (2017) 287-290.
[148] J. Xiong, Y. Lei, R. Li, Finite element analysis and experimental validation of thermal behavior for thinwalled parts in GMAW-based additive manufacturing with various substrate preheating temperatures, Appl. Therm. Eng. 126 (2017) 43-52.
[149] L. Mugwagwa, D. Dimitrov, S. Matope, I. Yadroitsev, Evaluation of the impact of scanning strategies on residual stresses in selective laser melting, Int. J. Adv. Manuf. Technol. 102 (2019) 2441-2450.
[150] P. Bian, J. Shi, Y. Liu, Y. Xie, Influence of laser power and scanning strategy on residual stress distribution in additively manufactured 316L steel, Opt. Laser Technol. 132 (2020) 106477.
[151] D. Koutny, D. Palousek, L. Pantelejev, C. Hoeller, R. Pichler, L. Tesicky, J. Kaiser, Influence of scanning strategies on processing of aluminum alloy EN AW 2618 using selective laser melting, Mater. 11 (2018) 298.
[152] C. Ye, C. Zhang, J. Zhao, Y. Dong, Effects of post-processing on the surface finish, porosity, residual stresses, and fatigue performance of additive manufactured metals: a review, J. Mater. Eng. Perform. 30 (2021) 6407-6425.
[153] A.B. Spierings, K. Dawson, T. Heeling, P.J. Uggowitzer, R. Schäublin, F. Palm, K. Wegener, Microstructural features of Sc-and Zr-modified Al-Mg alloys processed by selective laser melting, Mater. Des. 115 (2017) 52-63.
[154] G. Dinda, A. Dasgupta, J. Mazumder, Texture control during laser deposition of nickel-based superalloy, Scripta Mater. 67 (2012) 503-506.
[155] H. Wei, J. Mazumder, T. DebRoy, Evolution of solidification texture during additive manufacturing, Sci. Rep. 5 (2015) 1-7.
[156] S. Kou, Welding metallurgy, second ed., John Wiley & Sons Inc., New Jersey, 2002.

[157] M. Froend, V. Ventzke, F. Dorn, N. Kashaev, B. Klusemann, J. Enz, Microstructure by design: An approach of grain refinement and isotropy improvement in multi-layer wire-based laser metal deposition, Mater. Sci. Eng. A 772 (2020) 138635.
[158] J. Park, J. H. Kang, C. S. Oh, Phase-field simulations and microstructural analysis of epitaxial growth during rapid solidification of additively manufactured AlSi10Mg alloy, Mater. Des. 195 (2020) 108985.
[159] X. Li, W. Tan, Numerical investigation of effects of nucleation mechanisms on grain structure in metal additive manufacturing, Comput. Mater. Sci. 153 (2018) 159-169.
[160] W. Reschetnik, J. P. Brüggemann, M. Aydinöz, O. Grydin, K. P. Hoyer, G. Kullmer, H. Richard, Fatigue crack growth behavior and mechanical properties of additively processed EN AW-7075 aluminium alloy, Procedia Struct. Integr. 2 (2016) 3040-3048.
[161] L. Li, R. Li, T. Yuan, C. Chen, Z. Zhang, X. Li, Microstructures and tensile properties of a selective laser melted Al–Zn–Mg–Cu (Al7075) alloy by Si and Zr microalloying, Mater. Sci. Eng. A 787 (2020) 139492.
[162] M. Opprecht, J.-P. Garandet, G. Roux, C. Flament, M. Soulier, A solution to the hot cracking problem for aluminium alloys manufactured by laser beam melting, Acta Mater. 197 (2020) 40-53.
[163] X.P. Li, G. Ji, Z. Chen, A. Addad, Y. Wu, H. Wang, J. Vleugels, J. Van Humbeeck, J. P. Kruth, Selective laser melting of nano-TiB_2 decorated AlSi10Mg alloy with high fracture strength and ductility, Acta Mater. 129 (2017) 183-193.
[164] T. Zhao, M. Dahmen, W. Cai, M. Alkhayat, J. Schaible, P. Albus, C. Zhong, C. Hong, T. Biermann, H. Zhang, Laser metal deposition for additive manufacturing of AA5024 and nanoparticulate TiC modified AA5024 alloy composites prepared with balling milling process, Opt. Laser Technol. 131 (2020) 106438.
[165] T.Y. Ansell, T. Hanneman, A. Gonzalez-Perez, C. Park, A. Nieto, Effect of high energy ball milling on spherical metallic powder particulates for additive manufacturing, Part. Sci. Technol. 39 (2021) 981-989.
[166] W. Zhai, W. Zhou, S.M.L. Nai, J. Wei, Characterization of nanoparticle mixed 316 L powder for additive manufacturing, J. Mater. Sci. Technol. 47 (2020) 162-168.
[167] R. Wang, L. Xi, K. Ding, B. Gökce, S. Barcikowski, D. Gu, Powder preparation during ball milling and laser additive manufacturing of aluminum matrix nanocomposites: powder properties, processability and mechanical property, Adv. Powder Technol. 33 (2022) 103687.
[168] S. Catchpole-Smith, A.T. Clare, In-situ synthesis of titanium aluminides by direct metal deposition, J. Mater. Process. Technol. 239 (2017) 230-239.
[169] M.L. Montero-Sistiaga, R. Mertens, B. Vrancken, X. Wang, B. Van Hooreweder, J. P. Kruth, J. Van Humbeeck, Changing the alloy composition of Al7075 for better processability by selective laser melting, J. Mater. Process. Technol. 238 (2016) 437-445.
[170] D. Gu, H. Wang, D. Dai, P. Yuan, W. Meiners, R. Poprawe, Rapid fabrication of Al-based bulk-form nanocomposites with novel reinforcement and enhanced performance by selective laser melting, Scripta Mater. 96 (2015) 25-28.
[171] X. Wen, Q. Wang, Q. Mu, N. Kang, S. Sui, H. Yang, X. Lin, W. Huang, Laser solid forming additive manufacturing TiB_2 reinforced 2024Al composite: Microstructure and mechanical properties, Mater. Sci. Eng. A 745 (2019) 319-325.
[172] B. Jiang, L. Zhenglong, C. Xi, L. Peng, L. Nannan, C. Yanbin, Microstructure and mechanical properties of TiB_2-reinforced 7075 aluminum matrix composites fabricated by laser melting deposition, Ceram. Int. 45 (2019) 5680-5692.
[173] X. Xi, B. Chen, C. Tan, X. Song, J. Feng, Microstructure and mechanical properties of SiC reinforced AlSi10Mg composites fabricated by laser metal deposition, J. Manuf. Process. 58 (2020) 763-774.
[174] M. Ghasri-Khouzani, H. Karimialavijeh, M. Pröbstle, R. Batmaz, W. Muhammad, A. Chakraborty, T. Sabiston, J. Harvey, É. Martin, Processability and characterization of A20X

aluminum alloy fabricated by laser powder bed fusion, Mater. Today Commun. 35 (2023) 105555.
[175] J.R. Croteau, S. Griffiths, M.D. Rossell, C. Leinenbach, C. Kenel, V. Jansen, D.N. Seidman, D.C. Dunand, N.Q. Vo, Microstructure and mechanical properties of Al-Mg-Zr alloys processed by selective laser melting, Acta Mater. 153 (2018) 35-44.
[176] M. Bärtl, X. Xiao, J. Brillo, F. Palm, Influence of surface tension and evaporation on melt dynamics of aluminum alloys for laser powder bed fusion, J. Mater. Eng. Perform. 31 (2022) 6221-6233.
[177] D. Schimbäck, P. Mair, M. Bärtl, F. Palm, G. Leichtfried, S. Mayer, P.J. Uggowitzer, S. Pogatscher, Alloy design strategy for microstructural-tailored scandium-modified aluminium alloys for additive manufacturing, Scripta Mater. 207 (2022) 114277.
[178] A. Bandyopadhyay, K.D. Traxel, M. Lang, M. Juhasz, N. Eliaz, S. Bose, Alloy design via additive manufacturing: Advantages, challenges, applications and perspectives, Mater. Today 52 (2022) 207-224.
[179] L. Yan, Y. Chen, F. Liou, Additive manufacturing of functionally graded metallic materials using laser metal deposition, Addit. Manuf. 31 (2020) 100901.
[180] M. Li, J. Gazquez, A. Borisevich, R. Mishra, K.M. Flores, Evaluation of microstructure and mechanical property variations in AlxCoCrFeNi high entropy alloys produced by a high-throughput laser deposition method, Intermetallics 95 (2018) 110-118.
[181] M. Kottman, S. Zhang, J. McGuffin-Cawley, P. Denney, B.K. Narayanan, Laser hot wire process: a novel process for near-net shape fabrication for high-throughput applications, JOM 67 (2015) 622-628.
[182] D. Kong, C. Dong, X. Ni, L. Zhang, C. Man, G. Zhu, J. Yao, L. Wang, X. Cheng, X. Li, Effect of TiC content on the mechanical and corrosion properties of Inconel 718 alloy fabricated by a high-throughput dual-feed laser metal deposition system, J. Alloys Compd. 803 (2019) 637-648.
[183] H. Dobbelstein, E.P. George, E.L. Gurevich, A. Kostka, A. Ostendorf, G. Laplanche, Laser metal deposition of refractory high-entropy alloys for high-throughput synthesis and structure-property characterization, Int. J. Extreme Manuf. 3 (2020) 015201.
[184] I. El Naqa, M.J. Murphy, What is machine learning?, in: I. El Naqa, Li R., M.J. Murphy (Eds.), Machine Learning in Radiation Oncology, Springer, Cham, 2015, pp. 3-11.
[185] L. Meng, B. McWilliams, W. Jarosinski, H.-Y. Park, Y.-G. Jung, J. Lee, J. Zhang, Machine learning in additive manufacturing: a review, JOM 72 (2020) 2363-2377.
[186] M.I. Jordan, T.M. Mitchell, Machine learning: Trends, perspectives, and prospects, Science 349 (2015) 255-260.
[187] F. Chollet, Deep learning with Python, first ed., Manning Publications, Shelter Island, 2021.
[188] N. Johnson, P. Vulimiri, A. To, X. Zhang, C. Brice, B. Kappes, A. Stebner, Invited review: Machine learning for materials developments in metals additive manufacturing, Addit. Manuf. 36 (2020) 101641.
[189] H. Ko, P. Witherell, Y. Lu, S. Kim, D.W. Rosen, Machine learning and knowledge graph based design rule construction for additive manufacturing, Addit. Manuf. 37 (2021) 101620.
[190] W. Rong-Ji, L. Xin-Hua, W. Qing-Ding, W. Lingling, Optimizing process parameters for selective laser sintering based on neural network and genetic algorithm, Int. J. Adv. Manuf. Technol. 42 (2009) 1035-1042.
[191] C. Silbernagel, A. Aremu, I. Ashcroft, Using machine learning to aid in the parameter optimisation process for metal-based additive manufacturing, Rapid Prototyp. J. 26 (2020) 625-637.
[192] Y. Zhang, S. Yang, G. Dong, Y.F. Zhao, Predictive manufacturability assessment system for laser powder bed fusion based on a hybrid machine learning model, Addit. Manuf. 41 (2021) 101946.

[193] J. Li, Y. Zhang, X. Cao, Q. Zeng, Y. Zhuang, X. Qian, H. Chen, Accelerated discovery of high-strength aluminum alloys by machine learning, Commun. Mater. 1 (2020) 73.
[194] Z. Rao, P. Y. Tung, R. Xie, Y. Wei, H. Zhang, A. Ferrari, T. Klaver, F. Körmann, P.T. Sukumar, A. Kwiatkowski da Silva, Machine learning–enabled high-entropy alloy discovery, Science 378 (2022) 78-85.
[195] Z. Ren, L. Gao, S.J. Clark, K. Fezzaa, P. Shevchenko, A. Choi, W. Everhart, A.D. Rollett, L. Chen, T. Sun, Machine learning–aided real-time detection of keyhole pore generation in laser powder bed fusion, Science 379 (2023) 89-94.
[196] F. Caiazzo, A. Caggiano, Laser direct metal deposition of 2024 Al alloy: trace geometry prediction via machine learning, Mater. 11 (2018) 444.
[197] C. Wacker, M. Köhler, M. David, F. Aschersleben, F. Gabriel, J. Hensel, K. Dilger, K. Dröder, Geometry and distortion prediction of multiple layers for wire arc additive manufacturing with artificial neural networks, Appl. Sci. 11 (2021) 4694.
[198] Y. Han, R.J. Griffiths, Z.Y. Hang, Y. Zhu, Quantitative microstructure analysis for solid-state metal additive manufacturing via deep learning, J. Mater. Res. 35 (2020) 1936-1948.
[199] X. Xie, J. Bennett, S. Saha, Y. Lu, J. Cao, W.K. Liu, Z. Gan, Mechanistic data-driven prediction of as-built mechanical properties in metal additive manufacturing, NPJ Comput. Mater. 7 (2021) 1-12.
[200] C. Wang, S. Chandra, S. Huang, S.B. Tor, X. Tan, Unravelling process-microstructure-property correlations in powder-bed fusion additive manufacturing through information-rich surface features with deep learning, J. Mater. Process. Technol. 311 (2022) 117804.
[201] Z. Zhan, H. Li, Machine learning based fatigue life prediction with effects of additive manufacturing process parameters for printed SS 316L, Int. J. Fatigue 142 (2021) 105941.
[202] G.X. Gu, C. T. Chen, D.J. Richmond, M.J. Buehler, Bioinspired hierarchical composite design using machine learning: simulation, additive manufacturing, and experiment, Mater. Horiz. 5 (2018) 939-945.
[203] X. Yao, S.K. Moon, G. Bi, A hybrid machine learning approach for additive manufacturing design feature recommendation, Rapid Prototyp. J. 23 (2017) 983-997.
[204] I. Sosnovik, I. Oseledets, Neural networks for topology optimization, Russ. J. Numer. Anal. Math. Model. 34 (2019) 215-223.
[205] D.A. White, W.J. Arrighi, J. Kudo, S.E. Watts, Multiscale topology optimization using neural network surrogate models, Comput. Methods Appl. Mech. Eng. 346 (2019) 1118-1135.
[206] Y. Yu, T. Hur, J. Jung, Deep learning for topology optimization design, arXiv preprint arXiv:1801.05463 (2018).
[207] S. Rawat, M. Shen, A novel topology design approach using an integrated deep learning network architecture, arXiv preprint arXiv:1808.02334 (2018).
[208] K. Wasmer, T. Le-Quang, B. Meylan, S.A. Shevchik, In situ quality monitoring in AM using acoustic emission: A reinforcement learning approach, J. Mater. Eng. Perform. 28 (2019) 666-672.
[209] Y. Li, Y. Sun, Q. Han, G. Zhang, I. Horváth, Enhanced beads overlapping model for wire and arc additive manufacturing of multi-layer multi-bead metallic parts, J. Mater. Process. Technol. 252 (2018) 838-848.
[210] Z. Lanc, M. Zeljković, B. Štrbac, A. Živković, I. Drstvenšek, M. Hadžistević, The determination of the emissivity of aluminum alloy AW 6082 using infrared thermography, J. Prod. Eng. 18 (2015) 23-26.
[211] N. Schell, A. King, F. Beckmann, T. Fischer, M. Müller, A. Schreyer, The high energy materials science beamline (HEMS) at PETRA III, Mater. Sci. Forum 772 (2014), 57-61.
[212] M.T. Hutchings, P. J. Withers, T. M. Holden, T. Lorentzen, Introduction to the characterization of residual stress by neutron diffraction, first ed., CRC press, Boca Raton, 2005.
[213] H. Wern, R. Johannes, H. Walz, Dependence of the X-ray elastic constants on the diffraction plane, Phys. Status Solidi (B) 206 (1998) 545-557.

[214] M. Tang, J. Huang, Y. Zhang, S. Luo, Full strain tensor measurements with X-ray diffraction and strain field mapping: a simulation study, J. Synchrotron Rad. 27 (2020) 646-652.
[215] M. Steinzig, E. Ponslet, Residual stress measurement using the hole drilling method and laser speckle interferometry: part 1, Exp. Tech. 27 (2003) 43-46.
[216] J. Reijonen, A. Revuelta, T. Riipinen, K. Ruusuvuori, P. Puukko, On the effect of shielding gas flow on porosity and melt pool geometry in laser powder bed fusion additive manufacturing, Addit. Manuf. 32 (2020) 101030.